A STUDY OF COHERENT MOTIONS IN A TURBULENT FLOW SUBJECTED TO ADVERSE PRESSURE GRADIENT.

By

AKAMABE EMMANUEL TANJO

A thesis submitted to
the Faculty of Graduate Studies of the University of Manitoba
in partial fulfillment of the requirements for
the Doctor of Philosophy degree

Mechanical and Industrial Engineering Department
University of Manitoba
May 1992

ISBN 0-315-78026-6

A STUDY OF COHERENT MOTIONS IN A TURBULENT FLOW SUBJECTED TO ADVERSE PRESSURE GRADIENT

BY

AKAMABE EMMANUEL TANJO

A Thesis submitted to the Faculty of Graduate Studies of the University of Manitoba in partial fulfillment of the requirements for the degree of

DOCTOR OF PHILOSOPHY

ABSTRACT

The structure of turbulence in a conical diffuser with a fully developed pipe flow at entry and subjected to a varying adverse pressure gradient has been studied from measurements of long-time averaged turbulence quantities and from the evaluation of coherent motions. Macroscopic views of the structure of turbulence can be inferred from long-time averaged measurements but it is the evaluation of coherent structures that clearly establishes the mechanism of turbulence in the diffuser flow.

The four classes of fluid motions responsible for momentum transfer, outward interactions, ejections, inward interactions and sweeps, are found to be as important in an adverse pressure gradient turbulent flow as has been observed in other wall-bounded shear flows. However, the distribution of the dominating coherent motions, sweeps and ejections, are distorted as the flow proceeds towards separation. Based on the statistical properties of the coherent motions, a conceptual model is adopted from the literature to explain the dynamics of the educed structures and their distribution in the flow geometry. Thus, two shear layers are very important in evaluating the structure of turbulence in the conical diffuser. A mean shear layer close to the wall and a maximum shear stress layer, the peak region, which is gradually displaced towards the axis of the flow with prolonged wall divergence. Essentially, the dynamics of the turbulence structures involves the transport of typical eddies by large scale outer motions to the wall. The resulting interaction between the typical eddies

and the wall mean shear layer leads to the formation of pockets and hairspin vortices. The outward growth of these vortices from the wall is initially enhanced because characteristics that influence the outward motion of vortices rapidly increase upto the peak region then decrease towards the axis of the flow. Therefore, the region between the wall mean shear layer and the peak region is populated by pocket vortices which are initially the footprint of sweeps, then become associated with ejections at the later stages of growth. The rapid outward growth of vortices between the two shear layers also results in hairspin vortices re-connecting to form typical eddies further from the wall than in flows with slower outward growth. Hence the peak region, where the outward motion attains stability, is a logical location for vortex regeneration. This attribute of the peak region makes the explanation of other characteristics of this region possible. These characteristics include; (1) Maximum values of the averaged Reynolds shear stress and mean kinetic energy of turbulence, (2) maximum production and dissipation of turbulent kinetic energy, (3) nearly normal distributions of the probability density of fluctuating velocities, and (4) equal contributions of sweeps and ejections as well as equal contributions of inward and outward interactions to the averaged Reynolds stress. The domination of the coherent motions from the wall to the peak region by sweeps is strengthened by inactive motions which lead to high intensity of turbulence but not to burst producing stresses.

With regard to experimental techniques, this study has produced a correction procedure for static pressures in an adverse pressure gradient turbulent flow which does not depend on calibration constants of the pressure probes and the use of hot-wire anemometers to measure velocity fluctuations. Also, a pattern recognition scheme has been developed to evaluate temporal statistical characteristics of coherent structures. Unlike existing methods which are limited to low Reynolds number flows, the present pattern recognition scheme can be calibrated against known results and has been successfully applied in a fully developed pipe flow with high Reynolds number as well as in a high intensity, varying adverse pressure gradient turbulent flow.

ACKNOWLEDGEMENTS

The author would like to express his deepest gratitude to Dr. R. S. Azad for his guidance, help and advise during the course of this study. Thanks are also due to Dr. R. W. Derksen for reading and offering advice on the original manuscript and to Mr. K. Tarte for help with the maintenance and use of equipment.

I gratefully acknowledge the financial support of the National Science and Engineering Research Council of Canada through the grant to Professor R. S. Azad; interim graduate fellowship from the Faculty of Graduate Studies and teaching assistantship from the Department of Mechanical and Industrial engineering of the University of Manitoba. I am forever grateful to the Federal Government of Nigeria whose scholarship paved the way for graduate study.

I am very grateful for the love, support and understanding of my wife, Tracey and my son, Sitaron as well as to all members of my family. I could not have completed this program without their help. Finally, I dedicate this thesis to Francis Sitar Tanjo, my elder brother, who passed away just before this program was completed.

TABLE OF CONTENTS

LIST OF TABLES

LIST OF FIGURES

FIGURE		PAGE

NOMENCLATURE

A, B	Linearization constants for single-wire. (Subscripts 1 & 2 refer to the two sensors of x-wire)
B_s	Characteristic length scale of a boundary layer defined as a wall confined wake.
A', B'	Calibration constants of static and total pressure tubes respectively.
C_{pqr}	Coefficients in the power series expansion of the characteristic function.
$D_J(H,K)$	Array of the duration of events as a function of the quadrant, hole size and the position of event.
E	Mean voltage of the hot-wire.
$\tilde{E}$	Instantaneous mean voltage of the hot-wire.
E_{off}	Off-set voltage for the hot-wire signal.
$e, e_i, e_i(t)$	A.C. components of the hot-wire signal.
$F_{II}(x)$	Cumulative probability distribution function of second-order moments with respect to x.
f_k	Kolmogoroff's frequency.
G, G_1, G_2	Effective gain, pre-gain and post gain respectively. (Applied during signal processing)
H	Hole size or threshold for evaluating the relative strength of coherent structures $(= \lvert uv \rvert / u'v')$.
H_c	Characteristic hole size for which ejections are the only major contributors to the averaged Reynolds stress (Usually $H_c = 4$).
$H_n(\chi)$	One-dimensional Hermite polynomial.
I	An integer corresponding to the class interval of the A/D converter $(0 \leq I \leq 4096)$.

I_{lm}	Integral approximation of the p.d.f. of second-order moments by an infinite series of terms.
$I_n(\chi)$	Modified Bessel functions of the first kind of order n.
J	Quadrant in the u,v plane (=1,...4).
K	The sum of local variables , p+q+r, in the theoretical analysis of coherent structures.
k	Yaw factor.
$K_n(\chi)$	Modified Bessel functions of the second kind of order n.
k_{pqr}	Cumulants. (from the definition of characteristic function)
$k_0(J)$, $k_1(J)$	Constants for calibrating the pattern recognition scheme.
L(H,J)	Dummy arrays that indicate the initial points in a pattern.
l_J	Streamwise size of an event.
L_s	Distance from the wall to the position of maximum shear stress.
M(H,J)	Dummy array that places an event in the J^{Th} quadrant.
$M_e(i)$	An array containing the average values of mathematical operations on the fluctuating voltages.
m_{pqr}	Moments (from the definition of the characteristic function).
N	Total number of samples in a record.
N_I	Total number of samples in the I^{Th} class interval of the A/D converter.
$N_J(H)$	Frequency of occurrence of and event, J, evaluated at a hole size, H.
NSO(H,J)	Dummy array indicating the sample numbers of the leading edge of events.
NSF(H,J)	Dummy array indicating the sample number of the trailing edge of events.
P	Pressure. Subscripts: s, sm, sc $\Rightarrow$ static pressures subscripts: T, Tm $\Rightarrow$ total pressures

$P_J(H,K)$	Array indicating the time from the beginning of the record to the leading edge of each event.
P_T	Dimensionless parameter describing the relative influence of wall pressure gradient and the wall shear stress on each eddy that passes by (= $-u_*/[N_J(H)\tau_w]dP_w/dx$).
Q1,.. Q4	Quadrants in the u,v plane.
$\overline{q^2}$	Total turbulent energy (= $\overline{u^2}+\overline{v^2}+\overline{w^2}$)
R	Local radius at a measuring station.
R_p	Pipe radius.
R_{uv}, R_{uw}, R_{vw}	Correlation coefficient of the velocity components in subscript.
r	radial distance from the axis of the flow to the measuring point.
s_{ij}	Fluctuating strain rate.
T_J	Mean period between events in the J^{Th} quadrant.
T_J^*	Dimensionless form of T_J ($=T_JU_{c,p}/R_p$).
ΔT_J	Mean duration of events in the J^{Th} quadrant.
$T^*_{\frac{1}{2}}(x)$	Width at half height of the ensemble average signal of x.
t_i	Initial time of an event.
t_*	Inner time scale (= ν/u_*^2).
U	Local mean velocity in x-direction.
U^+	Dimensionless local mean velocity ($=U/u_*$).
U_b	Cross-sectional average mean velocity (x-direction) in pipe.
U_{cor}	Local mean velocity corrected from pressure measurements.
U_c	Local centerline velocity at a measuring station.
$U_{c,p}$	Centerline velocity in the pipe.

U_m	Velocity scale for flows approaching separation $(=\sqrt{-\overline{uv}})$.
U_f	Mean velocity obtained obtained from the half power law plot ($Y^{\frac{1}{2}}$ vs U).
U_{SL}	Local mean velocity obtained by measuring both the total and static pressures at a radial position.
U_{SL}	Local mean velocity obtained by taking the pressure difference between a total pressure tube at any radial position and the wall static pressure tappings.
U_∞	Free stream velocity.
u	Fluctuating velocity in x-direction.
u_*	Friction velocity.
V	mean radial velocity.
v	Fluctuating velocity in radial direction.
V_q	Turbulent transport velocity $(=\overline{vq^2}/\overline{q^2})$.
V_τ	turbulent transport velocity $(\sim\overline{uv^2}/\overline{uv})$.
w	Fluctuating velocity in the lateral direction.
Y	Radial distance from the wall and perpendicular to the axis.
Y^+	Dimensionless position $(= Yu_*/\nu)$.
α_1	Dimensionless pressure gradient $((10^{-6}\nu/\rho U_\infty^3)dp/dx)$.
α_2	Dimensionless pressure gradient $(= (2D_p/\rho U_b^2)dp/dx)$.
β	Turbulence parameter $(=\overline{u^2}/\overline{u_n^2})$.
ξ, η, λ	Arguments of the characteristic function.
$\psi(\xi, \eta, \lambda)$	The characteristic function.
λ_z	Spanwise spacings between strong ejections in cartesian coordinates.

λ_θ	Spanwise spacings between strong ejections in cylindrical coordinates
χ	Dummy argument used in Hermite polynomials.
δ^*	Displacement thickness.
τ	Time coordinate relative to the reference time in the evaluation of ensemble averages.
τ^+	Dimensionless form of τ $(= \tau/t_*)$.
τ_j	Time delay.
τ_w	Wall shear stress.
γ_J	Intermittency factor of $-\overline{uv}$ during bursting as a function of the event.

CHAPTER 1

INTRODUCTION

Turbulence is characterized by three-dimensional vorticity and consists of both large and small scale structures. Classical statistical methods consider the large scale structures to be mostly random and chaotic, while in the modern view, turbulence is populated with repeating, quasi-deterministic large scale structures. The new perception has greatly improved the understanding of the nature of turbulence and the search for the dynamic and statistical significance of the coherent motions has led to improvements in experimental techniques.

The study of turbulence is synonymous with the study of the Navier-Stokes equations which in spite of having been analyzed in great detail have no known quantitative solution. Statistical analysis of the equations of motion result in the closure problem of turbulence theory in which there are more unknowns than equations. However the statistical theory of turbulence is very important as it provides the basis for experimental investigations with the ultimate goal of solving the closure problem through selective elimination of less important terms. As pointed out by Townsend (1956), the dynamics of turbulence can best be understood from a consideration of the turbulent energy budget. Derivation of the turbulent kinetic energy (TKE) equation can be found in Hinze (1959) using rectangular coordinates and Laufer (1954) using cylindrical coordinates. The equation governing the mean kinetic energy , $\overline{u_i^2}/2$, of the turbulent velocity fluctuations can be written [Tennekes and Lumley (1985)] as

$$U_j \frac{\partial}{\partial x_j}\left(\frac{\overline{u_i^2}}{2}\right) = -\frac{\partial}{\partial x_j}\{\frac{1}{\rho}\overline{u_j p} + \frac{1}{2}\overline{u_i^2 u_j} - 2\nu\overline{u_i s_{ij}}\}$$

$$-\overline{u_i u_j}\left(\frac{\partial U_i}{\partial x_j} + \frac{\partial U_j}{\partial x_i}\right) + 2\nu\overline{s_{ij}s_{ij}} \qquad 1.1$$

where s_{ij} is the fluctuating strain rate

$$s_{ij} = \frac{1}{2}\left(\frac{\partial u_i}{\partial x_j} + \frac{\partial u_j}{\partial x_i}\right)$$

Physically Eq. (1.1) implies that the total change in the kinetic energy per unit mass $\overline{u_i^2}/2$ of a turbulent fluid is due to the transport of kinetic energy to and from the control volume (first term on the right) and energy created or lost due to deformation work within the control volume (last two terms on the right). The transport term is made up of interactions due to viscous stresses, pressure gradient work and turbulent velocity fluctuations. These quantities represent a divergence of energy flux and serve to redistribute energy internally within the flow if a control volume encompasses all the turbulent region. The turbulence energy production term, $-\overline{u_i u_j}(\partial U_i/\partial x_j + \partial U_j/\partial x_i)$ sustains turbulence by extracting energy from the mean flow. On the other hand, the dissipation term, $2\nu\overline{s_{ij}s_{ij}}$ is the rate at which viscous stresses perform deformation work against the fluctuating strain rate representing a drain of turbulent energy.

The local balance of production, transport and dissipation of TKE has great significance in all turbulent flows. Townsend (1956) had shown that the transfer of energy from the mean flow to turbulence attain very high values near the wall where incidentally the fluctuating strain rates also have high values resulting in large energy dissipation. It follows that the concentration of turbulence activity, large values of the production and dissipation of TKE, in the near wall region makes it a logical location for studying the structure of turbulence. Through similar reasoning, Kline et al. (1967) started flow visualization experiments in order to understand the mechanism of the production of TKE in wall bounded flows. Using a combined dye-injection and hydrogen-bubble technique it was observed that low-speed sublayer streaks intermittently oscillated then break up in a violent upward motion which was referred to as a 'burst'. The observed structures had a quasi-periodic repeating patterns with much larger scales than the background turbulence, fuelling the hope that statistical methods could be used to characterize them. One of the most important observations of the pioneering experiments was that more than 70% of the energy produced by turbulence occurred during the ejection phase. The other important TKE term is dissipation and has been actively studied via spectral analysis. Both production and dissipation of TKE are important for the maintenance of turbulence and as a result they are closely associated with coherent motions.

The present study is part of an ongoing research program established more than twenty years ago to study the structure of turbulence in a conical diffuser. A conical diffuser can be considered as a flow device with a gradual area increase above the inlet pipe value and designed to reduce velocity and kinetic energy of the inlet flow, while at the same time producing higher pressure. The increasing pressure in the diffuser is an unfavorable gradient and can result in highly variable flow patterns, boundary layer separation, and poor performance. The choice of a diffuser with a fully developed pipe flow at entry, 8 degrees included angle and an area ratio of 4:1, was based on established criteria for optimum pressure recovery [see Sprenger (1959) and Sovran and Klomp (1967)]. The program has produced numerous results which has greatly improved understanding of turbulence in the diffuser flow. These include the initial detailed set-up analysis and turbulence characteristics [Okwuobi and Azad (1973)], TKE balance and vorticity measurements [Arora and Azad (1980 a, b)], similarity of structure functions with other wall bounded flows [Azad and Hummel (1979, 1981)] and measurements of various characteristics of the flow and spectral analysis [Kassab (1986) and Azad and Kassab (1989)].

In the present work, the structure of turbulence in the conical diffuser is studied from the point of view of organized motions that contribute to the shear-stress production. Part of this topic, the contributions of different events to the time averaged Reynolds stress, had been investigated by Hummel (1978) using analogue circuits. Digital methods are used in the present study and, in addition, the contributions of the different fluid motions to the Reynolds stress production are independently obtained from conditional probability density distribution of velocity and the application of cumulant-discard method. Various temporal statistics of the coherent motions are also evaluated using a pattern recognition scheme developed during the course of this study. The trend of the educed structures across the flow at six measuring stations in the diffuser are compared with similar measurements in the fully developed pipe flow with a view of establishing the effect of adverse pressure gradient on the coherent motions.

A background review of the relevant literature is given in Chapter 2. The experimental set-up and procedures are briefly described in Chapter 3. Chapters 4 and 5 contain the results of long-time-averaged quantities and statistical evaluations of coherent structures respectively. In Chapter 6 an overview and the implications of the results are discussed. The concluding remarks are made in Chapter 7.

CHAPTER 2

LITERATURE REVIEW

2.1 OBSERVATION OF ORGANIZED MOTIONS IN TURBULENT FLOWS.

A large amount of literature exists from the study of the structure of turbulence using various flow configurations, therefore the scope of this review is limited to wall bounded shear flows. The reader is referred to more extensive reviews by Willmarth (1975), Cantwell (1981), Hussian (1983), Antonia (1983), Ho and Heurre (1984), Lui (1989) and Robinson (1991 a,b).

Pioneering investigations of the modern views on turbulence may be traced to the study of the intermittent nature of turbulence in free shear flows by Corrsin (1943), Townsend (1947) and Corrsin and Kistler (1955). Other investigations include the TKE balance in pipe flow [Laufer (1954)], and in boundary layer with zero pressure gradient [Klebanoff (1954)]. While it is evident that the existence of large scale eddies had been known [see Liepmann (1952) referenced in Lui (1988)], their importance in controlling turbulence transport and in the extraction of energy from the mean flow were first qualitatively described by Townsend (1956). Thereafter, the wall region of turbulent flows was closely studied resulting in new experimental techniques and philosophies on the structure of turbulence. For example, Liepmann (1962) had already suggested a relationship between the large scale structures and some form of instability mechanism which can only be qualitatively studied by controlled experiments. The development and use of conditional sampling to study the intermittent region of a turbulent boundary layer by Kovasznay et al. (1970) can be considered as a realization of such hypothesis. Other experimental techniques that have enhanced the understanding of turbulence include measurements of convection and decay of turbulent fluctuations using space-time correlations by Favre et al. (1957, 1958), coherent oscillations in turbulent shear flows [Bradshaw (1966)] and flow visualization [Kline et al. (1967), Corino and Brodkey (1969) and many others].

The importance of the wall region in the generation and maintenance of turbulence has been introduced in Chapter 1. Visualization experiments were initiated to better understand the mechanism of flow in the wall region. Improved flow visualization techniques involving the introduction of small hydrogen bubbles (produced from a fine wire by electrolysis) into the flow were first developed by Clutter et al. (1959) as referenced in Willmarth (1975). The advantage of this technique over the use of smoke or dye-injection is the fact that it provides both qualitative and quantitative information. A similar hydrogen bubble technique was developed by Kline et al. (1967) and used together with their previous results from dye-injection and still photography to deduce the sequence of activity in the turbulent boundary layer. Sublayer streaks with low velocity were observed to be regularly spaced and distributed in a spanwise direction in the region $0 \leq Y^+ \leq 10$. As they were convected with the flow, the low speed streaks were observed to gradually lift-up from the wall into the region $8 \leq Y^+ \leq 12$ where they intermittently oscillated. The oscillation increased with distance from the wall and the streaks were violently ejected $(10 \leq Y^+ \leq 30)$ into the outer part of the flow where they were broken up. At about the same time, Corino and Brodkey (1969) used high-speed motion photography to magnify the wall region in pipe flow and follow the trajectories of colloidal size particles suspended in the fluid. More detailed sequence of the same streaky phenomenon observed by Kline et al. was given. This includes a deceleration to about 50% of the local mean velocity of a parcel of fluid near the wall ($0 \leq Y^+ \leq 30$) which was followed by the appearance from upstream of accelerated fluid. If the accelerated and retarded fluids met at the same spanwise location, there was immediate interaction resulting in the formation of a shear layer between them. Soon after, the ejection phase starts with violent outward motion of low speed fluid which increases in intensity and continues for varying periods of time before ceasing gradually. The ejection phase ended due to inward rushes of fluids (called sweeps) with about the local mean velocity which removed the remnants of low speed fluids associated with the violent interaction of ejections with the high-speed fluids. Nychas et al. (1973) visualized the flow in the outer region of a channel flow using the same procedure as Corino and Brodkey. The cyclic nature of events was similar to previous observations. In addition they observed transverse vortices arising from the interaction between high- and low-speed fluid regions which appeared to be caused by Helmholtz type flow instability. Grass (1971) made similar observation as previous studies and also concluded that sweep motions may be more important than ejections in the production of Reynolds stress from the wall to the edge of the buffer region.

All pioneering flow visualization studies agree that ejections were very important in the production of TKE, and they estimated contributions of more than 70% to the Reynolds stress outside the sublayer.

2.2 QUANTITATIVE MEASUREMENTS OF COHERENT STRUCTURES.

Flow visualization provides a great deal of qualitative information but little quantitative data. In addition, it has other limitations which include the difficulty of application at high Reynolds number and the lack of depth of view captured by the camera.

More quantitative data in the study of coherent structures have been achieved using hot wire measurements and the application of conditional sampling. Conditional sampling has been appropriately defined by Blackwelder (1977) as a special type of generalized cross-correlation in which a signal is acquired when an event related to turbulence is detected. Following Blackwelder (1977) and Antonia (1981), the correlation can be defined as;

$$R(x,\Delta x,\tau_j) = \lim_{N\to\infty} \frac{1}{N}\sum_{i=1}^{N} d(x,t_i)f(x,\Delta x,t_i+\tau_j) \qquad 2.1$$

The digital conditioning function $d(x,t_i)$ can be derived from one or more signals and must determine the condition when averaging is to occur. $f(x,\Delta x,t_i+\tau_j)$ is the data signal, τ_j is the time delay (+ve or -ve), N is the number of data points to be averaged over and Δx is the distance between the detection probe which produces the function d, and the data probe which produces the function f.

The function $d(x,t_i)$ is the most important feature of any conditional sampling procedure. It is obtained from linear or non-linear operations on a signal, visual observations and so on. The identification and detection of an isolated event relevant to turbulence requires a very good imagination and the understanding of the nature of the problem being studied and it represents the most difficult task in conditional sampling. Most major contributions to conditional sampling can be traced to effective definition of the function $d(x,t_i)$. For example, measuring in the intermittent region, Kovasznay et al. (1970) used $\partial u/\partial y$ which is one term in the spanwise vorticity component while Antonia (1972) used a combination of flow visualization and the level of $(\partial uv/\partial t)^2$ as a detection criteria. In wall bounded shear flows, the detection of coherent structures includes visual observations by Kline et al. (1967), the use of the eulerian streamwise velocity signal by Kaplan and Laufer (1969) when its short time variance exceeds a predetermined level and by Willmarth and Lu (1971) as a trigger level at $Y^+=15$.

When Δx and τ_j in Eq. (2.1) are non-zero, detection and data acquisition are performed by different probes. Usually the detection probe is placed at the edge of the sublayer at $Y^+=15$ where the organized motions are assumed to originate while the data probe which acquires the signal is transversed perpendicular to the flow at a downstream location and at a distance Δx from the detection probe. This method is normally used for low Reynolds number flows and for flow geometries like channel flows where a large wall layer exist. The method also has limitations which have been addressed by Blackwelder (1977) and reviewed in Sect. (2.2.2). A variation of this method involves the use of a rake of hot wires as detection and data probes respectively in order to take into consideration the spanwise variation of the motions. More recent studies, especially in flows with a small wall layer or flows with high Reynolds number, rely on single point measurements in which τ_j and Δx in Eq. (2.1) are zero. The detection and acquisition of data is performed by the same probe, with the identification of events based on mathematical processing of the signal. The two well known methods that have been applied to single point measurements are the quadrant method of Wallace et al. (1972) and the variable interval time averaging (VITA) technique introduced by Blackwelder and Kaplan (1976).

The quadrant method depends on the sign of the streamwise velocity, u, and the transverse velocity signal, v, observed during bursting. It can be applied with a detection probe at the edge of the sublayer [Lu and Willmarth (1973)] or to single point measurements [Sabot and Comte-Bellot (1976)]. By sorting the uv-signal into four quadrants based on the u- and v-signals, it was found that the four classes of events (outward interactions, ejections, inward interactions and sweeps) that contribute to the shear stress production were uniquely defined. The events are classified as follows:

Quadrant 1 (Q1) : outward interactions ($u>0, v>0$),

Quadrant 2 (Q2) : ejections ($u<0, v>0$),

Quadrant 3 (Q3) : inward interactions ($u<0, v<0$),

Quadrant 4 (Q4) : sweeps ($u>0, v<0$).

A threshold condition, $uv \geq H u'v'$, was introduced by Lu and Willmarth (1973) so that the relative strength of events can be evaluated. The hole size H is defined as $H = | uv | / u'v'$.

The VITA technique is similar to the detection method applied by Kaplan and Laufer (1969). It is based on the fact that a thin shear layer or high speed front is formed during bursting. The short-time variance of the streamwise velocity is intermittent and its peak is considered to be an indication of the high speed front. Sampling takes place when the short-time non-dimensional variance of the streamwise velocity, u, exceeds a threshold value which varies from 0.5 to 2. Alfredsson and Johansson (1984) have shown that like the quadrant method, structures evaluated with VITA strongly depend on the averaging time and the value of the threshold.

2.2.1 Statistical properties of coherent structures.

Quantitative measurements have generally confirmed visual observations with regard to the importance of ejections in shear stress production. Therefore, the contribution to the average value of the Reynolds stress in the wall region of turbulent shear flows from different events can be estimated accurately irrespective of any of the existing methods used for analysis. Typical values are, 70-80% for ejections, 55-65% for sweeps and the excess percentage over 100% is due to small negative contributions from inward and outward interactions. In addition, the intermittency factor of ejections is about 0.25 to 0.3. This clearly shows the importance of ejections in shear stress production as more than 70% of the Reynolds stress is produced in the buffer region during an event that occurs only about one quarter of the time.

The evaluation of statistical quantities that depend on correctly identifying the time dependence of each structure does not enjoy similar collapse of data. The mean period and duration of events depend strongly on the detection criteria used. Rao et al. (1971) established, using various flow visualization and hot wire measurement results, that the mean period between ejections scaled with outer variables; the free stream mean velocity U_∞ and the boundary layer thickness δ (or the displacement thickness δ^*). Specifically, it was indicated that $(T_{II} U_\infty / \delta) \sim 5$ in channel flow for

$500 < Re_\theta < 9000$. Lu and Willmarth (1973) showed that the mean period between ejections using the quadrant splitting technique was a function of the threshold. However, it was found that a characteristic threshold which gives non-dimensional mean periods identical to the values obtained by Rao et al. occurred for values of H between 4 and 4.5. Similar results were obtained by Sabot and Comte-Bellot (1976) in pipe flow using single point measurements. While the early measurements seems to agree on the mean period between ejections in the wall region scaled with outer variables, it is now generally accepted that the numerical value is about 6 for the characteristic hole size of 4 [Cantwell (1981)]. The reason for the difference may be attributed to better signal processing. In addition, there is the unresolved question of the proper scaling that takes into consideration the Reynolds number dependency of the educed structures. Bogard and Tiederman (1986) have presented a wide variation in mean periods of ejections normalized with outer variables obtained by applying several detection algorithms. In the light of such deviations, even among results obtained using the same algorithm by different investigators, Luchik and Tiederman (1987) compared the scaling using outer variables with scaling using inner time scale (u_*^2/ν) originally applied by Blackwelder and Haritonidis (1983) and mixed (inner and outer) time scale introduced by Alfredsson and Johansson (1984). While the inner scaling was considered more appropriate, the question of proper scaling for mean periods remain controversial since most available data are limited to low Reynolds number flows.

2.2.2 Limitations of conditional sampling techniques.

Coherent structures are a random occurrence of organized motions embedded in an incoherent motion made up of smaller scales. In addition, the structures are present in the flow with a wide range of convection velocities, shapes, orientations and durations. Therefore conditional sampling has the task of selectively extracting the coherent motions while taking into consideration the wide range of properties of these structures which may influence statistical estimates. The scatter in the statistical properties of coherent structures evaluated using different detection algorithms [Bogard and Tiederman (1986)] is because each technique locks onto a different property of the bursting process and most of them do not address the fundamental distribution of individual events.

When two separate probes, one for detection and the other for data signal, are used in the experimental investigation of coherent structures the following problems have to be sorted out in signal processing.

(1) Some of the events that are triggered by the detection probe may be entirely different from those recorded by the data probe. This will either result in the acquisition of wrong events or in the acquisition of incoherent motions as well as the desired structures. Since the detection probe is normally fixed and the data probe transversed across the flow at a downstream location, the error associated with unwanted signal increases with the distance between the detection and data probes.

(2) Coherent structures have a wide range of convection velocities, sizes, shapes and orientations [Blackwelder (1977)]. This introduces a random phase when conditional averages are evaluated from the data signal.

Various signal processing techniques have been designed to correct for the loss of phase and incoherent structures or jitters associated with two-point velocity measurements. Blackwelder (1977) proposed a phase descrambling scheme which involves the matching of two different patterns associated with the velocity signal at two different locations. Another pattern recognition scheme involves the evaluation of a short-time temporal average of the raw uv-signal over the length of some acceptable patterns in the u-signal [Wallace et al. (1977)]. These patterns were produced by smoothing the u-signal, taking its time derivative and chosing only those patterns in which the absolute value of the positive slope was greater than the negative slope. By far the most accepted means of dealing with problems (1) and (2), is combined visual detection and acquisition of data by hot-wire. In this regards, each event can be traced and the degree of contact with the data probe ascertained [Bogard and Tiederman (1986)]. However, visual detection is limited to low Reynolds number flows, reducing the range of the combined method.

In single-point measurements, a continuous record of velocity is acquired at a chosen location. Both problems, (1) and (2), associated with two-point velocity measurements affects single-point data and (1) is worse since no attempt is made to detect events. Some of these problems can be resolved by the algorithm, quadrant or VITA technique, normally used to identify events in single-point records. For example, for sufficiently high threshold level, the application of the quadrant or VITA technique to single-point records of velocity can eliminate some of the small scaled incoherent motions. However, jitters and some small scale structures which do not contribute to the dynamic significance of the educed structures can still be present at higher thresholds. Pattern recognition schemes have been used in conjunction with the quadrant or VITA techniques to effectively process single-point records of velocity [Wallace et al. (1977)].

2.3 CURRENT TREND IN COHERENT STRUCTURE INVESTIGATIONS.

Robinson (1991 a,b) has categorized different aspects of the study of organized motions in terms of the decade in which community-wide interest was most intense. Thus, flow visualization belongs to the 60's, probe based measurements in the 70's and computer simulation became feasible in the 80's and is still of current interest. The shift in focus is because neither flow visualization nor conditional sampling techniques achieved the high expectations that was generated by their introduction. Both methods remain limited in application to canonical boundary layers, i.e. simple boundary layers on flat plates or smooth walls with two-dimensional mean flow, low Reynolds number and the absence of pressure gradients. Probe based measurements are still plagued by the limitations discussed in Sect. 2.2.2. In addition, most probe based conditional sampling schemes do not allow for spanwise variations resulting in typical ensemble averages that show sweeps followed by ejections [Robinson et al. (1988)] when it is known that sweeps and ejections are associated with quasi-streamwise vortices and so tend to occur in a side-by-side orientation [Moin (1987)]. While computer simulation has many advantages, it is also limited to canonical cases like existing probe based methods. Thus improvement in conditional sampling techniques and careful analysis of probe based data will still be of sufficient interest as the study of coherent motions address non-canonical cases.

Computer simulation ideally involves the numerical solution of the full non-linear, three-dimensional, time dependent Navier-Stokes equations for a given initial and boundary conditions without empirical closure assumptions. At any Reynolds number, the resolution achieved by simulation depends on obtaining correct statistics of the flow [Zang (1991) and Moin and Spalart (1989)]. The major statistical considerations include correct values of (1) mean flow based on accepted logarithmic layer, (2) root-mean-square velocity fluctuations, (3) spanwise spacing of the low-speed streaks, and (4) skewness and flatness statistics. Full simulation is limited by existing computer capabilities, by statistical considerations notably criteria (3) and (4) above, and is difficult to apply to all but the simplest flows. Limited simulation, for example large eddy simulation (LES) which uses a 'subgrid-scale' model for those length scales that are too small for the computational grid to resolve, achieves criteria (1), (2) and perhaps (3) [Zang (1991)]. Data bases generated by LES has been used in studying coherent motions by Kim (1983), Kim and Moin (1986), Robinson (1991 a,b), and many others. It is believed that computational methods, including LES, provide a better means of control and manipulation of data than probe based conditional sampling techniques [Kline (1988)]. Consequently in canonical boundary layers, conceptual models have been re-investigated and new ones proposed [Kim (1983) and Robinson (1991 a)], terminologies and concepts are made clearer [Kline (1988), Robinson et al. (1988) and Robinson (1991 a,b)], and numerical data has been used as a basis for better probe design [Moin and Spalart (1989)].

One of the main objectives of coherent structure investigations is the formulation of a conceptual model that governs the evolution and interaction of the structures. These models are strongly dependent on the three-dimensional vortical structures that are known to be associated with the coherent motions but the origin, nature, dynamics and interaction of the vortices are subject to many inferences and therefore remain controversial. However, it is agreed that coherent motions exhibit different structural features in the sublayer, buffer region and outer region of the boundary layer. More recent studies indicate that most of the vortices associated with ejections and sweeps, in the buffer and lower log-law regions, are single quasi-streamwise vortices [Moser and Moin (1987) and Robinson (1991 a,b)]. Streamwise vortices occurring as counter-rotating pairs, which were believed to be more frequent [Bakewell and Lumley (1967), Blackwelder and Eckelman (1979) and Kim (1983)], are found to be relatively few. The upper log-law and wake regions are predominantly populated with transverse vortices [Nychas et al. (1973), Praturi and Brodkey (1978) and Robinson (1991 a,b)]. They are other variations or types of vortices that occur throughout the boundary layer and have been used for conceptual models by others. For example, near-wall hairspin vortex models [Theodorsen (1952), Willmarth and Lu (1972) and Head and Bandyopadyay (1981)] and outward migrating horseshoe shaped vortices [Offen and Kline (1975) and Head and Bandyopadyay (1981)].

Predictive models based on mathematical description of boundary layer properties are also being used to study the dynamic significance of coherent structures.

Statistical analysis involving proper orthogonal decomposition [Bakewell and Lumley (1967), and Aubry et al. (1988)] have been used to infer streamwise vortices with counter-rotating pairs. Based on the attached eddy hypothesis of Townsend (1976) and some experimental data, Perry and Chong (1982) based their model formulation on 'Λ' shaped vortices which are shown to form 'heirarchies', random arrays of Λ −shaped vortices at different stages of stretching but with the same circulation, and are possibly formed by vortex pairing. 'Λ' vortices are a general name given to vortex loops, horseshoe and hairspin vortices which are topologically equivalent but at different levels of stretching without the need to distinguish between the different types. The Perry and Chong model for zero pressure gradient has been extended by Perry et al. (1991) in order to formulate a closure hypothesis for adverse pressure gradient turbulent boundary layers. Hussian (1983) and Lui (1988) have shown that what is normally regarded as turbulence in traditional Reynolds number averaging can be written as the sum of coherent and incoherent turbulence (double decomposition) or the coherent part may be further classified into even and odd modes (triple decomposition). Thus, terms like the production and dissipation of turbulent kinetic energy can be written in terms of the properties of the structures that contribute to them. Other mathematical formulations include vortex dynamics [Bridges et al. (1990)] and dynamical systems approach [Holmes et al. (1990)].

They are very few studies of coherent structures in non-canonical boundary layers, for example turbulent flows subjected to pressure gradients, in the open literature. Visualization experiments by Kline et al. (1967) indicated that wall streaks tend to be shorter and to wave more violently in adverse pressure gradient flow, while in favorable pressure gradient flow, the streaks appear to be drawn longer and be more quiescent. It was also observed that the bursting action tend to be suppressed in strongly favorable pressure gradient flow while in strongly adverse pressure gradient flow, back-flow occurred momentarily before the structures were swept downstream. These observations were found to be consistent with their evaluation of the bursting frequency per unit span which scaled on wall variables and was a function of the non-dimensional pressure gradient parameter, $\alpha_1 = -(\nu/\rho U_\infty^3)dp/dx$. Offen and Kline (1975) proposed a conceptual model for the bursting process in the wall region of boundary layers which was based on previous visual data. In the model, the arrival of a sweep at the wall led to a temporary adverse pressure gradient that was responsible for the ejection of low speed streaks from the point of interaction. The implication of this model is that in an adverse pressure gradient flow, more wall streaks will be ejected because the temporary adverse pressure gradient required for ejecting wall streaks will be supplemented by the local adverse pressure gradient, while in favorable pressure gradient flow, the lift up of wall streaks will be suppressed. However, the ejection of wall streaks by a temporary adverse pressure gradient imposed by sweeps has not been supported by wall-pressure pattern characteristics [Willmarth (1975) and Thomas and Bull (1983)], and more quantitative data from numerical simulations indicate that sweep and ejections are associated with quasi-streamwise vortices and so tend to occur in a side-by-side orientation [Moin (1987)] rather than a sweep upstream of an ejection. The non-applicability of the Offen and Kline model, which otherwise supports some known data in pressure gradient flows, is an indication that conceptual models derived from canonical boundary layers may not fully explain observations in pressure gradient flows where the structure is different.

CHAPTER 3

EXPERIMENTAL EQUIPMENT AND PROCEDURES

3.1 FULLY DEVELOPED PIPE FLOW AND DIFFUSER FLOW FACILITIES

A description of the basic set-up of the wind tunnel, feed pipe and conical diffuser can be found in the literature [see Okwuobi and Azad (1973)]. Figure 3.1(a) shows the set-up when measurements are taken in the fully developed pipe flow, whereas Fig. 3.1(b) shows the diffuser (detached from the pipe) and its traversing mechanism. The set-up consist of a variable speed centrifugal fan powered by a 25 hp DC motor which delivers air into a 2.20 m long settling chamber of 91.4 cm diameter. In the settling chamber the air passes through three sets of fine mesh double screens and feeds into a plywood contraction cone with an area ratio of 89:1. Air from the contraction cone discharges into a long steel pipe, 10.16 cm inside diameter, with No. 16 floor-sanding paper pasted to the inside surface of the initial 8 cm length to provide boundary layer tripping. The total length of pipe is 79 diameters long at the end of which air enters a conical diffuser that discharges to the atmosphere. The conical diffuser has an included angle of 8 degrees and it is 72 cm long with a nominal area ratio of 4:1.

A traversing mechanism was used as the probe support holder and to indicate the location of the probe in the measuring plane. In pipe flow measurements, a DISA 55E40 traversing mechanism attached to a milling table was used. Traversing was done along a horizontal diameter and the point where a probe touches the wall (with the tunnel shut off) was indicated by the deflection of a resistance meter (EICO 680). The resistance meter, with the positive and negative terminals connected to the probe and to the conducting wall respectively, deflects when the circuit was completed by contact with the wall. After contact with the wall, a digital micrometer head (MITUTOYO micrometer) with a range of 0-25 mm and 0.01 mm graduation was used for positioning of the probe. For the diffuser measurements, the traversing mechanism was attached to the open end of the diffuser by 50 cm long levers on both sides. The positioning of the probe was indicated by a Starret (NO. 469) micrometer dial-head with 0.001 mm increments. A resistance meter was also used to indicate contact with the wall before the fan was turned on.

3.2 INSTRUMENTATION

Pressure probes used in velocity measurements include a total pressure tube (USC-E-103-1), a static pressure tube (USC-E-103-2) and a static pressure probe shaped like a boundary layer type hot-wire probe used for measurements close to the wall (see Fig. 3.2). All pressure probes used in velocity measurements had outer diameters of 1.07mm. Preston tubes used to obtain pressure differences for calculating the friction velocity from Patel's calibration were locally made and their dimensions are given in Table 3.1. Pressure differences were measured using a Betz projection manometer which has graduations of 0.1 mm water and a range from -17 to 400 mm water. For low velocity measurements the pressure difference was obtained using a Combustion Instrument Ltd. micro-manometer with a graduation of 0.01 mm water and a range of 0 to 30 mm water.

Boundary layer type probes (DANTEC type 55P05) were used for single wire measurements while DANTEC type 55P51 were used for x-wire measurements. All probes were of standard specifications with a nominal diameter of $5\mu m$, a sensitive length of 1.25mm and gold plated ends. The anemometry system was almost exclusively DISA (DANTEC) equipment. This include 55M01 constant temperature anamometers with standard bridge, 55M25 linearizers, 55B25 turbulence processors and 55D90 calibration rig. Other equipment were KROHN-HITE model 3550 filters and a DATA TRANSLATION'S DT2821-F-16SE analogue and digital input/output board with a 12 bit A/D converter installed in an IBM PC/AT compatible computer. Auxiliary equipment include DISA 55D31 digital voltmeters, DISA 52A35 channel selector, Fluke 8050 digital multimeter and Tektronix 466 storage oscilloscope.

3.3 PROCEDURES

3.3.1 Pressure measurements.

In the pipe wall, sets of four static pressure holes of 1 mm diameter and spaced 90 degrees apart have been drilled at intervals of 1m along the length of the pipe to provide estimates of friction velocity from linear static pressure drop. The value of the friction velocity, u_* obtained from linear static pressure drop was 0.839 m/s at the operating cross-sectional average mean velocity ,U_b,of 18.2m/s and Reynolds number, $Re = U_b D_p / \nu$, of 119,000.This value of friction velocity in the fully developed pipe flow was similarly obtained using Preston tubes and Patel's (1965) calibration. All measurements in the pipe were done with the diffuser detached and at $0.25D_p$ from the open end of the pipe (i.e $L > 78D_p$ from the trip). The pipe flow has been determined to be fully developed by Dang (1987) at the chosen measuring position because moments of the fluctuating streamwise velocity up to third-order were shown to be constant downstream of $L=78D_p$ from the trip.

With the diffuser attached to the pipe, velocity characteristics in the pipe were found to be identical to those obtained without the diffuser. However, measurements in the pipe with the diffuser in place involve introducing more than 72 cm of probe holder and care had to be taken to insure that no cantilever effect was present at the measuring position. In the diffuser itself, a set of four static pressure taps of 0.6mm diameter and positioned at 90 degrees to each other are spaced at intervals of 6 cm along its length. These static pressure taps were externally identifiable by plastic hoses that connect each set and they represent the twelve measuring stations in the diffuser. In this presentation, stations are identified by a number which represents the distance in centimeters from the entrance of the diffuser to the measuring plane. Preston tube measurements and the Patel's calibration curves were used to obtain the friction velocities at various stations in the diffuser. Kassab (1986) and Trupp et al. (1986) have shown that in the early part of the diffuser where the wall shear stress decreases rapidly the smallest Preston tube (see Table 3.1) produces the lowest u_* values, whereas the largest Preston tube produces the highest u_* values. This pattern was shown to be reversed in the last half of the diffuser. However at any measuring station the mean value of u_*, obtained by averaging values obtained for all four Preston tubes in Table 3.1, was comparable to the values obtained by applying the correction procedures of Brown and Joubert (1969) and Frei and Thomann (1980) in which further corrections are made to the normal u_* values obtained from Preston tubes and the Patel's calibration.

3.3.2 Hot-wire measurements.

Standard procedures in DISA (DANTEC) manuals were followed in the set-up and use of equipment. Calibration of the hot-wires was done in a low turbulence intensity jet flow using the calibration rig (55D90). During measurements, the linearized signal was fed to the turbulence processor. For single wire measurements, the turbulence processor was used only for pre-gain amplification and DC offset. For x-wire measurements it was used to form the sum and difference of the two signals. The pre-gain was chosen such that the product of pre-gain and post-gain (applied during A/D conversion) results in a signal level of $\pm 10V$. The signal from the turbulence processor was further conditioned using the model 3550 filters with the high pass set at 2 Hz for all measurements. The low pass was set at the Kolmogoroff's frequency, f_k, of the flow at the measuring point to remove electronic noise, since no measurable energy exists in turbulence after this frequency. The Kolmogoroff frequency is defined as $f_k = U/(2\pi\eta)$, where the Kolmogoroff length scale, $\eta = (\nu^3/\epsilon)^{1/4}$. Here, ϵ is the mean dissipation rate and ν is the kinematic viscosity of the fluid. At any measuring position, a first guess of 20kHz was used as the initial setting of the low pass filter. Then measurements of U and $\overline{(\partial u/\partial t)^2}$ were made in order to estimate dissipation from the isotropic relationship, $\epsilon = 15\nu\overline{(\partial u/\partial t)^2}/U^2$. η and a new value of f_k were then calculated from the new value of ϵ. This procedure was repeated until successive values of f_k were constant. In the fully developed pipe flow, the low pass was set at 10 kHz whereas the sampling rate was 20 kHz. In the diffuser, Kassab (1986) has shown that the Kolmogoroff frequency varies from one station to another. For example at station 66, which gives the biggest deviation from pipe flow values, the values of f_k range from about 1 kHz near the wall to about 25 kHz at the axis of the flow. Therefore, typical sampling frequencies in the diffuser ranged from 10 to 50 kHz, based on estimates of at least $2f_k$ in order to avoid aliasing. The band passed signal was digitized using the A/D converter board in the computer which was controlled by software in which a post-gain and a sampling frequency were specified. The total amount of data acquired per measuring point was 200,000 for single-wire and 400,000 for x-wire. Direct Memory Access (DMA) mode was used in both data acquisition procedures and in the case of x-wire measurements, two channels were scanned simultaneously.

The hot-wire data were processed by simple Fortran programs in a look-up table format, which has been modified to process a linearized signal because of the bipolar data obtained from the A/D converter (see Appendix A, Sect. A1). In this procedure the mean voltage measured at any point and the linearization equation of the hot-wire can be used together with the class intervals of the A/D converter, which represents all possible values that the fluctuations will attend, to form a table containing 4096 instantaneous velocities without considering the actual data signal. The acquired signal is then sorted into the appropriate class intervals, each of which is associated with a fluctuating velocity, to give a histogram of the realizations which is then processed statistically to obtain the mean velocity and moments of the fluctuating velocities.

Measurements with x-wire were made both in the xr and $x\theta$ planes. Consequently, fluctuating quantities in the longitudinal (u) transverse (v) and lateral (w) directions were obtained. Yaw corrections were applied to x-wire measurements in the pipe (with k=0.2) using equations developed by Champagne and Sleicher (1967) and also presented by Vagt (1979). In the diffuser flow both yaw corrections (k=0.25) and high intensity corrections for mean velocity and second order moments of fluctuating velocities were applied as described in Vagt (1979). Data from x-wire measurements were also analyzed using the method developed by Chew and Simpson (1988), see summary of equations in Appendix A; Sect. A2. The fixed-angle calibration method described in that work produces the same results as the method presented by Vagt (1979) when a yaw factor of 0.25 and yaw angle of 45 degrees is used in both cases. The main advantage of this method over the previous correction is the fact that the linearization equation of the two sensors of x-wire need not be the same. In addition, an iterative procedure can be applied to obtain results comparable with the variable-angle calibration method. In the present case, the iterative procedure was applied by varying the yaw factor in order to match streamwise mean velocities and fluctuations with values obtained from single-wire measurements. For example, at station 66, the resulting values of the yaw factor ranged from 0.667 at 2 mm from the wall to 0.23 at the center-line. Figure 3.3 shows the variation of yaw factors in the diffuser flow from stations 36-66. The general trend in the wall region is an increase in yaw factor (decrease in yaw angle) from station 36 to station 66. It can be observed that the core region of the diffuser in the exit portion of the flow have a nearly constant yaw factors which tends to a value of 0.25. Flow characteristics from stations 6-30 are well predicted with a yaw factor of 0.25 across the flow field. This analysis justifies the choice of a constant yaw factor in the diffuser which has been used in many investigations [Kassab (1986), Turan (1988) and many others], i.e. k=0.25 which corresponds approximately with a yaw angle of 45 degrees in the velocity range 1 to

22 m/s, because it is consistent with the findings of Jorgensen (1971). It was shown by Jorgensen (1971) that a yaw factor at a higher angle (e.g. 45 degrees) can be used to minimize errors in velocity measurements if the yaw angle in the flow varies from 0 to 45 degrees.

The data was also used to form the time series of u-, v- and uv- signals (see Appendix A, Sect. A1). For this purpose, the data file was accessed sequentially and yaw factor applied to obtain u- and v- signals. The uv-signal and high-order moments of fluctuating velocities were obtained from the time trace of the u- and v-signals using Fortran programs. In addition, experimental probability density distribution functions were evaluated by the method given in Bendat and Piersol (1968, pp. 284-298). The number of cell required for the probability density distributions were estimated at 52, based on 95% level of significance, since the A/D converter gives 4096 distinct velocities. The probability density distributions of the fluctuating velocities, $\hat{u}$ and $\hat{v}$, were evaluated in the class interval, $-3 \leq \hat{u}, \hat{v} \leq 3$. Here the hat on the fluctuating velocity implies the fluctuating velocity normalized by its root-mean-square value. Higher order moments were evaluated in the interval [-8,8].

3.3.2.1 Accuracy analysis of hot-wire measurements.

Errors in hot-wire measurements depend on several factors. These include the characteristics of the instrumentation and experimental equipment, yaw sensitivity, interference effects, velocity gradients, proximity to the wall etc. Thus it is not always easy to trace the origin of errors since the true values of the measured quantities are not known in advance. In the present work, it is assumed that errors associated with single-wire measurements arising from the nature of the flow are negligible hence mean velocities and velocity fluctuations in the streamwise direction obtained using x-wires can be compared with them. In this regard, x-wire measurements obtained using a constant value of yaw factor, 0.25, in the diffuser flow had maximum errors of 3-5% in mean velocity and 3-7% in streamwise velocity fluctuations. These errors were as a result of underestimating the single-wire values and they were most noticeable in the wall region from stations 42-66. Errors arise in x-wire measurements because this region of the diffuser is characterized by high intensity of turbulence and possibly instantaneous backlflow as the flow proceeds towards separation. High intensity corrections applied in addition to the yaw correction did not produce any reasonable improvement on the results. Combined yaw and high intensity corrections resulted in maximum errors of 1-3% in mean velocity and 2-5% in streamwise velocity fluctuations. An alternate method, see Chew and Simpson (1988) and Appendix A, was then applied to address the observed errors. This method accounts for both the yaw sensitivity and the effect of the tangential cooling velocity which is not negligible in highly turbulent flows. Their constant angle calibration method, using a constant yaw factor of 0.25, produces similar results as the combined yaw and high intensity correction. However, the Chew and Simpson method could be used to obtain results that compare with the variable angle calibration method by iteration such that mean and fluctuating velocities obtained from single wire are reproduced. This later analysis resulted in the variation of yaw factors in the wall region of stations 42-66 as shown in Fig. 3.3. This figure implies that yaw factors have to change significantly from the constant value of 0.25 in order to duplicate mean velocities and streamwise fluctuations obtained from single-wires. The matching of these velocity components also accounts for the velocity gradients produced by separation of the two sensors of the x-wire. The maximum errors between the later x-wire measurements and those with constant angle calibration had maximum deviations of; 3% for mean velocity, 5% for streamwise fluctuations, about 5% for the averaged Reynolds stress and 8% for the fluctuating velocity in the transverse direction. It should be noted that these maximum errors occur very close to the wall, i.e. within a distance of about 2 mm from the wall. Therefore, due to the finite length of x-wires which spans 3 mm between the prongs, only the first two data points from the wall in stations 42-66 have any significant errors. In Chapter 4, mean velocities and moments of fluctuating velocities across the diffuser are further compared with measurements in other complex flows.

CHAPTER 4

CHARACTERIZATION OF THE DIFFUSER FLOW

4.1 PRESSURE MEASUREMENTS

Pressure probes are uniquely designed for measurements in laminar flows and turbulent flows with low intensity. These flows are characterized by constant values of static pressures across any perpendicular plane and have negligible fluctuating velocity components. In practical applications, pressure probes are often used in flow situations that deviate from such ideal behavior. Existing correction procedures [Goldstein (1936) and Hinze (1959, 1975)] indicate that errors from pressure measurements can be minimized by taking into consideration the directional sensitivity of the probes to the fluctuating velocity components. These equations are given in Appendix B, Sect. B1 as Eqs. B1 and B2 for the total and static pressure tubes respectively. Equations B1 and B2 by themselves have no practical significance since pressure probes can respond to but cannot measure fluctuating velocities. However, they indicate that if the fluctuating components of velocity are small, the Bernoulli equation can be used as an estimate of mean velocity.

Hinze (1975) has noted that mean velocities obtained from pressure measurements deviate from true values when the static pressures are not constant across the flow. Measured static pressures across the flow at various stations in the diffuser are shown in Figs. 4.1(a) and (b) for stations 6-36 and 42-66 respectively.

Stations 6-36 in Fig. 4.1(a) have relatively constant values of static pressures with maximum deviations of 3% to 10% from the wall values. Stations 42-66 have larger variations of static pressures which attain values greater than twice the wall static pressure at station 66. The axial variation of the wall static pressures are presented in Fig. 4.2(a) while the wall static pressure gradients are given in Fig. 4.2(b). The latter figure shows that the flow in the diffuser has a varying adverse pressure gradient. This variation of pressure gradient include a constant negative pressure gradient in the fully developed pipe flow which becomes more negative due to entrance effects then increases to a maximum value of adverse pressure gradient at $X/D_p \sim 0.3$. The adverse pressure gradient then decreases rapidly to about station 18 and finally more gently in the rest of the flow. Two dimensionless forms, $\alpha_1 = (10^{-6}\nu/\rho U_\infty^3)dp/dx$ and $\alpha_2 = (2D_p/\rho U_b^2)dp/dx$ have been used to present the pressure gradients. The experimental values of dp/dx were obtained by numerically differentiating the measured wall static pressures given in Fig. 4.2(a). In addition, theoretical values of dp/dx were evaluated by applying the Bernoulli equation between two points in the flow and taking into consideration the diverging walls of the diffuser and presented in the form of α_2. Two observations may be made in connection with the pressure gradients in the flow. Firstly, the decreasing portion of the adverse pressure gradient is accurately predicted by simple application of the Bernoulli equation. Secondly, the values of the dimensionless parameter α_1 falls between 0.2 and 0.7, therefore in accordance with the classification of pressure gradients by Kline et al. (1967), most of the diffuser flow belongs to the mild adverse pressure gradient category. At the peak position of adverse pressure gradient, the values of $\alpha_1 = 0.91$ and $\alpha_2 = 0.45$ were obtained, indicating that a strong adverse pressure gradient may exist in a small portion of the diffuser.

Due to the variation of static pressures across the flow, two estimates of mean velocity can be obtained at any point in the flow. The first U_{SW}, is the velocity calculated using the Bernoulli equation from the pressure difference between the total pressure measured at any point and the wall static pressure. The second, U_{SL} requires the measurement of both the static and total pressures at the same point in the flow. Both velocities have errors when compared to the more accurate hot-wire measurements. In Appendix B, the magnitude of these errors are quantified and correction procedures are derived for both mean velocity and static pressure measurements.

4.2 HOT-WIRE MEASUREMENTS

4.2.1 Mean Velocities

In Fig. 4.3 the mean velocity profiles obtained from single-wire measurements are presented in the pipe and six measuring stations in the diffuser. The accuracy of these measurements can be tested by simple continuity criterion by calculating the mass flow rate from the measured velocity profiles. The mass flow rate calculated from the velocity profiles obtained from hot-wire measurements are within ± 3 % of the pipe flow values at any station in the diffuser [see Appendix B, Fig. B.2]. Mean velocity distributions near the wall in the diffuser have been presented in terms of wall variables by Kassab (1986) and Trupp et al. (1986). It was shown that the law of the wall for the fully turbulent and buffer regions which exist in the fully developed pipe flow [see Fig. 4.4], breakdown as soon as the flow enters the diffuser. Most of the measurements in the diffuser indicated dual log-law regions (i.e. two boundary layers); the inner one developing on the diffuser wall, and the outer one representing a decaying remnant of the feed pipe boundary layer. However, since these log regions had variable and abnormally high slopes and did not scale with the wall variables, attempts at fitting log-law distributions were abandoned. These results are consistent with recent findings by Simpson (1991) that the breakdown of the boundary layer concept can occur before flow reversal takes place.

Mean velocity profiles measured in the diffuser can be compared with correlations that take into consideration the breakdown of the boundary layer concepts. One of these, a universal velocity defect law for turbulent boundary layers in adverse pressure gradient, has been proposed by Schofield and Perry (1972). This law is applicable in flows where $-\rho\overline{uv}_{max} > 1.5\tau_w$, where τ_w is the wall shear stress. In the diffuser the values of $-\rho\overline{uv}_{max}/\tau_w$ varies from 2.0 at station 6 to 51.6 at station 66 (see Table 4.1). An empirically derived equation for mean velocity in two-dimensional adverse pressure gradient was obtained by correlating a large number of data from various sources [see Schofield and Perry (1972)]. This equation can be written as;

$$\frac{U_c - U}{U_s} = 1 - 0.4\left(\frac{Y}{B_s}\right)^{0.5} - 0.6\sin\left(\frac{\pi Y}{2B_s}\right) \qquad 4.1$$

Where,

$U_s = U_c - U_f$

$$B_s = \delta^* \frac{U_c}{U} N_s$$

$$= L_s Q_s^2 \left(\frac{U_s}{U_m} \right)^2$$

and

$$\delta^* = \int_0^\infty (1 - \frac{U}{U_c}) dy$$

$$U_m = \sqrt{(\overline{uv})_{\max}}$$

U_c and U are mean velocities at the center-line and local measuring position respectively. U_f is obtained from the half power law plot $\left(Y^{\frac{1}{2}} \;\; vs \;\; U\right)$. B_s is a characteristic length scale of a boundary layer defined as a wall confined wake. B_s may be obtained from the displacement thickness, δ^* or from a knowledge of the maximum shear stress $(\overline{uv})_{\max}$ and its location with respect to the wall, L_s. N_s and Q_s are universal constants with values of 2.86 and 1/8 respectively.

The above model is compared with velocities obtained in the present flow in Fig. 4.5. Stations 18-42 represent the portion of the diffuser where the measured velocities are most like the primary data used to obtain Eq. 4.1. Results for stations 6-12, lie below station 18 while those of stations 48-66 lie above station 42. Stations 6 and 66 are also shown in addition to stations 18-42 to indicate maximum deviations. It can be concluded that the application of this model divides flow in the diffuser into three groups of stations: 6-18, 24-36, and 42-66. This classification is identical to inner, intermediate and outer stations used to analyze the fit of static pressure corrections (see Appendix B) and therefore represents an integral part of the flow structure in the conical diffuser. The inner stations may show deviations from Eq. 4.1 due to high values of adverse pressure gradient and because the sudden switch from favorable to adverse pressure gradient may result in a complex flow pattern. On the other hand, flow in the outer stations is characterized by low mean velocities and high intensity of turbulence in the streamwise, transverse and lateral directions which indicates a flow that is close to detachment [Simpson (1991)]. Since in addition to similar flow characteristics, values of α_1 [see Fig. 4.2(b)] in the outer stations are approximately 0.2 like the flow investigated by Simpson (1991), therefore some degree of instantaneous backflow is likely at the outer stations and this will introduce errors in hot-wire measurements [see Dengel et al. (1981)]. Flow in the intermediate stations are accurately fit by two-dimensional models for adverse pressure gradient turbulent flows.

The most important physical significance of Eq. 4.1 is the fact that outer flow motion is characterized by the maximum shear stress and its location (necessary to evaluate B_s). The method of evaluating B_s sheds further light on the deviations shown in Fig. 4.5. Figure 4.6 shows the shear stress distribution in six stations of the diffuser and in the fully developed pipe flow. The maximum shear stress and its location is difficult to evaluate for the inner stations due to closeness to the wall, hence in those stations B_s is evaluated from the displacement thickness. For the intermediate stations, 24-36 the values of $(\overline{uv})_{max}$ and L_s are well defined and the values of B_s obtained from them are identical to values obtained from the displacement thickness. The outer stations show flat values of the maximum shear stress and Schofield and Perry (1972) have similarly noted that such shear stress profiles produce errors in the use of Eq. 4.1 due to the difficulty of evaluating L_s and defining B_s. It has been shown that U_m is an important velocity scale for flows that are near separation [Simpson (1991)] and similarly the position defined by L_s can be considered important because of its association with the velocity scale. The position defined by L_s (or the position of maximum value of $-\overline{uv}$) is important in understanding the nature of turbulence in the diffuser. This position will be referred to as the 'peak region' and its significance will become apparent as more properties of the flow are investigated. Basic properties of the peak region in the diffuser are given in Table 4.1.

4.2.2 Moments of fluctuating velocities.

The physical processes involved in turbulence manifest themselves in the moments of fluctuating velocities. For example, additional mean momentum fluxes within the fluid is a consequence of the fluctuating velocities superimposed on the mean flow. The third-order moments are important in turbulent diffusion while the skewness and flatness of velocity represents a measure of the asymmetry and the extent of skirt of the probability density distribution respectively. The Reynolds stress tensor is symmetric and for an axisymetric flow like the present diffuser, the time averaged odd powers of w (i.e. $\overline{uw}$ and $\overline{vw}$) are negligible. In addition the eventual application of the moments of fluctuating velocities to the evaluation of coherent structure properties is based on the use of the moments of u and v. Therefore, the complete moments of fluctuating velocities up-to forth-order required in the present study are contained in the five by five matrix defined as;

$$\begin{bmatrix} \overline{u^0v^0} & \overline{u} & \overline{u^2} & \overline{u^3} & \overline{u^4} \\ \overline{v} & \overline{uv} & \overline{u^2v} & \overline{u^3v} & \overline{u^4v} \\ \overline{v^2} & \overline{uv^2} & \overline{u^2v^2} & \overline{u^3v^2} & \overline{u^4v^2} \\ \overline{v^3} & \overline{uv^3} & \overline{u^2v^3} & \overline{u^3v^3} & \overline{u^4v^3} \\ \overline{v^4} & \overline{uv^4} & \overline{u^2v^4} & \overline{u^3v^4} & \overline{u^4v^4} \end{bmatrix} \qquad 4.2$$

From the x-wire data, these moments are normalized as follows:

$$\overline{\hat{u}^m\hat{v}^n} = \frac{\overline{u^mv^n}}{(\overline{u^2})^{\frac{m}{2}}(\overline{v^2})^{\frac{n}{2}}} \qquad 4.3$$

where m and n may vary from 0 to 4. Note that $\overline{u^0v^0} = 1$, and $\overline{u} = \overline{v} = 0$.

The experimental values of the moments normalized as in Eq. 4.3are given in Appendix C and they compare favorably with analogue measurements in the same set-up by Arora (1978) and Kassab (1986). Therefore, the following section will be more concerned with their significance while a further test of their accuracy will be made in Chapter 5 where probability density distributions and coherent structures are deduced from them.

4.2.2.1 Second-order moments.

The second-order moments necessary for the present analysis can be obtained directly from the computer program and they include the normal stresses $\overline{\hat{u}^2}$, $\overline{\hat{v}^2}$and the shear stress correlation $\overline{\hat{u}\hat{v}}$. However, $\overline{\hat{w}^2}$was also evaluated mainly for the purpose of high intensity corrections. With the normalization given in Eq. 4.3, $\overline{\hat{u}^2}$, $\overline{\hat{v}^2}$, $\overline{\hat{w}^2}$ are all unity, hence the best presentation of these quantities is in terms of the local intensity of turbulence u'/U v'/U and w'/U as given in Figs. 4.7(a), (b) and (c) respectively. These figures show that the initial perturbation of the flow as it enters the diffuser has little effect on the magnitude of the intensity of turbulence since the values of u'/U v'/U and w'/U obtained in the pipe flow are similar to the values in the initial stations (6-18). However, these values become progressively larger than the pipe flow values in the intermediate and outer stations. Since x-wire measurements give significant errors when the local intensity of turbulence exceeds about 40%, high intensity corrections [see Vagt (1979)] were applied to measured mean velocities and second-order moments in the outer stations (42-66) in the region $r/R_p > 1.2$. It can also be observed that the intensity of turbulence along the center-line increases above pipe flow values from station 42-66. This fact has been noted by previous measurements in this set-up, and Azad and Kassab (1989) explained the increase in intensity as a consequence of increased focusing of low speed fluid from the opposite wall over the same effect in the feed pipe. The evaluation of organized motions in Chapters 5 and 6 addresses this phenomenon.

Intensity profiles can also be presented in terms of the ratio $\overline{v^2}/\overline{u^2}$ [see Smits et al. (1979) and Azad and Kassab (1989)]. The values of $\overline{v^2}/\overline{u^2}$ given in Fig. 4.8 compare favorably with those of Kassab (1986) in the same flow and have a similar trend like the measurements of Smits et al. (1979) in spite of differences in flow geometry. In the present work all comparison of parameter in the pipe and different stations of the diffuser are given with respect to r/R_p in order to emphasize the results in the diverging part of the diffuser flow (i.e. for $r/R_p > 1$). In view of the breakdown of the boundary layer concept in this type of flow [Trupp et al. (1986) and Simpson (1991)], the use of outer scaling to observe trends is justifiable. However, the present flow has been previously analyzed using outer scales [Arora (1978)] and inner scales [Kassab (1986)] with no indication of one being superior to the other in determining trends. It can be observed from Fig. 4.8 that the values of $\overline{v^2}/\overline{u^2}$ very close to the wall are smaller than the pipe flow values at all stations of the diffuser. The initial stations as the flow diverges have consistently lower values of $\overline{v^2}/\overline{u^2}$ than in the pipe at all points across the flow. With prolonged wall divergence, the outer stations, 42-66, have lower values of $\overline{v^2}/\overline{u^2}$ near the wall which increase above pipe values in the mid-section and finally decrease below pipe values in the core region. High values of $\overline{v^2}/\overline{u^2}$ of about 2 which have been associated with irrotational flow by Hoffmann et al. (1985) do not exist in the present flow geometry but most of their results are consistent with the present measurements.

The profile of turbulent energy, $\overline{q^2} = \overline{u^2} + \overline{v^2} + \overline{w^2}$ given in Figs. 4.9, indicate similar effects of wall divergence as observed by Castro and Bradshaw (1976) and Kassab (1986). The near wall values of $\overline{q^2}$ shows a decrease in turbulence energy at all stations in the diffuser. The value of $\overline{q^2}$ then increases outward from the wall and attains maximum values which are greater than the equivalent maximum in the pipe flow (e.g. by about a factor of 2 at station 66) before decreasing asymptotically to the pipe flow value in the core region. Stations 42-66 indicate slight increases above feed pipe value of turbulence energy along the axis of the flow. Azad and Kassab (1989) attributed this increase to larger focusing effects [see Sabot and Comte-Bellot (1976)] at these stations above the same phenomenon in the feed pipe. Focusing effect is further investigated from the statistical properties of coherent motions in Chapter 5. It can also be noted from Fig. 4.9 that similar to other quantities evaluated earlier, the initial perturbation of the flow as it enters the diffuser has little effect on properties at stations 6 and 18 except near the wall. The trend of $-\overline{uv}$, see Fig. 4.6, is similar to that of $\overline{q^2}$. Maximum values of $-\overline{uv}$ and $\overline{q^2}$ in the diffuser occur at approximately the same radial position in each station and this location gradually shifts towards the axis of the flow with prolonged wall divergence. Thus, the peak region which has been defined as the location of the maximum values of $-\overline{uv}$ in the diffuser flow is also the location of maximum values of the total turbulence energy. Maximum production and dissipation of turbulent kinetic energy have also been associated with this region [see Kassab (1986)].

The correlation coefficient of Reynolds stress, $-\overline{\hat{u}\hat{v}}$, which gives a measure of the efficiency of turbulence mixing [Murlis et al. (1982)], is given in Fig. 4.10. In the fully developed pipe flow, the correlation has a value of 0.4 in the inner region, $0.6 \leq r/R_p < 1$, similar to measurements of Sabot and Comte-Bellot (1976) and Saleh (1978) whose pipe geometry and velocity characteristics are similar to the present set-up. In the diffuser, the shear stress correlation have values less than the pipe values in the core region but the near wall values remain of the order of 0.4. Hoffmann et al. (1985) has shown that irrotational flow regions in some complex flows produces high values of the anisotropy parameter, $\overline{v^2}/\overline{u^2}$, between 1 and 2, and in turn the shear stress correlation is of the order of 0.5. Values of $\overline{v^2}/\overline{u^2}$ in the wall region of the diffuser, see Fig. 4.8, does not indicate irrotational flow regions. Since this parameter is of the same order of magnitude in the wall regions of both the diffuser and pipe flows, the values of $-\overline{\hat{u}\hat{v}}$ of the order of 0.4 obtained in the wall region of the diffuser are justifiable.

Apart from $\overline{v^2}/\overline{u^2}$, the other anisotropy parameter $-\overline{uv}/\overline{q^2}$ is given in Fig. 4.11. The values are comparable to those of Kassab (1986). The values of $-\overline{uv}/\overline{q^2}$ in the core region, $r/R_p < 1$ are similar in the pipe and diffuser. The diverging part of the flow, $r/R_p > 1$ show a definite trend. This trend is similar but more spectacular than that of the shear stress correlation coefficient in Fig. 4.10 as has also been noted in other types of complex flows by Hoffmann et al. (1985) and by Saddoughi et al. (1991). The pipe value of $-\overline{uv}/\overline{q^2}$ closest to the wall is 0.11 which decreases slowly at first then rapidly to about 0.08 at station 66. The trend outward from the wall to $r/R_p \sim 1$ in each of the stations in the diffuser go through a plateau with the maximum value increasing with prolonged wall divergence. This trend in the wall region is essentially similar to the results of Smits et al. (1979) who evaluated the same quantity in the boundary layer of a diverging wall. As observed by Smits et al. (1979), the low values very close to the wall may be attributed to inactive motion because the high turbulence activity in the peak region (outer part of the boundary layer in their case) where eddies are large produces irrotational motions in the x, θ plane near the wall. This results in an increase in values of $\overline{u^2}$ and $\overline{w^2}$ but not $\overline{v^2}$ and $-\overline{uv}$. In Figs. 4.6 and 4.7(a), (b), (c) the trend of $-\overline{uv}$ and u'/U, v'/U, w'/U close to the wall support the above notion of inactive motions which has also been discussed elsewhere [see Townsend (1961) and Bradshaw (1967)].

4.2.2.2 Third-order moments

The skewness of u is shown in Fig. 4.12. The skewness like most measured parameters tend to have comparable values in the pipe and the initial stations of the diffuser. The values in the pipe and at station 6 as shown in Fig. 4.12 have negative values in all practical measuring positions and they have maximum negative values close to the axis of the flow. Other measuring stations have both negative and positive values. The non-zero values indicate the asymmetry of the probability density distribution of u, while the probability density distribution is symmetrical at the point where the skewness changes sign [see Hummel (1978)]. In addition, the point where the skewness changes sign at each station is similar to the position of maximum value of Reynolds stress in Fig. 4.6 which defines the peak region. Consistent with the definition of peak region, the point where $\overline{\hat{u}^3}$ changes sign moves towards the axis of the flow as the flow progresses. Similar change of sign in the pipe occurs at $Y^+ \sim 15$ (outside the range of standard x-wire probes in the current pipe geometry and flow characteristics), where the values of the turbulence intensity and Reynolds stress are maximum and the probability density distribution of u is symmetrical. $Y^+ \sim 15$ is at the edge of the buffer region in pipe flow and the similarity of properties with the peak region is essential for the understanding of the structure of turbulence in the diffuser flow. The skewness of v (see Fig. 4.13) show a similar trend like that of u at each station.

Other third-order moments of interest are presented as $\overline{\hat{u}^2\hat{v}}$ and $\overline{\hat{u}\hat{v}^2}$ in Figs. 4.14 and 4.15 respectively. The variations across the flow are similar to the skewness of u and v. The triple products appear in the equation for turbulent energy as the turbulent-transport term. In addition, third-order moments have been associated with the large eddies and Nakagawa and Nezu (1977), Nagano and Tagawa (1988) have shown that they can be used to deduce the contribution of large scale motions in turbulent flows because of their importance in turbulent diffusion. However, the theoretical models for the triple products are very poor. Nagano and Tagawa (1988) have shown significant deviations between measured triple products and the gradient diffusion model in pipe flow, while Castro and Bradshaw (1976) have shown the inapplicability of both the gradient diffusion and bulk-convection models in complex flows. Castro and Bradshaw indicated that the model based on transport velocities was the better of the two because it had a better collapse of data based on a simple choice of scale. Measured transport velocities in the present flow are given in Figs. 4.16 and 4.17. The transport velocities are defined as;

$$V_\tau = \frac{(\overline{pu} + \overline{uv^2})}{\overline{uv}}$$

$$\sim \frac{\overline{uv^2}}{\overline{uv}} \qquad 4.3$$

and

$$V_q = \frac{\left(\overline{pv} + \frac{1}{2}\overline{vq^2}\right)}{\frac{1}{2}\overline{q^2}}$$

$$\sim \frac{\overline{vq^2}}{\overline{q^2}} \qquad 4.4$$

In the final form of both Eqs. 4.3 and 4.4, the pressure velocity correlation has been neglected because the values are of the same order of magnitude as the error in measurement. In Figs. 4.16 and 4.17, the transport velocities have been normalized with the average bulk velocity in the pipe. In the case of V_q, $\overline{vq^2} = \overline{vu^2} + \overline{v^3} + \overline{vw^2}$. Since $\overline{vw^2}$ was not measured in this study, the value is approximated as $\overline{vw^2} = \frac{1}{2}(\overline{vu^2} + \overline{v^3})$, which has been similarly used by Smits et al (1979). Both V_τ and V_q in Figs. 4.16 and 4.17 respectively have similar shapes and values when compared to the results of Kassab (1986) even though in the case of V_q, $\overline{vw^2}$ was measured experimentally in that investigation. Both V_τ and V_q show positive values from the wall to the peak region. This is consistent with measurements of Smits et al. (1979) where all positive values were obtained for these quantities in the wall layer of a diverging boundary layer. In the present study, the average value of $V_q/V_\tau = 0.4$ is obtained from Figs. 4.16 and 4.17 in the wall layer. The values given by Smits et al. (1979) range from 0.5-0.7 and the difference may be due to their use of a $20°$ half-angle of divergence as opposed to $4°$ in the present work. In addition the core region which was not analyzed in the case of Smits et al. gives an average value of $V_q/V_\tau = 0.114$ while the average value for the entire flow is 0.257. This is practically identical to the value of 0.250 obtained by Azad and Kassab (1989) as the average value of V_q/V_τ in the diffuser. In the initial stations and the core region of stations 18-66, all values of V_τ and V_q are negative. The profile of V_q show both maximum and minimum values while that of V_τ show a maximum but no minimum.

4.2.2.3 Fourth-order moments

The flatness factors of u and v are given in Figs. 4.18 and 4.19 respectively. In the pipe and initial stations of the diffuser, $\overline{\hat{u}^4}$ tend to a constant value, approximately 2.8, in the wall region. The core region of these stations show increased values. On the other hand, stations 30-66 in Fig. 4.18 have high values of $\overline{\hat{u}^4}$ in the wall and core regions while a distinct minimum, with values ranging from 2.8-3.0, between the two extremes. The position of this minimum in many cases is approximately the same as the location where the skewness of u changes sign and hence is around the peak region. The high flatness values in the wall and core regions of the diffuser is related to the large amplitude and intermittency of velocity signals at these locations. $\overline{\hat{v}^4}$ in Fig. 4.19 show the same trend as $\overline{\hat{u}^4}$ but the minimum values are slightly above 3.

The fourth-order moment, $\overline{\hat{u}^2\hat{v}^2}$ are given in Fig. 4.20. Like the flatness factor of u and v, the inner stations have values of $\overline{\hat{u}^2\hat{v}^2}$ decreasing from the core region to the wall while the rest of the stations indicate a distinct minimum value around the peak region. The values of $\overline{\hat{u}^2\hat{v}^2}$ range from 1.2 to 1.6 which is consistent with the measurements in this flow by Arora (1978) and the reported range of 1-3 in high intensity turbulent flows by Guitton (1974). Other fourth-order moments, $\overline{\hat{u}^3\hat{v}}$ and $\overline{\hat{u}\hat{v}^3}$ are given in Figs. 4.21 and 4.22 respectively. When compared with each other, these later moments show nearly similar values and trend.

CHAPTER 5

STATISTICAL CHARACTERISTICS OF COHERENT STRUCTURES

5.1 CONDITIONAL AVERAGES.

In the present work, single point measurements are used to compute the contribution of different fluid motions to the Reynolds stress production. As described in the literature review, measured turbulent flow signals contain information due to coherent motions as well as incoherent turbulence. However, in evaluating conditional averages no attempt is usually made to eliminate the incoherent turbulence, probably because their contributions is small if a large amount of data is averaged in the analysis. The application of the quadrant splitting technique [Wallace et al. (1972)] including the modification to account for the magnitude of the contributions of events in each quadrant [Lu and Willmarth (1973)] is shown with respect to the quadrants in the uv-plane in Fig. 5.1. Briefly, the threshold is a parabolic curve that defines a constant value of $|uv|$ and can be varied by defining a hole size, H, such that $|uv| = H u'v'$. H can vary from zero to infinity but in most applications it is given integer values from 0-10. The signal obtained from x-wire is used to form a simultaneous time trace of u-, v-and uv-signals. Each data point in the uv-signal can be sorted into any of the quadrants (see Fig. 5.1) based on the sign of the u- and v- signals or from the sign of the u- and uv-signals. Once a data point is identified, the threshold criteria is applied, the value of $-uv(t)$ obtained at that point must be on or above the threshold (expressed mathematically as $|uv(t)| \geq H u'v'$). At the end of the record and for a particular hole size, the contributions to averaged Reynolds stress from each quadrant are averaged. This procedure is self explanatory in the flow chart given in Fig. 5.2. The major advantage of single point measurements is the use of the same data set for calculating mean quantities as in Chapters 3 and 4, hence no new experimental techniques are required.

5.1.1 Theoretical prediction of coherent structures

5.1.1.1 Probability density function (p.d.f)

Let the three-dimensional joint p.d.f with three components of a velocity vector, $\vec{V}(u,v,w)$ be defined as P(u,v,w). A more generalized presentation can be obtained by normalizing all fluctuating velocities by their respective rms values; $\hat{u}=u/u'$, $\hat{v}=v/v'$ and $\hat{w}=w/w'$. The characteristic function ψ, which represents the Fourier transform of $P(\hat{u},\hat{v},\hat{w})$ can be written as indicated by Monin and Yaglom (1971) as

$$\psi(\xi,\eta,\lambda)=\int\int\int_{-\infty}^{\infty}P(\hat{u},\hat{v},\hat{w})\exp\{i(\hat{u}\xi+\hat{v}\eta+\hat{w}\lambda)\}d\hat{u}d\hat{v}d\hat{w} \qquad 5.1$$

ξ, η and λ are the arguments of the characteristic function. One way of defining $\psi(\xi,\eta,\lambda)$ is in terms of moments, $\overline{\hat{u}^p\hat{v}^q\hat{w}^r}$ or m_{pqr}. Then it can be shown that ψ is related to m_{pqr} as

$$m_{pqr}=\frac{1}{i^K}\frac{\partial^K\psi(\xi,\eta,\lambda)}{\partial\xi^p\partial\eta^q\partial\lambda^r}\bigg|_{\xi=\eta=\lambda=0} \qquad 5.2$$

where K=p+q+r.

Monin and Yaglom (1971) has shown that ψ can be represented by Taylor series, hence the moments can be written as the coefficients in the expansion.

Thus

$$\psi(\xi,\eta,\lambda)=\sum_{p,q,r=0}^{\infty}\frac{i^K}{p!q!r!}m_{pqr}\xi^p\eta^q\lambda^r \qquad 5.3$$

In most applications ψ is often defined in terms of cumulants, k_{pqr} because for near Gaussian distributions the high-order cumulants can be discarded. The cumulants correspond to the coefficients in the Taylor series expansion of $\ln\psi$ and can be written as

$$k_{pqr}=\frac{1}{i^K}\frac{\partial^K\ln\psi(\xi,\eta,\lambda)}{\partial\xi^p\partial\eta^q\partial\lambda^r}\Big|_{\xi=\eta=\lambda=0} \qquad 5.4$$

and

$$\psi(\xi,\eta,\lambda)=\exp\left(\sum_{p,q,r=0}^{\infty}\frac{i^K}{p!q!r!}k_{pqr}\xi^p\eta^q\lambda^r\right) \qquad 5.5$$

The relationship between m_{pqr} and k_{pqr} can be obtained successively from Eqs. 5.2and 5.4,the Taylor series expansion of $\psi(\xi,\eta,\lambda)$ about $\xi=\eta=\lambda=0$ and noting that $\psi(0,0,0)=1$. For $K\le 4$ it can be shown that

$$\begin{aligned}
&K=0: && k_{000}=0, \quad m_{000}=1\\
&1\le K\le 3: && m_{pqr}=k_{pqr}\\
&K=4: && m_{400}=k_{400}+3, \quad m_{040}=k_{040}+3, \quad m_{004}=k_{004}+3\\
& && m_{310}=k_{310}+3m_{110}, \quad m_{301}=k_{301}+3m_{101},\ldots, \quad m_{013}=k_{013}+3m_{011}\\
& && m_{220}=k_{220}+2(m_{110})^2+1, \quad \ldots,\\
& && m_{112}=k_{112}+2m_{101}m_{011}+m_{110}
\end{aligned} \qquad 5.6$$

In turbulence phenomena, high-order cumulants are usually discarded [Nakagawa and Nezu (1977) and Nagano and Tagawa (1988)] because the probability distributions are assumed to be close to a Gaussian distribution. Therefore, for cumulants less than fourth-order the following Taylor series can be obtained from Eqs. 5.5 and 5.6.

$$\psi(\xi,\eta,\lambda)=\exp\{-\frac{1}{2}(\xi^2+\eta^2+\lambda^2+2R_{uv}\xi\eta+2R_{uw}\xi\lambda+2R_{vw}\eta\lambda)$$

$$+\sum_{K=3}^{4}\frac{i^K}{p!q!r!}k_{pqr}\xi^p\eta^q\lambda^r\} \qquad 5.7$$

where the correlation coefficients are given by

$$k_{110}=m_{110}=\overline{\hat{u}\hat{v}}=R_{uv}$$

$$k_{101}=R_{uw}$$

$$k_{011}=R_{vw}$$

Equation 5.7 can be written as

$$\psi(\xi,\eta,\lambda)=\exp\left\{-\frac{1}{2}(\xi^2+\eta^2+\lambda^2)\right\}\sum_{p,q,r=0}^{\infty}C_{pqr}i^K\xi^p\eta^q\lambda^r \qquad 5.8$$

Where the constants C_{pqr} can be calculated from Eqs. 5.7 and 5.8 and using the experimental values of moments given in Chapter 4 to obtain numerical values.

For $K \leq 4$ the values are

$$C_{000} = 1, \quad C_{100} = C_{010} = C_{001} = 0, \quad C_{200} = C_{020} = C_{002} = 0$$

$$C_{110} = R_{uv}, \quad C_{101} = R_{uw}, \quad C_{011} = R_{vw}$$

$$C_{300} = \frac{1}{6}k_{300}, \quad C_{030} = \frac{1}{6}k_{030}, \quad C_{003} = \frac{1}{6}k_{003}$$

$$C_{210} = \frac{1}{2}k_{210}, \quad \ldots\ldots, \quad C_{012} = \frac{1}{2}k_{012}, \quad C_{111} = k_{111}$$

$$C_{400} = \frac{1}{24}k_{400}, \quad \ldots\ldots, \quad C_{310} = \frac{1}{6}k_{310}, \quad \ldots\ldots, \quad C_{013} = \frac{1}{6}k_{013}$$

$$C_{220} = \frac{1}{4}(k_{220} + 2R^2_{uv}), \quad \ldots\ldots \quad C_{022} = \frac{1}{4}(k_{022} + 2R^2_{vw}), \quad \ldots,$$

$$C_{112} = \frac{1}{2}(k_{112} + 2R_{uw}R_{vw}) \tag{5.9}$$

Once ψ has been expressed in terms of cumulants as in Eq. 5.7, the final form will depend on whether $P(\hat{u}, \hat{v}, \hat{w})$ will be represented as the product of one-dimensional Hermite polynomials or by two-dimensional conjugate Hermite polynomials. Kampé de Fériet (1966) has shown that the later polynomials degenerate into the former in a two-dimensional velocity field if $\overline{\hat{u}\hat{v}}$ is zero. Solutions based on the two-dimensional conjugate Hermite polynomials can be found in Antonia and Atkinson (1973) and Nakagawa and Nezu (1977). The present work uses the one-dimensional Hermite polynomials because the resulting solution is compact and it gives excellent results as shown by Nagano and Tagawa (1988).

Therefore by taking the inverse Fourier transform of Eq. 5.1, substituting Eq. 5.8 in the resulting equation one obtains

$$P(\hat{u},\hat{v},\hat{w}) = \frac{1}{(2\pi)^2}\int\int\int_{-\infty}^{\infty}\psi(\xi,\eta,\lambda)\exp\{-i(\hat{u}\xi+\hat{v}\eta+\hat{w}\lambda)\}d\xi d\eta d\lambda$$

$$= \frac{1}{(2\pi)^{\frac{3}{2}}}\sum_{p,q,r=0}^{\infty} C_{pqr}H_p(\hat{u})H_q(\hat{v})H_r(\hat{w})\exp\left\{-\frac{1}{2}(\hat{u}^2+\hat{v}^2+\hat{w}^2)\right\} \quad 5.10$$

Where the one-dimensional Hermite polynomial, $H_n(\chi)$ is defined as

$$H_n(\chi) = (-1)^n \exp\left(\frac{1}{2}\chi^2\right)\frac{d^n}{d\chi^n}\exp\left(-\frac{1}{2}\chi^2\right) \quad 5.11$$

5.1.1.2 Probability density distribution of velocity

The probability density distributions $P(\hat{u})$, $P(\hat{v})$ and $P(\hat{w})$ can be obtained from Eq. 5.10 as follows:

$$P(\hat{u}) = \int\int_{-\infty}^{\infty}P(\hat{u},\hat{v},\hat{w})d\hat{v}d\hat{w}$$

$$= P_G(\hat{u})\{1 + C_{300}(\hat{u}^3 - 3\hat{u}) + C_{400}(\hat{u}^4 - 6\hat{u}^2 + 3)\} \quad 5.12$$

Using a similar procedure, it can be shown that,

$$P(\hat{v}) = P_G(\hat{v})\{1 + C_{030}(\hat{v}^3 - 3\hat{v}) + C_{040}(\hat{v}^4 - 6\hat{v}^2 + 3)\} \quad 5.13$$

and

$$P(\hat{w}) = P_G(\hat{w})\{1 + C_{003}(\hat{w}^3 - 3\hat{w}) + C_{004}(\hat{w}^4 - 6\hat{w}^2 + 3)\} \quad 5.14$$

where $P_G(\chi)$ is the first-order Gaussian p.d.f defined as

$$P_G(\chi) = \exp\left(-\frac{1}{2}\chi^2\right)/(2\pi)^{\frac{1}{2}}; \qquad \chi = \hat{u},\hat{v} \text{ or } \hat{w} \quad 5.15$$

5.1.1.3 Probability density distribution of second-order moments.

The two-dimensional joint p.d.f $P(\hat{u},\hat{v})$ can be obtained from the three-dimensional p.d.f, Eq. 5.10 as;

$$P(\hat{u},\hat{v}) = \int_{-\infty}^{\infty} P(\hat{u},\hat{v},\hat{w})\,d\hat{w}$$

$$= \frac{1}{2\pi} \sum_{p,q=0}^{K\le 4} C_{pq0} H_p(\hat{u}) H_q(\hat{v}) \exp\left\{-\frac{1}{2}(\hat{u}^2+\hat{v}^2)\right\} \qquad 5.16$$

The probability density distribution of second-order moments can be evaluated by differentiating the cumulative probability distribution function, $F_{II}(x)$ with respect to x [see Lin (1967) and Nagano and Tagawa (1988)]. For the case of $x = \hat{u}\hat{v}$, $F_{II}(x)$ can be defined as

$$F_{II}(x) = Prob(\hat{u}\hat{v} < x)$$

$$= \int_0^{\infty} d\hat{u} \int_{-\infty}^{\frac{x}{\hat{u}}} P(\hat{u},\hat{v})\,d\hat{v} + \int_{-\infty}^{0} d\hat{u} \int_{\frac{x}{\hat{u}}}^{\infty} P(\hat{u},\hat{v})\,d\hat{v} \qquad 5.17$$

Therefore, the p.d.f of $\hat{u}\hat{v}$ is given by

$$P_{II}(\hat{u}\hat{v}) = \frac{dF_{II}(x)}{dx}$$

$$= \int_0^{\infty} \left[P\left(\hat{u},\frac{x}{\hat{u}}\right) + P\left(-\hat{u},-\frac{x}{\hat{u}}\right)\right] \frac{d\hat{u}}{\hat{u}} \qquad 5.18$$

and by substituting Eq. 5.16 yields

$$P_{II}(\hat{u}\hat{v}) = \frac{1}{\pi} \sum_{p+q=even}^{K\le 4} C_{pq0} \int_0^{\infty} H_p(\hat{u}) H_q\left(\frac{x}{\hat{u}}\right) \exp[-\frac{1}{2}\{\hat{u}^2 + (\frac{x}{\hat{u}})^2\}] \frac{d\hat{u}}{\hat{u}} \qquad 5.19$$

Equation 5.19 can be solved numerically. However, the integral in Eq. 5.19 can be approximated by an infinite series of terms [Antonia and Atkinson (1973)]. If the integral is written as

$$I_{lm} = \int_0^\infty \hat{u}^l \left(\frac{x}{\hat{u}}\right)^m \exp\left[-\frac{1}{2}\left\{\hat{u}^2 + \left(\frac{x}{\hat{u}}\right)^2\right\}\right]\frac{d\hat{u}}{\hat{u}} \tag{5.20}$$

Where the Hermite polynomials are replaced by their argument raised to power l and m respectively. Then the solution of 5.20 [see Erdélyi (1954, p. 146) and Antonia and Atkinson (1973)] can be written as

$$I_{lm} = (x)^m |x|^{\frac{1}{2}(l-m)} K_{\frac{1}{2}(l-m)}(|x|) \tag{5.21}$$

Where $K_{(l-m)/2}(|x|)$ is the modified Bessel function of the second kind and order $(l-m)/2$. When Eq. 5.20 is used as a solution of the integral in Eq. 5.19, errors in the evaluation of the Bessel functions can introduce deviations in the prediction of $P_{II}(\hat{u}\hat{v})$. Initial calculations in this study indicate that if a single formula is used to estimate the Bessel functions over large class intervals, deviations of the order shown by Antonia and Atkinson (1973) can be introduced as well as negative values of the probability density at the tail of the distributions. Therefore, the accuracy of evaluating the Bessel functions was improved by using the method given by McCormick and Salvadori (1985, p. 290). In this method, for small class intervals, $x < (n+3)$ where $n = (l-m)/2$, $K_0(x)$ is evaluated from the power series involving $I_0(x)$ while $K_1(x)$ is evaluated by Wronskian formulas. Asymptotic expansions are used to obtain $K_n(x)$ for $x > (n+3)$; where $I_n(x)$ is the modified Bessel function of the first kind. By substituting non-zero constants, C_{pqr}, from Eq. 5.9 and all Hermite polynomials using Eq. 5.11 into Eq. 5.19, using Eq. 5.21 as solution of integrals in the form of Eq. 5.20, applying the Bessel function recurrence relations and finally rearranging terms, one obtains

$$\begin{aligned} P_{II}(\hat{u}\hat{v}) = {} & \pi^{-1} K_0(|\hat{u}\hat{v}|)\{(1 + C_{220} + 3C_{400} + 3C_{040}) + \hat{u}\hat{v}(C_{110} - 3C_{310} - 3C_{130}) \\ & + \hat{u}\hat{v}^2(C_{400} + C_{040} + C_{220})\} \\ & + \frac{|\hat{u}\hat{v}|}{\pi} K_1(|\hat{u}\hat{v}|)\{-2(C_{220} + 2C_{400} + 2C_{040}) + \hat{u}\hat{v}(C_{310} + C_{130})\} \end{aligned} \qquad 5.22$$

5.1.1.4 Probability density distribution of third-order moments.

The probability density distribution of third-order moments are obtained using the same procedure applied to second-order moments by defining $F_{III}(x)$ and using Eq. 5.10. The result of that analysis is

$$P_{III}(\hat{v}\hat{u}\hat{v}) = \frac{1}{\pi} \sum_{q-even}^{K\leq 4} C_{pq0} \int_0^\infty H_p\left(\frac{x}{\hat{v}^2}\right) H_q(\hat{v}) \exp\left[-\frac{1}{2}\left\{\left(\frac{x}{\hat{v}^2}\right)^2 + \hat{v}^2\right\}\right] \frac{d\hat{v}}{\hat{v}^2} \qquad 5.23$$

and

$$P_{III}(\hat{u}\hat{v}\hat{u}) = \frac{1}{\pi} \sum_{p-even}^{K\leq 4} C_{pq0} \int_0^\infty H_p(\hat{u}) H_q\left(\frac{x}{\hat{u}^2}\right) \exp\left[-\frac{1}{2}\left\{\hat{u}^2 + \left(\frac{x}{\hat{u}^2}\right)^2\right\}\right] \frac{d\hat{u}}{\hat{u}^2} \qquad 5.24$$

Where $x = \hat{v}\hat{u}\hat{v}$ or $\hat{u}\hat{v}\hat{u}$ respectively.

Similar to the method used to solve Eq. 5.19, it can be shown that the solution of Eq. 5.23 (with $x = \hat{v}\hat{u}\hat{v}$) is

$$P_{III}(\hat{v}\hat{u}\hat{v}) = \frac{1}{\pi}\{[(1 + C_{220} + 3C_{400} + 3C_{040}) + x^2(C_{220} + C_{400} + C_{040})]K_0(|x|)$$

$$+ [(-2C_{220} - 4C_{400} - 4C_{040}))]|x|K_1(|x|)$$

$$+ [xC_{120}]|x|^{\frac{1}{2}}K_{\frac{1}{2}}(|x|)$$

$$+ [x(-C_{120} - 3C_{300})]|x|^{-\frac{1}{2}}K_{-\frac{1}{2}}(|x|)$$

$$+ [x^3C_{300}]|x|^{-\frac{3}{2}}K_{-\frac{3}{2}}(|x|)\} \qquad 5.25$$

The solution of Eq. 5.24 can be obtained from Eq. 5.25 by defining $x = \hat{u}\hat{v}\hat{u}$ and interchanging values of p and q in C_{pq0}.

5.1.1.5 Contributions of different fluid motions to the average Reynolds stress

Nakagawa and Nezu (1977) and Nagano and Tagawa (1988), have successfully evaluated the contributions of different motions to the bursting process using the conditional probability density distribution of the Reynolds stress. Unlike the probability density distribution of Reynolds stress, $P_{II}(\hat{u}\hat{v})$ which contains no information on the bursting process, the conditional probability density distribution of Reynolds stress retains third-order cumulants which are associated with turbulent diffusion. As shown by Nakagawa and Nezu (1977) the presence of these third-order cumulants is necessary to relate probability density distributions with coherent structures.

Similar to the presentation of Nagano and Tagawa (1988), sign functions of the fluctuating velocities are defined to correspond with the quadrant methods classifications.

$$\sigma_{u,J} = (1, -1, -1, 1) \quad \text{and}$$

$$\sigma_{v,J} = (1, 1, -1, -1) \qquad 5.26$$

where the suffix J, denotes the quadrant in the (u,v) plane and a 1 or -1 indicate the sign of u or v in each quadrant. The right hand side of Eq. 5.26 is the sign equivalent of (J=1, J=2, J=3, J=4). With the quadrant classification it can also be shown that

$$P_{II}(\hat{u}\hat{v}) = \sum_{J=1}^{4} P_{II,J}(\hat{u}\hat{v}) \qquad 5.27$$

where J=1,..4 and $P_{II,J}(\hat{u}\hat{v})$ is the conditional probability density distribution of Reynolds stress. Conditional calculation can then be used to evaluate the p.d.f of $\hat{u}\hat{v}$ in each quadrant similar to the calculations in Sect. 5.1.1.3 with $P(\hat{u}, \hat{v})$ replaced by $P_{II,J}(\sigma_{u,J}\hat{u}, \sigma_{v,J}\hat{v})$. Resulting in

$$P_{II,J}(\hat{u}\hat{v}) = \frac{1}{2\pi}\sum_{p,q=0}^{K\le 4} \sigma_{u,J}^{p}\sigma_{v,J}^{q} C_{pq0} \int_0^{\infty} H_p(\hat{u}) H_q\left(\frac{\hat{u}\hat{v}}{\hat{u}}\right) \exp\left\{-\frac{1}{2}\left(\hat{u}^2 + \left(\frac{\hat{u}\hat{v}}{\hat{u}}\right)^2\right)\right\}\frac{d\hat{u}}{\hat{u}} \qquad 5.28$$

The moments $\overline{\hat{u}^l\hat{v}^m}$ in each quadrant can then be calculated to satisfy the threshold requirement, $uv \ge Hu'v'$, where the hole size is defined as, $H = |uv|/u'v'$. Thus, the moments $\overline{\hat{u}^l\hat{v}^m}$ is a weighted function defined as

$$(\overline{\hat{u}^l\hat{v}^m})_{H,J} = \int_H^{\infty} \sigma_{u,J}^{l}\sigma_{v,J}^{m}\hat{u}^l\hat{v}^m P_{II,J}(\hat{u}\hat{v})\, d(\hat{u}\hat{v}) \qquad 5.29$$

Equation 5.29 can be written in a compact form [Nagano and Tagawa (1988)] by substituting the conditional probability density distribution of Reynolds stress, normalizing the limits and setting $l = 1$ and m=1 to give

$$(\overline{\hat{u}\hat{v}})_{H,J} = \frac{1}{2\pi} \sum_{p,q=0}^{K\leq 4} \sigma_{u,J}^{1+p} \sigma_{v,J}^{1+q} C_{pq0} \int_0^\infty b_{1,p}(\hat{u}) \left\{ \int_{\frac{H}{\hat{u}}}^\infty b_{1,q}(\hat{v}) d\hat{v} \right\} d\hat{u} \qquad 5.30$$

Where,

$$b_{j,k}(\chi) = \chi^j H_k(\chi) \exp\left(-\frac{1}{2}\chi^2\right)$$

When the hole size, H is zero Eq. 5.30 can be written in the form of Eqs. 5.19, 5.23 and 5.24 hence the same method of solution is applicable. When H is not zero, Eq. 5.30 can be solved by using two dimensional numerical integration and noting that a singularity exists in the lower limit of the inner integral because the outer integral is integrated from zero to infinity. It should also be noted that a full expansion of Eq. 5.30 in terms of the non-zero values of C_{pq0} contains eleven double integrals which make the evaluation extremely tedious.

5.1.2 Results in the pipe and diffuser flows.

The probability density distributions of velocity, $P(\hat{u})$ and $P(\hat{v})$ in the pipe flow are shown in Figs. 5.3(a) and (b) respectively. Due to the similarity of trend from one measuring station to another, these characteristics in the diffuser are given at station 66 in Figs. 5.4(a) and (b) respectively. Station 66 is also chosen because it gives the maximum deviation of turbulence quantities from the pipe flow values. As noted in Chapter 4, the skewness of velocity should change sign at $Y^+ = 15$ at the edge of the buffer region in pipe flow and ideally this position should have a symmetrical probability density distribution. $Y^+ = 15$ Is not accessible with the present probe size and velocity characteristics but the inner part of the pipe flow, $Y^+ = 168$ in Fig. 5.3(a) still show a nearly symmetrical distribution of the probability density of u. This symmetrical shape of the probability density distribution of u is observed up-to $Y^+ = 1063$. In the core region, $P(\hat{u})$ is negatively skewed and it deviates from the Gaussian profile, $P_G(\hat{u})$ obtained from Eq. 5.15. Similar behavior is observed for $P(\hat{v})$ in Fig. 5.3(b) but the comparison with the Gaussian profile is only approximate. In the core region, $P(\hat{v})$ in pipe flow is positively skewed. Both $P(\hat{u})$ and $P(\hat{v})$ in pipe flow are accurately fit by the theoretical probability density distribution of velocity, i.e. Eqs. 5.12 and 5.13 respectively in the entire flow field. The probability density distribution of velocity in pipe flow compare favorably with similar analysis by Nagano and Tagawa (1988). Similar to the analysis in the pipe, the skewness of velocity in the diffuser changes sign around the peak region which in the case of station 66 is located at Y/R$\sim$0.586 ($r/R_p \sim 0.76$). Therefore in accordance with the discussion of moments in Chapter 4 and the observation of Hummel (1978), a symmetrical distribution that approximates the Gaussian probability density profile of velocity is expected at the peak region. This is found to be the case as shown in Figs. 5.4(a) and (b) for $P(\hat{u})$ and $P(\hat{v})$respectively. In the wall region (Y/R$<$0.586) $P(\hat{u})$ is skewed positively which is an indication of a sweep dominated type of motion as noted by Nagano and Tagawa (1988). $P(\hat{v})$ in the wall region is not skewed but the Gaussian profile show greater deviation from the experimental values. In the core region (Y/R$>$0.586), $P(\hat{u})$ is positively skewed similar to the observation in pipe flow which is an indication of ejection dominated flow. On the other hand, $P(\hat{v})$ is negatively skewed in the core region with more pronounced deviations than in the core region of the pipe in Fig. 5.3(b). Even with the complex nature of flow in the diffuser, the theoretical predictions of Eqs. 5.12 and 5.13 fit the observed experimental profiles of $P(\hat{u})$ and $P(\hat{v})$ respectively.

The probability density distribution of second-order moments are shown in Figs. 5.5 and 5.6 for the pipe and station 66 respectively. In both the pipe and station 66, the structures are similar across the flow and have long tails which indicates the intermittency of momentum transfer. The experimental points are well predicted by Eq. 5.22 which is the solution of Eq. 5.19. Similar goodness of fit of experimental data and Eq. 5.19 was obtained by Nagano and Tagawa (1988) in pipe flow but slight deviations were indicated by Antonia and Atkinson (1973) in channel flow. As can be observed from the solution of Eq. 5.19 given as Eq. 5.22, the accuracy of the theoretical prediction depends on experimental evaluation of second- and fourth-order moments that are used to evaluate the constant C_{pq0}, and the evaluation of zero- and first-order Bessel functions. Since measured moments up-to fourth-order have been successfully used to evaluate $P(\hat{u})$ and $P(\hat{v})$ from Eqs. 5.12 and 5.13 without Bessel functions, these experimental moments can be considered to be accurate. Therefore, the goodness of fit of the experimental values of $P_{II}(\hat{u}\hat{v})$ by the theoretical prediction can be attributed to a good estimation of the Bessel functions by the method given in Sect. 5.1.1.3.

The probability density distributions of third-order moments $P_{III}(\hat{v}\hat{u}\hat{v})$ and $P_{III}(\hat{u}\hat{v}\hat{u})$ in the pipe flow are given in Figs. 5.7(a) and (b) respectively, while at station 66, they are given respectively in Figs. 5.8(a) and (b). In both the pipe and diffuser, the slight deviation of theoretical predictions using Eqs. 5.23 and 5.24 from experimental values is of the same order of magnitude. From the solution of Eq. 5.23 given as Eq. 5.25, it can be noted that the constant C_{pq0} which is evaluated from experimentally measured moments contain moments evaluated when p+q=odd, unlike in the solution of $P_{II}(\hat{u}\hat{v})$ [see Eq. 5.22]. These third-order cumulants have been associated with turbulent diffusion by Nakagawa and Nezu (1977). Therefore, their presence in $P_{III}(\hat{v}\hat{u}\hat{v})$ and $P_{III}(\hat{u}\hat{v}\hat{u})$ indicates that the probability density distribution of third-order moments is related to turbulent diffusion and the long tails shown goes to indicate the intermittent nature of turbulent diffusion. The same introduction of third-order cumulants also results in Bessel functions of fractional order as indicated in Eq. 5.25. These Bessel functions of fractional order are evaluated using single hyperbolic relations over large class intervals and this may be the origin of the small deviations between experimental and theoretical predictions.

The fractional contributions of the different events to the averaged Reynolds stress are given in Figs. 5.9(a) for the fully developed pipe flow evaluated with a hole size of zero. The present experimental conditional averages in the pipe flow agree with similar measurements by Saleh (1978), Comte-Bellot et al. (1978) and the theoretical predictions using Eq. 5.30. As noted previously, standard x-wire probes cannot access the sublayer in the pipe, hence Fig. 5.9(a) shows mainly ejection dominated flow unlike the measurements of Nagano and Tagawa (1988) where custom made probes were used to indicate sweep dominated motions for $Y^+ < 15$. In the diffuser flow represented by stations 30 and 66 in Figs. 5.9(b) and (c) respectively, large sweep dominated motions are observed in the wall region consistent with the positively skewed values of $P(\hat{u})$ as indicated in Fig. 5.4(a). In addition, the transition from a sweep dominated wall region to ejection dominated core region occurs at Y/R$\sim$0.3 and Y/R$\sim$0.6 for stations 30 and 66 respectively. These positions represent the approximate location of the peak region at the respective stations. Therefore an additional characteristic of the peak region is the equal contributions of sweeps and ejections as well as equal contributions of inward and outward interactions to the Reynolds stress production as shown in Figs. 5.9(b) and (c). The theoretical prediction shown in Figs. 5.9(a)-(c) were obtained by using two-dimensional numerical integration algorithms to solve Eq. 5.30. It can easily be shown that when H=0, Eq. 5.30 can be written in a similar form as Eqs. 5.23 and 5.24 and hence has a solution similar to Eq. 5.25 which involves fractional Bessel functions and third-order cumulants. Therefore, the fact that numerical solution of Eq. 5.30 for H=0 produces a good fit as shown in Figs. 5.9(a)-(c), while the exact solution of Eqs. 5.23 and 5.24 produces slight deviations from experimental values as shown in Figs. 5.7 and 5.8, is an indication that some errors may be introduced by errors in the evaluation of the fractional Bessel functions. The numerical solution of Eq. 5.30 is compared with experimental values at various hole sizes at station 66 and presented in Figs. 5.10(a)-(c). The use of Eq. 5.30 produces slight deviations from experimental curves in the wall region [see Fig. 5.10(a)], but in the peak and core regions [see Figs. 5.10(b) and (c) respectively], the experimental values are well predicted. The peak region in Fig. 5.10(b) shows the approximate equality of ejections and sweeps as well as equality of inward and outward interactions for all hole sizes. A sweep dominated wall region [see Fig. 5.10(a)] and ejection dominated core region, Fig. 5.10(c), are also shown clearly for all hole sizes. The slight deviations of Eq. 5.30 from experimental values at higher hole sizes may be due to that fact that a singularity always exist in the lower limit of the inner integral when $\hat{u} = 0$ since in the numerical integration of the double integral, the inner integral is evaluated completely for each value in the limit of the outer integral.

Purely experimental curves obtained from smooth fitting to the experimental data of the four classes of events are given in Figs. 5.11(a)-(d), Figs. 5.12(a)-(d) and Figs. 5.13(a)-(d) for the pipe flow, station 30 and station 66 respectively. The fractional values of events less than 0.01 are not significant, so they are not shown in the figures. For the pipe flow, ejections and inward interactions compare with the data of Saleh (1978) and Comte-Bellot et al. (1978) over a wide range of hole sizes while outward interactions and sweeps show some deviations at higher hole sizes. The variation of events across the flow in Figs. 5.11-5.13 is consistent with the description of the variation of these quantities in the pipe and diffuser flow evaluated with H=0 and given in Fig. 5.9. In addition it can be noted that in the core region of both the pipe and diffuser, ejections and inward interactions are very strong. Sabot and Comte-Bellot (1976) attributed this phenomenon to focusing effects in which the increase in the values of inward interactions is associated with ejections originating from the opposite wall (which manifest themselves as inward interactions) and vice versa. Focusing effect will be further investigated in Chapter 6. In the diffuser flow, sweeps and outward interactions have high values in the wall region. The sweep domination of the wall region is so strong in the diffuser that its conditional average is still statistically significant at a hole size of 6.

5.2 TEMPORAL STATISTICS OF COHERENT STRUCTURES.

Temporal statistical characteristics of coherent structures, e.g., ensemble averages, mean period and duration of each event as well as intermittency factor of the Reynolds stress for each event require a knowledge of the instantaneous position of individual events in the entire series of the uv-signal. Therefore, unlike conditional averages, the presence of incoherent turbulence in the record erodes the dynamic significance of these characteristics. Since the quadrant and VITA techniques are not designed to eliminate the incoherent motions, further signal processing is required to compliment their usage in such circumstances. As noted by Hussian (1983), further processing includes the unenviable task of deciding which and how many realizations are to be discarded while retaining the dynamic significance of the educed structures. The pattern recognition scheme of Wallace et al. (1977), introduced in Chapter 2 is one of the well known selective ensemble averaging technique. This recognition scheme is, however, limited to flows with low Reynolds number and it depends on the sampling rate. For example, Wallace et al. used an 11 point (0.22 second) moving-window average to eliminate fluctuations. For flows with a higher Reynolds number or higher sampling frequency, a typical equivalent number of points within the range of 0.22 second will be 4,400 based on the present values of 200,000 data points of u-signal in a 10 second record. Therefore, it is evident that the application of this technique in the present flow will be extremely difficult and subjective. Moreover, Alfredsson and Johansson (1984) found that the v- and uv-signals contained more information on the bursting process than the u-signal which is made up of inactive events that do not contribute to the uv-signal. Therefore, too much dependence on the u-signal has its limitations and thus it is one of the reasons the quadrant method is considered a more reliable technique than VITA [Bogard and Tiederman (1986)]. By producing patterns from the u-signal, the pattern recognition scheme of Wallace et al. (1977) also appears to be a natural complimentary technique for VITA since both methods evaluate properties of the high speed front observed during bursting. In another signal processing technique, Bogard and Tiederman (1986) deduced that since ejections have a finite duration, the distribution of the time between successive ejections should not be expected to include those periods with values less than the mean duration. This argument was used together with the quadrant method to calculate the maximum period between ejections originating from the same burst. However, the limiting mean period (the minimum acceptable time between successive ejections) was evaluated to correspond with the mean duration at $Y^+ = 15$ in channel flow which is not accessible in some other flow geometries at high Reynolds number using standard x-wire probes e.g., in diffuser flow. They are also other signal processing procedures like the computer programs of Saleh (1978) which apparently apply some form of selective elimination but the method is not explicit in the presentation.

In the next section, a new pattern recognition scheme is presented which has been used in conjunction with the quadrant method to evaluate the temporal statistical characteristics of coherent structures in the present set-up. Due to the complex nature of the diffuser flow; high turbulence levels, varying adverse pressure gradient and high Reynolds number flow in the feed pipe, the proposed signal processing technique attempts to address the following desirable elements of selective eduction:

(a) A recognition scheme based on the uv-signal which contains more information about the bursting process than the u-signal.

(b) Easily recognizable patterns which provide a mental picture of the different scales and their distribution as they are recorded by the x-wire and convected past the sensor. The discarded realizations should also provide a strong link between selective ensemble averaging of the signal and the small scale structures that are not statistically significant in coherent motions.

(c) Calibration of the procedure using reliable results from other methods including flow visualization [Antonia (1990)] and the applicability of the procedure to high Reynolds number flows.

(d) Universality of applications. For example, the same calibration constants should be used in other types of flow (in the present case fully developed pipe flow and in the diffuser flow).

5.2.1 Recognition of patterns in the uv-signal.

The complex and random uv-signal obtained from x-wire measurements in turbulent flows can be adequately represented by a series of data points. Above an arbitrary threshold, $Hu'v'$ as defined in the quadrant splitting technique, a collection of data points have different durations; six basic patterns of these are shown schematically in Fig. 5.14. Patterns I-V indicate some special features, discussed later, and they represent a subset of events whose signal have more than one data point on or above the threshold. Pattern VI represent events whose signal have only one data point above the threshold. The following points should be noted when patterns in a hot-wire signal are identified from data points:

(1) The patterns in a hot-wire signal does not necessarily indicate the real coherent structure but the manner in which they are identified is related to some property of the structure of turbulence. Thus, the pattern obtained by smoothing and time differentiating the u-signal by Wallace et al. (1977) indicate events with strong acceleration and decelerations, while in Fig. 5.14 the emphasis is on the duration of each event above the threshold which accounts for the different scales of structures that are convected past the sensor.

(2) When patterns are represented by data points, they are easily affected by a choice of sampling rate. However sampling rates are fixed at any position in a flow by the Nyquist criterion hence any hot-wire measurements that do not indicate durations of data points above a threshold may not be useful for evaluating coherent motions. The application of this or any other probe based eduction schemes for coherent motions should note the range of sampling frequencies in the original investigation.

Jitters and small scale structures are undesirable in processing a signal for coherent motions because they erode the dynamic significance of the educed structures. In a time series of uv-signal, the small scale structures appear as fingerprints with small durations hence the most likely pattern associated with them in Fig. 5.14 is pattern VI. In pattern VI events, the single point above the threshold forms a triangle (if the points are connected by lines) with the duration defined by the threshold. The number of different durations presented by this single pattern in a record will depend on the height of the single point above the threshold. Thus, the uncertainty involved in selective eduction is evident because a decision has to be made to eliminate all or some of pattern VI events. This decision is not a trivial matter because cut-off durations that uniquely define jitters in a signal have never been defined. To overcome this difficulty we introduce the following expressions which are applicable to pattern VI type events.

$$uv \geq k_0(J)u'v' \quad ; \qquad for \quad H=0 \tag{5.31}$$

$$uv - Hu'v' \geq k_1(J)uv \quad ; \qquad for \quad H>0 \tag{5.32}$$

where $k_0(J)$ and $k_1(J)$ are constants with values ranging from zero to unity for any quadrant J. When the constants $k_0(J)$ and $k_1(J)$ are zero, all patterns VI events are taken into consideration in evaluating the statistical properties of events and when the values of these constants are taken as unity, no pattern VI event is considered in the analysis. Note that in this formulation, the hole size, H, is taken as an integer but similar subdivisions can be made between any consecutive values of H. There are two constants, namely, for H=0 and H>0, since the origin of the small scale structures can be completely different in the two cases. For example, at zero hole size pattern VI events arise mainly because of electronic noise in the signal and due to the breakup of structures. These are the small scale structures which exist naturally in the signal and some of them can be eliminated by higher threshold criteria of the quadrant or VITA algorithms. However at higher hole sizes, similar structures can be produced by truncation of the signal. For example, an event embedded in the hole may have spikes i.e. patterns I-IV in Fig. 5.14 can become pattern VI if the threshold is changed. These latter single point excursions above the threshold cannot be eliminated by merely defining higher thresholds, hence the threshold criteria of VITA and quadrant techniques are not sufficient conditions to eliminate them. Therefore, Eqs. (5.31) and (5.32) imply conditions that test the statistical significance of the small scale structures by stipulating that in order to be acceptable at H=0 and H>0, these structures simultaneously satisfy higher threshold criteria $k_0(J)$ and $H/[1-k_1(J)]$ respectively. It will be worthy to note that when these constants are zero, the method reduces to the application of the quadrant method. Since $k_0(J)$ and $k_1(J)$ vary from 0-1, the actual constants which retain the dynamic significance of the educed structure can only be obtained experimentally by calibration. In this study, $k_0(J)$ and $k_1(J)$ for hole size of 0 and 4 respectively were obtained at $Y/R_p=0.2$ in pipe flow by iteration such that the mean period evaluated with optimum values of the constants was equal to the mean periods between events obtained by Comte-Bellot et al. (1978). This calibration procedure was used for two reasons. Firstly, the pipe diameter and flow characteristics used by Comte-Bellot et al. (1978) are similar to the present set-up. Secondly, when the value of the mean period between ejections was made non-dimensional with outer variables it resulted in 6 for H=4 which is a commonly quoted figure in the inner part of a fully developed pipe flow. This same value has been obtained in other flows and with different detection techniques [see Bogard and Tiederman (1986) and many others]. Once the calibration is obtained at one point in a flow field, e.g. in pipe flow at $Y/R_p=0.2$, then the same calibration constants can be used at other locations in the flow field, e.g. in diffuser flow. The values of these constants are given in Table 5.1.

It is known that ejections and sweeps are motions with larger scales compared to outward or inward interactions. Therefore, the values of $k_0(J)$ in Table 5.1 reflect the fact that ejections and sweeps require tougher criteria for pattern VI events than outward and inward interactions. At higher hole sizes $k_1(2)$ is approximately equal to $k_1(4)$, while $k_1(1)$ is very different from $k_1(3)$. The difference in the values of $k_1(1)$ and $k_1(3)$ is because these constants were evaluated at the characteristic hole size of 4 which will result in negligible contributions to the average Reynolds stress by outward and inward interactions. Therefore the error between these quantities is a reflection of the difficulty involved in evaluating insignificant structures at a high hole size. In using this procedure, better values of $k_1(1)$ and $k_1(3)$ can be obtained with $H=1$.

The uniqueness of patterns I-V, which represent a broad range of possible patterns with more than one data points above a threshold, as shown in Fig. 5.14 should be noted. Patterns I and II types, are strong events with long durations and well defined leading and trailing edges hence their duration can be easily evaluated. In pattern III types, the trailing edge (or leading edge or both) is not well defined and some estimation of its duration may be required. Pattern IV types consist of more than one data points on the threshold followed by a well defined event (same type of pattern for points on the threshold after a well defined event). In using this recognition scheme in conjunction with the quadrant method, the duration of pattern IV events should be evaluated from the first data point. However when $H=0$ those leading or trailing points on the threshold are not defined by the quadrant classification, hence for that case the duration is estimated from the third point. A similar problem exist for pattern V events where the top of the pattern is on the threshold. Since all conditional sampling techniques are ultimately compared with visual evaluations, events such as pattern V are not visible above the threshold and are not defined for H=0. It is suspected that events of type V and those with very small durations of type VI which were counted by the application of the quadrant technique for non- zero hole sizes but not observed visually are responsible for the level of false detections noted by Bogard and Tiederman (1986).

The distribution of patterns VI during ejections in a fully developed pipe flow at $Y/R_p = 0.295$ as a function of hole size is given in Table 5.2. The total number of all other patterns with more than one data point above the threshold is also given. The number of pattern VI ejections rejected are high for H=0 due to the large value of $k_0(J)$ which makes Eq. 5.31 a very strict criterion. For $H > 0$ where Eq. 5.32 is applicable, the percentage of ejections rejected increase as the hole size increases. These percentages are of the same order of magnitude as the values obtained by Wallace et al. (1977) with their pattern recognition technique in a low Reynolds number turbulent flow and consequently the present method is valid for selectively discarding jitters in a high Reynolds number turbulent flow. The non-dimensional mean period between ejections, $T^* = TU_{c,p}/R_p$, where $U_{c,p}$ is the center-line mean velocity in the fully developed pipe flow, is evaluated when all patterns are used and when some pattern VI ejections are rejected as shown in Table 5.2. A detailed comparison of the two values of T^* is given in Sect. 5.2.2.

5.2.1.1 Evaluation technique.

A generalized flow chart for the technique which involves the evaluation of durations and conditional analysis of Reynolds stress (DCARS) is shown in Fig. 5.2. DCARS may include preliminary processing of the raw x-wire data to give relevant mean quantities followed by the formation of uv-signal time series from a simultaneous trace of u- and v-signals. The data file is accessed sequentially so that the signature of each event and its position in time is maintained.

The core of the program involves dummy arrays which are functions of the hole size, H and quadrant, J and uniquely identify each data point during an event. L(H,J) switches from a value of zero when the data point is the leading point of an event to one after the event has been initialized. M(H,J) is an indicator from the quadrant methods classification. It takes on a value of one if the sign of u and v places the event in the J^{Th} quadrant and zero otherwise. NS0(H,J) records the sample number of the leading edge of an identified event while subsequent data points that belong to the same event are continuously updated as final points, NSF(H,J). These dummy arrays are initialized at the beginning of the program and after the properties of each event has been calculated.

A brief summary of the process of identifying an event follows. The first data point that satisfies a particular threshold criterion is classified into the appropriate quadrant using the quadrant method. Being an initial point, the dummy array L(H,J) is set equal to one and the leading position noted as NS0(H,J). This process can be repeated for all hole sizes as long as the same data point is on or above the threshold.

If the event under consideration has more than one data point above the threshold (some of which occur as patterns I-V), the next data point will also satisfy the threshold criterion, will be sorted into the same quadrant and finally since L(H,J) is not zero, NSF(H,J) will be updated. The last process will continue till a data point falls into the hole resulting in the counting of the event, NE(H,J). The duration of the event $D_J(H, K)$ and time from the beginning of the record to the leading edge, $P_J(H, K)$ are also evaluated as functions of the event K as well as the hole size and quadrant. If the event under consideration were of pattern VI type, only one data point could have satisfied the threshold criterion. Therefore, NS0(H,J) will be initialized for the first point while next data point passes control to the box shown in Fig. 5.2. The calculations that take place in the box are not given in order to keep the flow chart as simple as possible. These calculations include a check for non-zero value of NS0(H,J) followed by the extra conditions specified by Eqs. 5.31 or 5.32. If the pattern VI event satisfies all conditions, then the duration of the event is taken as 1/(sampling rate), which is the maximum duration a pattern VI type event can attend, while other parameters are evaluated as shown previously. The duration of accepted pattern VI events is an approximate value because the exact value will be difficult to evaluate. Pattern VI events that do not satisfy all conditions are discarded and the dummy arrays are reset.

5.2.2 Results obtained from the application of DCARS.

5.2.2.1 Ensemble averages.

An important temporal statistical property of coherent structures is their ensemble averages which represent the signature of an event in the record. Alfredsson and Johansson (1984) compared their ensemble averages obtained in channel flow with those of Comte-Bellot et al. (1978) in pipe flow. They found that for equivalent measuring position ($y/b= 0.375$ in channel flow and $y/R_p=0.4$ in pipe flow) the observed frequency of occurrence for ejections normalized with outer time scale was 0.2 compared to 0.18 obtained by Comte-Bellot et al. at a hole size of four. In spite of the close agreement between this and other measured quantities, the duration was a factor three larger in viscous units or a factor of two smaller in outer time scale in the case of the uv-pattern of Comte-Bellot et al. (1978). Therefore it was concluded that the duration of the uv-pattern scaled neither with inner nor with outer variables at that point. Using the present procedure, the ensemble averages of u-, v-, and uv-signals are computed at $y/R_p=0.394$. The values of the frequency of occurrence normalized with outer variables is 0.24 when all patterns are used in the analysis and 0.19 when only acceptable patterns are used. The result evaluated using acceptable patterns as shown in Fig. 5.15 are phase aligned with the mid-point of the event and presented in the same format as Fig. 15 of Alfredsson and Johansson (1984). Asterisks on the velocities indicate the ensemble averages normalized by the product of the square root of the hole size and the respective rms value, the uv-pattern normalized with $Hu'v'$ and $\tau^+ = \tau / t_*$. Where τ is the time coordinate relative to the reference time and $t_* = \nu / u_*^2$ (ν is the kinematic viscosity and u_* is the friction velocity). The values for the uv-pattern of Comte-Bellot et al. (1978) were obtained from Fig. 15 of Alfredsson and Johansson (1984) where they had been corrected for time shift due to different setting of the reference time. The present quantitative shape of the uv-pattern is comparable with that of Alfredsson and Johansson (1984). In addition the width at half height, $T^+_{1/2}(v) = 4$ and $T^+_{1/2}(uv) = 3$ were obtained by Alfredsson and

Johansson (1984) at Y+=50. These are comparable with $T^+_{1/2}(v) = 5$ and $T^+_{1/2}(uv) = 4$ obtained by Bogard and Tiederman (1987) at Y+=15 in channel flow and the present result $T^+_{1/2}(v) = 5.9$ and $T^+_{1/2}(uv) = 3.4$ in pipe flow at y/R_p=0.394 (Y+=1063). The fact that the uv-pattern in the present pipe flow compare with results in channel flow more closely than the results of Comte-Bellot et al. (1978) indicate that any attempt to compare the scaling of uv-patterns in different flows [see Alfredsson and Johansson (1984)] must take into consideration the eduction procedure and phase alignment of the signal. The versatility of the present eduction procedure is also evident from the above analysis. That is, calibration of the constants in Eqs. 5.31 and 5.32 using experimental values of Comte-Bellot et al. does not necessarily produce the same velocity signals during bursting.

In Fig. 5.16(a) the ensemble averages are presented at y/R_p=0.394 with a hole size of one so that the effect of the hole size in normalizing the velocity and uv-patterns is removed. The peak values of the velocity and uv-patterns are greatly improved and the width at half height are $T^+_{1/2}(u) = 11.9$, $T^+_{1/2}(v) = 10.0$ and $T^+_{1/2}(uv) = 5.5$. To re-emphasize the importance of phase alignment, the same samples as in Fig. 5.16(a) were phase aligned with the maximum value of -uv. It can be observed by comparison with Fig. 5.16(a) that while the u- and v-signal peaks only increased slightly, the uv-signal peak is nearly doubled in Fig. 5.16(b). Bogard and Tiederman (1987) similarly observed increases in peak by a factor of 3 when their samples were phase aligned with the -uv peak instead of the mid-point of the sample in a channel flow. While in the presentation of Bogard and Tiederman (1987), the peak position of the uv-signal in Fig. 5.16(b) was taken as $\tau^+ = 0$, in the present case the peak is shown relative to the time scale based on the mid-point of detection. The shift in the peak value of the uv-pattern to positive values of τ^+ indicate that detection criteria that are based on the mid-point of the events will be triggered before the full impact of the event. Since bursting is associated with large values of the Reynolds stress, ensemble averages phase aligned with the -uv peak are a better representation of the phenomenon than phase alignment with the mid-point of the samples.

The ensemble averages evaluated with H=1 during ejections at station 66 are shown in Figs. 5.17(a)-(c). Station 66 is chosen because the signatures are similar at other stations and the ensemble averages evaluated near the wall, at the peak and core regions of the flow are presented in Figs. 5.17(a), (b) and (c) respectively. The samples are phase aligned with the mid-point of the event and τ is normalized with t_* values obtained in the fully developed pipe flow. As shown in Table 3.1, values of u_* vary along the length of the diffuser, thus calculated values of the inner time scale, t_* will vary from 0.022 ms in pipe flow to 0.533 ms at Station 66. Therefore, normalization with t_* obtained in pipe flow ensures a better comparison between ensemble averages of ejections evaluated at different stations. The velocity and uv- patterns are similar across the flow and qualitatively compare with similar evaluations in other wall bounded turbulent flows. The width at half height near the wall in Fig. 5.17(a) are $T^+_{1/2}(u) = 43.0, T^+_{1/2}(v) = 35.1$ and $T^+_{1/2}(uv) = 15.5$. At the peak and core regions of the diffuser, the values are 21.0, 17.3, 7.7 and 19.1, 16.4, 7.7 obtained from Figs.5.17(b) and (c) respectively. An equivalent region of the pipe flow dominated by the sweep event is in the sublayer (i.e. $Y^+ < 15$) and it is outside the range of standard x-wire probes used in the present investigation. Therefore only the ensemble averages obtained at the peak region of the diffuser can be compared with the pipe flow values shown in Fig. 5.16(a) which represent ensemble averages in the inner part of the pipe flow. The comparison indicates that the velocity and uv- patterns obtained in the inner region of the pipe flow have more pronounced peaks than those obtained in the peak region of the diffuser [see Fig. 5.17(b)]. However, the ensemble averages in the diffuser flow show longer durations as represented by the calculated width at half height.

5.2.2.2 Mean period of events.

Due to the fact that the conditions imposed on the small scale patterns by Eqs. 5.31 and 5.32 depend on the choice of existing experimental values used in calibration, some of the analysis of the signal was performed in two ways. Firstly all patterns observed in the signal were used to estimate the statistical quantities. Secondly, all patterns with more than one data point above the threshold (patterns I-V inclusive) and some pattern VI events that satisfy the extra conditions imposed by Eqs. 5.31 and 5.32 were used. The result of this analysis was used to evaluate the non-dimensional mean period, T^* between ejections which is presented in Fig. 5.18 and also in Table 5.2 at Y/R_p=0.295 in pipe flow. It can be seen from this figure that when all patterns were taken into consideration an approximately constant value of 4 was obtained for T^* in the inner part of the pipe flow evaluated with the characteristic hole size of 4. Similar results had been obtained in the pre-pattern recognition years (i.e before 1977) as shown in Fig. 5.18 by the results of Lu and Willmarth (1973) in channel flow and Sabot and Comte-Bellot (1976) in pipe flow. The difference between the present result and those of Sabot and Comte-Bellot (1976) may be due to the fact that their analog circuits limited their analysis to low amplitudes of the signal. When only some of pattern VI ejections were used due to the application of Eq. 5.32 as well as all other patterns, the resulting values of T^* in pipe flow were comparable with those of Comte-Bellot et al. (1978) as shown in fig. 5.18. While $k_0(J)$ and $k_1(J)$ were evaluated by matching T^* values in the inner part of the pipe flow at $Y/R_p=0.2$ with values obtained by Comte-Bellot et al. (1978), the level of collapse at other measuring locations can only be good if pattern VI events are correctly identified and the conditions imposed by Eqs. 5.31 and 5.32 have physical significance. This appears to be the case from the comparison shown in Fig. 5.18. A complete comparison between the present values of T^* in pipe flow and the values obtained by Saleh (1978) as well as Comte-Bellot et al. (1978) are given in Figs. 5.19(a), (b), (c) and (d) for outward interactions, ejections, inward interactions and sweep respectively. The close agreement at various hole sizes is remarkable considering the scatter in T^* values obtained from applying different signal processing algorithms as presented by Bogard and Tiederman (1986). Therefore, by inference the present data should also compare favorably with T^* values if they were obtained using the pattern recognition scheme of Wallace et al. (1977) since Bogard and Tiederman (1986) showed that their estimates from flow visualization were similar to values obtained by applying the methods by Wallace et al. and Comte-Bellot et al. respectively in the same flow. Also, as can be inferred from Antonia (1990) the present method clearly incorporates the ability to calibrate the detection procedure unlike existing methods which can only be calibrated against visualization method and are limited to low Reynolds number flows.

The mean period between individual events at stations 30 and 66 of the diffuser are presented as a function of the thresholds are shown in Figs. 5.20(a)-(d) and 5.21(a)-(d) respectively. The mean periods have been normalized with the outer time scale ($R_p/U_{c,p}$) obtained in pipe flow. Similar to the wall time scale, R/U_c varies from 2.34 ms in the pipe flow to 6.99 ms at Station 66 hence the constant pipe value is a better quantity for normalizing all measurements in the diffuser for the purpose of comparison. With respect to ejections at station 66, Fig. 5.21(b) shows that for small hole sizes the mean period between ejections decrease from a high value close to the wall to smaller values near the axis of the flow. At higher hole sizes, e.g., H=4, the mean period near the wall attains a maximum value roughly around $y/R_p=0.2$ before finally decreasing towards the axis of the flow. A different trend exist for the sweep type motion as shown in Fig. 5.21(d). For higher hole sizes the sweep events attain a minimum value slightly shifted ($y/R_p \sim 0.3$) from the maximum value observed for ejections. It can be observed that the trend for inward interactions are similar to those of ejections while the trend of outward interactions are similar to sweep. This is a consequence of focusing effect as observed by Sabot and Comte-Bellot, (1976). The trend of mean periods at station 30 are similar to those at station 66.

5.2.2.3 Intermittency factor of Reynolds stress during bursting.

The fraction of time spent in any phase of the bursting cycle is represented by the intermittency factor of $-\overline{uv}$ during each event. These are given for the fully developed pipe flow in Figs. 5.22(a)-(d) and Figs. 5.23(a)-(d) for the diffuser flow at station 66 respectively. In Figs. 5.22(a)-(d), values of the intermittency factor of $-\overline{uv}$, γ_J in the fully developed pipe flow are also compared with results obtained by Saleh

(1978) and Comte-Bellot et al. (1978). As similarly noted by Comte-Bellot et al., the values of γ_J are relatively constant in the inner part of the pipe flow for moderate values of H. For the ejection and sweep events, values of γ_J tend to decrease towards the axis of the pipe which is a consequence of focusing from the opposite wall. Outward interactions and sweeps compare more favorably with the values of γ_J obtained by Comte-Bellot, at al (1978) at different hole sizes than ejections and inward interactions.

Values of γ_J in the diffuser, Figs. 5.23(a)-(d), show more pronounced variations across the flow than in the fully developed pipe. However, the overall trend are similar with ejections and sweeps indicating the presence of focusing effect by decreasing towards the axis. Like the mean periods, the variation of γ_J across the diffuser for each event show pronounced maximum or minimum values at some point in the flow which may imply a complex bursting mechanism in the diffuser. The significance of such variations will be discussed in Chapter 6.

5.2.2.4 Mean duration of events.

The mean duration of events are given in Figs. 5.24(a)-(d) for the pipe flow and in Figs. 5.25(a)-(d) at station 66 of the diffuser. The values of ΔT_J obtained from DCARS are normalized with the outer time scale in the pipe flow and the values show that events have small durations of the order of milliseconds. The duration of events decrease with the truncation level, H, in both the pipe and diffuser flows. The values of ΔT_J in the pipe flow are not compared with similar evaluations given by Comte-Bellot et al. (1978) because their normalization was an attempt to estimate the mean streamwise size of events, l_J. l_J is normally estimated from the Taylor hypothesis; $l_J = U \triangle T_J$ which is not satisfactory due to large velocity defects during ejection and sweep events as indicated by the ensemble averages in Fig. 5.16(a). Therefore, more reliable estimates were obtained by Comte-Bellot et al. by defining $l_J = \tilde{U}_J \triangle T_J$; where $\tilde{U}_J$ is the conditional averages of the instantaneous streamwise velocity. In spite of their indirect approach designed to estimate the integral length scale, values of $\tilde{U}_J \triangle T_J / R_p$ approximately varied from 0.07-0.11 and 0.09-0.13 for ejections and sweeps respectively at zero hole size which is comparable to values shown in Figs. 5.24(b) and (d). Moreover, the good correspondence between values of γ_J and T_J obtained in the present work and theirs imply that values of $\triangle T_J$ obtained from the relation, $\triangle T_J = \gamma_J T_J$ will be similar within experimental errors. Comparison between the mean duration of events in the pipe and at various stations of the diffuser is given in Chapter 6.

CHAPTER 6

AN OVERVIEW AND IMPLICATIONS OF THE RESULTS

Characterization of the diffuser flow presented in Chapter 4 described several long-time averaged quantities with the view of establishing basic structural features of the flow. In spite of the fact that long-time averaged quantities may obscure the structure of turbulence [see Mollo-Christensen (1971)], some basic characteristics of the nature of turbulence in the diffuser can be deduced. Flow in the conical diffuser changes continuously both in the longitudinal and radial directions. Longitudinally, the diffuser flow can be divided into initial, intermediate and outer stations. The initial stations, from the entrance of the diffuser to station 18, are characterized by moderately high adverse pressure gradients as well as mixing and instability of the flow due to the initial perturbation. The intermediate stations, 24-36, have flow characteristics that are similar to a two-dimensional mild adverse pressure gradient flow. While stations 42-66 which represent the outer stations are characterized by low mean velocities accompanied by high intensity of turbulence in the wall region. The outer stations also have very mild adverse pressure gradients and their velocity characteristics are identical to flows that are close to detachment. Radially, measured quantities tend to have comparable values as in the fully developed pipe flow in the inner stations, then they show progressively larger deviations in the intermediate and outer stations. Regardless of the three different longitudinal flow classifications, all radial measurements show unique characteristics at the peak region.

6.1 COMMON FEATURES OF TURBULENCE STRUCTURE DEDUCED FROM LONG-TIME AVERAGED QUANTITIES AND COHERENT MOTIONS.

The most important feature of the diffuser flow is the peak region which is approximately located along an imaginary cylindrical surface with a radius equal to that of the feed pipe. A more representative location of the peak region is sketched in Fig. 6.1 which also indicates the dominating coherent motions based on the analysis given in Chapter 5. The peak region has been uniquely defined by a characteristic velocity scale, U_m, and a length scale, L_s, which are important parameters for flows that are near separation [Schofield and Perry (1972) and Simpson (1991)]. From long-time averaged statistics, it has been deduced that the peak region has similar characteristics like the edge of the sublayer $(Y^+ \sim 15)$ in canonical boundary layers. These characteristics include, (a) maximum values of the averaged Reynolds stress, turbulence velocity fluctuations, and total turbulence energy; (b) zero values of the third-order moments of fluctuating velocity; (c) symmetrical distribution of the probability density of velocity; and (d) maximum values of the production and dissipation of turbulent kinetic energy [Kassab (1986)]. The above similarity of the peak region and the edge of the sublayer in canonical boundary layers is supported by the evaluated properties of coherent structures in this region which indicates equal contributions of sweeps and ejections, as well as equal contributions of inward and outward interactions, to the averaged Reynolds stress. In addition, like the edge of the sublayer in the canonical case, sweep events dominate the flow structure from the wall to the peak region while ejection events dominate the structure in the core region. The sweep domination of the turbulence structure close to the wall and the ejection domination in the core region could also be accurately predicted from the positive and negative skewness of the probability density distribution of velocity respectively (see Sect. 5.1.2).

As a rule of thumb, the presence or absence of strong coherent motions can be inferred from the magnitude of the Reynolds stress production. In complex flows, curved flows [Castro and Bradshaw (1976)] and diverging flows [Smits et al. (1979); Simpson (1991)], there is a strong evidence of 'inactive' motions near the wall in which large scale eddies contribute to the Reynolds stress further from the wall than at the point of observation [Townsend (1961) and Bradshaw (1967)]. In the present flow, the presence of 'inactive' motions has been deduced from the anisotropy parameter, $-\overline{uv}/\overline{q^2}$ in Fig. 4.11, and from the observed trend of shear stress, total turbulence energy, and the turbulence intensities across the flow. Therefore, as concluded by Simpson (1991) from the evaluation of diverging flows close to separation, there should be little evidence of stress producing burst in the near wall region. The above observation, based as it is on long-time averaged statistics, is further investigated by evaluating the distributions of strong coherent structures across the flow. Strong coherent structures are defined as event for which $|uv| \geq 4u'v'$. This is similar to the definition used by Lu and Willmarth (1973), but Kline (1988) and Robinson (1991 a) used a slightly different definition based on the wall shear stress, $u'v' \leq 4\rho u_*^2$. Figures 6.2(a) and (b) show the distributions of strong ejections and strong sweeps respectively in the pipe and at several measuring stations in the diffuser. It is difficult to indicate clearly the position of the peak region for each station on the figures hence a range is shown, see Figs. 6.2(a) and (b), from $r/R_p \sim 1$ for the pipe and the initial stations to

$r/R_p \sim 0.8$ for station 66. Figure 6.2(a) indicates that minimum contributions from the ejection phase, mainly in the outer stations, occur between the wall and the peak region. The same location has been associated with 'inactive' motions in Fig. 4.11. The sweep event shows a slight maximum at the location of 'inactive' motions [Fig. 6.2(b)].

A major observation in complex flows is the fact that the time averaged Reynolds stress and total energy attain maximum values (at the peak region of curved or diverging flows) which are greater than the maximum values attained by these quantities in the feed flow. This overshoot of feed flow values have not been satisfactorily explained. As a consequence of 'inactive' motions, large scale eddies could re-establish slower than other energy containing eddies further from the wall [Castro and Bradshaw (1976)]. This concept is capable of explaining large amounts of Reynolds stress away from the wall, however, it is not a sufficient reason for the observed overshoot because the stress to intensity ratio which is a measure of the efficiency of Reynolds stress productions is of the same order of magnitude in both the diffuser and pipe flows (see Fig. 4.11). A possible explanation of the overshoot may involve the existence of significant Reynolds stress production at the peak region which is supplemented by the effect of 'inactive' motions. Such an origin of the peak region can be attributed to memory effects which as shown by Trupp et al. (1986) may be responsible for the dual log-law regions observed in the outer stations of the diffuser where both maximum values of Reynolds stress are attained and 'inactive' motions most intense. By inference, while a thin mean shear layer is being formed near the wall as the flow enters the diffuser, a maximum shear stress layer (peak region) which retains some properties of the edge of the sublayer in the feed pipe is simultaneously formed. Thus, the stress producing capability of the peak region only decreases progressively in spite of the abrupt changes in velocity profiles [see Nash and Hick (1969)]. At the initial stations where 'inactive' motions are negligible, the observed Reynolds stress profile shows no overshoot of pipe flow values [see Fig. 4.6]. Thus, as 'inactive' motions becomes more intense in the intermediate and outer stations, progressively larger maximum values of shear stress and the overshoot of the feed pipe values are noted.

Observation of Figs. 6.2(a) and (b) indicate that while the location of 'inactive' motions is accurately predicted by the absence of stress producing burst, the peak region does not show higher values of strong ejections when compared to the near wall regions of the pipe ($r/R_p \sim 1$). The observed trend of strong ejections and sweeps at the peak region is a rapid increase and decrease outward from the wall respectively. This may imply that the special features of the peak region are produced by some complex mechanism involving the evolution of strong structures and can only be accurately deduced from conceptual models and vortex dynamics. Some inferences on the possible mechanism of strong structures based on the present results and existing conceptual models is given in Sect. 6.4.1

6.2 COMPARISON OF STRONG COHERENT STRUCTURES IN THE PIPE AND DIFFUSER FLOWS.

The variation of strong ejections and sweeps in the pipe and various stations, given in Figs. 6.2(a) and (b) respectively, have been used in the previous section to explain some of the structural features of turbulence observed in the diffuser. In addition, the trend of strong ejections and sweeps across the pipe flow from the wall gently decrease and increase respectively outside the sublayer in the interval $0.4 < r/R_p < 1$. The sharp rise of these two events in the core region of the pipe for $r/R_p < 0.4$ is due to focusing effects [Sabot and Comte-Bellot (1976)]. In the diffuser stations, the variation of ejections and sweeps in the core region ($r/R_p < 1$) are comparable with the trend in the pipe but significant changes exist at each station between the wall mean shear layer and the peak region.

The mean period between ejections and between sweeps across the flow in the pipe and at different diffuser stations are given in Figs. 6.3(a) and (b) respectively. In Fig. 6.3(a), the trend of the mean period between ejections in the initial part of the diffuser, Stations 6-18, are similar to those obtained in pipe flow. This is consistent with the fact that conditionally averaged Reynolds stress are also comparable with the pipe flow values. However, since the mean period between ejections shown in Fig. 6.3(a) at station 6-18 are equal or less than pipe values, the frequency of ejections on the average will be higher than pipe flow values at the initial stations. For Stations 24-66, where regions of 'inactive' motions near the wall result in significant differences between the averaged Reynolds stress in the feed pipe and the measuring stations, the mean periods between ejections show similar differences. In general, the mean periods tend to maximum values between the wall mean shear layer and the peak region where there is a deficiency of stress producing bursts. Figure 6.3(a) also shows that ejections in the intermediate and outer stations of the diffuser will occur less frequently across most part of the wall region, since the mean periods are less than pipe flow values. However, in the core region the values tend to a constant value, approximately equal to the pipe value, at about $r/R_p \sim 0.2$. At this location in the pipe, the frequency of strong ejections is 81 per second. While at $r/R_p=0.9$, in the pipe, the frequency is 49 per second. Since the frequency at $r/R_p \sim 0.2$ is the highest in the pipe, it represents the approximate location where focusing effects are most intense [see Sabot and Comte-Bellot (1976)]. However, since the mean period between ejections evaluated in the diffuser tend to the values obtained in pipe flow for $r/R_p > 0.2$, it can be expected that focusing effect in the diffuser will have comparable intensity to that in the pipe flow. The analysis of focusing effects in the core region of the pipe and diffuser flows in the following section will investigate the above observation. In Fig. 6.3(b) the mean periods between sweeps has minimum values at the location where strong sweeps attain maximum values. The overall trend indicates that the frequency of occurrence of sweeps is greater in the diffuser flow than in the fully developed pipe flow.

The mean durations and the intermittency factor of ejections across the flow are shown in Figs. 6.4 and 6.5 respectively. The mean duration of ejections in the exit part of the diffuser flow are generally greater than the pipe flow values. The trend of the mean durations compares with high and low values of the conditional averages of ejections at various locations in the flow and is consistent with the comparison between the width at half height of ensemble averages in the pipe and diffuser flow presented in Chapter 5. The amount of time spent in the ejections phase is relatively constant in the pipe and equal to values obtained at corresponding positions in the initial stations of the diffuser. In the exit portions of the diffuser flow, the intermittency factor of ejections attains higher and lower values than the values in the pipe flow reflecting a more complex bursting mechanism which may be produced by prolonged wall divergence.

6.3 THE CORE REGION: FOCUSING EFFECTS IN THE DIFFUSER FLOW.

Some fundamental properties of coherent structures in the core region can be investigated from the variation of the characteristic hole size, H_c across the flow. H_c is defined as the truncation level of signal for which the ejection phase contributes more than 10% to the average value of the local Reynolds shear stress while the contributions of other events are negligible. It can be seen from Figs. 5.9(a)-(c) at station 66 that such a definition is only valid between the peak region and the axis of the diffuser. The variation of H_c across the pipe and diffuser stations is given in Fig. 6.6. H_c has a constant value of 4 from the peak region (or close to the wall in the case of pipe flow) to an average position of $r/R_p \sim 0.625$ from the axis of the flow in both the pipe and diffuser. After $r/R_p \sim 0.625$, H_c decreases linearly to a value of about 3 near the axis of the flow. Sabot & Comte-Bellot (1976) explained the linear decrease of H_c in the core region of pipe flow in terms of a focusing effect caused by the circular geometry of the wall and the preferential sensitivity of the x-wire probe. The similar observed trend of H_c in the diffuser flow, therefore, confirms the existence of low-speed momentum fluid crossing the axis of the flow. Specifically, the effect of focusing is manifested as ejections from one wall becoming inward interactions at the opposite wall and vice versa. Sweeps and outward interactions are also interchanged on crossing the axis. As shown in Fig. 6.6, the point where H_c starts to decrease shifted slightly in the outer stations of the diffuser. This shift is equivalent to errors in evaluating H_c of 0.2 or a maximum displacement from the pipe position of 3mm. The above order of errors is negligible in highly turbulent flows and it can be concluded that focusing effects do not appear to be more intense in the diffuser than in the pipe. This conclusion is consistent with the fact that the frequency of ejections in the pipe and diffuser flows tend to the same value at $r/R_p \sim 0.2$ as discussed in Sect. 6.2. Therefore, contrary to the observations of Azad & Kassab (1989), the increase in turbulence activity in the core region of the outer stations of the diffuser cannot be attributed to an increase in focusing effect over the same phenomenon in pipe flow. However, since the peak region does not remain constant at $r/R_p \sim 1$ throughout the flow as shown in Fig. 6.1, it can be noted that constant values of H_c span a distance of about $0.39R_p$ in the flow field from the pipe to about station 30, then it gradually decreases to $0.12R_p$ at station 66. In other words, the sweep dominated wall flow is well buffered from flow in the core region from the pipe to station 30, while in the outer stations the two types of flow structures are nearly interacting. The effects of such interactions may be the probable cause of higher turbulence activity in the core region of the outer stations.

6.4 THE EFFECT OF ADVERSE PRESSURE GRADIENT ON THE COHERENT MOTIONS.

The average frequency, $N_J(H)$, of strong ejections and sweeps (with $H=4$) are given in Figs. 6.7(a) and (b) as a function of the non-dimensional adverse pressure gradient parameter, α_1. The frequencies are made non-dimensional using the kinematic viscosity and the friction velocity in the pipe prior to the application of the pressure gradient. In Fig. 6.7(a) the frequency of ejections near the wall, $Y/R_p=0.1$, drops rapidly as the pressure gradient becomes less adverse. In a related study, Badri Narayanan et al. (1977) observed a decrease in burst rate with downstream distance in the region of strong acceleration. Similar results have also been presented by Kline et al. (1967) using a slightly different parameter; the burst rate per unit span. Apart from the similarity of trend, further comparison of the frequency of strong ejections with the results of Badri Narayanan et al. is unnecessary since their method of analysis identified burst which can be made up of more than one ejection [See Bogard and Tiederman (1986)]. Further from the wall, in Fig. 6.7(a), the variation of the frequency of strong ejections with pressure gradient appears to be made up of two curves. A gently decreasing frequency of ejections in the region of strong adverse pressure gradient, followed by a precipitous drop in the region of mild adverse pressure gradient. In Fig. 6.7(b), near the wall at ($Y/R_p=0.1$), the frequency of sweeps increases with decreasing adverse pressure gradient to about station 30 then drops off to lower values in the downstream stations. This trend in the frequency of sweeps persist with little variations up to $Y/R_p=0.4$ from the wall. For $Y/R_p>0.4$, the frequency of sweeps is relatively constant in the initial part of the diffuser, then suddenly increases from about station 18 to station 42 where it momentarily drops off then rise sharply to station 66. The shape of these curves, Figs. 6.7(a) and (b), depends on the position of the peak region. If the wall layer in the diffuser is considered as the area between the wall and the peak region, then the shape of these curves depends on whether measurements at a particular Y/R_p location is inside or outside the wall layer. For example in Fig. 6.7(a), except for station 6, all measurements at $Y/R_p=0.1$ are within the wall layer at any downstream location in the diffuser and the curves are continuous. Whereas, measurements at $Y/R_p=0.95$ are outside the wall layer upstream of station 54. Comparison of the location of the peak region in Table 4.1 and these curves show that sudden changes in shape occur when a measuring location is within the wall layer in a downstream location. Both Figures, 6.7(a) and (b) show that downstream from station 30, when eruptions from the wall decreases dramatically the structure of turbulence is dominated by the large scale eddies associated with sweeps. Simpson (1991) has similarly made this observation and deduced that the large eddies agglomerate with one another resulting in a decrease of the average frequency of passage as detachment is approached. The drop in the frequency of ejections and sweeps near the wall in the latter part of the diffuser supports the above inference.

One of the limitations of probe based, single point measurements is the inability to account for spanwise variation of the coherent motions. However, recent studies by Simpson (1991) has shown that a non-dimensional parameter can be defined which permits a monotonic variation of the non-dimensional spanwise spacing up to detachment. Similar to Simpson (1991), $u_*/N_J(H)$ is proportional to the average streamwise spacing of structures in the wall region, while $(1/\tau_w)dP_w/dx$ is the ratio of the stresses acting in the wall region which influence the spanwise structure. Therefore, $P_T = -[u_*/N_J(H)\tau_w]dP_w/dx$ can be considered as a non-dimensional parameter describing the relative influence of the wall pressure gradient and the wall shear stress on each eddy which passes by. The variation of P_T defined for strong ejections and sweeps, with H=4, in the diffuser flow are given in Figs. 6.8(a) and (b) respectively. In Fig. 6.8(a), the influence of the wall pressure gradient and the wall shear stress is drastic near the wall, $Y/R_p=0.1$, then becomes weaker away from the wall. Compared with the position of the peak region given in Table 4.1, the values of P_T for strong ejections show significant variation along the diffuser if measurements at a fixed distance from the wall cuts into the wall layer at a downstream location. Thus, for $Y/R_p=0.95$ which is outside the wall layer in all but two stations, 54 and 66, the observed values of P_T in Fig. 6.8(a) are relatively constant. Strong sweeps shown in Fig. 6.8(b) are only influenced by the wall pressure gradient and the wall shear stress in the high pressure gradient region, initial stations, of the diffuser. Since sweeps are large scale eddies that bring outer region momentum to the wall, the effect of P_T is observed outside the peak region. In the latter part of the diffuser where all measurements are presented for Y/R_p values within the peak region, there is little effect of P_T on the structures associated with sweeps.

The values of P_T shown in Fig. 6.8(a) and the monotonic variation of the non-dimensional spanwise spacing with P_T given by Simpson (1991) has been used to estimate the spanwise spacings between strong ejections in the present flow. The estimate of $\lambda_\theta^+ = \lambda_\theta u_* / \nu$ shown in Fig. 6.9(a) are based on the following assumptions;

(1) The variation of the non-dimensional spanwise spacings, λ_z^+, in a plane diverging flow with P_T is roughly the same as that of λ_θ^+ with P_T in an axisymmetric conical diffuser flow.

(2) The eddies identified as burst by Simpson (1991) can be considered as strong ejections or quadrant 2 events with H=4.

(3) The monotonic variation of λ_z^+ with P_T given by Simpson is asymptotic to $\lambda_z^+ = 20$ for $P_T < -20$.

Similar to other results presented previously, the variation of λ_θ^+ from one station to another depends on the measuring distance from the wall being inside or outside the wall layer [see Fig. 6.9(a)]. Near the wall, $Y/R_p = 0.1$, λ_θ^+ is constant at 20 from stations 18-54 then increases to a value of about 80 as detachment is approached at station 66. However, the observed constant values may be the consequence of assumption (2) above but actual values should be of the same order of magnitude since the structures must maintain a finite spanwise spacing. The high values obtained near detachment at station 66,$\lambda_\theta^+ \sim 100$, is justifiable. Since as separation is approached the wall pressure gradient in the streamwise direction tends to zero, it is appropriate that λ_θ^+ should tend to values obtained in zero pressure gradient flows of about 100. For $Y/R_p > 0.1$, the curves in Fig. 6.9(a) show that the values of the spanwise separation between ejections are generally greater than the near wall values. Simpson (1991) has indicated that the spanwise spacings between bursts in flows near separation scale better with the characteristic velocity scale obtained at the peak region, $U_m = \sqrt{-(uv_{max})}$, and that the non-dimensional form $(\lambda_\theta U_m/\nu)$ results in values closer to 100 similar to observations in zero pressure gradient flows than λ_θ^+ shown in Fig. 6.9(a). Values of λ_θ obtained from Fig. 6.9(a) have been used to form the non-dimensional parameter $\lambda_\theta U_m/\nu$ and presented in Fig. 6.9(b). For $0.1 \leq Y/R_p \leq 0.5$, the values of $\lambda_\theta U_m/\nu$ are indeed closer to the zero pressure gradient value of 100 from stations 18-54 than in Fig. 6.9(a). It can be concluded from Figs. 6.9(a) and (b) that the usual wall scaling is appropriate for scaling the spanwise spacings between ejections only in the region where $dp/dx \sim 0$, while most of the diffuser flow scales with the velocity scale obtained at the peak region.

Estimates of the spanwise spacings for structures associated with the sweep motions cannot be made because the variation of P_T with spanwise spacings is unavailable. However, it is reasonable to expect similar variation of P_T and the non-dimensional spanwise spacings for the sweep motions since, for example, in the wall layer of canonical boundary layers ejections and sweeps tend to occur in a side by side orientation. Thus, Fig. 6.8(b) indicates that the spanwise spacings between sweeps are likely to attain maximum values close to the wall. This imply that near the wall, $0.1 \leq Y/R_p \leq 0.6$, values of the spanwise spacing between sweeps will be consistently greater than those of ejections from station 18-54, while as detachment is approached at station 66, the two values will become nearly equal [see Figs. 6.8(a) and (b)]. The above inference that the spanwise spacings between sweeps and ejections tend to be equal at station 66 is in accordance with the simulation data of Robinson (1991a); because the pressure gradient at this station is nearly zero like in the canonical case.

6.4.1 Justification of the results by comparison with conceptual models

Based on the present results, a conceptual model for turbulence in the diffuser flow must address the basic properties shown in Fig. 6.10. The present diffuser is not long enough for the flow to separate from the wall. However, the attached section in the figure is based on the model developed by Simpson (1991) for detachment and it is used to show the backflow involved as detachment is approached. The core region of the diffuser has been shown to have similar turbulence characteristics as the core region of the feed pipe flow. Therefore, the structure of turbulence in the core region should be consistent with known observations and involves large scale motions and a variety of vortical structures. The region from the wall to the maximum shear stress (peak region), however, requires careful analysis.

Two shear layers of interest can be identified in the conical diffuser flow; a mean shear layer near the wall and the maximum shearing stress layer at the peak region. The wall mean shear layer in the diffuser is equivalent to the sublayer and buffer regions of canonical boundary layers but it is unusually thin because the basic rate of shear strain in the streamwise direction is much larger than the extra strain rate in the radial direction [Castro and Bradshaw (1976) and Azad and Kassab (1989)]. Based on the closeness to the wall, nearly all existing conceptual models for the formation and propagation of coherent structures can be made to apply to the wall mean shear layer. The consequence of such application is that the rest of the flow, from the wall to the axis, becomes the outer region. Hence the observed sweep domination of the flow from the wall to the peak region conflicts with the distribution of the major contributing coherent motions to the turbulence structure as observed in canonical boundary layers. On the other hand, the maximum shearing stress at the peak region which should be used in the models to provide similar distribution of sweep and ejections as in other flows is too far from the wall and hence cannot account for the roll-up of vortices. Nevertheless the peak region has been shown to have several turbulence properties that are identical to those obtained at the buffer region and it should play a major role in the dynamics of coherent structures.

One of the few coherent structure models that can be applied to explain some of the turbulence features observed in this flow (as shown in Fig. 6.10) is the typical eddy (TE) concept and the TE-wall interaction [see Falco (1991)]. TEs are local, compact regions of vorticity concentration with a distorted vortex ring-like configuration and evolution. They are transported to the wall by large scale outer motions associated with sweeps. Falco (1991) has shown that TEs are a major contributor to the Reynolds stress in the outer region. In addition, the importance of TEs in boundary layer dynamics was shown by normalizing the rms streamwise velocity fluctuations and the Reynolds stress with the velocity of the TEs to provide a collapse of data in the wall region and outside it where the wall scaling usually fails.

Chu and Falco (1988) identified several factors that influence the level of TE-wall interactions. These include; the instantaneous thickness of the wall layer to the scale of the TE ring, the angle of incidence of the eddy with the wall, the convection velocity of the eddy and the distance of the TE from the wall. In the present flow (see Fig. 6.10), the initial and intermediate stations, 6-36, have practically no wall mean shear layer [Trupp et al. (1986)] which implies a strong TE-wall interaction. While in the outer stations, 42-66, the resurrection of the wall layer as detachment is approached indicate a weaker TE-wall interaction. The angle of incidence of the rings was found to be the second most important factor. Due to the diverging wall it can be expected that the angle of incidence for structures originating from the core region will be maximum near the entrance of the diffuser then decrease with prolonged wall divergence. Thus, the decreasing angle of incidence enhances the level of TE-wall interaction deduced from the thickness of the mean shear layer. The deterioration of the TE-wall interaction in the outer region can also be traced to inactive motions. Falco (1991) has shown that weaker large scale motions in the outer region, which can be associated with the deceleration of the flow in the diffuser, are inefficient transporters of TEs resulting in inactive motions (see Sect. 6.1) which contribute to high turbulence intensities but not to the shear stress. However, weak or strong TE-wall interactions results in the creation of pocket and hairspin vortices. Pockets are vortices with roughly circular regions which are visualized as regions devoid of marked fluid when distributed markers are introduced into the sublayer of a turbulent boundary layer. On the other hand, hairspin vortices are similar to horseshoe vortices except that they are longer in the streamwise direction than they are wide. Hairspin vortices are more common than horseshoe vortices in moderate and high Reynolds number turbulent flows. Mechanisms for the creation of pockets similar to the above have also been observed by Smith (1984) and Robinson (1991 a). Thus the ejected low speed fluid outside the wall mean shear layer of the diffuser consist of pocket vortices, hairspin vortices, TEs and varying proportions of other types of vortices. Since definitive knowledge concerning the different types of vortices that can occur in turbulent shear flow is not available at present, it is necessary to speculate about the dynamics of these coherent structures in order to understand the physics of a given flow. The speculation given below serve to provide a fundamental physical understanding of the diffuser flow on the basis of present results.

Based on the above reasoning, the initial and intermediate stations where the TE-wall interactions are strong will result in a large number of pocket and hairspin vortices being produced. Since pocket vortices are initially the footprint of sweeps [Robinson et al. (1988), Falco (1991) and Robinson (1991 a)], there should be a strong evidence of quadrant 4 contributions to the Reynolds stress just outside the wall mean shear layer. This is evident in Fig. 6.7(b) where the frequencies of sweeps are maximum near the wall, stations 6-30, then decrease with increasing distance from the wall. On the other hand, the frequency for ejections, Fig. 6.7(a), increases from the wall outwards since in the later stages of development pockets are associated with the ejection of low speed fluid [see Falco (1991)]. Thus vortical structures associated with ejections move outwards rapidly up-to the peak region then gradually into the core region as their frequency decreases [see Fig. 6.7(a)]. This outgrowth is different from the observed gradual motion by Robinson (1991 a) in zero pressure gradient flows which is justifiable at station 66 [see Fig. 6.7 (a)] where the pressure gradient is close to zero. While it has been observed that instantaneous pressure gradient of either signs applied to a zero pressure gradient flow has little effect on the ejection process [Thomas and Bull (1983)], the rapid outgrowth inferred from the present data is consistent with other observations in a decreasing adverse pressure gradient [see Offen and Kline (1975)]. All vortical structures produced by the TE-wall interaction along the mean shear layer are convected outwards to downstream locations by the mean flow. The special properties of the peak region may well be produced by the stability of this region with respect to the flow on either side of it. The following inferences can be made about the peak region based on this and other studies.

(1) In canonical boundary layers, hairspin vortices produced by the TE-wall interactions have a short life span while in transitional flows they are found throughout the boundary layer [Falco (1991]. Note that the perturbation produced as air expands into the diffuser produces turbulence characteristics that are similar to transitional boundary layers. Therefore, the rapid outgrowth of vortical structures in this flow indicate that hairspin vortices may re-connect to form new TEs further from the wall than will be the case in canonical boundary layers. Thus, the peak region may be viewed as the location of stable vortex regeneration. Such stable vortex pairing at the peak region can result in the observed large increases in turbulence intensities and Reynolds stress [see Hussian (1983)].

(2) The association of the peak region with vortex regeneration above introduces the similarity between the maximum shearing stress occurring at the peak region and

near-wall shear layers observed in canonical boundary layers [Robinson (1991 a)]. It has also been shown by Robinson (1991) that near-wall shear layers are not necessarily confined to the wall region, though further from the wall their ability to roll up into vortices is questionable. The ingredients for a large production term in the turbulence kinetic energy equation requires the existence of both high shear and high value of the averaged Reynolds stress. Thus as noted by Alfredsson et al. (1988), maximum production will occur at a near-wall shear layer with these properties whether or not the shear layer rolls up into vortices. The observation of maximum production and dissipation of turbulent kinetic energy in this flow at the peak region by Azad and Kassab (1988) is therefore consistent with its present attribute as a vortex regeneration site.

The dynamics of the vortical structures produced from the wall mean shear layer in the outer stations is slightly different. The TE-wall interaction is reduced due to a thicker mean shear layer and because inactive motions (see Fig. 6.10) limits the number of TEs transported to the wall. Thus in Fig. 6.7(b), the frequency of sweeps decreases dramatically near the wall since fewer pocket vortices are produced. The frequency of ejections also decreases from stations 42-66, Fig. 6.7(a), reflecting the decreasing number of pocket vortices which latter in their evolution become associated with ejections as well as the absence of burst producing stresses due to inactive motions.

CHAPTER 7

CONCLUSIONS

A fully developed, constant negative pressure gradient turbulent flow in the feed pipe has been observed to produce a complex turbulent flow in a conical diffuser. The initial perturbation and the deceleration of the flow as it enters the diffuser results in a strong adverse pressure gradient flow with unstable behavior due to mixing. On relaxation, the flow attains a moderate adverse pressure gradient with a two-dimensional velocity characteristic in the intermediate stations. Then in the exit portion, it finally settles into a mild adverse pressure gradient flow with high intensity of turbulence in the wall region and possible instantaneous back-flow as it approaches separation.

The most important feature of the diffuser flow is the peak region. It is approximately located along an imaginary cylindrical surface in the diffuser with a radius equal to that of the feed pipe from the axis of the flow. It divides the flow radially into a wall layer and a core region. In the diffuser, the wall layer becomes abnormally large with prolonged divergence. The peak region is characterized by maximum values of turbulent energy and shear stress, nearly equal and maximum values of production and dissipation of turbulent kinetic energy, nearly normal distribution of probability density of fluctuating velocities as well as equal values of ejections and sweep events, and of inward and outward interactions. These characteristics of the peak region are similar to the edge of the sublayer in pipe flow. In spite of this similarity, the diffuser like all wall-bounded flows does have a thin mean shear layer close to the wall. One possible conceptual model for this flow involves typical eddies transported by large scale motions from the outer region interacting with the wall mean shear layer. This interaction results in the formation of pockets and hairspin vortices. The outward growth of vortices from the wall mean shear layer to the peak region is enhanced by the decreasing adverse pressure gradient. Thus, the region between the wall mean shear layer and the peak region is populated by pocket vortices which initially are the footprint of sweeps then become associated with ejections at the latter stages of growth. The rapid outward growth of vortices also results in hairspin vortices re-connecting to form new eddies further from the wall than will be the case in a slower outward motion. Hence, the peak region, where this outward motion attends stability, may be considered as the site of stable vortex regeneration. This attribute of the peak region explains nearly all the observed turbulence properties of the region. In the later part of the diffuser flow, the large sweep dominated zone between the wall mean shear layer and the peak region is further enhanced by inactive motions.

This study involved the experimental evaluation of turbulence quantities by the traditional long-time averaging methods and the eduction of the statistical properties of coherent motions. The following conclusions have been arrived at from the independent aspects of the study.

7.1 LONG-TIME AVERAGED QUANTITIES.

(a) The conventional method of correcting static pressures measured in turbulent streams require the use of hot-wire anemometry to obtain the fluctuating components of velocity and calibration of the static tube. The use of x-wire measurements defeats the purpose of correcting static pressures if the end result is to obtain accurate mean velocities from pressure probes. The present approach uses uncorrected pressure measurements to correct static pressures and mean velocities in a turbulent flow subjected to adverse pressure gradient. The results obtained by applying the present corrections compare favorably with hot-wire measurements. In addition, the analysis of the deviation of corrected and true mean velocities produces an insight into the nature of turbulence in the conical diffuser which was subsequently deduced from coherent motions.

(b) The variation of the moments of fluctuating velocities across the flow reflects strongly on the macro-structure of turbulence in the conical diffuser. The most important feature of the diffuser flow, the peak region, is clearly indicated by maximum values and overshoot of turbulent energy and shear stress. In addition, stress to intensity ratio indicate inactive motions, where large scale eddies contribute to higher intensities but not to the Reynolds stress, between the peak region and the wall. Minimum values of conditional averages from the ejection phase which should otherwise contributes to more than 70% of the Reynolds stress production in the near wall region confirms the notion of inactive motions in the same location. The accuracy of the moments and their distribution across the flow is validated, by virtue of the fact that they are used in the theoretical probability distributions to accurately predict experimentally evaluated probability density distributions.

7.2 COHERENT STRUCTURES.

(a) The four classes of fluid motions responsible for momentum transfer; outward interactions, ejections, inward interactions and sweeps are found to play similar roles in a conical diffuser subjected to a varying adverse pressure gradient turbulent flow as in other wall-bounded flows. The experimentally evaluated values of these events are well predicted theoretically by applying conditional calculations to the probability density distribution of Reynolds stress accomplished through the use of the cumulant-discard method and one-dimensional Hermite polynomials.

(b) The structure of turbulence across the diffuser flow is dominated by sweeps from the wall to the peak region and by ejections in the core region. The peak region has equal contributions from the ejection and sweep events and also the interactions are equal.

(c) Focusing effect in the core region is found to be relatively unaffected by adverse pressure gradient from the feed pipe to the exit portion of the diffuser. Therefore, the increase in turbulence activity in the core region of the outer stations of the diffuser over pipe flow values cannot be solely attributed to similar increase in focusing effects.

(d) The temporal statistics of coherent structures obtained in the fully developed pipe flow are comparable with existing results. In the diffuser, these quantities have values that reflect the complex bursting mechanism in the flow. Their distribution across the flow is in accordance with the variation of conditional averages which were not subjected to selective eduction. Therefore, the new pattern recognition technique developed is at least comparable with existing methods.

REFERENCES

ALFREDSSON, P. H. and JOHANSSON, A. V. 1984 On the detection of turbulence generating events. *J. Fluid Mech.* 139, 325-345.

ALFREDSSON, P. H., JOHANSSON, A. V. and KIM, J. 1988 Turbulence production near walls: The role of flow structure with spanwise asymmetry. *Proc. 1988 summer program Cent. Turbul. Res.*, Stanford, Calif.: Cent. Turbul. Res., 131-141.

ANTONIA, R. A. 1972 Conditionally sampled measurements near the outer edge of a turbulent boundary layer. *J. Fluid Mech.* 56, 1-18.

ANTONIA, R. A. and ATKINSON, J. D. 1973 High-order moments of Reynolds stress fluctuations in a turbulent boundary layer. *J. Fluid Mech.* 58, 581-593.

ANTONIA, R. A. 1981 Conditional sampling in turbulence measurement. *Ann. Rev. Fluid Mech.* 13, 131-156.

ANTONIA, R. A. 1990 The role of coherent structures. *Whither turbulence? Turbulence at the crossroads; Lecture Notes in Physics* (J.L. Lumley, ed.), Springer-Verlag Berlin Heidelberg. 357, 156-169.

ARORA, S. C. 1978 *Ph.D. Thesis,* The University of Manitoba, Winnipeg, Canada.

ARORA, S. C. and AZAD, R. S. 1980 (a) Applicability of the isotropic vorticity theory to an adverse pressure gradient flow. *J. Fluid Mech.* 97, 385-404.

ARORA, S. C. and AZAD, R. S. 1980 (b) Turbulent kinetic energy balance in a flow with adverse pressure gradient. *AIAA* paper 80-0073.

AUBRY, N., HOLMES, P., LUMLEY, J. and STONE, E. 1988 The dynamics of coherent structures in the wall region of a turbulent boundary layer. *J. Fluid Mech.* 192, 115-173.

AZAD, R. S. and HUMMEL, R. H. 1979 Similarities of turbulence structure in a conical diffuser with other wall-bounded flows. *AIAA J.* 17, 884-891.

AZAD, R. S. and HUMMEL, R. H. 1981 Structure functions of turbulence in an adverse pressure gradient. *Phys. Fluids* 24, 1774-1779.

AZAD, R. S. and KASSAB, S. Z. 1989 Turbulent flow in a conical diffuser: Overview and implications. *Phys. Fluids* A1, 564-573.

BADRI NARAYANAN, M. A., RAJACOPALAN, S. and NARASIMHA, R. 1977 Experiments on the fine structure of turbulence. J. Fluid Mech. 80, 237-257.

BARAT, M. 1969 Pressure measurements in highly turbulent flows. *Paper given at the International Summer School for Heat and Mass transfer,* Herceg Novi, Jugoslavia, September 1969.

BAKEWELL, P. and LUMLEY, J. L. 1967 Viscous sublayer and adjacent wall region in turbulent pipe flow. *Phys. Fluids* 10, 1880-1889.

BECKER, H. A. and BROWN, A. P. G. 1974 Response of pitot probes in turbulent streams. *J. Fluid Mech.* 62, 85-114.

BENDAT, J. S. and PIERSOL, A. G. 1968 *Measurement and analysis of random data.* John Wiley and Sons Inc., New York.

BLACKWELDER, R. F. 1977 On the role of phase information in conditional sampling. *Phys. Fluids* 20, S232-S242.

BLACKWELDER, R. F. and KAPLAN, R. E. 1976 On the structure of turbulent boundary layer. *J. Fluid Mech.* 76, 89-112.

BLACKWELDER, R. F. and ECKELMANN, H. 1979 Streamwise vortices associated with the bursting phenomenon. *J. Fluid Mech.* 94, 577-594.

BLACKWELDER, R. F. and HARITONIDIS, J. H. 1983 Scaling of the bursting frequency in turbulent boundary layers. *J. Fluid Mech.* 132, 87-103.

BOGARD, D. G. and TIEDERMAN, W. G. 1986 Burst detection with single-point velocity measurements. *J. Fluid Mech.* 162, 389-413.

BOGARD D. G. and TIEDERMAN, W. G. 1987 Characteristics of ejections in turbulent channel flow. *J. Fluid Mech.* 179, 1-19.

BRADSHAW, P. 1966 The effect of initial conditions on the development of free shear layer. *J. Fluid Mech.* 26, 225-235.

BRADSHAW, P. 1967 'Inactive' motion and pressure fluctuations in turbulent boundary layers. *J. Fluid Mech.* 30, 241-258.

BRIDGES, J., HUSAIN, H. S. and HUSSIAN, F. 1990 Whither coherent structures? *Whither turbulence? Turbulence at the crossroads, Lecture notes in Physics* (J.L. Lumley, ed.), Springer-Verlag, Berlin Heidelberg 357, 132-151.

BROWN, K. C. and JOUBERT, P. N. 1969 The measurement of skin friction in turbulent boundary layers with adverse pressure gradient. *J. Fluid Mech.* 35, 737-757.

BRUUN, H. H. 1988 Use of computers in HWA. Post graduate school of Mechanical and Manufacturing Systems Engineering, University of Bradford, G. Britain. (Private communications).

CANTWELL, B. J. 1981 Organized motion in turbulent flows. *Ann. Rev. Fluid Mech.* 13, 457-515.

CASTRO, I. P. and BRADSHAW, P. 1976 The turbulence structure of a highly curved mixing layer. *J. Fluid Mech.* 73, 265-304.

CHAMPAGNE, F. H. and SLEICHER, C. A. 1967 Turbulence measurements with inclined hot-wires, part 2. Hot-wire response equations. *J. Fluid Mech.* 28, 177-182.

CHEW, Y. T. and SIMPSON, R. L. 1988 The non-real-time explicit data analysis method of crossed hot-wire anemometer measurements including tangential cooling velocity correction. *J. Phys. E.: Sci. Instrum.* 21, 310-316.

CHU, C. C. and FALCO, R. E. 1988 Vortex ring/viscous wall layer interaction model of turbulence production process near walls. *Exp. Fluids* 6, 305.

CHUE, S. H. 1975 Pressure probes for fluid measurement. *Prog. Aerospace Sci.* 18, 271-323.

CLUTTER, D. W., SMITH, A. M. O. and BRAZIER, J. G. 1959 Technique of flow visualization using water as the working medium. Rep. No ES 29075, Douglas Aircraft Co., El Segundo, Calif.

COMTE-BELLOT, G., SABOT, J. and SALEH, I. 1978 Detection of intermittent events maintaining Reynolds stress. *In Proc. Dynamic Flow Conf. - Dynamic measurements in unsteady flows,* Marseille, Baltimore, 213-229.

CORINO, E. R. and BRODKEY, R. S. 1969 A visual investigation of the wall region in turbulent flow. *J. Fluid Mech.* 37, 1-30.

CORRSIN, S. 1943 Investigations of flow in an axially symmetric heated jet of air. *N.A.C.A. Adv. Conf. Rep.* No. 3123.

CORRSIN, S. and KISTLER, A. L. 1955 Free-stream boundaries of turbulent flows. *N.A.C.A. (Nat. Adv. Comm. Aero.),* Rep. No. 1244.

DANG, T. H. 1987 *M.Sc. Thesis,* The University of Manitoba, Winnipeg, Canada.

DENGEL, P., FERNHOLZ, H. H. and VAGT, J. D. 1982 Turbulent and mean flow measurements in an incompressible axisymmetric boundary layer with incipient seperation. *Turbulent shear flows 3* (ed. Bradbury, et. al.), Springer.

EICKHOFF, H. 1969 Zum Fehler von Druck-und Geschwindigkeits-messungen in turbulenten Stromungen. *Chemie Ing. Techn.* 41, 721.

ERDELYI, A. (Ed.) 1954 *Tables of integral transforms, Vol. 1*, McGraw-Hill.

FALCO, R. E. 1991 A coherent structure model of the turbulent boundary layer and its ability to predict Reynolds number dependence. *Phil. Trans. R. Soc. Lond. A* 336, 103-129.

FAVRE, A., GAVIGLIO, J., and DUMAS, R. 1957 Space-time double correlations and spectra in a turbulent boundary layer. *J. Fluid Mech.* 2, 313-342.

FAVRE, A., GAVIGLIO, J. and DUNAS, R. 1958 Further space-time correlations of velocity in a turbulent boundary layer. *J. Fluid Mech.* 3, 344-356.

FREI, D. and THOMANN, H. 1980 Direct measurements of skin friction in a turbulent boundary layer with a strong adverse pressure gradient. *J. Fluid Mech.* 101, 79-95.

GOLDSTEIN, S. 1936 *Proc. Royal Society, London* A155, 576.

GRASS, A. J. 1971 Structural features of turbulent flows over smooth and rough boundaries. *J. Fluid Mech.* 50, 233-255.

GUITTON, D. E. 1974 The effect of high intensity turbulence on the response of a hot-wire. *CASI Trans.* 7, 69-80.

HEAD, M. R. and BANDYOPADHYAY, P. 1981 New aspects of turbulent boundary layer structure. *J. Fluid Mech.* 107, 297-337.

HINZE, J. O. 1959 *Turbulence.* McGraw-Hill, New York

HINZE, J. O. 1975 *Turbulence.* 2nd Ed. McGraw-Hill, New York

HO, C.M. and HUERRE, P. 1984 Perturbed free shear layers. *Ann. Rev. Fluid Mech.* 16, 365-424.

HOFFMANN, P.H., MUCK, K.C. and BRADSHAW P. 1985 The effect of concave surface curvature on turbulent boundary layers. *J. Fluid Mech.* 161, 371-403.

HOLMES, P. 1990 Can dynamical systems approach turbulence? *Whither turbulence? Turbulence at the crossroads, Lecture notes in Physics* (J.L. Lumley, ed.), Springer-Verlag, Berlin Heidelberg 357, 195-249.

HUMMEL, R.H. 1978 *Ph.D. Thesis,* The University of Manitoba, Winnipeg, Canada.

HUSSIAN, A.K.M.F. 1983 Coherent structures - reality and myth. *Phys. Fluids* 26, 2816-2850.

JORGENSEN, F.E. 1971 Directional sensitivity of wire and fibre films probes. *DISA Information* 11, 31-37.

KAMPE DE FERIET, J. 1966 The Gram-Charlier approximation of the normal law and the statistical descriptions of a homogeneous turbulent flow near statistical equilibrium. *David Taylor model basin report,* No 2013.

KAPLAN, R. E. and LAUFER, J. 1969 The intermittently turbulent region of the boundary layer. *Proc. 12th Int. Congr. Mech.,* p. 236.

KASSAB, S.Z. 1986 *Ph.D. Thesis,* The University of Manitoba, Winnipeg, Canada.

KIM, J. 1983 On the structure of wall- bounded turbulent flows. *Phys. Fluids* 26, 2088-2097.

KIM, J. and MOIN P. 1986 The structure of the vorticity field in turbulent channel flow: Part 2. Study of ensemble-averaged fields. *J. Fluid Mech.* 162, 339-363.

KLEBANOFF, P.S. 1954 Characteristics of turbulence in a boundary layer with zero pressure gradient. *N.A.C.A. (Nat. Adv. Comm. Aero.),* Rep. No 3178.

KLINE, S. J., REYNOLDS, W. C., SCHRAUB, F. A. and RUNSTADLER, P. W. 1967 The structure of turbulent boundary layers. *J. Fluid Mech.* 30, 741-773.

KLINE, S. J. 1985 The purpose of uncertainty analysis. *J. Fluid Eng.* 107, 153-160.

KLINE, S. J. 1988 Quasi-coherent structures in the turbulent boundary layer: Part I. Status report on a community-wide summary of the data. *Zoran P. Zaric memorial international seminar on near-wall turbulence*, Dubrovnik, Yugoslavia.

LAUFER, J. 1954 The structure of turbulence in fully developed pipe flow. *N.A.C.A. (Nat. Adv. Comm. Aero.)*, Wash., Rep. No 1174.

LIEPMANN, H. W. 1952 Aspects of the turbulence problem Part II. *Z. Angew. Math. Phys.* 3, 407-426.

LIEPMANN, H. W. 1962 Free turbulent flows. In "Mecanique de la turbulence", *Int. Symp. Nat. Sci. Res. Centre,* Marseille 1961, CNRS, PARIS., 211-227.

LIN, Y. K. 1967 *Probabilistic theory of structural dynamics*. McGraw-Hill, New York.

LU, S. and WILLMARTH, W. W. 1973 Measurements of the structure of Reynolds stress in a turbulent boundary layer. *J. Fluid Mech.* 60, 481-511.

LUCHIK, T. S. and TIEDERMAN, W. G. 1987 Timescale and structure of ejections and bursts in turbulent channel flows. *J. Fluid Mech.* 174, 529-552.

LUI, J. T. C. 1988 Contributions to the understanding of large-scale coherent structures in developing free turbulent shear flows. In "*Advances in applied Mechanics*" Vol. 16 (J. W. Hutchinson and T. Y. Wu, ed.), Academic Press, London, 183-309.

LUI, J. T. C. 1989 Coherent structures in transitional and turbulent free shear flows. *Ann. Rev. Fluid Mech.* 21, 285-315.

McCORMIC, J. M. and SALVADORI, M. G. 1985 *Numerical methods in Fortran.* Prentice-Hall, New Delhi.

MOLLO-CHRISTENSEN, E. 1971 Physics of turbulent flow. *AIAA J.* 9, 1217.

MOIN, P. 1987 Analysis of turbulence data generated by numerical simulation. *AIAA Pap.*, No 87-0194.

MOIN, P. and SPALART, P. R. 1988 Contributions of numerical simulation data bases to the physics, modelling and measurement of turbulence. *Advances in turbulence* (W.K. George and R. Arndt, ed.), Springer-Verlag.

MONIN, A. S. and YAGLOM, A. M. 1971 *Statistical Fluid Mechanics: Mechanics of Turbulence*, Vol. 1, MIT press, Cambridge.

MOSER, R. D. and MOIN, P. 1987 The effect of curvature in wall-bounded turbulent flows. *J. Fluid Mech.* 175, 479-510.

MURLIS, J., TSAI, H. M. and BRADSHAW, P. 1982 The structure of turbulent boundary layers at low Reynolds number. *J. Fluid Mech.* 122, 13-56.

NAGANO, Y. and TAGAWA, M. 1988 Statistical characteristics of wall turbulence with passive scalar. *J. Fluid Mech.* 196, 157-185.

NAKAGAWA, H. and NEZU, I. 1977 Prediction of the contributions to the Reynolds stress from bursting events in open-channel flows. *J. Fluid Mech.* 80, 99-128.

NASH, J. F. and HICKS, J. G. 1969 *Proc. Comp. Turbulence Boundary layers*: 1968 AFOSR-IFP-*Stanford Conf. Vol. 1. Thermosci. Div., Mech. Engng. Dept.*, Stanford University.

NYCHAS, S. G., HERSHEY, H. C. and BRODKEY, R. S. 1969 A visual study of turbulent shear flow. *J. Fluid Mech.* 61, 513-540.

OFFEN, G. R. and KLINE, S. J. 1975 A proposed model of the bursting process in turbulent boundary layers. *J. Fluid Mech.* 70, 209-228.

OKWUOBI, P. A. C. and AZAD, R. S. 1973 Turbulence in a conical diffuser with fully developed flow at entry. *J. Fluid Mech.* 57, 603-622.

PATEL, V. C. 1965 Calibration of preston tube and limitations on its use in pressure gradients. *J. Fluid Mech.* 23, 185-208.

PERRY, A. E. and CHONG, M. S. 1982 On the mechanism of wall turbulence. *J. Fluid Mech.* 119, 173-217.

PERRY, A. E., LI, J. D. and MARUSIC, I. 1991 Towards a closure scheme for turbulent boundary layers using the attached eddy hypothesis. *Phil. Trans. R. Soc. Lond. A* 336, 67-79.

PRATURI, A. K. and BRODKEY, R. S. 1978 A stereoscopic visual study of coherent structures in turbulent shear flow. *J. Fluid Mech.* 89, 251-272.

RAO, K. N., NARASIMHA, R. and BADRI NARAYANAN, M. A. 1971 The "bursting" phenomenon in a turbulent boundary layer. *J. Fluid Mech.* 48, 339-352.

ROBINSON, S.K., KLINE, S.J. and SPALART, P.R. 1988 Quasi-coherent structures in the turbulent boundary layer: Part II. Verification and new information from a numerically simulated flat-plate layer. *Zoran P. Zaric memorial international seminar on near-wall turbulence*, Dubrovnik, Yugoslavia.

ROBINSON, S. K. 1991 (a) The kinematics of turbulent boundary layer structure. *NASA TM* 103859.

ROBINSON, S.K. 1991 (b) Coherent motions in the turbulent boundary layer. *Ann. Rev. Fluid Mech.* 23, 601-639.

SADDOUGHI, S. G. and JOUBERT, P. N. 1991 Lateral straining of turbulent boundary layers, Part I. Streamline divergence. *J. Fluid Mech.* 229, 173-204.

SABOT, J. and COMTE-BELLOT, G. 1976 Intermittency of coherent structures in the core region of fully developed pipe flow. *J. Fluid Mech.* 74, 767-796.

SALEH, I. 1978 *Ph.D. Thesis,* L'Universite Claude Bernard De Lyon.

SCHOFIELD, W. H. and PERRY, A. E. 1972 The turbulent boundary layer as a wall confined wake. *Australian Defence Scientific Services,* ARL/M.E. 134, Melbourne.

SIMPSON, R. L. 1991 The structure of near-wall region of two-dimensional turbulent seperated flow. *Phil. Trans. R. Soc. Lond. A* 336, 5-17.

SMITH, C. R. 1984 A synthesized model of the near-wall behavior in turbulent boundary layers. *In Proc. 8Th symp. on turbulence* (ed. G. K. Patterson and J. L. Zakin), University of Missouri-Rolla.

SMITS, A. J., EATON, J. A. and BRADSHAW, P. 1979 The response of a turbulent boundary layer to lateral divergence. *J. Fluid Mech.* 94, 243-268.

SOVRAN, G. and KLOMP, E. 1967 Experimentally determined optimum geometries for rectilinear diffusers with rectangular, conical or annular cross sections. *Proc. General Motors symp. on Fluid Mechanics of Internal flow* (ed.: G. Sovran), Elsevier Pub. Co., 270-319.

SPRENGER, H. 1959 Experimentelle untersuchungen an geraden und gekrummten diffusoren, *Mitteilung aus dem Institute fur Aerodynamik an der ETH*, Zurich, No 27 (Translation: Experimental research on straight and curved diffusers, Obtained from the Ministry of Aviation, Gt. Britain).

TENNEKES, H. and LUMLEY, J. L. 1985 *A first course in turbulence.* MIT press, Cambridge, Massachussetts.

THEODORSEN, T. 1952 Mechanism of turbulence. *Proc. 2nd Midwest Conf. Fluid Mech.*, Columbus, Ohio, 1-18.

THOMAS, A. S. W. and BULL, M. K. 1983 On the role of wall-pressure fluctuations in deterministic motions in turbulent boundary layer. *J. Fluid Mech.* 128, 283-322.

TOOMRE, A. 1960 The effect of turbulence on static pressure measurements. *A. R. C.* 22010.

TOWNSEND, A. A. 1947 Measurements in the turbulent wake of a cylinder. *Proc. Royal Soc. Lond.* A190, 551-561.

TOWNSEND, A. A. 1956 *The structure of turbulent shear flows*. Cambridge University Press.

TOWNSEND, A. A. 1976 *The structure of turbulent shear flows*. 2nd Ed. Cambridge University press.

TOWNSEND, A. A. 1961 Equilibrium layers and wall turbulence. *J. Fluid Mech.* 11, 97-120.

TRUPP, A. C., AZAD, R. S. and KASSAB, S. Z. 1986 Near-wall velocity distributions within a straight conical diffuser. *Exp. Fluids* 4, 319-331.

TURAN, O. 1988 *Ph.D. Thesis*, The University of Manitoba, Winnipeg, Canada.

VAGT, J. D. 1979 Hot-wire probes in low speed flow. *Prog.Aerospace Sci.* 18, 271-323.

WALLACE, J. M., ECKELMANN, H. and BRODKEY, R. S. 1972 The wall region in turbulent shear flow. *J. Fluid Mech.* 54, 39-48.

WALLACE, J. M., BRODKEY, R. S. and ECKELMANN, H. 1977 Pattern-recognized structures in bounded turbulent shear flows. *J. Fluid Mech.* 83, 673-693.

WALSCHE, D. E. and GARNER, H. C. 1960 Usefulness of various pressure probes in fluctuating low speed flows. *Brit. A. R. C.*, 21714

WILLMARTH, W. W. and LU, S. S. 1972 Structure of the Reynolds stress near the wall. *J. Fluid Mech.* 55, 65-92.

WILLMARTH, W. W. 1975 Structure of turbulence in Boundary layers. In "*Advances in Applied Mechanics*", Vol. 15 (C. S. Yih, ed.), 159-254, Academic press, New York.

ZANG, T. A. 1991 Numerical simulation of the dynamics of turbulent boundary layers: perspectives of a transition simulator. *Phil. Trans. R. Soc. Lond. A* 336, 95-102.

APPENDIX A

DIGITAL DATA PROCESSING

A1 A method for processing the digital data.

A generalized block diagram of the signal processing sequence is given in Fig. A.1. Signal from single or x-wire is fed into the constant temperature anemometer (CTA) system. The CTA system consist of constant temperature anemometers and linearizers (Note that linearization can also be performed by computer programs). The linearized output from the CTA system is fed to the signal conditioning system which is made up of turbulence processors and filters. At this stage a DC offset and partial amplification (pre-gain) may be applied to the signal. The conditioned signal is fed to the data acquisition system where more gain is applied to saturation and the signal is digitized.

For single-wire set-up, let the signal from the CTA system be denoted by $\tilde{E}(t)$. After conditioning, the mean component, E, is removed and an offset voltage, E_{off}, as well as a pre-gain, G_1, are applied. Therefore the signal to the data acquisition system is;

$$e_1 = G_1[\tilde{E}(t) - E - E_{off}] \qquad A1$$

Before A/D conversion the signal is further amplified by a gain, G_2, so as to cover the complete $\pm 10V$ of the converter. Thus, the output from the converter can be written as:

$$e_0 = G_2 e_1$$
$$= G_1 G_2[\tilde{E}(t) - E - E_{off}] \qquad A2$$

But $\tilde{E}(t) - E = e(t)$, the voltage fluctuation recorded by the hot wire.

Therefore,

$$e_0 = G_1 G_2[e(t) - E_{off}]$$
$$= G[e(t) - E_{off}] \qquad A3$$

Where $G = G_1 G_2$; the effective gain of A/D conversion.

For a 12 bit A/D converter in bipolar operation, the $\pm 10V$ range is divided into 2^{12} or 4096 distinct voltages. Define an integer I, as $0 \le I \le 4096$. Then the voltage corresponding to the I^{Th} element can be written as:

$$e_{0,I} = \left[\frac{20}{4096}\right] I - 10 \qquad A4$$

If the gain settings are such that the output from the A/D converter covers the whole $\pm 10V$ range, then $e_0 = e_{0,I}$ and from Eqs. A3 and A4,

$$G[e(t) - E_{off}] = \left[\frac{20}{4096}\right] I - 10 \qquad A5$$

Therefore the voltage fluctuation measured by the hot-wire is related to the A/D converter parameters as:

$$e(t) = \frac{1}{G}\left[\frac{20}{4096} I - 10\right] + E_{off} \qquad A6$$

The linearization equation of the hot-wire signal can be written in terms of instantaneous voltage, $\tilde{E}(t)$ and instantaneous velocity, $\tilde{U}$ as;

$$\tilde{E}(t) = A + B\tilde{U}$$

Therefore, the instantaneous velocity can be written in terms of the A/D parameters as follows:

$$\tilde{U}_I = \frac{\tilde{E}(t) - A}{B}$$

$$= \frac{E + e(t) - A}{B}$$

$$= \frac{E + \frac{1}{G}\left[\frac{20}{4096} I - 10\right] + E_{off} - A}{B} \qquad A7$$

Equation A7 gives the range of instantaneous velocities obtainable from the A/D converter for any given linearization with constants A and B as well as for an effective gain G and mean voltage E. E_{off} is usually zero. Therefore, as I varies from 0 to 4096, 4096 distinct velocities are obtained. Note: In the usual look-up method of data analysis, the output from the anemometers are not linearized and can be described by a King's law type of equation. This methods is normally applied to unipolar operations where the range of the A/D converter varies from 0-10 V [see Bruun (1988)]. The present method is a modification of the look-up method using a linearized signal to account for the bipolar set-up of the A/D converter.

The number of times the real signal in the flow falls in a particular A/D converter range depends on the level of fluctuation of the signal and the length of acquisition.

Therefore, each data point in the acquired signal must satisfy the condition derived from Eq. A6 as:

$$\frac{1}{G}\left[\frac{20}{4096}I-10\right]+E_{off}<e(t)\leq\frac{1}{G}\left[\frac{20}{4096}(I+1)-10\right]+E_{off} \qquad A8$$

$$for \quad 0\leq I\leq 4095$$

For each value of I, the number of times Eq. A8 is valid in the record length is noted as N_I and the corresponding instantaneous velocity can be looked up from a table produced from Eq. A7 which contains $\tilde{U}_I$ values as a function of I. In single-wire measurements the mean velocity and the moments of fluctuating velocity can then be calculated as follows:

$$N=\sum_{I=1}^{4096}N_I \qquad A9$$

$$U=\sum_{I=1}^{4096}\tilde{U}_I N_I \qquad A10$$

$$\overline{u^m}=\frac{1}{N}\sum_{I=1}^{4096}[\tilde{U}_I-U]^m \qquad A11$$

Where N is the total number of samples in the record.

In x-wire measurements two linearization equations are obtained, one for each wire. In addition the sum and difference of the two signals are acquired in order to minimize phase shifts.

The corresponding time-averaged linearization equation for each sensor are

$$E_1 = A_1 + B_1 U_1$$

$$E_2 = A_2 + B_2 U_2 \qquad A12$$

The signal acquired by the two channels of the A/D converter can be defined as

$$e_p = e_1 + e_2$$

$$e_n = e_1 - e_2 \qquad A13$$

Therefore,

$$e_1 = 0.5(e_p + e_n)$$

$$e_2 = 0.5(e_p - e_n) \qquad A14$$

where e_1 and e_2 are the fluctuating voltage signals from the two sensors. The number of times the fluctuating voltages e_p, e_n, e_1 and e_2 satisfy the condition specified by Eq. A8 is noted as N(1,I), N(2,I), N(3,I) and N(4,I) respectively. Using Eq. A6, the mean of the second order moments of fluctuating voltages required for the calculation of velocity characteristics from x-wire measurements can be evaluated as;

$$M_e(i) = \frac{1}{N_i} \sum_{I=1}^{4096} N(i,I)e(t)^2 \qquad A15$$

where

$$N_i = \sum_{I=1}^{4096} N(i,I), \qquad i = 1,4$$

$$M_e(1) = \overline{(e_1 + e_2)^2}; \qquad M_e(2) = \overline{(e_1 - e_2)^2};$$

$$M_e(3) = \overline{e_1^2}; \qquad M_e(4) = \overline{e_2^2}$$

Therefore, the values of $\overline{u^2}, \overline{v^2}$ and $\overline{uv}$ can be calculated by applying the equations given in Vagt (1979) which takes into consideration the directional sensitivity of the x-wire. In using the correction given in Vagt, the linearization equations of the two sensors should be the same with A_1 and A_2 equal to zero.

To produce the time-series of u, v and uv-signals, Eqs. A12-A14 are still valid. However, no sorting of the signals is done. Instead each pair of data points (voltages) which have been acquired simultaneously are used to calculate instantaneous velocities and Reynolds stress.

A2 Non-real-time explicit data analysis of x-wire data

Chew and Simpson (1988) proposed the following method for the analysis of x-wire data. It relates the mean velocity components and the Reynolds stresses in laboratory coordinates to the mean and mean square sensor output voltages via orthogonal wire coordinates and the cooling velocities. The method also takes into consideration the cooling effect of the tangential velocity component which is not negligible in high turbulence flows. A summary of the equations in the three stages of derivation is presented as follows:

1. Conversion of x-wire output voltages to cooling velocities:

Equation A12 represents the linearization equations of the two sensors of the x-wire. Unlike the equations given in Vagt (1979), the two linearization equations need not be similar. It can be shown that the cooling velocities are related to the sensor output voltages as

$$\overline{V}_1 = \frac{1}{B_1}(E_1 - A_1)$$

$$\overline{V}_2 = \frac{1}{B_2}(E_2 - A_2)$$

$$\overline{v_1^2} = \frac{1}{B_1^2}\overline{e_1^2}$$

$$\overline{v_2^2} = \frac{1}{B_2^2}\overline{e_1^2}$$

$$\overline{v_1 v_2} = \frac{1}{4B_1B_2}[\overline{(e_1+e_2)^2} - \overline{(e_1-e_2)^2}] \qquad A16$$

As shown in the analysis of x-wire data by the modified look-up table method (Sect. A1), the values of $M_e(i)$ from Eq. A15 can be used to evaluate the quantities in Eq. A16.

2. Cooling velocities to orthogonal wire coordinates:

The cooling effect of the tangential velocity can be included in the analysis in order to obtain the two mean velocity components and the three Reynolds stresses in the wire coordinates (x, y), see Fig. A.2 for coordinates drawn with respect to the probe. The result of such analysis gives

$$\overline{V}_x = \overline{V}_{x0}\left(1 + \frac{\overline{v^2}_{x0}}{2\overline{V}^2_{x0}} - \frac{\Delta_x}{2\overline{V}^4_{x0}}\right)$$

$$\overline{V}_y = \overline{V}_{y0}\left(1 + \frac{\overline{v^2}_{y0}}{2\overline{V}^2_{y0}} - \frac{\Delta_y}{2\overline{V}^4_{y0}}\right)$$

$$\overline{v^2}_x = \overline{v^2}_{x0} + \overline{V}^2_{x0} - \overline{V}^2_x$$

$$\overline{v^2}_y = \overline{v^2}_{y0} + \overline{V}^2_{x0} - \overline{V}^2_y$$

$$\begin{aligned}\overline{v_x v_y} = \{&\sum_{j=1}^{2}\sum_{i=1}^{2} a_i b_j (\overline{V}^2_i \overline{V}^2_j + \overline{V}^2_i \overline{v^2}_i + \overline{V}^2_j \overline{v^2}_j \\ &+ 4\overline{V}_i \overline{V}_j \overline{v_i v_j}) - \overline{V}^2_x \overline{V}^2_y - \overline{V}^2_x \overline{v^2}_y \\ &- \overline{V}^2_y \overline{v^2}_x\} / 4\overline{V}_x \overline{V}_y\end{aligned} \qquad A17$$

where,

$$\begin{bmatrix} \overline{V}^2_{x0} \\ \overline{V}^2_{y0} \end{bmatrix} = \begin{bmatrix} a_1 & a_2 \\ b_1 & b_2 \end{bmatrix} \begin{bmatrix} \overline{V}^2_1 \\ \overline{V}^2_2 \end{bmatrix}$$

$$\begin{bmatrix} \overline{v^2}_{x0} \\ \overline{v^2}_{y0} \end{bmatrix} = \begin{bmatrix} a_1 & a_2 \\ b_1 & b_2 \end{bmatrix} \begin{bmatrix} \overline{v^2}_1 \\ \overline{v^2}_2 \end{bmatrix}$$

$$\Delta_x = \sum_{j=1}^{2}\sum_{i=1}^{2} a_i a_j \overline{V}_i \overline{V}_j \overline{v_i v_j}$$

$$\Delta_y = \sum_{j=1}^{2}\sum_{i=1}^{2} b_i b_j \overline{V}_i \overline{V}_j \overline{v_i v_j}$$

$$\begin{bmatrix} a_1 & a_2 \\ b_1 & b_2 \end{bmatrix} = \begin{bmatrix} -\dfrac{k^2}{1-k^4} & \dfrac{1}{1-k^4} \\ \dfrac{1}{1-k^4} & -\dfrac{k^2}{1-k^4} \end{bmatrix}$$

where, k is the yaw factor.

3. Conversion of wire coordinate velocities to laboratory coordinates:

Finally the two mean velocities and three Reynolds stresses in the wire coordinates are transformed to the laboratory coordinates;

$$\begin{bmatrix} U \\ V \end{bmatrix} = \begin{bmatrix} d_1 & d_2 \\ f_1 & f_2 \end{bmatrix} \begin{bmatrix} \overline{V}_x \\ \overline{V}_y \end{bmatrix}$$

$$\begin{bmatrix} \overline{u^2} \\ \overline{v^2} \\ \overline{uv} \end{bmatrix} = \begin{bmatrix} d_1^2 & d_2^2 & 2d_1 d_2 \\ f_1^2 & f_2^2 & 2f_1 f_2 \\ d_1 f_1 & d_2 f_2 & d_1 f_2 + d_2 f_1 \end{bmatrix} \begin{bmatrix} \overline{v^2}_x \\ \overline{v^2}_y \\ \overline{v_x v_y} \end{bmatrix} \qquad A18$$

where

$$\begin{bmatrix} d_1 & d_2 \\ f_1 & f_2 \end{bmatrix} = \begin{bmatrix} \cos\theta & \sin\theta \\ -\sin\theta & \cos\theta \end{bmatrix}$$

θ is the angle between the laboratory X-direction and the sensor (wire axes).

The above method is a fixed-angle calibration procedure but can be adapted to produce results comparable with the more complex variable-angle calibration of x-wires. In this regards, the velocity vector computed from Eq. A18 can be compared with known values and the process repeated by chosing more suitable values of the yaw factor from an array of calibration curves. These calibration curves can be obtained by varying the yaw angle such that the yaw factor and the cooling velocities are approximately constant in the interval.

APPENDIX B

CORRECTIONS FOR PRESSURE MEASUREMENTS

B1 Basic Equations

The governing equations of pressure probes in turbulent streams have been analyzed by Goldstein (1936) and Hinze (1959, 1975). These equations are semi-empirical modifications to the response of pressure probes in laminar flow to account for their directional-sensitivity in turbulent streams. In spite of the simplicity of pressure probes, the resulting equations are very difficult to apply. Becker and Brown (1974) used custom made differential pitot-tubes and a modification of the equation given by Hinze (1959) to obtain fairly accurate estimates of mean velocities and turbulence intensities in jet flows. Toomre (1960) and Barat (1969) used Goldstein's equation to arrive at a correction of static pressures.

The basic response equations of pressure probes in turbulent flows used in the present study have been derived by Hinze (1975). These equations can be written as;

$$P_{Tm} = P_s + \frac{\rho U^2}{2}\left[1 + \frac{\overline{u^2} + (1 - B')\overline{u_n^2}}{U^2}\right] \qquad B1$$

$$P_{sm} = P_s - \frac{\rho A'}{2}\overline{u_n^2} \qquad B2$$

Equations B1 and B2 represents the response of the total and static pressure probes respectively. These equations relates the ideal static pressure, P_s and velocity characteristics at any point in the flow to the measured total pressure, P_{Tm} and static pressure, P_{sm} respectively. A' is a constant that depends on the geometry of the static pressure tube while B' is a similar constant for the total pressure tube. The numerical values of these constants are, $A' = 1$ and $B' = 1.2$, when the probes are stationary in the flow or greater values when some vibration is applied or induced by flow around the probes. $\overline{u_n^2}$ is the sum of the mean of the squared fluctuations in the transverse and lateral directions (i.e $\overline{v^2} + \overline{w^2}$).

Two types of velocity measurements are possible when pressure probes are used in a turbulent flow.

1. If both the total and static pressures are measured at any location, a mean velocity, U_{SL}, can be estimated from a direct application of the Bernoulli equation and this can be shown to be related to Eqs. B1 and B2 as (the following equation is also given in Hinze (1975, as Eq. 2-104);

$$U_{SL}^2 = \frac{2}{\rho}[P_{Tm} - P_{sm}]$$

$$= U^2\left[1 + \frac{\overline{u^2} + (1 + A' - B')\overline{u_n^2}}{U^2}\right] \qquad B3$$

2. Alternatively, if the static pressure across the flow is constant and equal to the wall static pressures, then a mean velocity, U_{SW} can be obtained from the Bernoulli equation by taking the pressure difference between the total pressure tube at any radial location and the static pressure tapping at the wall.

This can be expressed as;

$$U_{SW}^2 = \frac{2}{\rho}[P_{Tm} - P_{sw}]$$

$$= U^2\left[1 + \frac{\gamma}{U^2}\right] \qquad B4$$

where,

$$\gamma = \overline{u^2} + (1 - B)\overline{u_n^2} \qquad B5$$

Equation B4 is an idealized equation. It assumes that the static pressure taps have optimal depth to diameter ratios such that the fluid apparently comes to rest inside the pressure taps thus providing a no-slip condition at the openings similar to the rigid wall. Under these conditions both $\overline{v^2}$ and $\overline{w^2}$ tend to zero and therefore in Eq. B2 the measured static pressure becomes a close estimate of the ideal (or true) static pressure which is then used in Eq. B1 to obtain Eq. B4.

When the static pressure across the flow is constant, the two mean velocities obtained from Eqs. B3 and B4 become identical. Equation B3 is also applicable to pitot-static tubes which can estimate mean velocities for small variations in static pressures across the flow. When static pressures vary significantly across the flow, mean velocities obtained from Eqs. B3 and B4 deviate from the true mean velocities. Equation B3 may give wrong results in such cases because large variations in static pressures are associated with high turbulence intensities, which normally occurs in flows near separation resulting in instantaneous back-flow, and inducing vibrations on the probes leading to higher values of the constants A' and B'. Note that the values of these constants are known for the case when the probes are stationary in the flow or when controlled vibrations can be applied to the probes. In the case of vibrations induced by high intensity turbulence, the values of these constants are unknown. On the other hand, Eq. B4 produces wrong mean velocities because in addition to A' being affected by turbulence, the basic assumption of constant static pressure across the flow is wrong. In spite of the fact that both Eqs. A3 and A4 are not applicable in flows with strong variations in static pressures, a simple empirically formulated combination of these velocities have been used to obtain more accurate mean velocities as shown in the next section.

B2 Correction of mean velocities

The static pressures vary significantly across the flow at any station in the diffuser. For example, at station 66 which gives the maximum variation, the maximum static pressure is more than twice the wall value. Therefore, as observed by Hinze (1975), the use of Bernoulli equation produces mean velocities in such circumstances that deviate from the actual values. In addition, the use of the Bernoulli equation in this flow is strictly not applicable since the flow does not have regular streamline patterns due to mixing in the initial part of the diffuser as the air expands into the flow geometry. Nevertheless, it was found that when mean velocities estimated using Eqs. B3 and B4 were greater than the actual mean velocities obtained from hot-wire measurements, they could be corrected empirically by simple continuity considerations. This empirical correction is applied at station 66 as shown graphically in Fig. B.1. The measured mean velocities, U_{SL}, U_{SW} and U (assumed reference or correct velocities from single-wire measurements) at various probe positions are plotted as, rU_x vs r where x identifies the type of mean velocity under consideration, so that the area under each curve is proportional to the mass flow rate. As shown in Fig. **B.2**, while the mass flow rate calculated from single-wire measurements of mean velocity is constant at the pipe flow value in all stations of the diffuser, the mass flow rate calculated using U_{SL} and U_{SW} deviate significantly in the outer portions of the diffuser. It is apparent from Fig. B.1 that when the difference between the velocities calculated from pressure measurements, $rU_{SL} - rU_{SW}$, is subtracted from rU_{SW} at any radial position, the resulting velocity, rU_{cor}, is a better estimate of the hot-wire value. From the above graphical considerations, the corrected mean velocity (U_{cor}) at any point is related to U_{SL} and U_{SW} as;

$$\begin{aligned} U_{cor} &= 2U_{SW} - U_{SL} \\ &= U_{SW} - (U_{SL} - U_{SW}) \end{aligned} \qquad B6$$

Equation B6 indicates that the mean velocity, U_{SW} is corrected by a quantity (U_{SL}-U_{SW}). Since U_{SL} and U_{SW} are given by Eqs. B3 and B4 respectively, the physical meaning of the correction term can be deduced by writing it in terms of turbulence quantities. By taking the square root of both sides of Eqs. B3 and B4, expanding the right hand side by Taylor series and neglecting term higher than second order, it can be shown that

$$U_{SL} = U\left[1 + \frac{\overline{u^2} + (1 + A' - B')\overline{u_n^2}}{2U^2}\right]$$

and

$$U_{SW} = U\left[1 + \frac{\overline{u^2} + (1 - B')\overline{u_n^2}}{2U^2}\right] \qquad B7$$

Therefore, the correction term to U_{SW} in Eq. B6 can be written as;

$$U_{SL} - U_{SW} = \frac{A'}{2U}\overline{u_n^2}$$

$$= \frac{UA'}{2}\left(\frac{\overline{v^2}}{U^2} + \frac{\overline{w^2}}{U^2}\right) \qquad B8(a)$$

Equation B8(a) shows that the correction term to U_{SW} in Eq. B6 is a function of the true mean velocity, the constant A' which accounts for the geometry and the level of vibrations of the static probe and the sum of the square of the intensity of the transverse and lateral components of fluctuating velocities. This correction term can also be written in terms of static pressures by manipulating Eq. B2 to give

$$U_{SL} - U_{SW} = \frac{A'}{2U}\overline{u_n^2}$$

$$= \frac{U}{2}\frac{[P_{sm} - P_s]}{\frac{1}{2}\rho U^2} \qquad B8(b)$$

In the form of Eq. B8(b), the correction term is a function of the true mean velocity, the error in static pressure measurements and the true dynamic pressure head. Therefore it can be concluded that the correction term in Eq. B6 makes the measured mean velocity U_{SW} more sensitive to any vibration of the static probe and the presence of transverse and lateral fluctuations. The correction term is also equivalent to the correction of U_{SW} for errors associated with the difference between the measured and true static pressures. The later notion is fundamentally right because the same total pressure is used in the evaluation of both U_{SL} and U_{SW} while the static pressure used depends on local or wall measurements.

The empirical equation, B6 can also be written in terms of turbulence quantities by substituting Eqs. B7 and B8(a) to give;

$$U_{cor} = U\left[1 + \left\{ 1 + \frac{1}{\beta}(1 - B' - A') \right\} \frac{\overline{u^2}}{2U^2} \right] \qquad B9$$

where, $\beta = \overline{u^2}/\overline{u_n^2}$.

Equation B9 will represent a perfect correction for mean velocities obtained from pressure measurements if $U_{cor} = U$, and this is true for

$$1 + \frac{1}{\beta}(1 - B' - A') = 0 \qquad B10$$

Assuming that probes do not vibrate in the flow then the ideal values of A' and B' as 1 and 1.2 respectively can be substituted into Eq. B10 to obtain the value of β. The value of β from such a substitution is 1.2. Since β has a value of about 1 for turbulence shear flows and a value of about 0.5 for isotropic turbulence, it can be concluded that in the ideal case the empirical correction is more applicable in turbulence shear flows.

B3 Correction of static pressures

The equation that can be applied to the correction of static pressures have been derived by Barat (1969). This equation can be written as;

$$P_{sc} = P_{sm} \pm \rho A' \overline{u_n^2} \qquad B11$$

Note: This equation can also be obtained by assuming the empirically corrected velocity profile given by Eq. B9. U_{cor}^2 can be written as $2[P_{Tm} - P_{sc}]/\rho$ and then equated to the R.H.S of Eq. B9. The term $2P_{Tm}/\rho$ can further be substituted from Eq. B3 to give Eq. B11. The fact that Eq. B11 can be obtained from the empirical velocity correction indicates the applicability of the method.

The use of positive or negative sign in Eq. B11 depends on whether the scale of turbulence is large or small in comparison with the static probe size [Toomre (1960)]. The application of Eq. B11 is very difficult for the following reasons;

1. The scale of turbulence is difficult to estimate, hence it is difficult to judge when the positive or negative sign is applicable.
2. The constant A' depends on the scale of turbulence and the geometry of the static probe. For flow out of a rectangular duct, Barat (1969) obtained, $-0.3 \leq A' \leq 0.3$. Fage (1936) had values of -0.28 and -0.22 for pipe flow and flow in rectangular duct respectively. Theoretical calculations based on Goldstein's (1936) equation gives $A' = -0.25$ for isotropic turbulence. A' takes on a value of one or greater when Hinze's (1975) equation is applied. The choice of this constant for any application is therefore very uncertain since it may vary across the flow in a manner similar to the eddy sizes.
3. The fluctuating component of velocity can only be obtained from hot-wire measurements. When static pressures are corrected in order to estimate more accurate mean velocities, the use of hot-wire anemometry which can independently provide accurate velocities defeats the purpose of the whole correction exercise.

The correction of static pressures using Eq. B11 is modified in the present work in order to eliminate the above difficulties. The following identity can be formed from Eqs. B3 and B4;

$$U_{SL}^2 - U_{SW}^2 = A'\overline{u_n^2} \qquad B12$$

Substitution of Eq. B12 into Eq. B11 gives;

$$P_{sc} = P_{sm} \pm \rho\,(U_{SL}^2 - U_{SW}^2) \qquad B13$$

In Eq. B13 the ambiguous static pressure constant and the sum of the transverse and lateral turbulence fluctuations which can only be obtained from hot-wire measurements are replaced by easily measurable mean velocities obtained using pressure probes. In addition, the use of positive or negative sign in Eq. B13 can be decided by a simple rule of thumb. Any of the following criteria can be used. First, if U_{SW} is greater than the true mean velocity (i.e. U measured with hot-wire if available) then the positive sign applies otherwise the negative sign is used. Second, the positive sign is always applicable for flows near separation. Third, a quick calculation using both signs will indicate which velocities provide accurate and constant mass flow across various sections of the flow.

B4 Results from pressure corrections.

B4.1 Mean velocity corrections.

The mean velocity profiles for stations 6, 36 and 66 are presented in Fig. B.3(a), (b) and (c) respectively. In Fig. B.3(a), representing stations 6 and 12, the correction for mean velocity is obtained by applying the static pressure correction using the negative sign in Eq. B13 together with measured total pressures. For stations 18-66, where the mass flow rate at each station exceed actual values (see Fig. B.2), the corrected velocities using similar application of Eq. B13 (with positive sign) or the empirical correction given by Eq. B6, give the same values hence the latter equation is used to calculate the values shown in Figs. B.3(b) and (c). The corrected velocities at stations 6 and 36 compare favorably with hot-wire measurements, probably due smaller variations in static pressures across the flow in these stations. For stations 42-66, similar agreements are limited to the range $0 \leq r/R < 0.7$ as shown in Fig. B.3(c) for station 66. Therefore, errors in applying the present correction procedure in the diffuser occur mostly in the wall region of outer stations 42-66. The wall region of these stations are characterized by high intensity of turbulence and small values of streamwise mean velocities. Simpson (1991) has observed that characteristics similar to those observed in stations 42-66 occur because the flows approaches separation resulting in instantaneous back-flows. The effect of nearly equal velocity fluctuations in the streamwise, transverse and lateral direction on the pressure probes is similar to a time distribution of pitched and yawed incident flow at the impact orifice and may results in fluctuations in the mean velocity component [Chue (1975)]. Walsche and Garner (1960), as referenced in Chue (1975), simulated velocity fluctuations in a steady flow by subjecting different types of Pitot tubes to angular and linear oscillations. They concluded that a flow with velocity characteristics similar to those observed in the wall region of stations 42-66 will result in total pressure readings being lower than actual values. Therefore the errors shown by the corrected velocities in the wall region of these stations may be related to errors in total pressure measurements which were not corrected in the present study.

Errors may be propagated from measured quantities and affect the results obtained by applying the empirical correction (Eq. B6). Propagated errors of any mathematical relationship can be estimated by performing an uncertainty analysis [see Kline (1985)]. The uncertainty involved in the empirically corrected velocity based on the use of Eq. B6 at different stations in the diffuser is shown in Fig. B.4. In applying the uncertainty analysis, it was assumed that the uncertainty in measurements of the density of air and manometer height readings were ±1.35% and ±1.00% respectively. With these assumptions the uncertainty in calculating U_{SW} and U_{SL} from the Bernoulli equation was ±1.35% and hence propagation of measured errors when calculations are done with Eq. B6 was deduced. Figure B.4 show very little errors associated with the use of Eq. B6 in the core region but these errors tend to increase near the wall. The higher uncertainty in the wall region, especially for stations 42-66, supports the observed deviations between corrected velocities and the hot-wire values in Fig. B.3(c). Overall, the low uncertainty values of less than 4% indicates the validity of the empirical procedure.

B4.2 Static pressure corrections.

The mean velocity correction procedure is completely empirical and is applicable to the exit portion of the diffuser (stations 24-66) where U_{SW} and U_{SL} at any radial location are greater values than the actual mean velocity. In addition, Eq. B8(b) show that the correction term actually accounts for errors in static pressure estimates since the total pressure used in the calculation of U_{SW} and U_{SL} at any point is the same. Therfore, an alternate method of correcting mean velocity is to use measured total pressures and corrected static pressure (using Eq. B.13) in the Bernoulli equation. In applying Eqs. B11 and B13, the positive sign is used for stations 24-66 where the mass flow rate calculated from uncorrected velocity profiles are greater than the pipe flow value while the negative sign is used for stations 6-18 (see Fig. B.2 for mass flow rates). However, for the purpose of presenting the results, the stations in the diffuser are grouped into three categories based on similarity of flow properties. Stations 6-18 will be referred to as the initial stations and the negative sign is applicable when Eqs. B11 or B13 are used. The intermediate stations, 24-36 and the outer stations, 42-66 require the use of the positive sign in Eqs. B11 or B13 but are so divided because the latter has more pronounced deviations of flow properties with respect to the pipe flow. In Sect. B4.1, velocities obtained first by applying static pressure correction followed by the use of Bernoulli equation are shown in Fig. B.3(a) for station 6. For the intermediate and outer stations, the procedure used for the inner stations give similar values of mean velocity as the use of the empirical correction.

Figures. B.5(a), (b) and (c) show the pressures at stations 6, 36 and 66 respectively, representing one station in each group. The pressure difference ΔP, is $P_{s(local)}$-$P_{s(ref)}$. $P_{s(local)}$ represents measured or corrected static pressures while $P_{s(ref)}$ is the reference pressure usually a constant value of static pressure and it is taken as the value of static pressure (constant value) far upstream in the fully developed pipe flow. The difference between the measured and corrected static pressures is an indication of the error involved in measurements. The corrected static pressures were obtained from Eq. B13. Corrected static pressures are also shown using Eq. B11 with $A' = 1$ and $\overline{u_n^2} = \overline{v^2} + \overline{w^2}$ obtained from x-wire measurements. When $A' = 1$ and $B' = 1.2$, the static and total pressure probes do not vibrate during measurements [Hinze (1975)]. For values of $A' > 1$ and $B' > 1.2$, some vibration, intentionally applied or induced by flow around the probes, affects their performance. Therefore, difference between the two corrected static pressures, in Fig. B.5(a) - (c), is an indication that some vibration is induced on the pressure probes by the fluid motion. Note that correction using Eq. B13 accounts for the actual values of A' whereas Eq. B11 with $A' = 1$ assumes no vibration. Thus, none of the constant values of A' given in the literature which are generally less than one, see Sect. B3, can account for similar deviations from the measured values as the present correction. Since the present corrected static pressures produce accurate mean velocity as shown in Sect. B4.1, it can be assumed that the corrected static pressures in Fig. B.5(a) - (c) are accurate or that the correction procedure, Eq. B13, is an improvement on existing correction methods.

A' and B' can be calibrated at any point in the flow by using Eqs. B3 and B4 [see Eichoff (1969)] which involves combined pressure and hot-wire measurements. The values of A' and B' across various stations in the diffuser flow are given in Figs. B.6(a) and (b) respectively. In the initial stations, the magnitude of A' and B' suggests strong induced vibration of the probes due to fluid motions around the probes since $A' \gg 1$ and $B' \gg 1.2$. This can be expected because at these stations more than 72cm of probe holder is introduced from the open end of the diffuser and the stations are characterized by large values of mean velocities and are affected by mixing due to entrance effects as the air diverges. The scatter in corrected static pressures in Fig. B.5(a) maybe an indication of this random vibration. The intermediate and outer stations show values of $A' \sim 1$ and $B' \sim 1.2$ in the wall region but have different values around the axis of the flow. Deviations around the axis of the flow in which these constants have greater than normal values can be attributed to increasing yaw angles brought about by the divergence of streamlines. Values of B' are observed to become less than 1.2 for the outer stations around the axis of the flow. This is a further indication of the complex nature of flow in the diffuser since values of $B' = 1.2$ and $A' = 1$ as given by Hinze (1975) were calculated in simple turbulent flows similar to Eichoff (1969) where assumptions of isotropic turbulence are valid.

APPENDIX C

EXPERIMENTAL DATA

Experimental data obtained in this study are presented in the following tables. Pressure measurements can be accurately reproduced hence the presentation in Figs. 4.1 and 4.2 as well as in Figs. B.1-B.6 is sufficient. The accuracy of single and x-wire measurements depend on the method of data acquisition and the experience of the investigator. Therefore, in the following tables the raw data from hot-wire measurements have been processed to give relevant velocities and their moments. All quantities except for the mean velocities have been normalized. Moments of fluctuating velocities are normalized as shown in Eq. 4.3.

Table C1 which gives the measuring positions is the key to understanding the tables. Column 1 in all tables show a serial numbering of the rows, and the turbulence characteristics in each station corresponding to each row is associated with the measuring position in Table C1. The measuring positions are presented with respect to the axis of the flow and they are normalized with the radius of the feed pipe. In Table C1, the first measuring position (row 1) is at the axis of the flow while row 20 is the normalized radius of the measuring station. The actual diameters of each measuring position and their location from the entrance of the diffuser are given in Table 3.1.

	pipe	6	18	30	42	54	66
1	0.000	0.000	0.000	0.000	0.000	0.000	0.0
2	0.053	0.055	0.065	0.074	0.083	0.091	0.1
3	0.105	0.111	0.130	0.148	0.166	0.182	0.2
4	0.158	0.166	0.194	0.222	0.249	0.273	0.3
5	0.211	0.222	0.259	0.296	0.332	0.365	0.4
6	0.263	0.277	0.324	0.371	0.414	0.456	0.5
7	0.316	0.333	0.388	0.445	0.497	0.547	0.6
8	0.368	0.388	0.453	0.519	0.580	0.638	0.7
9	0.421	0.443	0.518	0.593	0.663	0.729	0.8
10	0.474	0.499	0.583	0.667	0.746	0.820	0.9
11	0.526	0.554	0.647	0.741	0.829	0.912	1.0
12	0.579	0.610	0.712	0.815	0.912	1.003	1.1
13	0.632	0.665	0.777	0.889	0.995	1.094	1.2
14	0.684	0.720	0.842	0.963	1.078	1.185	1.3
15	0.737	0.776	0.906	1.037	1.161	1.276	1.4
16	0.789	0.831	0.971	1.112	1.243	1.367	1.5
17	0.842	0.887	1.036	1.186	1.326	1.459	1.6
18	0.895	0.942	1.101	1.260	1.409	1.550	1.7
19	0.947	0.998	1.165	1.334	1.492	1.641	1.8
20	1.000	1.053	1.230	1.408	1.575	1.732	1.9

Table C1: Measuring positions in the pipe and diffuser flows, r/R_p

	pipe	6	18	30	42	54	66
1	21.720	21.161	18.355	16.928	15.476	14.716	13.809
2	21.621	21.172	18.317	16.919	15.447	14.617	13.628
3	21.510	21.105	18.287	16.722	15.271	14.323	13.248
4	21.376	20.932	18.178	16.474	14.984	13.916	12.723
5	21.223	20.732	17.927	16.189	14.610	13.381	12.059
6	21.054	20.535	17.598	15.834	14.135	12.689	11.210
7	20.864	20.325	17.238	15.406	13.547	11.914	10.268
8	20.648	20.081	16.855	14.910	12.885	11.109	9.366
9	20.409	19.795	16.432	14.335	12.163	10.263	8.487
10	20.139	19.474	15.943	13.677	11.361	9.344	7.572
11	19.817	19.116	15.396	12.908	10.424	8.382	6.657
12	19.448	18.714	14.818	12.011	9.382	7.428	5.815
13	19.067	18.279	14.219	11.017	8.360	6.502	5.066
14	18.692	17.819	13.519	9.926	7.413	5.616	4.430
15	18.238	17.308	12.547	8.725	6.392	4.785	3.860
16	17.674	16.648	11.295	7.401	5.172	4.037	3.307
17	17.001	15.691	9.817	6.075	4.238	3.358	2.771
18	16.226	14.739	8.016	4.902	3.427	2.800	2.416
19	15.192	12.546	6.024	3.814	2.646	2.210	1.977

Table C2: Mean velocities in the pipe and diffuser flows, U (m/s).

	pipe	6	18	30	42	54	66
1	0.033	0.033	0.041	0.047	0.050	0.065	0.095
2	0.034	0.034	0.041	0.039	0.051	0.064	0.105
3	0.036	0.035	0.045	0.050	0.059	0.079	0.118
4	0.038	0.038	0.050	0.060	0.067	0.087	0.135
5	0.041	0.042	0.055	0.066	0.076	0.100	0.157
6	0.044	0.046	0.060	0.072	0.090	0.128	0.181
7	0.047	0.051	0.066	0.079	0.112	0.161	0.208
8	0.050	0.054	0.073	0.090	0.136	0.188	0.236
9	0.054	0.057	0.080	0.103	0.160	0.213	0.269
10	0.056	0.060	0.089	0.121	0.184	0.240	0.310
11	0.062	0.063	0.099	0.143	0.211	0.272	0.350
12	0.066	0.069	0.110	0.170	0.242	0.308	0.373
13	0.071	0.076	0.123	0.203	0.276	0.347	0.388
14	0.076	0.082	0.139	0.246	0.312	0.385	0.409
15	0.081	0.088	0.164	0.290	0.348	0.417	0.439
16	0.086	0.093	0.198	0.326	0.384	0.435	0.476
17	0.096	0.110	0.242	0.383	0.424	0.475	0.506
18	0.104	0.119	0.296	0.416	0.477	0.517	0.532
19	0.114	0.153	0.367	0.453	0.530	0.562	0.602

Table C3: Longitudinal intensity of turbulence, u'/U.

	pipe	6	18	30	42	54	66
1	0.026	0.032	0.038	0.038	0.046	0.059	0.081
2	0.026	0.032	0.038	0.038	0.049	0.058	0.083
3	0.027	0.033	0.039	0.038	0.052	0.064	0.089
4	0.028	0.034	0.040	0.039	0.055	0.072	0.099
5	0.029	0.035	0.041	0.040	0.059	0.079	0.111
6	0.030	0.037	0.044	0.043	0.066	0.090	0.128
7	0.032	0.038	0.047	0.046	0.075	0.104	0.148
8	0.034	0.040	0.051	0.050	0.087	0.122	0.169
9	0.035	0.042	0.054	0.054	0.098	0.140	0.190
10	0.036	0.044	0.058	0.058	0.112	0.157	0.213
11	0.038	0.047	0.062	0.062	0.127	0.174	0.238
12	0.039	0.049	0.066	0.065	0.145	0.191	0.259
13	0.041	0.051	0.072	0.068	0.166	0.215	0.269
14	0.043	0.054	0.081	0.074	0.188	0.244	0.278
15	0.046	0.056	0.094	0.084	0.210	0.270	0.295
16	0.048	0.059	0.112	0.100	0.230	0.289	0.313
17	0.052	0.063	0.136	0.124	0.251	0.300	0.329
18	0.055	0.070	0.165	0.158	0.281	0.300	0.350
19	0.062	0.097	0.182	0.179	0.261	0.268	0.307
20	0.104	0.162	0.195	0.186	0.221	0.202	0.247

Table C4: Transverse intensity of turbulence, v'/U.

	pipe	6	18	30	42	54	66
1	0.026	0.030	0.035	0.034	0.049	0.063	0.082
2	0.026	0.030	0.036	0.035	0.050	0.059	0.086
3	0.027	0.031	0.037	0.036	0.052	0.065	0.093
4	0.028	0.032	0.039	0.038	0.057	0.074	0.103
5	0.029	0.033	0.040	0.039	0.064	0.085	0.118
6	0.030	0.035	0.043	0.041	0.073	0.099	0.137
7	0.032	0.037	0.046	0.044	0.084	0.116	0.156
8	0.034	0.039	0.051	0.047	0.097	0.137	0.178
9	0.035	0.041	0.057	0.052	0.113	0.159	0.201
10	0.036	0.044	0.063	0.058	0.130	0.179	0.219
11	0.038	0.047	0.068	0.066	0.150	0.199	0.239
12	0.039	0.049	0.071	0.078	0.172	0.226	0.263
13	0.041	0.052	0.075	0.094	0.196	0.253	0.283
14	0.043	0.056	0.082	0.116	0.223	0.269	0.294
15	0.046	0.059	0.093	0.144	0.246	0.274	0.299
16	0.048	0.063	0.112	0.173	0.260	0.281	0.304
17	0.052	0.068	0.139	0.204	0.274	0.295	0.317
18	0.055	0.074	0.177	0.234	0.300	0.311	0.344
19	0.062	0.091	0.226	0.265	0.339	0.358	0.346
20	0.104	0.127	0.309	0.295	0.449	0.465	0.499

Table C5: Lateral intensity of turbulence, w'/U.

	pipe	6	18	30	42	54	66
1	0.000	0.000	0.000	0.000	0.000	0.000	0.000
2	0.103	0.102	0.088	0.161	0.197	0.240	0.435
3	0.208	0.194	0.180	0.311	0.389	0.523	0.968
4	0.313	0.279	0.289	0.441	0.571	0.896	1.678
5	0.419	0.374	0.425	0.557	0.782	1.343	2.366
6	0.524	0.486	0.575	0.695	1.099	1.840	2.851
7	0.629	0.606	0.714	0.895	1.549	2.345	3.234
8	0.734	0.725	0.826	1.145	2.021	2.798	3.596
9	0.839	0.835	0.923	1.400	2.418	3.184	3.863
10	0.945	0.938	1.036	1.645	2.761	3.523	3.950
11	1.050	1.039	1.207	1.937	3.102	3.758	3.858
12	1.155	1.139	1.398	2.369	3.420	3.703	3.612
13	1.260	1.241	1.560	2.873	3.612	3.379	3.359
14	1.366	1.344	1.689	3.203	3.524	3.152	3.133
15	1.471	1.447	2.010	3.315	3.034	2.792	2.654
16	1.576	1.552	2.585	3.189	2.529	2.376	1.962
17	1.681	1.689	3.063	2.815	2.110	1.799	1.504
18	1.787	1.890	3.170	2.258	1.653	1.366	1.044
19	1.892	2.140	2.571	1.556	1.030	0.726	0.589

Table C6: Reynolds shear stress in the pipe and diffuser flows, $-\overline{uv}/U_b^2 x 10^3$.

($U_b = 18.2 m/s$, the average bulk velocity in the pipe flow).

	pipe	6	18	30	42	54	66
1	0.000	0.000	0.000	0.000	0.000	0.000	0.000
2	0.091	0.100	0.116	0.100	0.125	0.134	0.145
3	0.151	0.161	0.151	0.180	0.190	0.199	0.216
4	0.206	0.196	0.187	0.227	0.244	0.259	0.269
5	0.255	0.229	0.224	0.250	0.269	0.310	0.315
6	0.295	0.261	0.258	0.272	0.293	0.344	0.348
7	0.327	0.289	0.288	0.293	0.315	0.364	0.371
8	0.351	0.313	0.310	0.312	0.335	0.375	0.388
9	0.369	0.333	0.325	0.328	0.352	0.383	0.400
10	0.381	0.348	0.335	0.341	0.366	0.387	0.408
11	0.390	0.359	0.341	0.352	0.376	0.390	0.413
12	0.396	0.369	0.346	0.362	0.383	0.391	0.416
13	0.400	0.376	0.351	0.370	0.387	0.391	0.420
14	0.402	0.382	0.357	0.374	0.386	0.391	0.423
15	0.403	0.388	0.365	0.373	0.382	0.393	0.418
16	0.401	0.395	0.376	0.369	0.375	0.392	0.400
17	0.400	0.402	0.387	0.363	0.365	0.383	0.370
18	0.392	0.411	0.396	0.355	0.354	0.358	0.330
19	0.386	0.420	0.404	0.346	0.342	0.310	0.284

Table C7: Correlation coefficient of Reynolds stress, $-\overline{\hat{u}\hat{v}}$

	pipe	6	18	30	42	54	66
1							
2	−0.441	−0.443	−0.446	−0.605	−0.558	−0.589	−0.681
3	−0.453	−0.429	−0.419	−0.521	−0.452	−0.529	−0.544
4	−0.437	−0.414	−0.394	−0.434	−0.341	−0.472	−0.408
5	−0.405	−0.395	−0.368	−0.348	−0.238	−0.398	−0.278
6	−0.374	−0.369	−0.341	−0.269	−0.157	−0.285	−0.159
7	−0.335	−0.337	−0.311	−0.204	−0.103	−0.155	−0.049
8	−0.281	−0.301	−0.275	−0.154	−0.059	−0.048	0.051
9	−0.232	−0.261	−0.237	−0.116	−0.009	0.024	0.143
10	−0.201	−0.220	−0.193	−0.090	0.047	0.085	0.227
11	−0.180	−0.182	−0.131	−0.064	0.101	0.145	0.304
12	−0.161	−0.151	−0.076	−0.024	0.156	0.204	0.371
13	−0.135	−0.128	−0.047	0.036	0.219	0.262	0.426
14	−0.104	−0.109	−0.031	0.107	0.289	0.311	0.466
15	−0.079	−0.086	−0.020	0.188	0.338	0.346	0.490
16	−0.057	−0.056	−0.001	0.273	0.357	0.367	0.497
17	−0.030	−0.018	0.042	0.356	0.362	0.375	0.487
18	−0.012	−0.025	0.111	0.434	0.379	0.382	0.461
19	−0.007	−0.070	0.201	0.507	0.433	0.403	0.430

Figure 4.a Skewness factor of u

Table C8: Skewness factor of u, $\overline{\hat{u}^3}$

	pipe	6	18	30	42	54	66
1							
2	0.129	0.114	0.215	0.336	0.238	0.256	0.351
3	0.191	0.171	0.230	0.337	0.299	0.351	0.354
4	0.239	0.221	0.248	0.337	0.366	0.439	0.356
5	0.272	0.257	0.267	0.337	0.422	0.486	0.342
6	0.288	0.277	0.282	0.341	0.451	0.455	0.300
7	0.290	0.285	0.292	0.351	0.439	0.370	0.230
8	0.281	0.285	0.293	0.363	0.391	0.290	0.139
9	0.264	0.279	0.286	0.364	0.307	0.227	0.044
10	0.242	0.268	0.275	0.346	0.213	0.148	−0.041
11	0.219	0.251	0.263	0.313	0.139	0.044	−0.116
12	0.196	0.227	0.250	0.267	0.080	−0.057	−0.185
13	0.179	0.198	0.236	0.198	−0.003	−0.140	−0.250
14	0.167	0.168	0.219	0.098	−0.118	−0.213	−0.307
15	0.160	0.141	0.194	0.013	−0.197	−0.283	−0.352
16	0.158	0.122	0.153	−0.080	−0.287	−0.348	−0.380
17	0.164	0.128	0.092	−0.170	−0.382	−0.401	−0.394
18	0.179	0.175	0.013	−0.193	−0.430	−0.420	−0.394
19	0.200	0.253	−0.075	−0.215	−0.365	−0.378	−0.374

Table C9: Skewness factor of v, $\overline{\upsilon^3}$

	pipe	6	18	30	42	54	66
1							
2	0.100	0.128	0.169	0.243	0.241	0.267	0.096
3	0.158	0.145	0.167	0.226	0.221	0.262	0.140
4	0.193	0.161	0.166	0.208	0.201	0.255	0.183
5	0.208	0.173	0.166	0.190	0.181	0.237	0.199
6	0.206	0.178	0.164	0.174	0.159	0.196	0.170
7	0.194	0.176	0.159	0.161	0.135	0.139	0.107
8	0.179	0.169	0.151	0.151	0.106	0.086	0.027
9	0.164	0.156	0.139	0.143	0.072	0.042	−0.046
10	0.151	0.139	0.128	0.135	0.034	0.003	−0.096
11	0.140	0.121	0.116	0.119	−0.003	−0.033	−0.131
12	0.129	0.107	0.103	0.080	−0.038	−0.071	−0.162
13	0.116	0.095	0.091	0.027	−0.072	−0.110	−0.197
14	0.102	0.085	0.077	−0.012	−0.102	−0.140	−0.236
15	0.088	0.075	0.059	−0.048	−0.125	−0.152	−0.255
16	0.075	0.063	0.033	−0.085	−0.141	−0.157	−0.238
17	0.062	0.048	−0.004	−0.125	−0.150	−0.164	−0.190
18	0.047	0.033	−0.051	−0.166	−0.156	−0.160	−0.130
19	0.031	0.017	−0.104	−0.195	−0.159	−0.128	−0.112

Table C10: Third-order moments, $\overline{\hat{u}^2\hat{v}}$

	pipe	6	18	30	42	54	66
1							
2	−0.284	−0.253	−0.275	−0.363	−0.223	−0.302	−0.411
3	−0.281	−0.254	−0.261	−0.323	−0.213	−0.310	−0.373
4	−0.272	−0.254	−0.247	−0.277	−0.204	−0.316	−0.329
5	−0.259	−0.247	−0.233	−0.232	−0.194	−0.304	−0.279
6	−0.241	−0.231	−0.219	−0.195	−0.183	−0.257	−0.221
7	−0.220	−0.212	−0.203	−0.177	−0.168	−0.186	−0.149
8	−0.200	−0.190	−0.185	−0.173	−0.146	−0.123	−0.061
9	−0.180	−0.168	−0.169	−0.172	−0.111	−0.073	0.021
10	−0.161	−0.148	−0.155	−0.166	−0.068	−0.026	0.081
11	−0.144	−0.129	−0.143	−0.148	−0.019	0.027	0.127
12	−0.129	−0.112	−0.131	−0.111	0.033	0.090	0.169
13	−0.115	−0.097	−0.118	−0.059	0.087	0.162	0.218
14	−0.103	−0.082	−0.099	−0.009	0.141	0.221	0.274
15	−0.088	−0.067	−0.073	0.049	0.191	0.252	0.316
16	−0.073	−0.050	−0.036	0.126	0.232	0.273	0.329
17	−0.060	−0.039	0.016	0.210	0.266	0.301	0.325
18	−0.054	−0.041	0.083	0.273	0.296	0.322	0.311
19	−0.054	−0.051	0.158	0.324	0.324	0.313	0.299

Table C11: Third-order moments, $\overline{\hat{u}\hat{v}^2}$

	pipe	6	18	30	42	54	66
1							
2	3.381	3.273	3.305	3.581	3.921	3.926	4.184
3	3.365	3.338	3.263	3.556	3.755	3.901	3.900
4	3.321	3.366	3.220	3.532	3.577	3.891	3.616
5	3.258	3.378	3.176	3.508	3.420	3.805	3.355
6	3.188	3.306	3.134	3.480	3.321	3.553	3.136
7	3.117	3.202	3.094	3.444	3.287	3.222	2.973
8	3.050	3.094	3.058	3.395	3.249	3.006	2.879
9	2.995	3.006	3.027	3.326	3.143	2.947	2.853
10	2.954	2.940	2.999	3.230	3.002	2.957	2.893
11	2.921	2.892	2.975	3.125	2.890	2.976	2.972
12	2.891	2.862	2.956	3.029	2.839	2.982	3.066
13	2.859	2.845	2.938	2.962	2.865	2.969	3.152
14	2.829	2.835	2.922	2.935	2.955	2.969	3.226
15	2.813	2.824	2.907	2.943	3.019	3.012	3.314
16	2.808	2.806	2.891	2.981	3.056	3.103	3.427
17	2.805	2.788	2.877	3.052	3.094	3.243	3.530
18	2.808	2.780	2.866	3.155	3.163	3.386	3.604
19	2.820	2.780	2.858	3.274	3.296	3.479	3.661

Table C12: Flatness factor of u, $\overline{\hat{u}^4}$.

	pipe	6	18	30	42	54	66
1							
2	3.680	3.607	3.534	4.042	3.698	4.220	4.505
3	3.654	3.646	3.543	4.009	3.830	4.312	4.265
4	3.623	3.676	3.553	3.974	3.974	4.303	4.024
5	3.588	3.682	3.562	3.940	4.097	4.385	3.784
6	3.550	3.663	3.571	3.911	4.163	4.142	3.548
7	3.512	3.627	3.578	3.892	4.141	3.769	3.338
8	3.472	3.581	3.580	3.878	4.022	3.479	3.179
9	3.436	3.533	3.578	3.853	3.795	3.329	3.093
10	3.402	3.483	3.573	3.807	3.519	3.238	3.090
11	3.372	3.434	3.565	3.745	3.272	3.174	3.138
12	3.348	3.385	3.552	3.671	3.105	3.164	3.205
13	3.336	3.339	3.532	3.555	3.049	3.220	3.263
14	3.334	3.306	3.506	3.376	3.115	3.289	3.308
15	3.341	3.293	3.475	3.298	3.231	3.343	3.384
16	3.353	3.311	3.441	3.278	3.331	3.465	3.583
17	3.369	3.351	3.409	3.296	3.475	3.748	4.088
18	3.387	3.399	3.385	3.512	3.787	4.168	4.843
19	3.405	3.456	3.372	3.909	4.430	4.683	5.232

Table C13: Flatness factor of v, $\overline{\upsilon^4}$.

	pipe	6	18	30	42	54	66
1							
2	1.311	1.279	1.185	1.597	1.259	1.606	1.653
3	1.320	1.277	1.200	1.556	1.282	1.619	1.564
4	1.325	1.275	1.218	1.511	1.307	1.637	1.476
5	1.327	1.275	1.235	1.468	1.330	1.625	1.392
6	1.326	1.276	1.251	1.431	1.348	1.549	1.321
7	1.324	1.278	1.261	1.407	1.356	1.427	1.268
8	1.319	1.277	1.262	1.392	1.349	1.314	1.238
9	1.315	1.271	1.261	1.378	1.320	1.236	1.233
10	1.311	1.262	1.261	1.358	1.281	1.202	1.255
11	1.307	1.252	1.264	1.327	1.249	1.209	1.295
12	1.302	1.244	1.267	1.280	1.233	1.227	1.347
13	1.296	1.239	1.265	1.234	1.232	1.241	1.407
14	1.288	1.236	1.254	1.221	1.248	1.257	1.469
15	1.278	1.237	1.238	1.215	1.274	1.286	1.525
16	1.264	1.242	1.224	1.213	1.311	1.334	1.567
17	1.247	1.251	1.216	1.234	1.355	1.405	1.596
18	1.227	1.264	1.220	1.295	1.404	1.460	1.609
19	1.207	1.280	1.245	1.381	1.454	1.449	1.605

Table C14: Forth-order moments, $\overline{\hat{u}^2\hat{v}^2}$.

	pipe	6	18	30	42	54	66
1							
2	−0.379	−0.407	−0.559	−1.033	−0.851	−1.109	−0.640
3	−0.666	−0.582	−0.627	−1.048	−0.886	−1.118	−0.771
4	−0.864	−0.741	−0.699	−1.064	−0.921	−1.128	−0.901
5	−0.984	−0.865	−0.771	−1.079	−0.955	−1.134	−1.001
6	−1.046	−0.950	−0.840	−1.093	−0.986	−1.131	−1.052
7	−1.076	−1.006	−0.899	−1.103	−1.014	−1.121	−1.074
8	−1.093	−1.039	−0.943	−1.108	−1.037	−1.110	−1.090
9	−1.103	−1.056	−0.971	−1.108	−1.053	−1.104	−1.114
10	−1.111	−1.061	−0.987	−1.100	−1.064	−1.104	−1.152
11	−1.117	−1.057	−0.997	−1.089	−1.074	−1.109	−1.201
12	−1.121	−1.049	−1.007	−1.076	−1.082	−1.115	−1.257
13	−1.120	−1.039	−1.019	−1.064	−1.090	−1.119	−1.318
14	−1.117	−1.032	−1.031	−1.055	−1.097	−1.126	−1.375
15	−1.120	−1.037	−1.044	−1.050	−1.102	−1.141	−1.404
16	−1.121	−1.059	−1.059	−1.051	−1.106	−1.155	−1.385
17	−1.105	−1.092	−1.074	−1.059	−1.110	−1.157	−1.319
18	−1.075	−1.132	−1.094	−1.075	−1.112	−1.131	−1.208
19	−1.041	−1.176	−1.121	−1.095	−1.113	−1.058	−1.067

Table C15: Forth-order moments, $\overline{\hat{u}^3 \hat{v}}$.

	pipe	6	18	30	42	54	66
1							
2	−0.336	−0.370	−0.424	−1.045	−0.650	−1.012	−0.780
3	−0.571	−0.538	−0.523	−1.057	−0.736	−1.040	−0.906
4	−0.764	−0.692	−0.630	−1.069	−0.824	−1.068	−1.022
5	−0.910	−0.824	−0.736	−1.082	−0.909	−1.092	−1.099
6	−1.009	−0.930	−0.836	−1.093	−0.984	−1.107	−1.103
7	−1.071	−1.010	−0.920	−1.103	−1.045	−1.109	−1.073
8	−1.107	−1.062	−0.977	−1.109	−1.084	−1.096	−1.050
9	−1.127	−1.084	−1.013	−1.110	−1.095	−1.073	−1.044
10	−1.138	−1.085	−1.036	−1.105	−1.088	−1.060	−1.067
11	−1.145	−1.073	−1.053	−1.094	−1.075	−1.064	−1.114
12	−1.151	−1.060	−1.065	−1.082	−1.066	−1.086	−1.182
13	−1.159	−1.050	−1.070	−1.069	−1.068	−1.125	−1.274
14	−1.167	−1.046	−1.069	−1.057	−1.087	−1.177	−1.386
15	−1.169	−1.055	−1.069	−1.050	−1.120	−1.238	−1.486
16	−1.163	−1.079	−1.077	−1.053	−1.165	−1.298	−1.551
17	−1.149	−1.120	−1.095	−1.069	−1.218	−1.341	−1.586
18	−1.125	−1.177	−1.123	−1.098	−1.271	−1.349	−1.575
19	−1.095	−1.248	−1.166	−1.137	−1.317	−1.305	−1.458

Table C16: Forth-order moments, $\overline{\hat{u}\hat{v}^3}$.

TABLES AND FIGURES

serial No.	d_p (mm)	d_p/d_i
1	0.508	0.700
2	1.067	0.714
3	2.032	0.825
4	3.175	0.680
5	4.750	0.701

Table 3.1: Preston tube dimensions.
(d_p= outside diameter, d_i=inside diameter).

STATION (X cm)	D (m)	X/D_p	U_{max} (m/s)	u_* (m/s)
Pipe	0.1016	0.000	21.700	0.839
6	0.107	0.591	21.161	0.638
12	0.116	1.181	19.580	0.472
18	0.125	1.772	18.355	0.375
24	0.134	2.362	17.642	0.309
30	0.143	2.953	16.928	0.268
36	0.151	2.543	15.830	0.238
42	0.160	4.134	15.476	0.213
48	0.168	4.724	15.049	0.195
54	0.176	5.315	14.716	0.185
60	0.186	5.906	13.934	0.175
66	0.193	6.496	13.810	0.170

Table 3.2: Dimensions and basic velocity characteristics in the pipe and diffuser flow.
(Subscript p refers to pipe values, D= local diameter, U_{max}= local center line maximum velocity, u_*= friction velocity, X= distance from entrance of diffuser to the measuring station).

STATION (X cm)	$L_s \times 10^3$ (m)	U_m (m/s)	$-\rho\overline{uv}_{max}/\tau_w$
Pipe	-	-	1.005
6	-	-	2.030
18	7.3	1.025	7.470
30	19.5	1.048	15.290
42	29.8	1.094	26.630
54	40.9	1.116	39.330
66	53.7	1.144	51.590

Table 4.1: Dimensions and some flow properties at the peak region.

	QUADRANT			
	1	2	3	4
$k_0(J)$	0.27	0.85	0.27	0.85
$k_1(J)$	0.12	0.15	0.03	0.18

Table 5.1: Values for the constants $k_0(J)$ and $k_1(J)$ in Eqs. 5.31 and 5.32. (Obtained in pipe flow at $Y/R_p=0.2$, $Y=$ radial distance measured from the wall and $R_p=$ radius of the pipe).

	Total Number of Patterns				Non- Dimensionalized mean periods	
H	I- V (accepted)	VI	VI (rejected)	Percentage rejected.	T* (all patterns)	T* (accepted patterns)
0	5387	2970	2885	35.5	0.256	0.390
1	1528	1287	350	12.4	0.759	0.867
2	809	900	375	21.9	1.250	1.601
3	402	539	256	27.2	2.270	3.118
4	198	325	175	33.5	4.084	6.137
5	103	169	123	45.2	7.852	14.334
6	41	101	75	52.8	15.041	31.878
7	23	46	41	59.4	30.954	76.280

Table 5.2: The distribution of patterns during ejections as a function of hole size. (Y/R_p=0.295 in pipe flow).

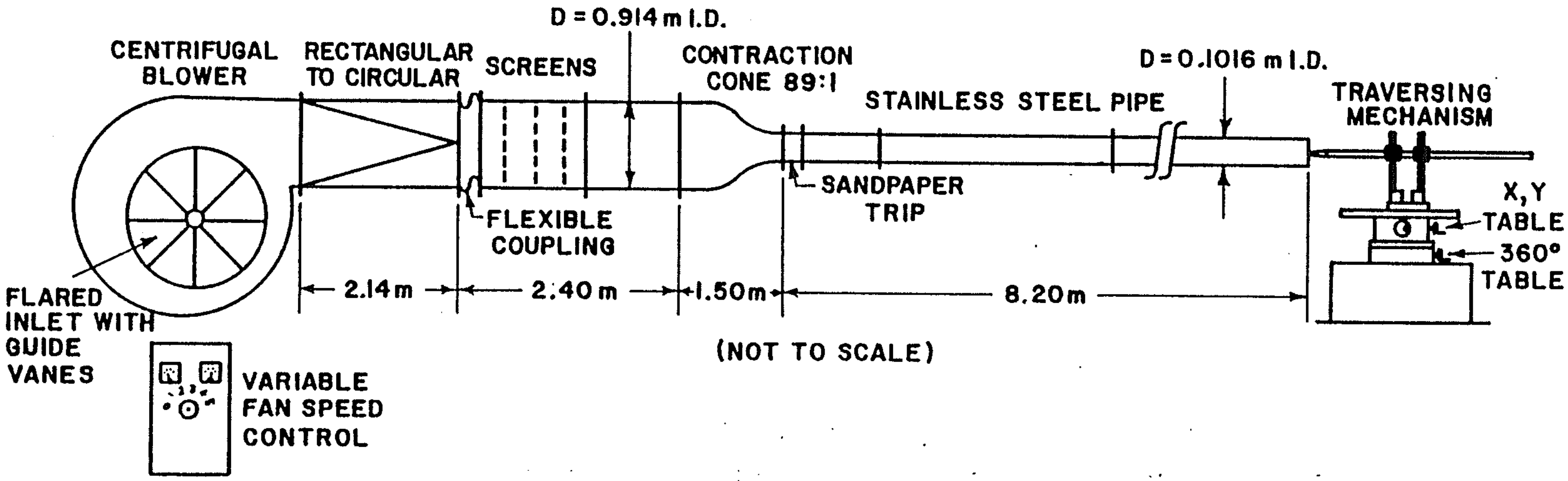

FIGURE 3.1(a): Wind tunnel and fully developed pipe flow.
(Diffuser can be attached to the end of pipe)

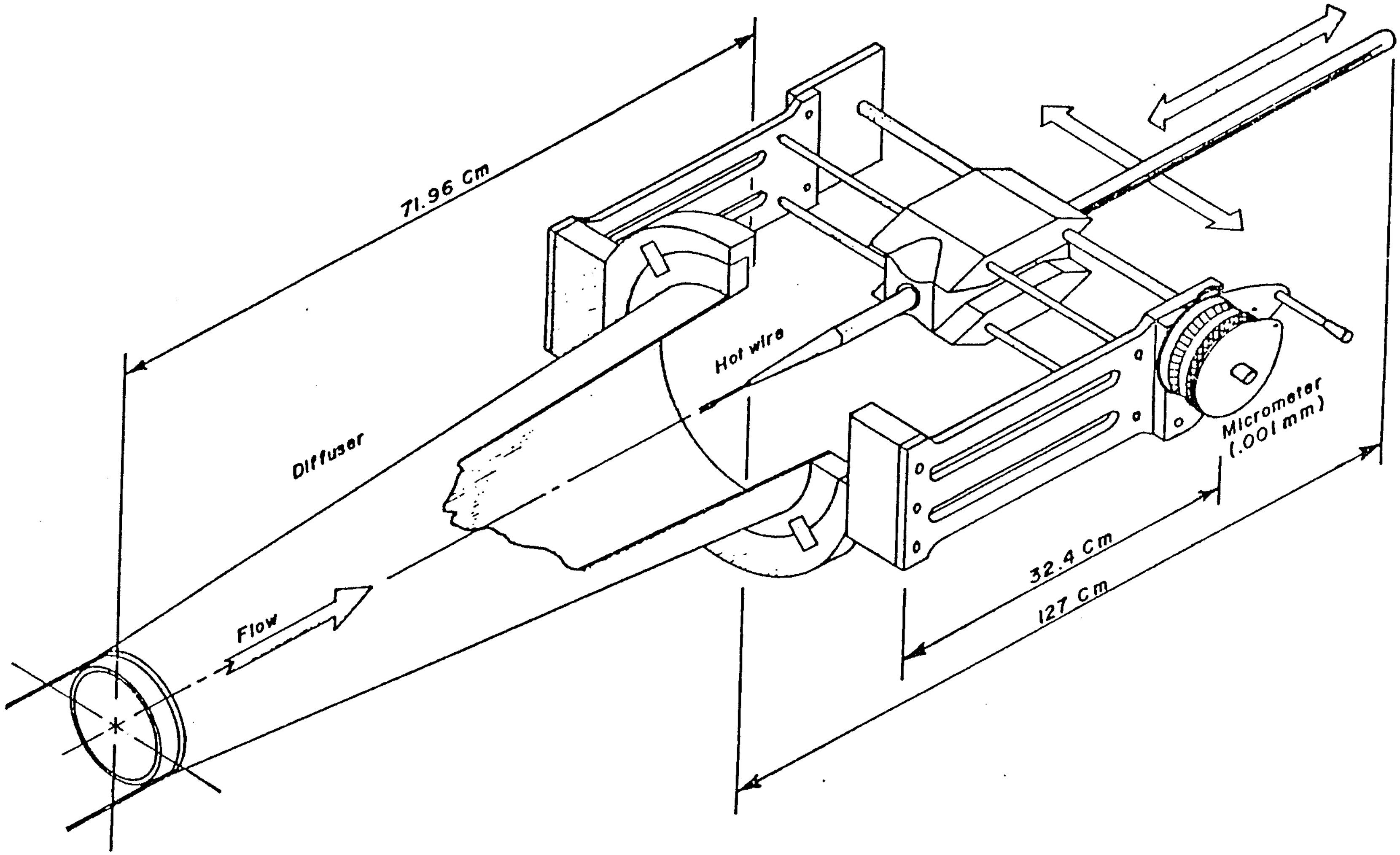

FIGURE 3.1(b): Conical diffuser and traversing mechanism.

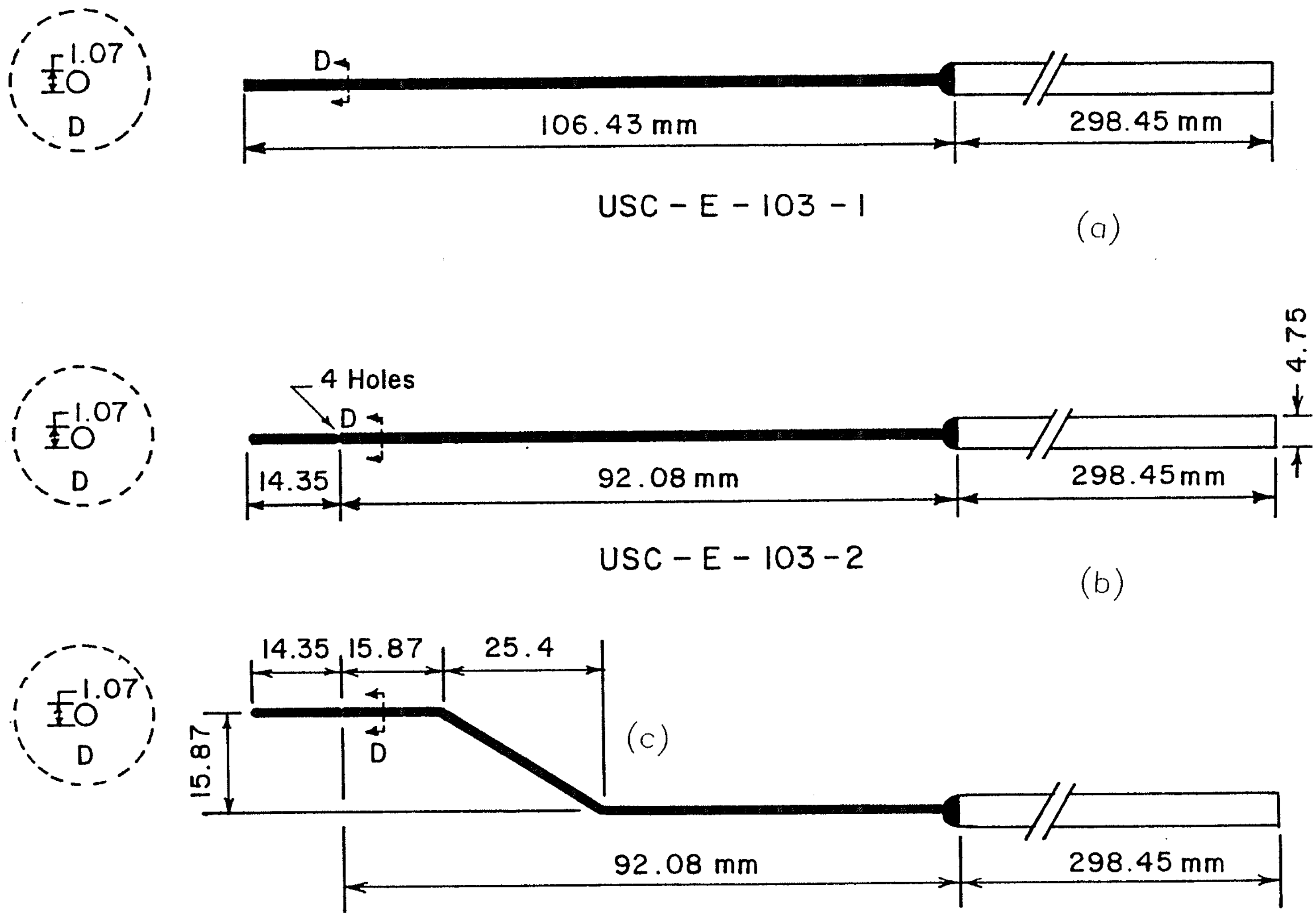

FIGURE 3.2: Pressure probes.
(a) Total pressure tube (b) Standard static pressure tube (c) Static pressure tube for wall measurements.

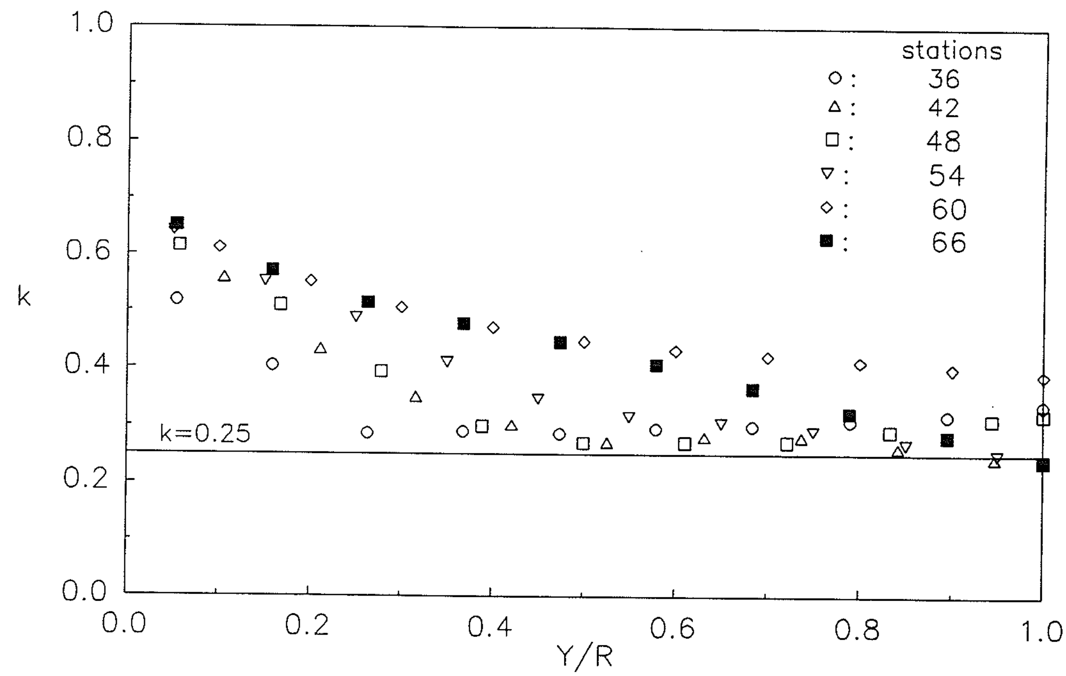

FIGURE 3.3: Variation of Yaw factor in the diffuser flow.

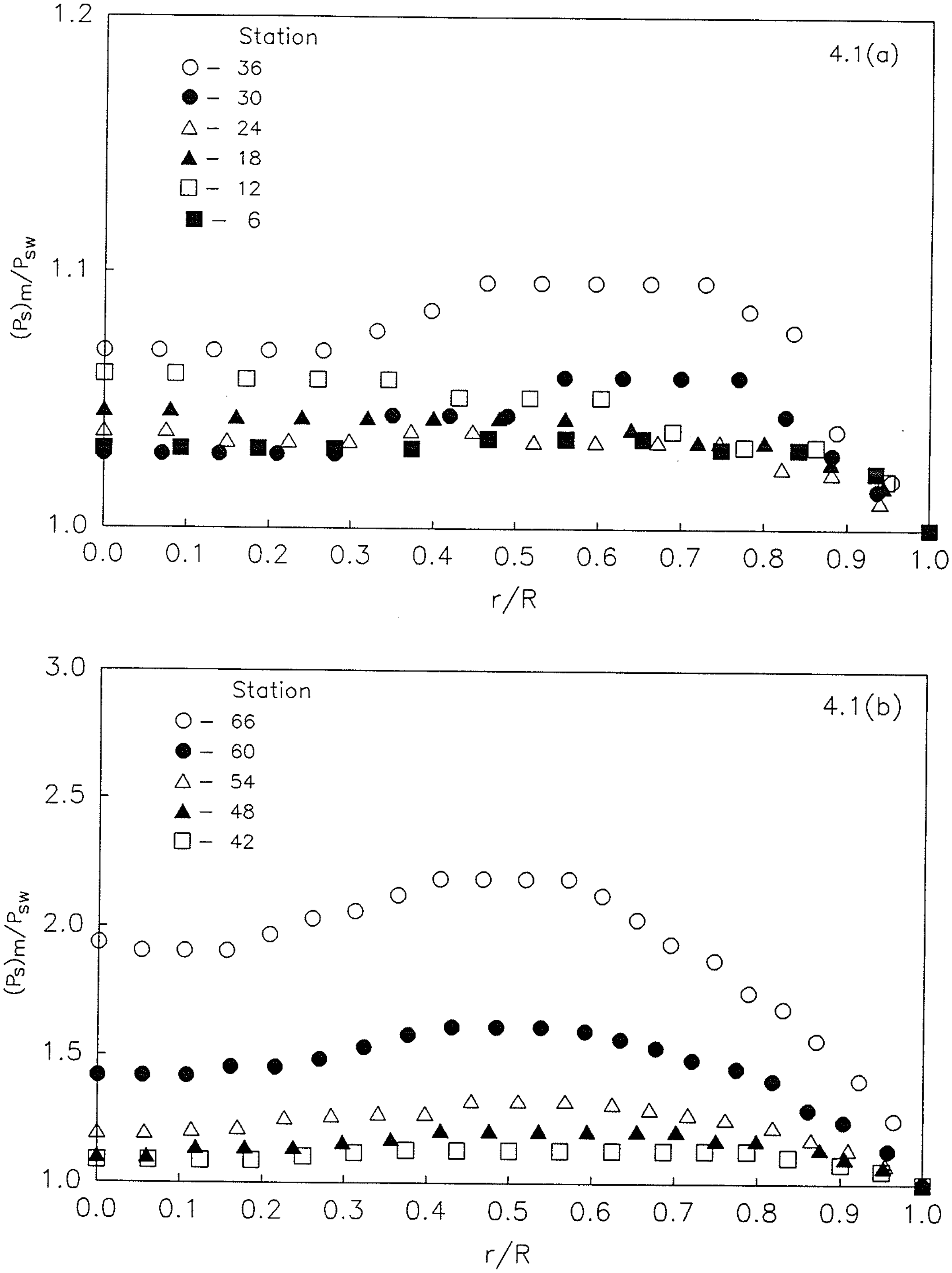

FIGURE 4.1: Variation of static pressures across the diffuser flow.
(a) Stations 6–36 (b) Stations 42–66

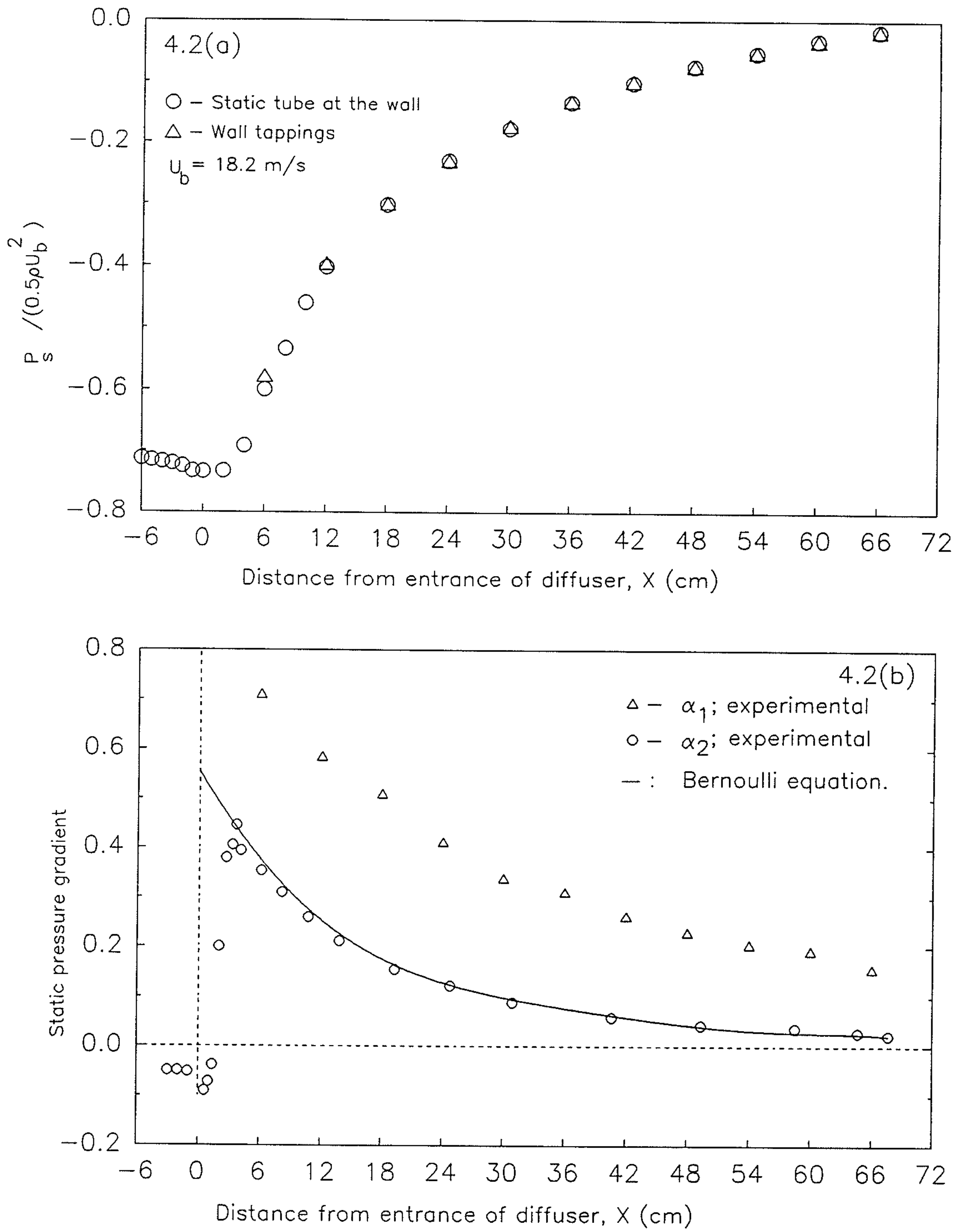

FIGURE 4.2: Wall static pressures in the diffuser flow.
(a) Axial variations (b) Static pressure gradients

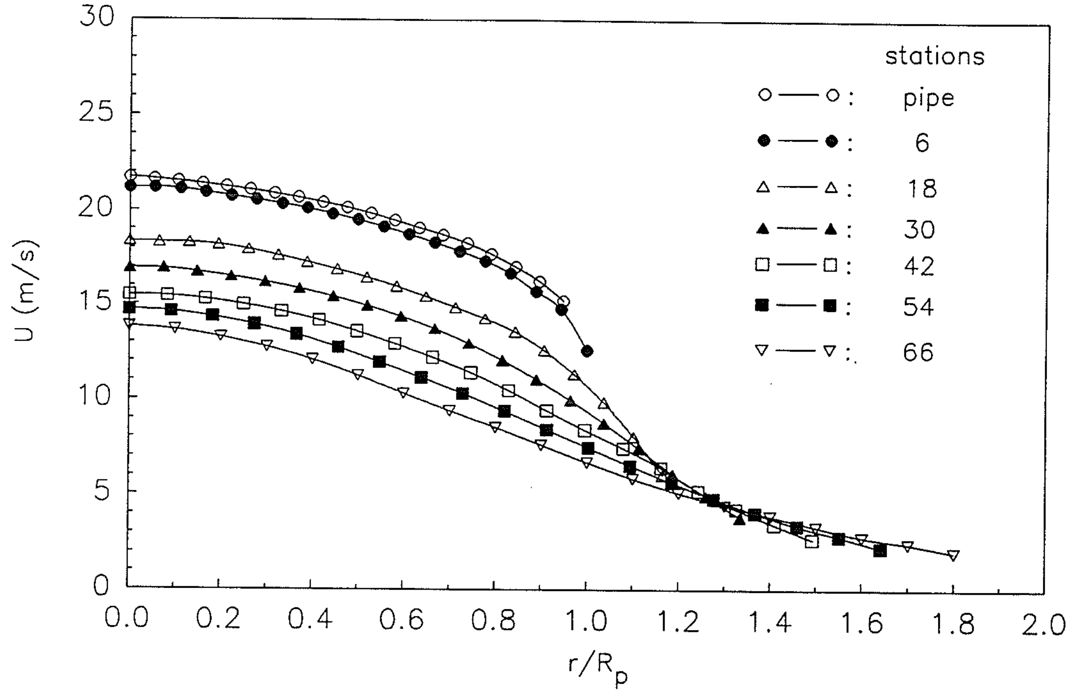

FIGURE 4.3: Mean velocity profiles in the pipe and diffuser flows.
(obtained from hot–wire measurements)

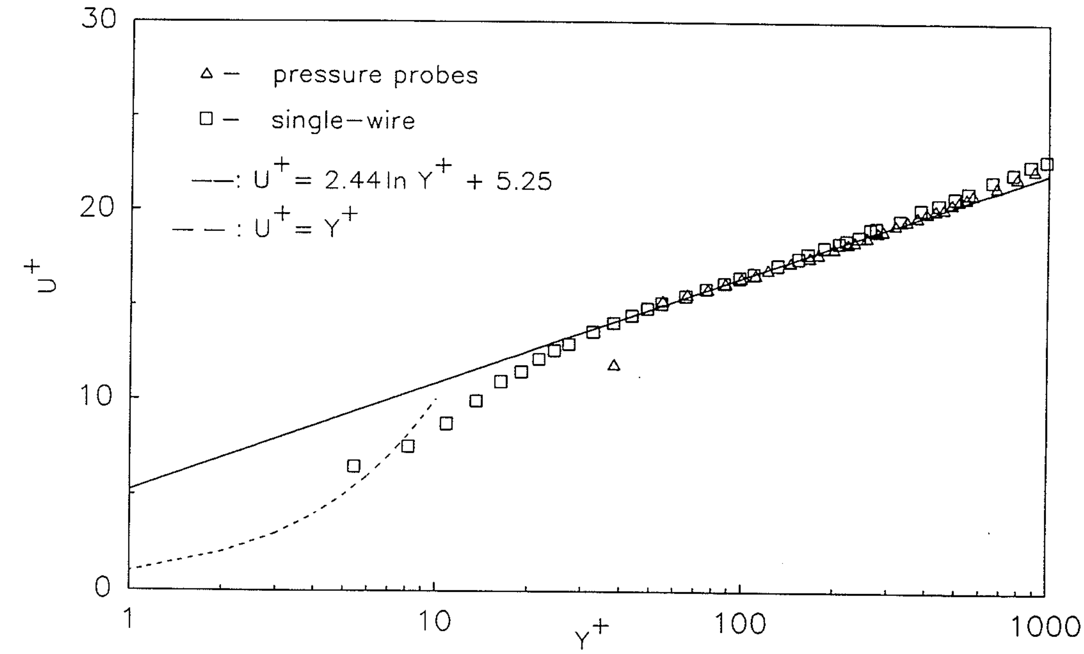

FIGURE 4..4: Log–Law plot in the fully developed pipe flow.

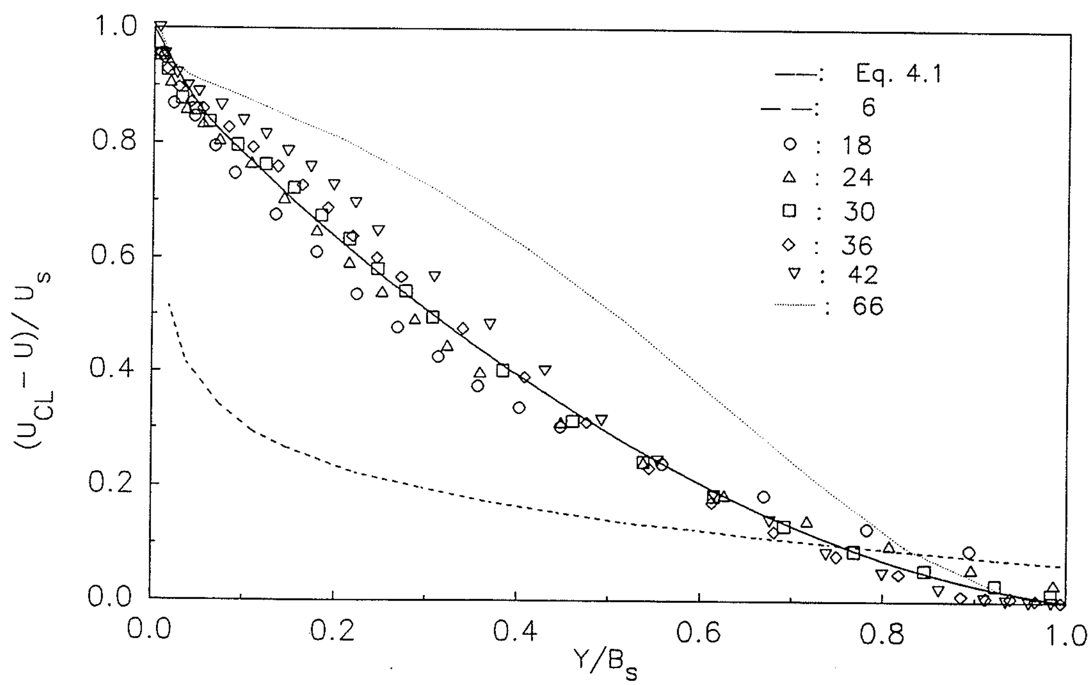

FIGURE 4.5: Comparison of mean velocity profiles at various stations of the diffuser with the universal velocity defect distribution.

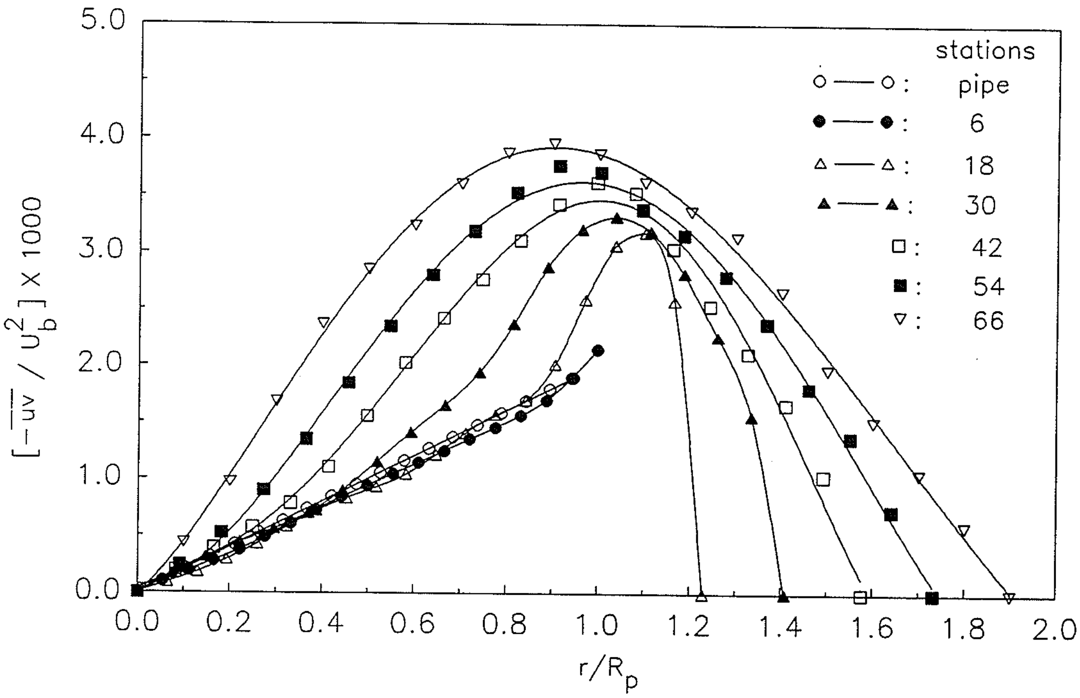

FIGURE 4.6: The profile of Reynolds shear stress in the pipe and diffuser flows.

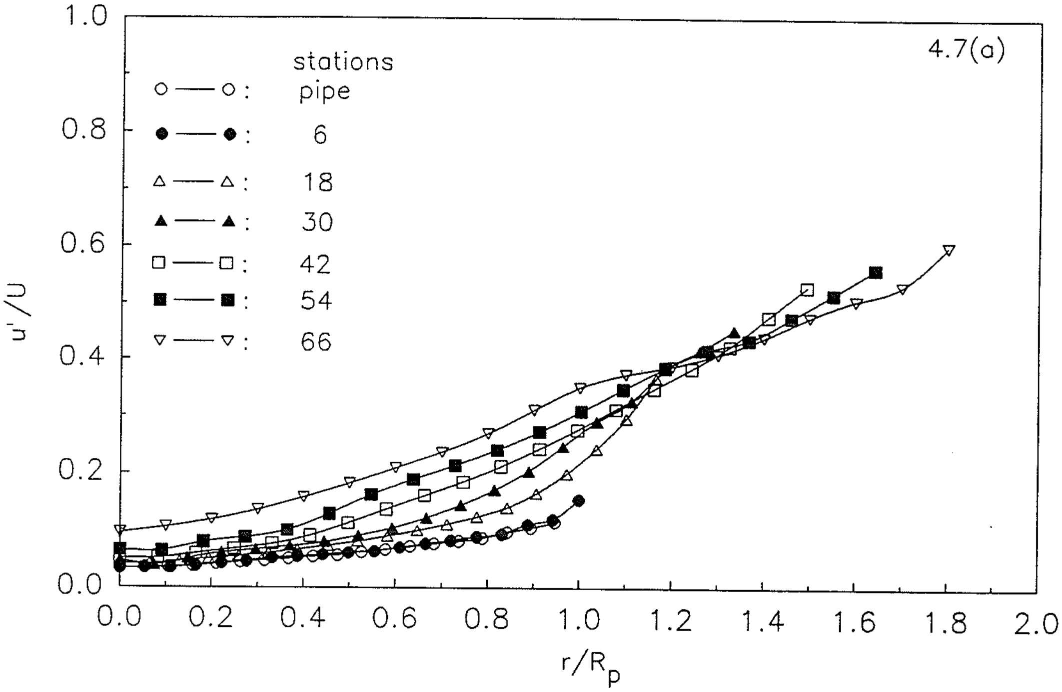
4.7(a)
stations
pipe
6
18
30
42
54
66
u'/U
r/Rp
1.0
0.8
0.6
0.4
0.2
0.0
0.0 0.2 0.4 0.6 0.8 1.0 1.2 1.4 1.6 1.8 2.0

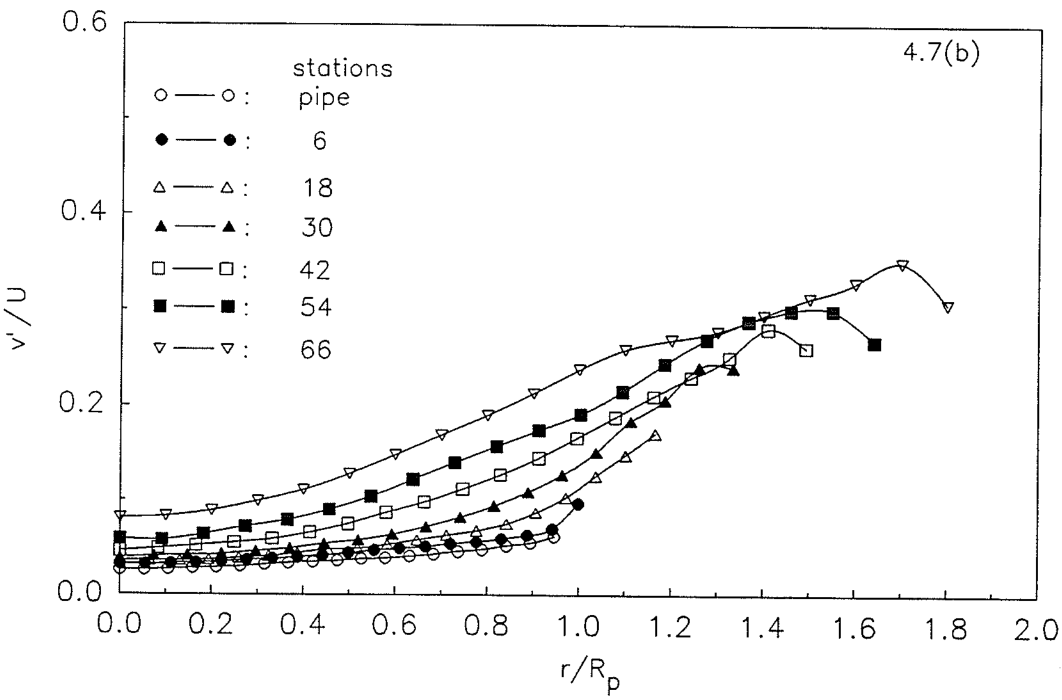
4.7(b)
stations
pipe
6
18
30
42
54
66
v'/U
r/Rp
0.6
0.4
0.2
0.0
0.0 0.2 0.4 0.6 0.8 1.0 1.2 1.4 1.6 1.8 2.0

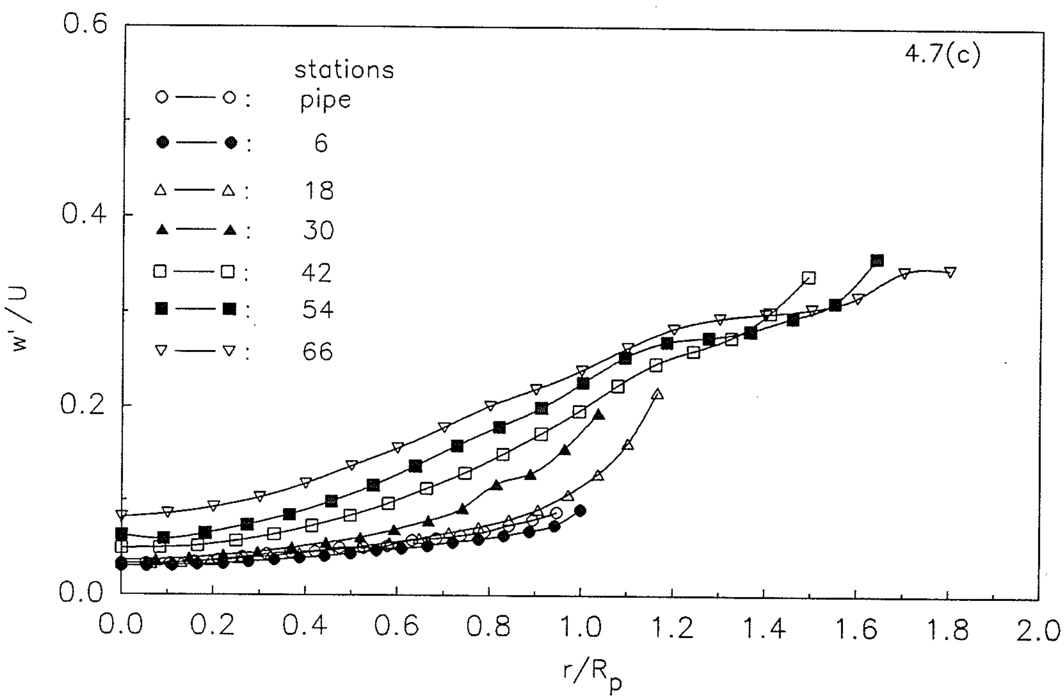

FIGURE 4.7: Local intensity of turbulence in the pipe and diffuser flows.
(a) u'/U (b) v'/U (c) w'/U

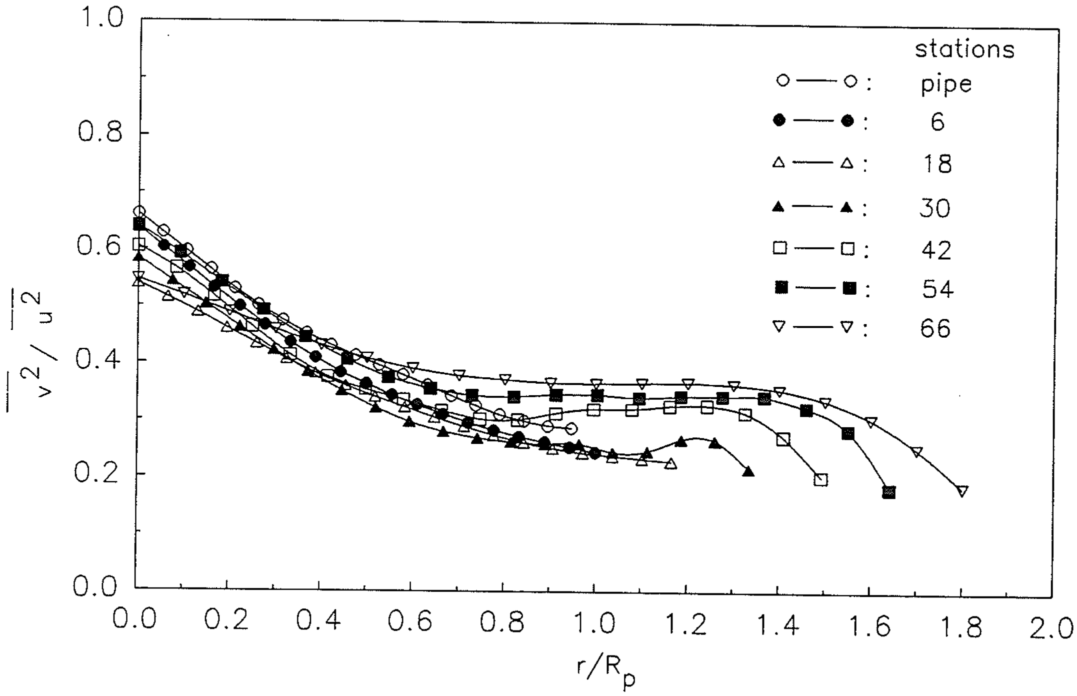

FIGURE 4.8: The ratio of transverse to longitudinal mean-square turbulence intensity in the pipe and diffuser flows.

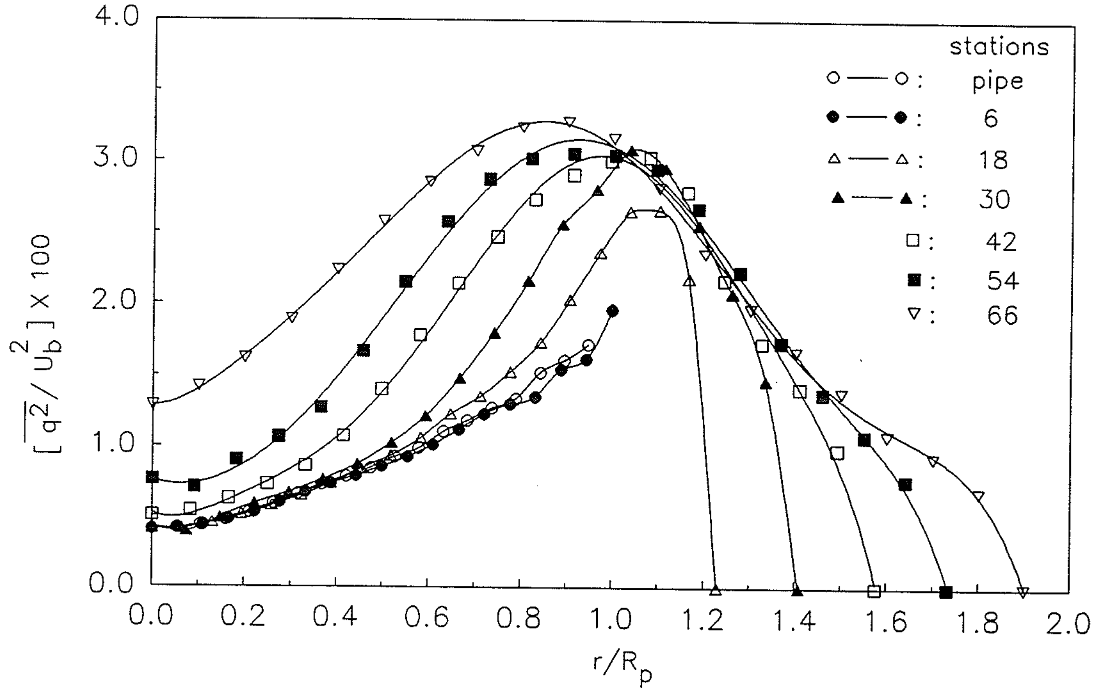

FIGURE 4.9: The profile of turbulence energy in the pipe and diffuser flows.

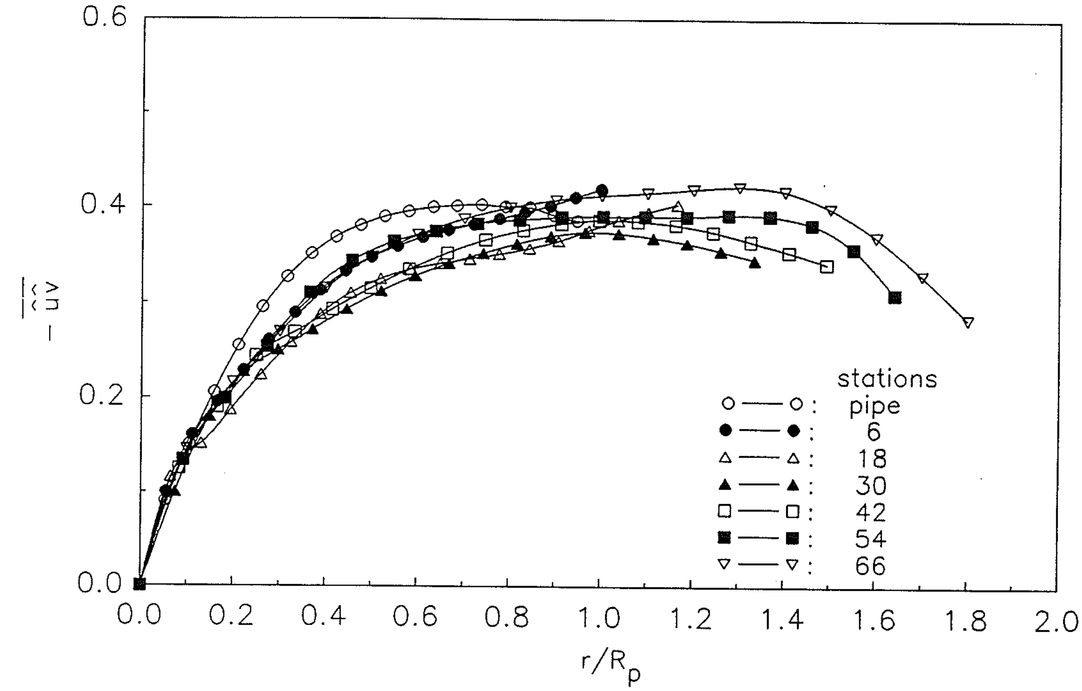

FIGURE 4.10: Correlation coefficient of Reynolds stress in the pipe and diffuser flows.

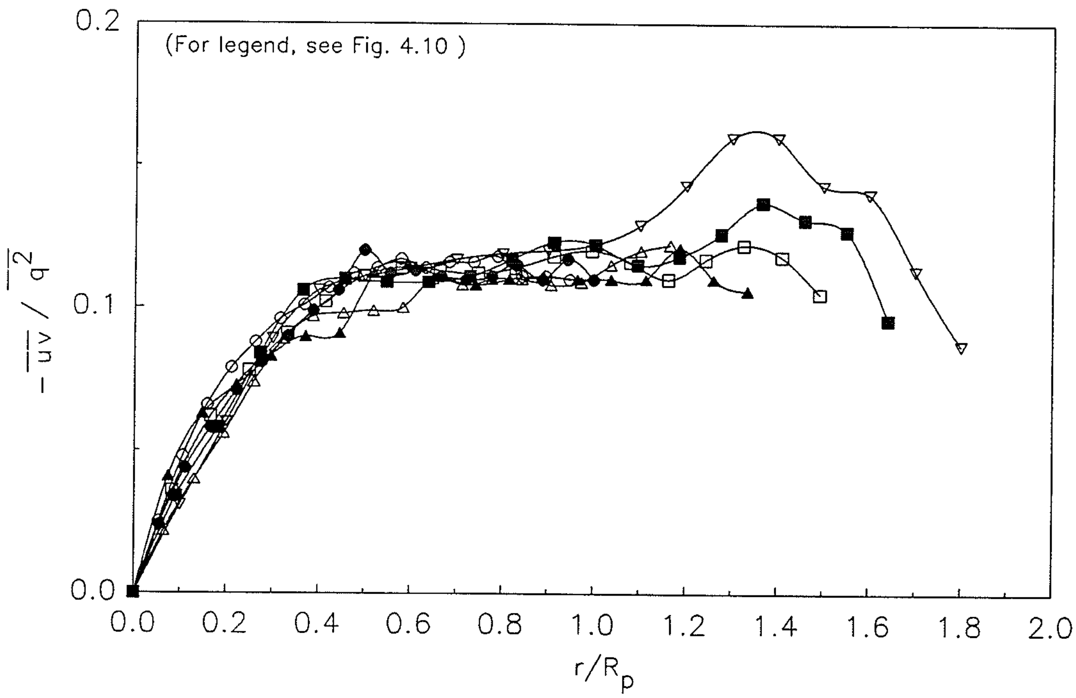

FIGURE 4.11: Variation of the stress coefficient in the pipe and diffuser flows.

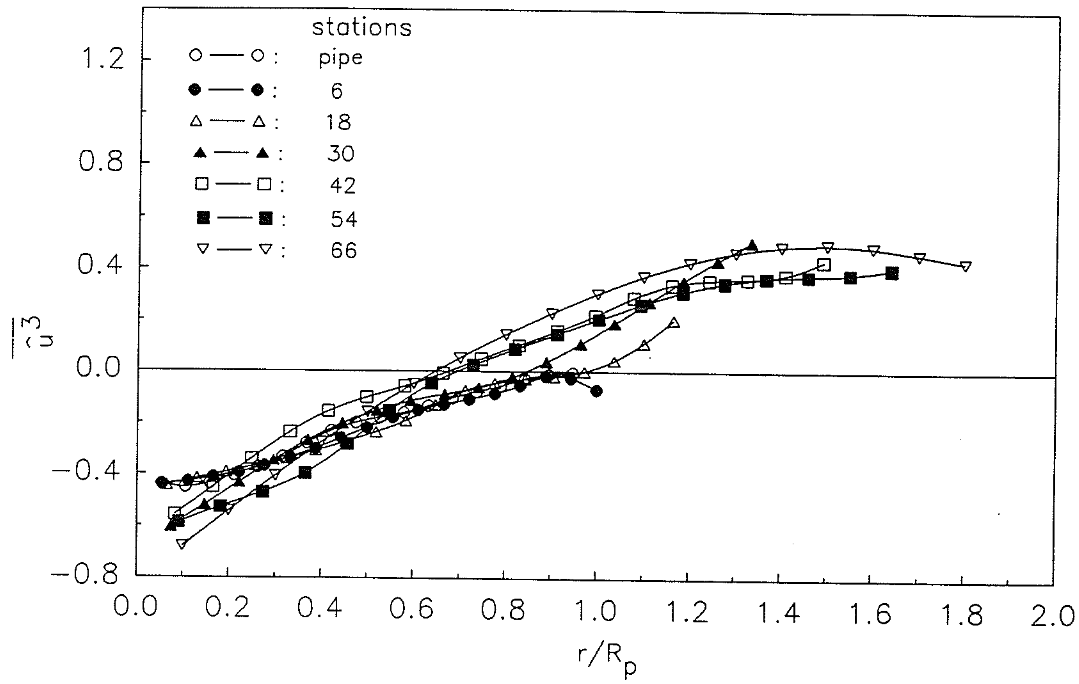

FIGURE 4.12: Skewness factor of u in the pipe and diffuser flows.

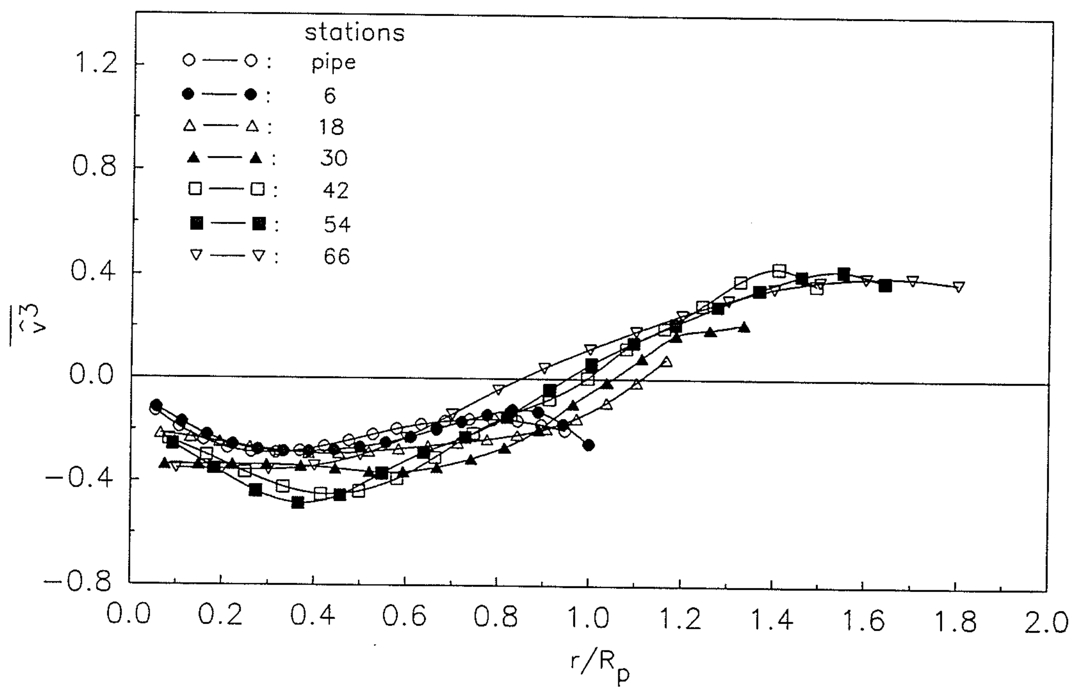

FIGURE 4.13: Skewness factor of v in the pipe and diffuser flows.

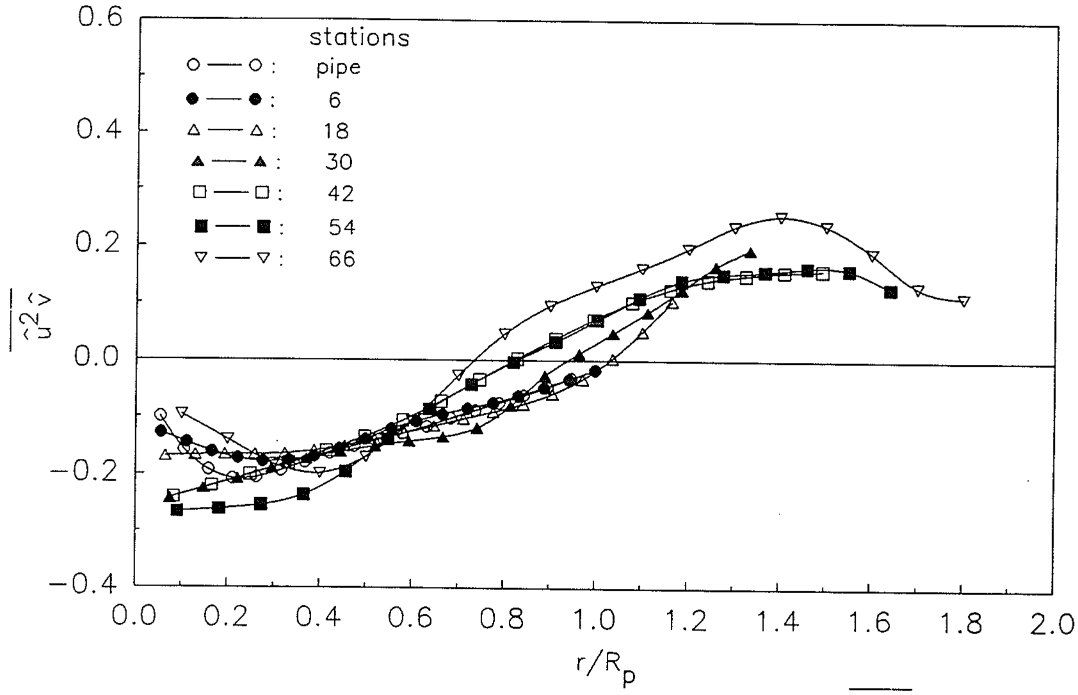

FIGURE 4.14: The distribution of third−order moments, $\overline{\hat{u}^2\hat{v}}$ in the pipe and diffuser flows.

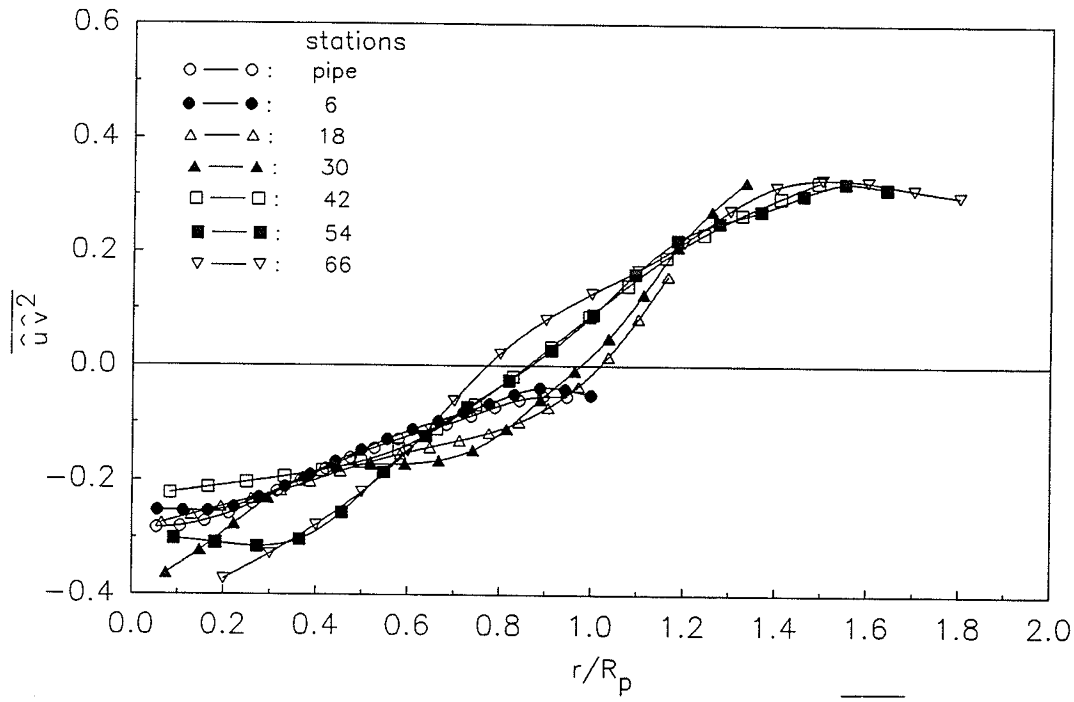

FIGURE 4.15: The distribution of third−order moments, $\overline{\hat{u}\hat{v}^2}$ in the pipe and diffuser flows.

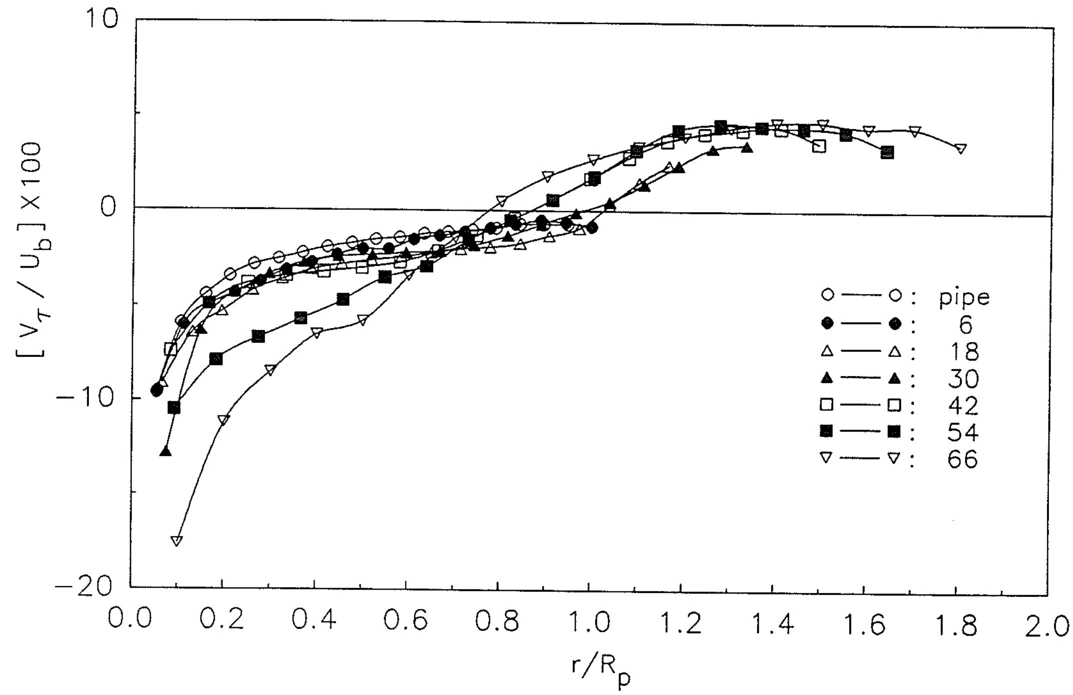

FIGURE 4.16: The profile of turbulent transport velocity, V_τ in the pipe and diffuser flows.

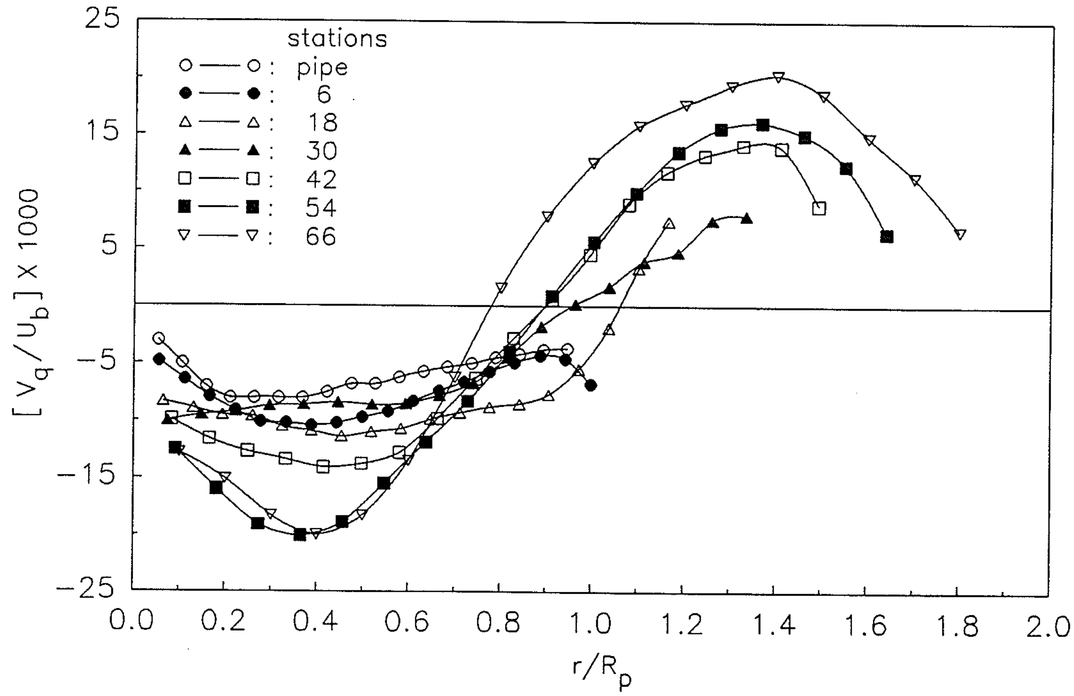

FIGURE 4.17: The profile of turbulent transport velocity, V_q in the pipe and diffuser flows.

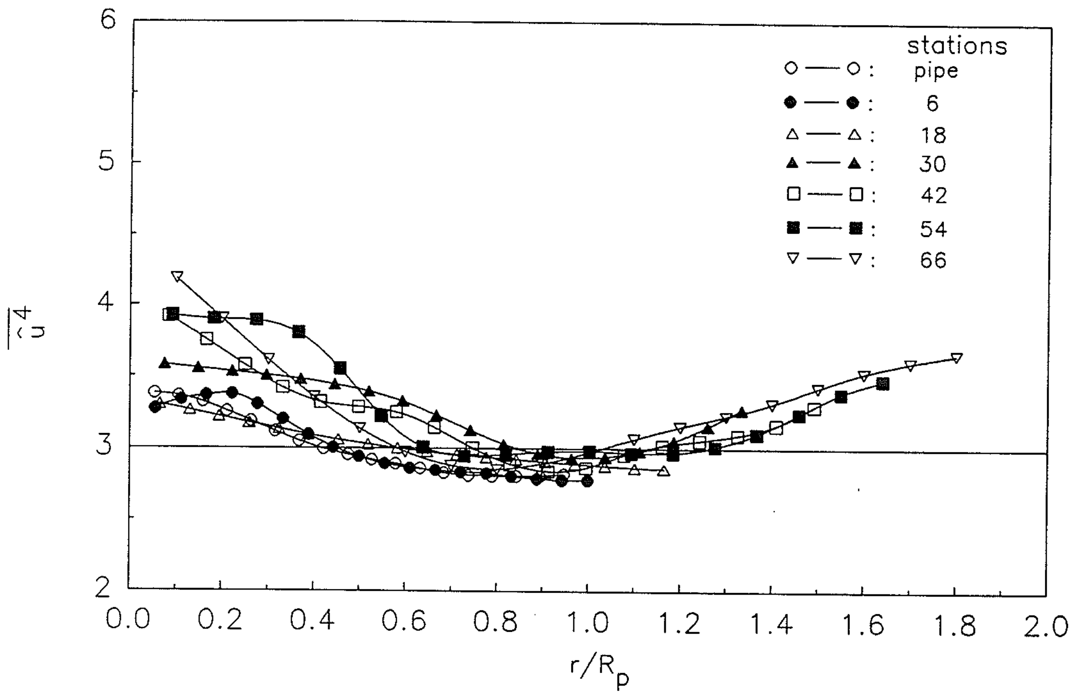

FIGURE 4.18: Flatness factor of u in the pipe and diffuser flows.

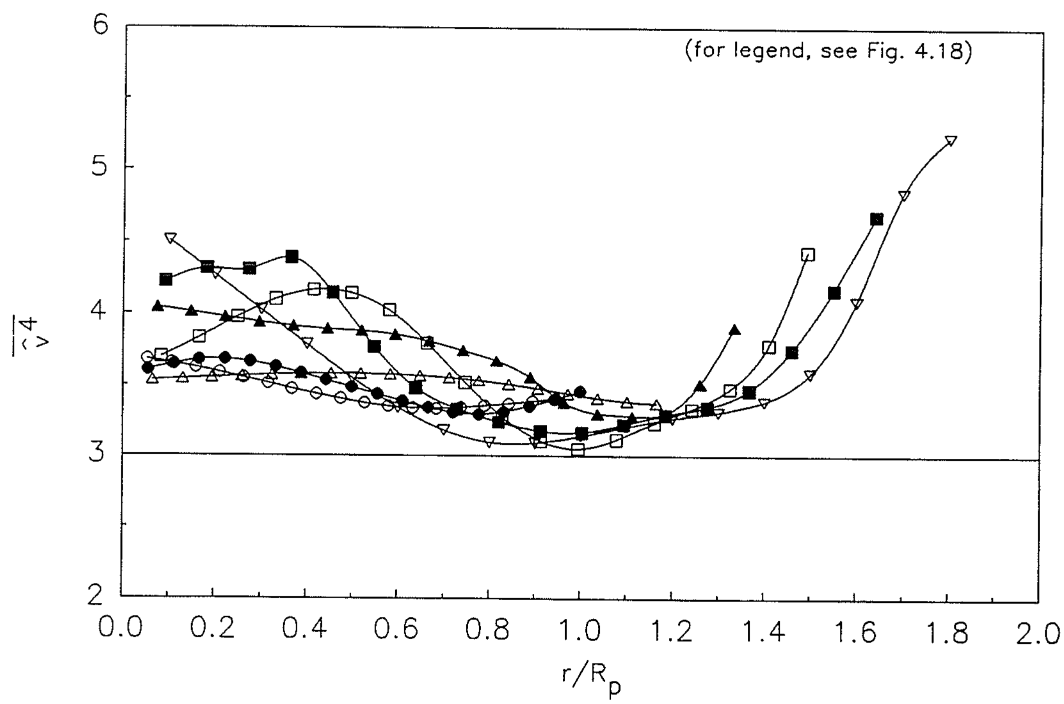

FIGURE 4.19: Flatness factor of v in the pipe and diffuser flows.

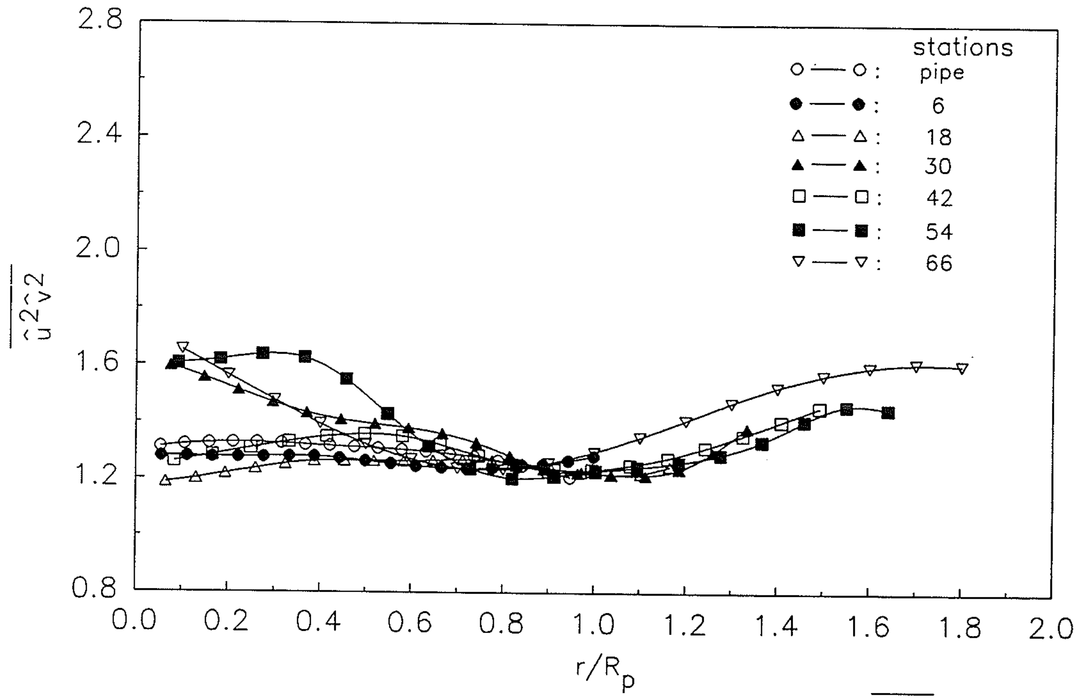

FIGURE 4.20: The distribution of fourth-order moments, $\overline{\hat{u}^2\hat{v}^2}$ in the pipe and diffuser flows.

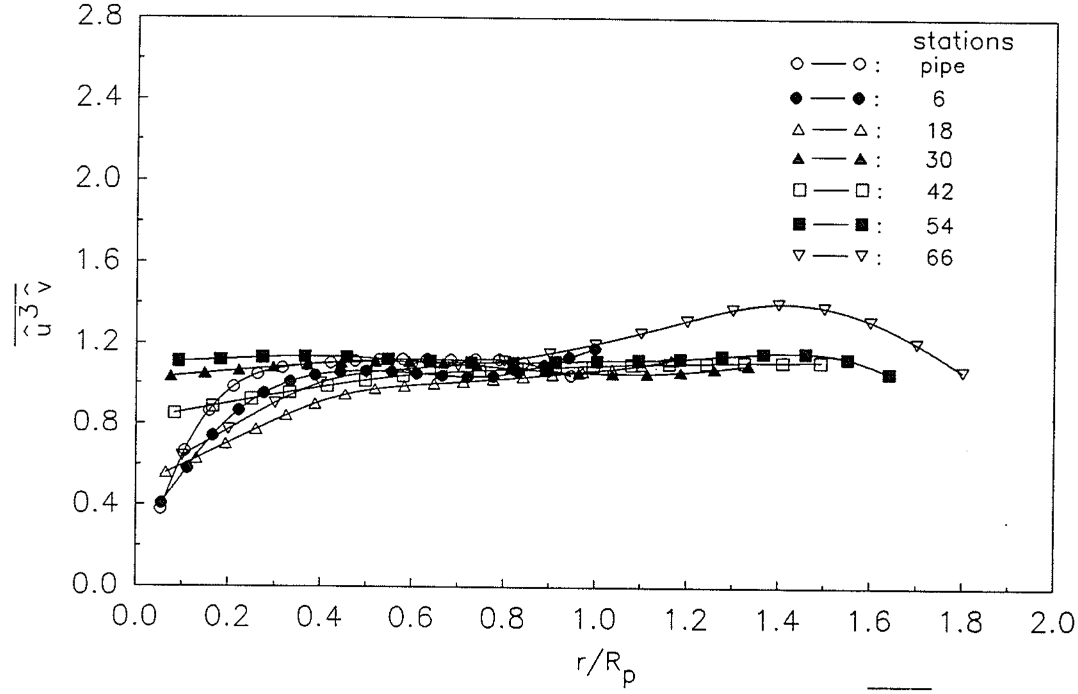

FIGURE 4.21: The distribution of fourth–order moments, $\overline{\hat{u}^3\hat{v}}$ in the pipe and diffuser flows.

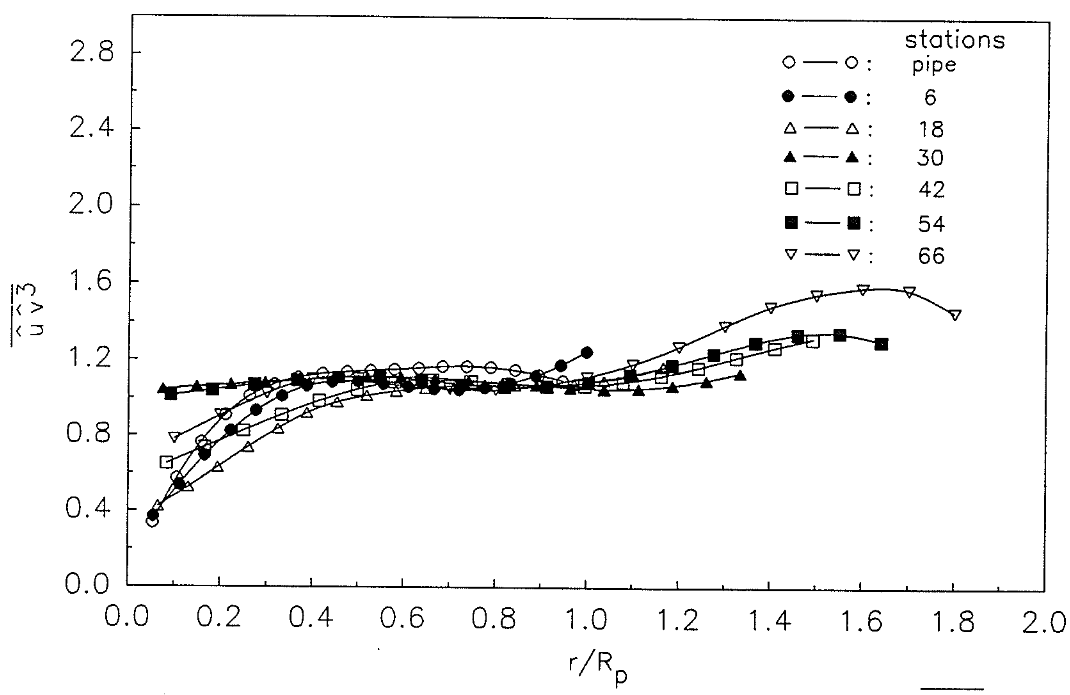

FIGURE 4.22: The distribution of the fourth–order moments, $\overline{\hat{u}\hat{v}^3}$ in the pipe and diffuser flows.

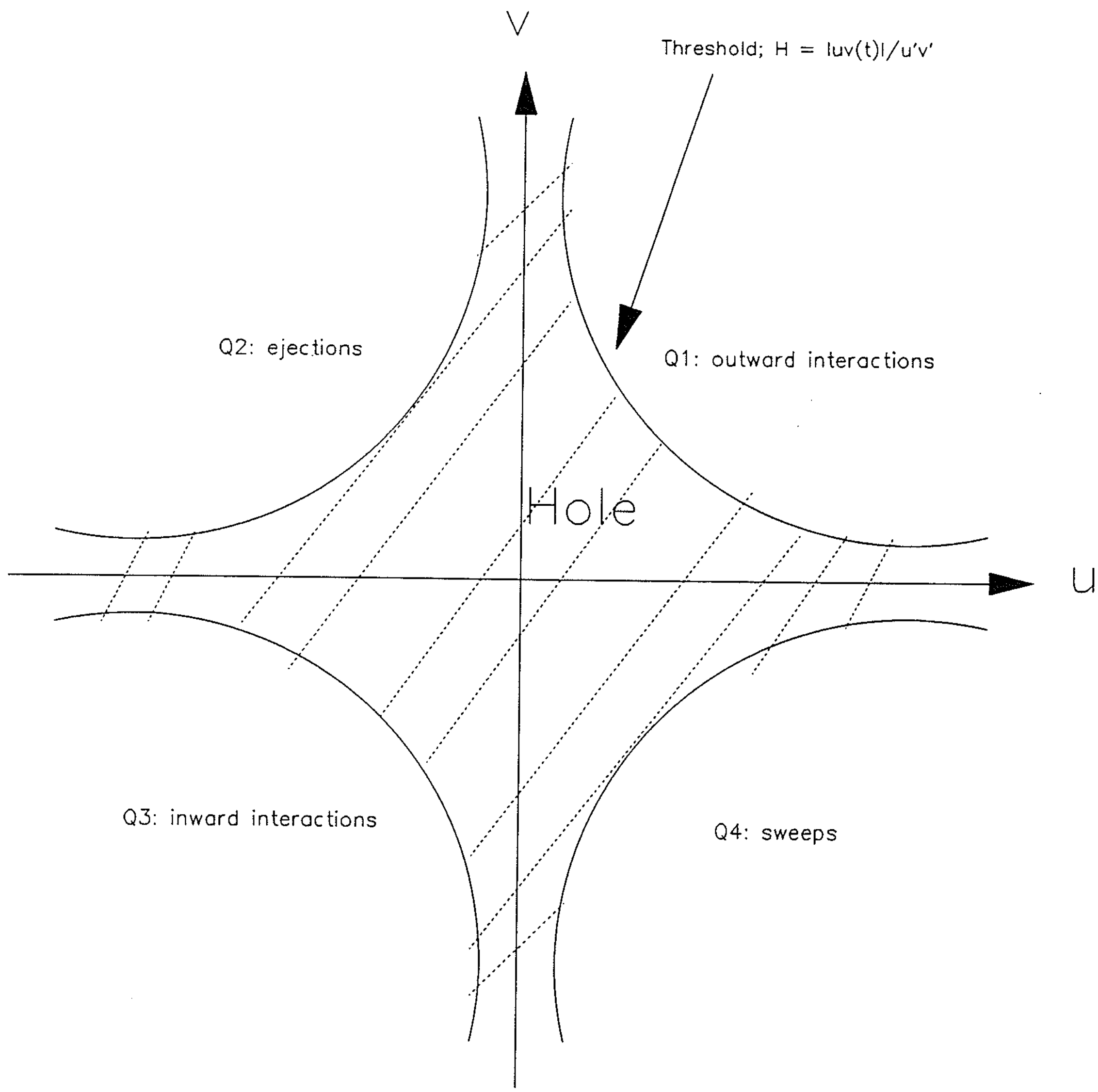

FIGURE 5.1: Classification of coherent motions in the (u,v)–plane.

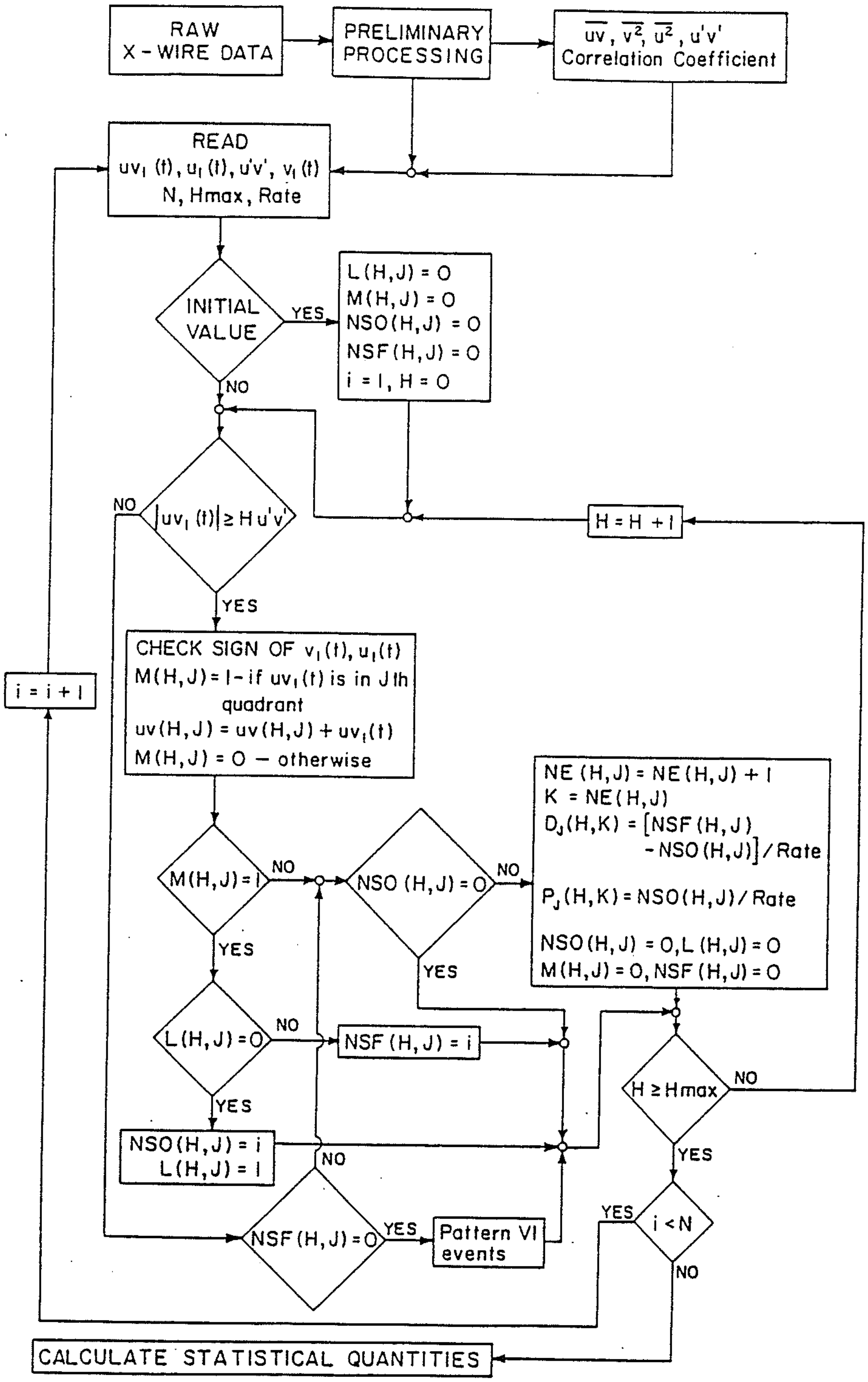

FIGURE 5.2: Flow chart for pattern recognition and DCARS.

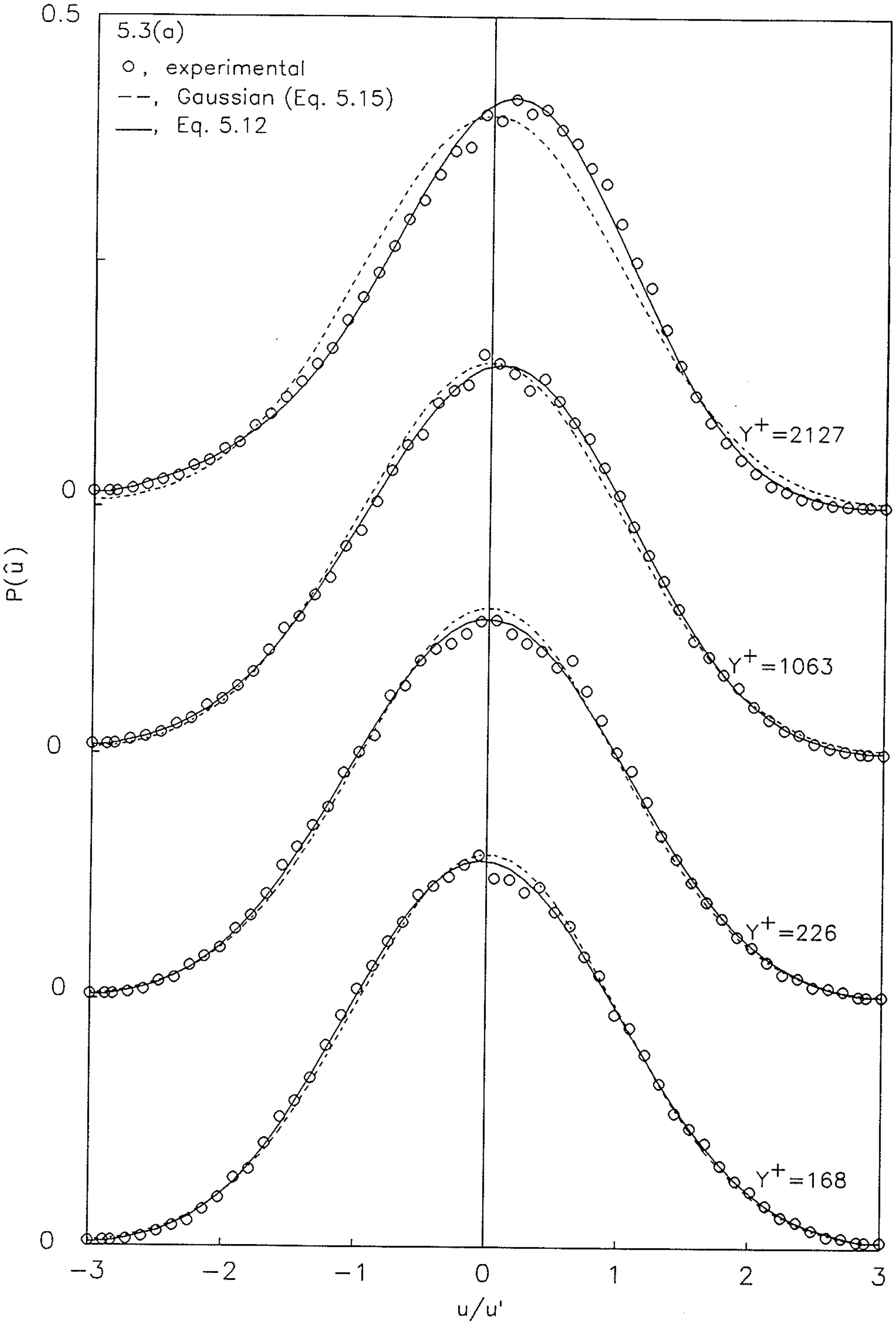

5.3(a)
o, experimental
− −, Gaussian (Eq. 5.15)
——, Eq. 5.12
0.5
0
0
0
0
P(û)
Y+=2127
Y+=1063
Y+=226
Y+=168
−3
−2
−1
0
1
2
3
u/u'

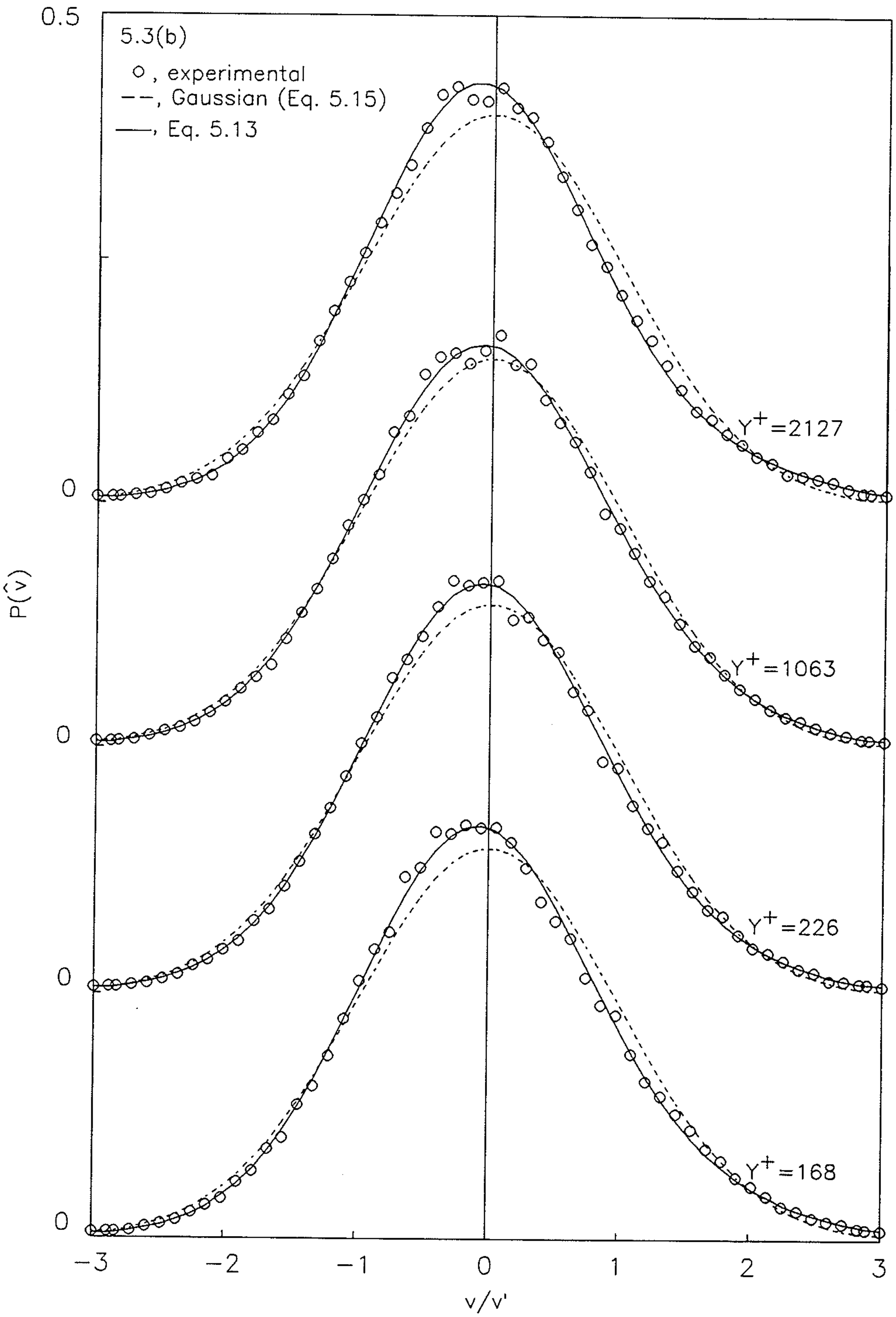

FIGURE 5.3: Probability density distribution of velocity in pipe flow.
(a) P(û) (b) P(v̂).

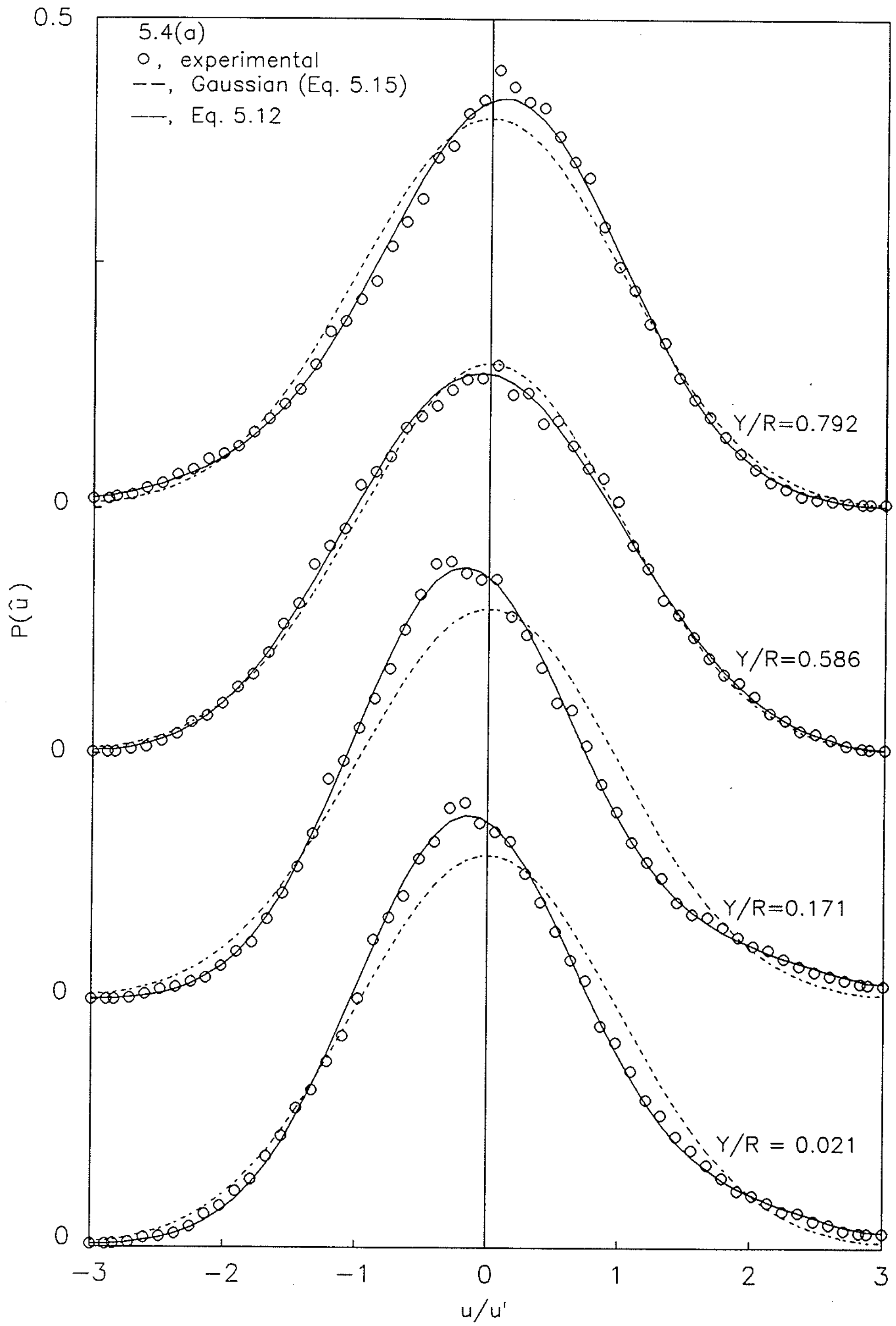
0.5
5.4(a)
o, experimental
--, Gaussian (Eq. 5.15)
—, Eq. 5.12
Y/R=0.792
Y/R=0.586
Y/R=0.171
Y/R = 0.021
0
0
0
0
P(û)
−3
−2
−1
0
1
2
3
u/u'

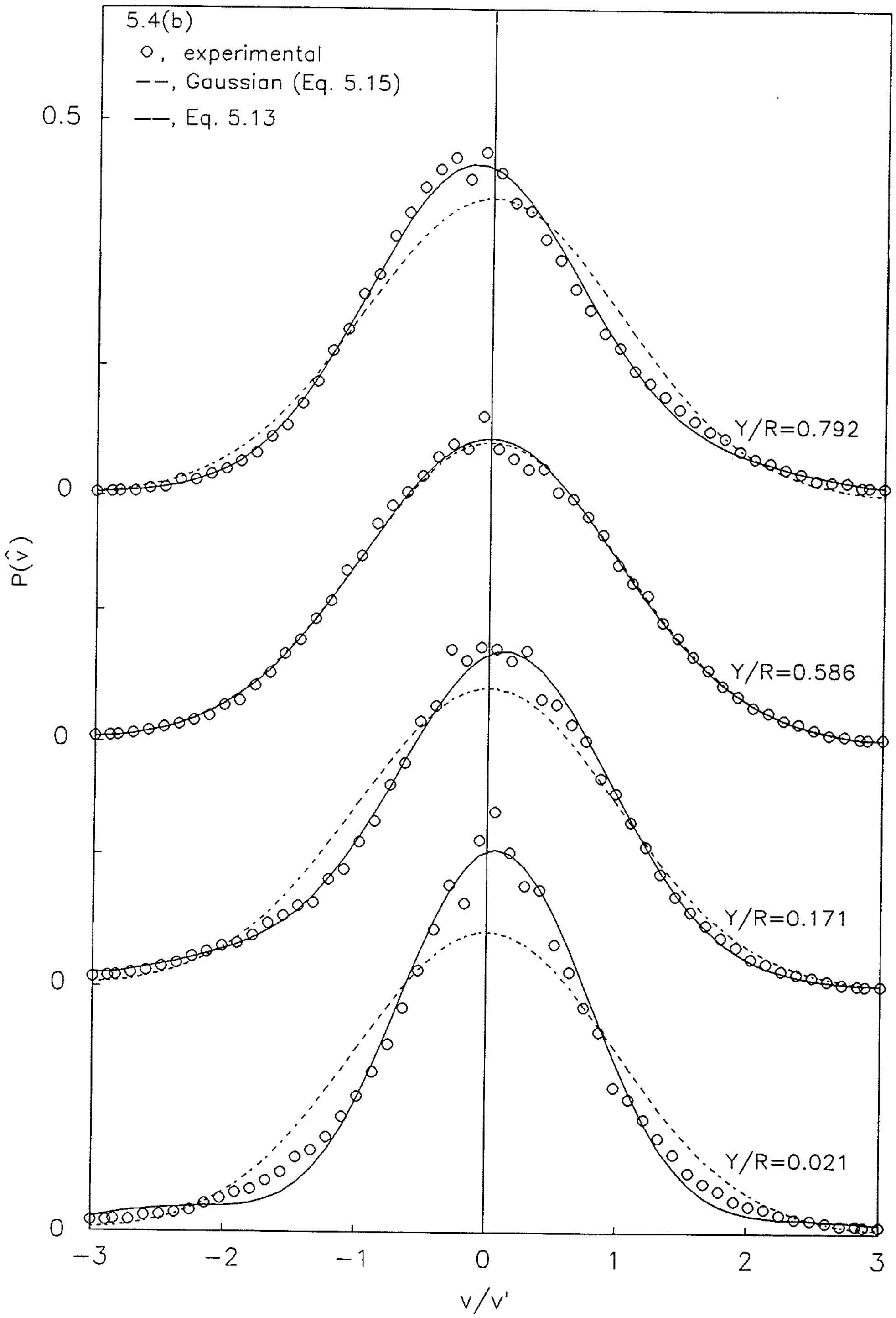

FIGURE 5..4 Probability density distributions of velocity at station 66.

(a) P($\hat{u}$) (b) P($\hat{v}$)

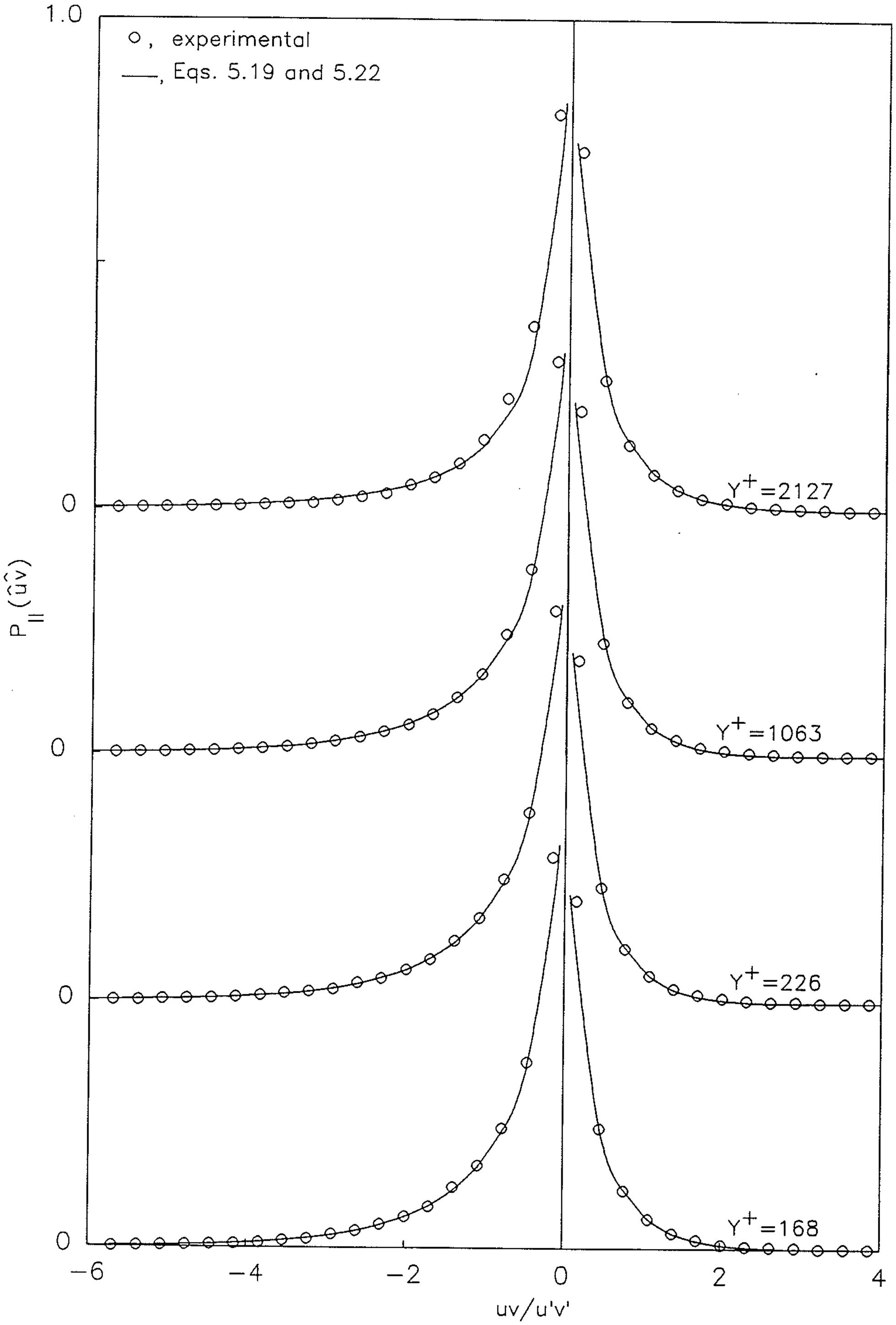

FIGURE 5.5: Probability density distributions of second-order moments in pipe flow.

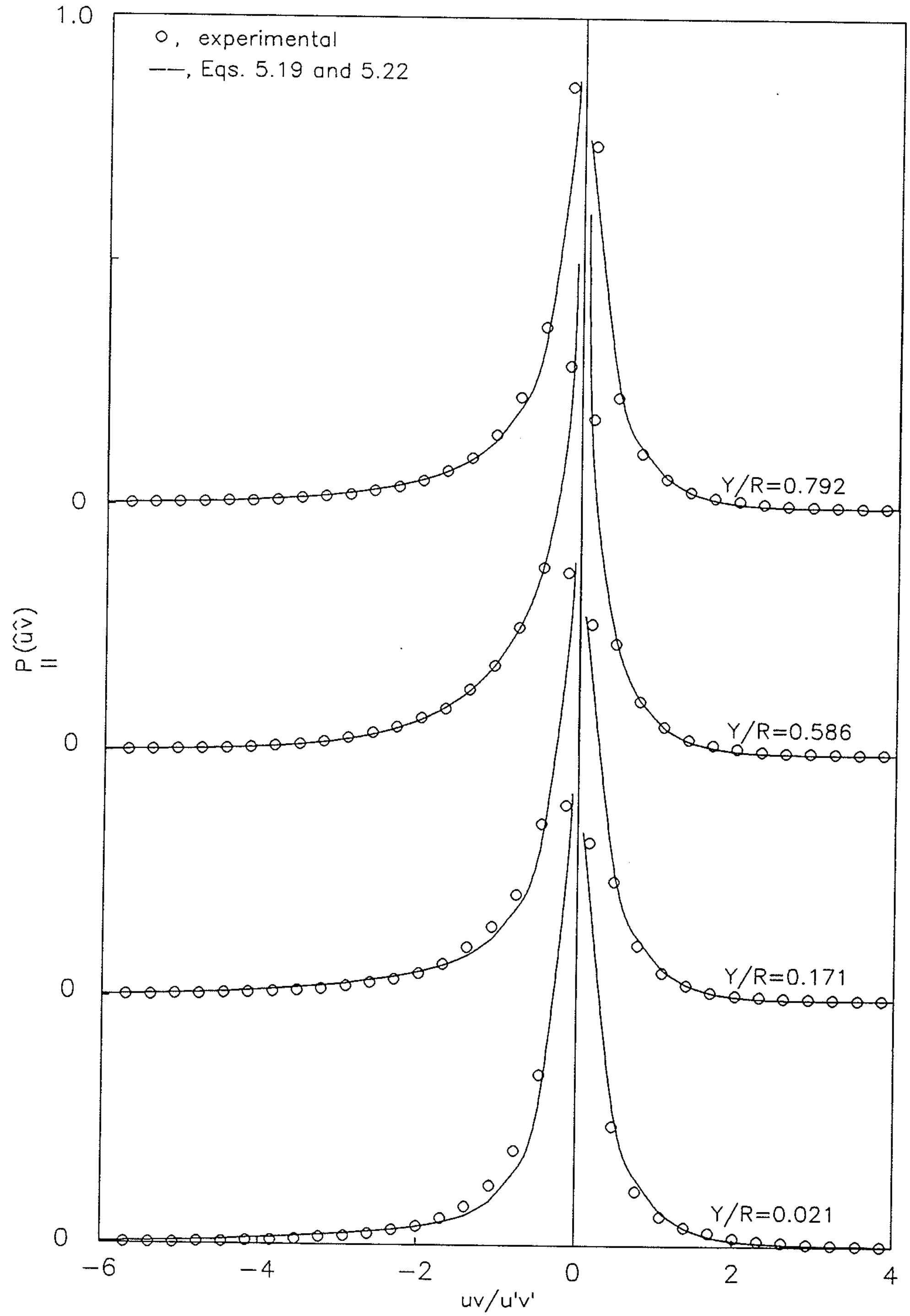

FIGURE 5.6: Probability density distributions of second−order moments at Station 66.

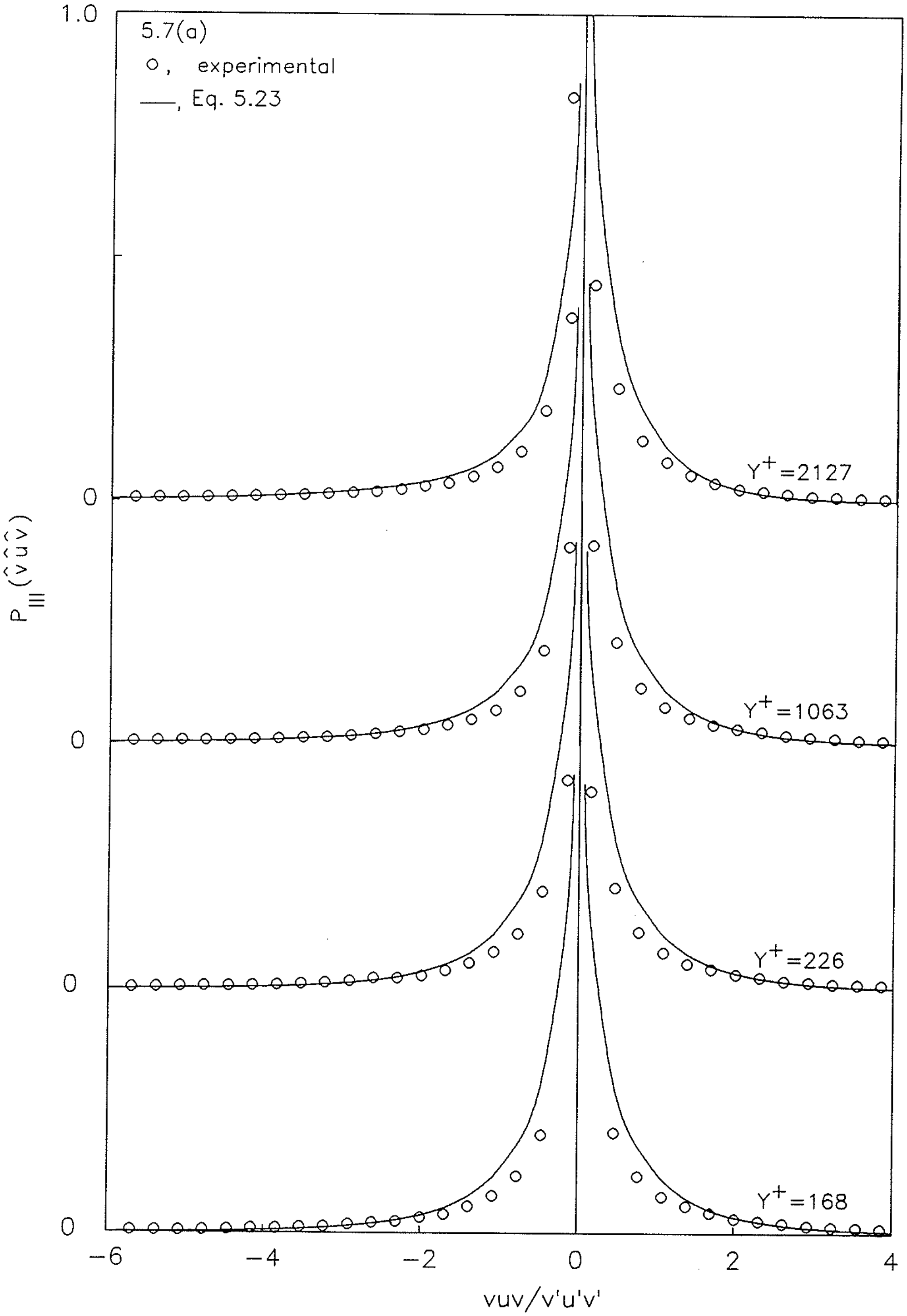
5.7(a)
o, experimental
—, Eq. 5.23
1.0
0
0
0
0
$Y^+=2127$
$Y^+=1063$
$Y^+=226$
$Y^+=168$
$P_{III}(\hat{v}\hat{u}\hat{v})$
−6
−4
−2
0
2
4
vuv/v'u'v'

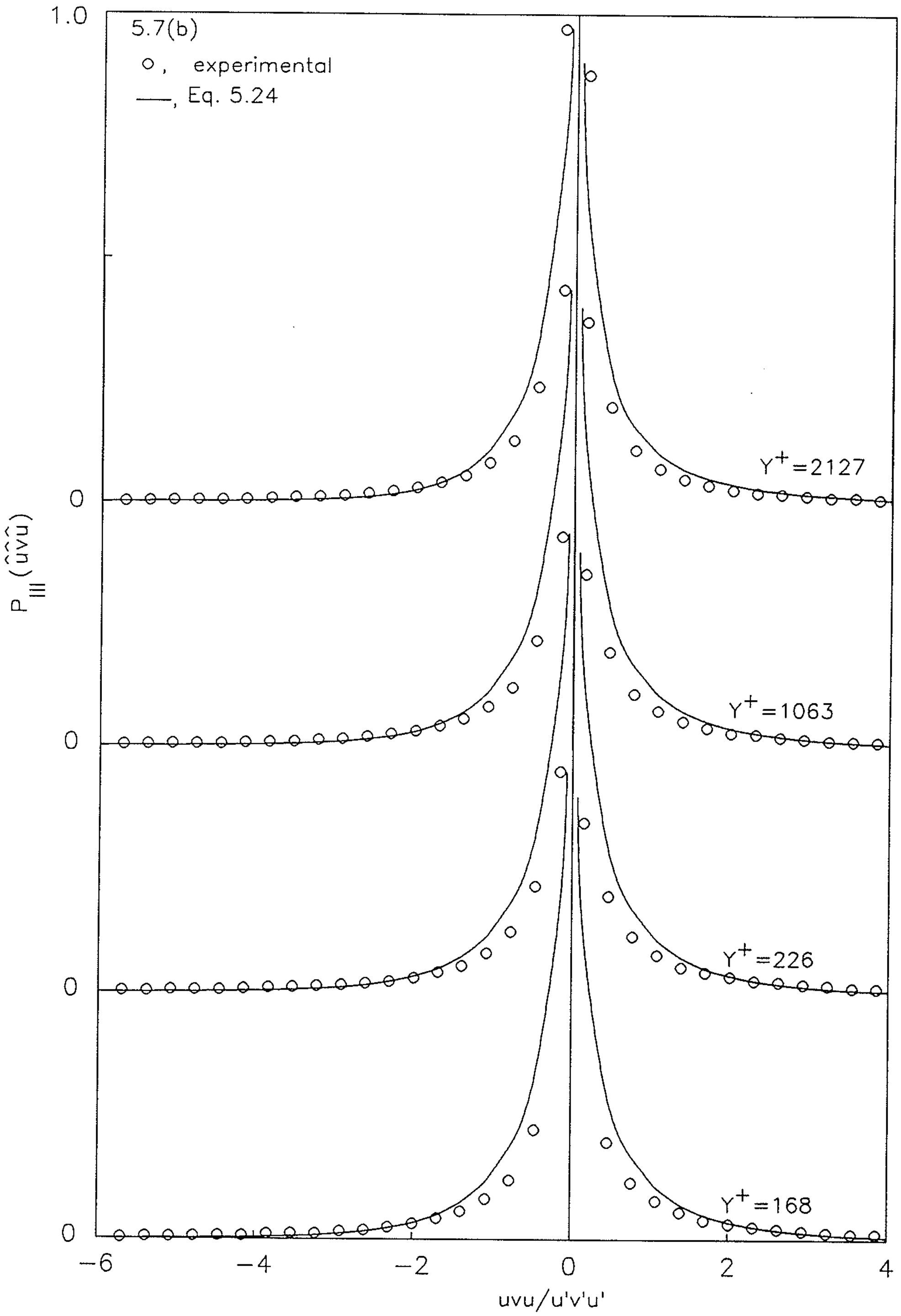

FIGURE 5.7: Probability density distributions of third-order moments in pipe flow. (a) $P_{III}(\hat{v}\hat{u}\hat{v})$ (b) $P_{III}(\hat{u}\hat{v}\hat{u})$

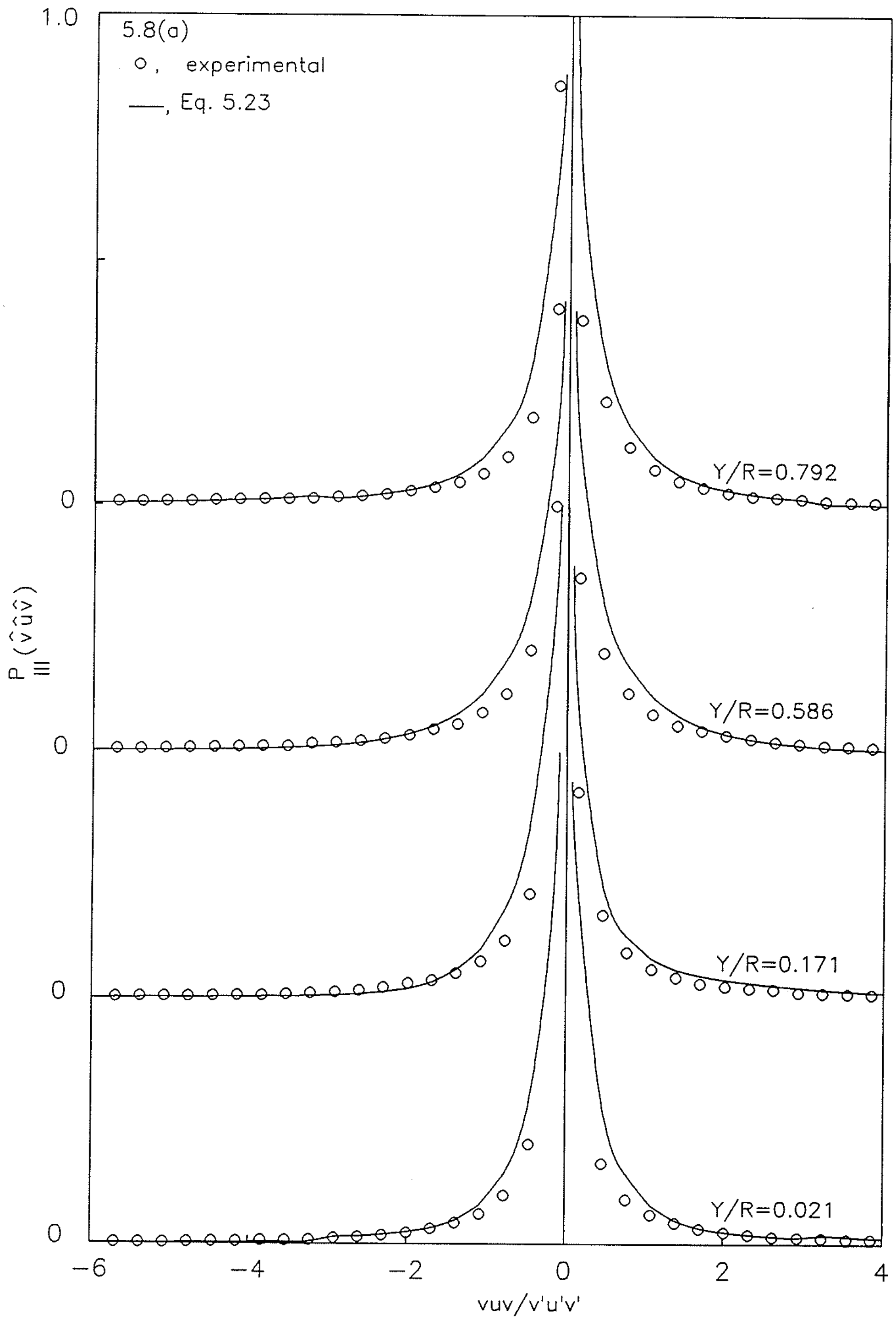
1.0
5.8(a)
o, experimental
——, Eq. 5.23
Y/R=0.792
Y/R=0.586
Y/R=0.171
Y/R=0.021
0
0
0
0
P_III (v̂ûv̂)
−6
−4
−2
0
2
4
vuv/v'u'v'

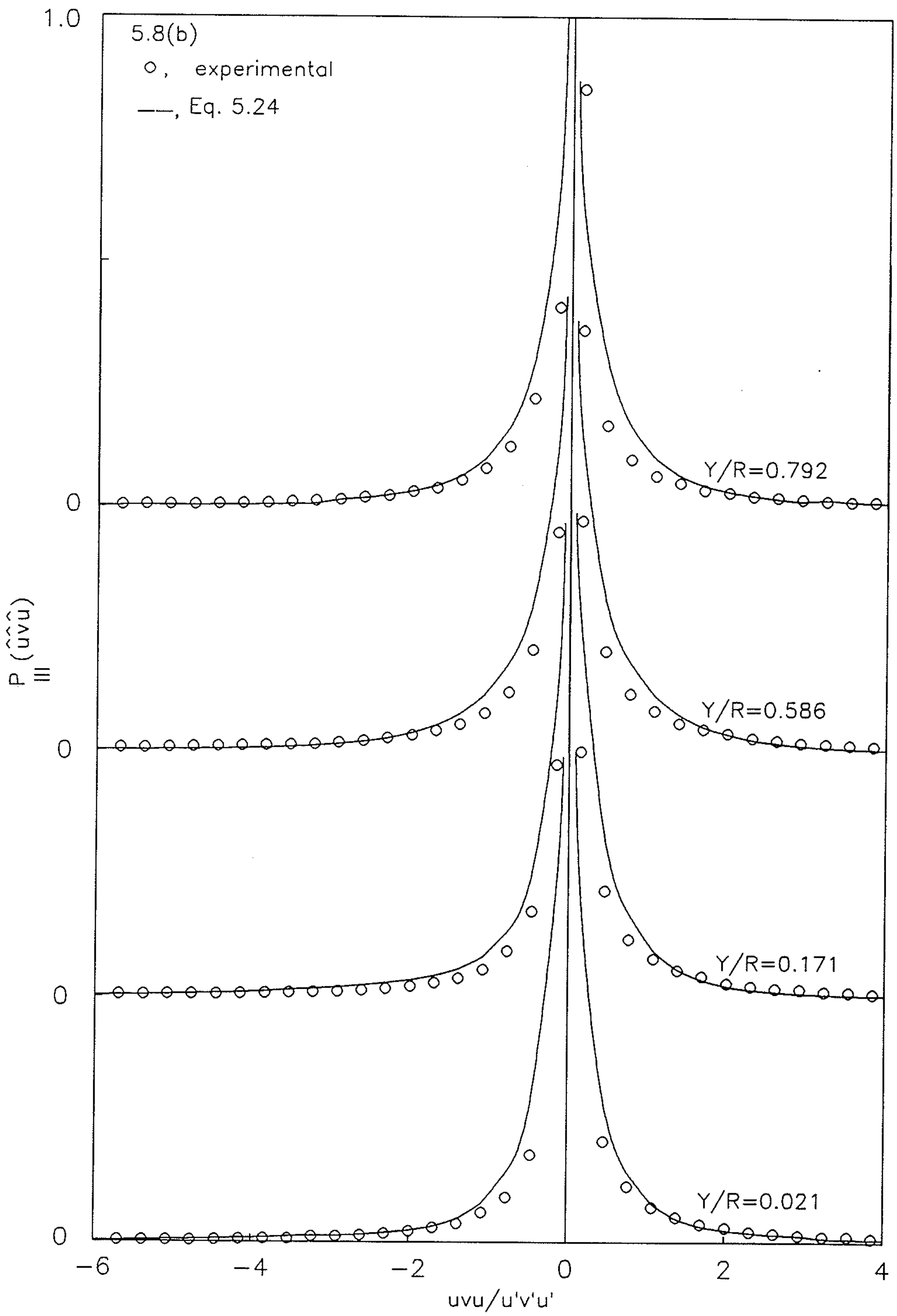

FIGURE 5.8: Probability density distributions of third-order moments at Station 66. (a) $P_{III}(\hat{v}\hat{u}\hat{v})$ (b) $P_{III}(\hat{u}\hat{v}\hat{u})$

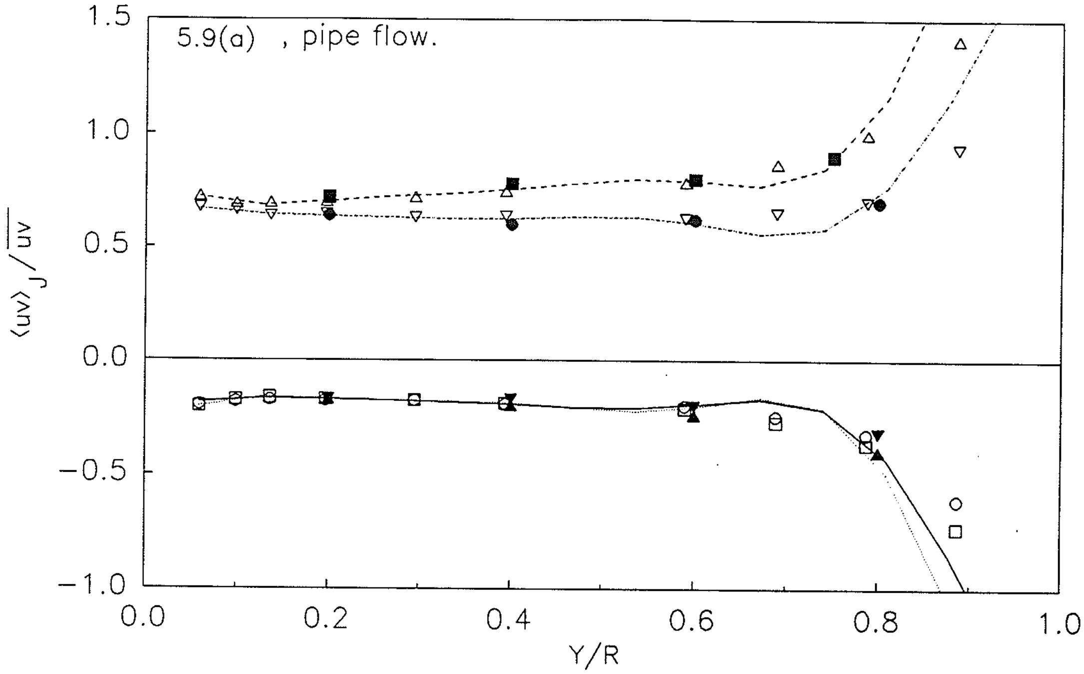

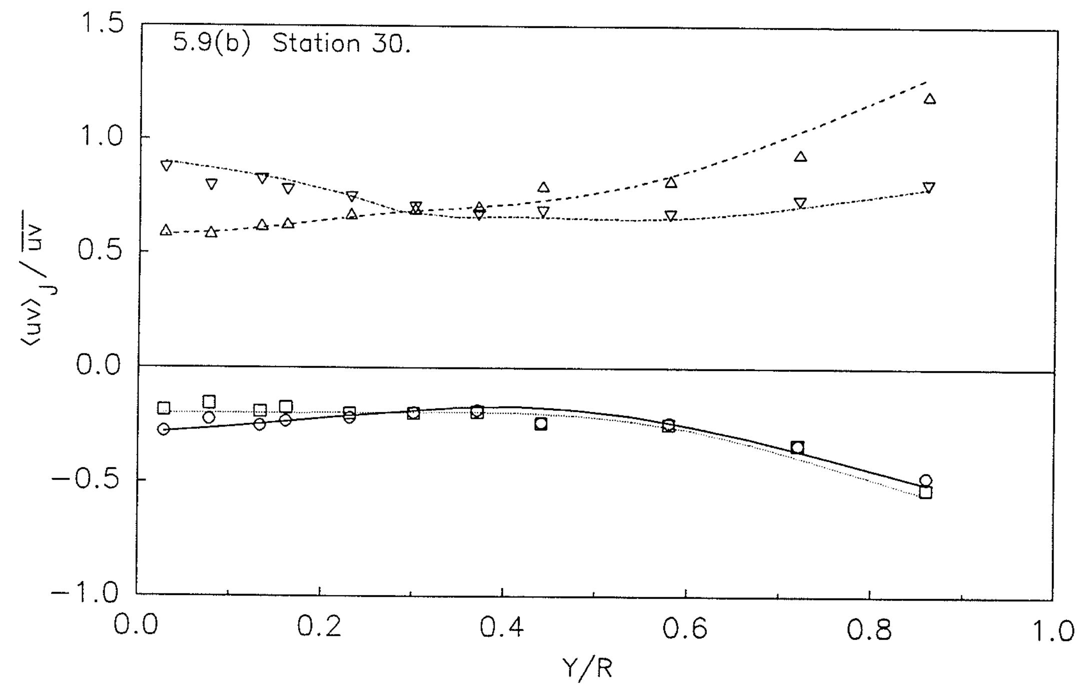

(For legend, see Fig. 5.9(c))

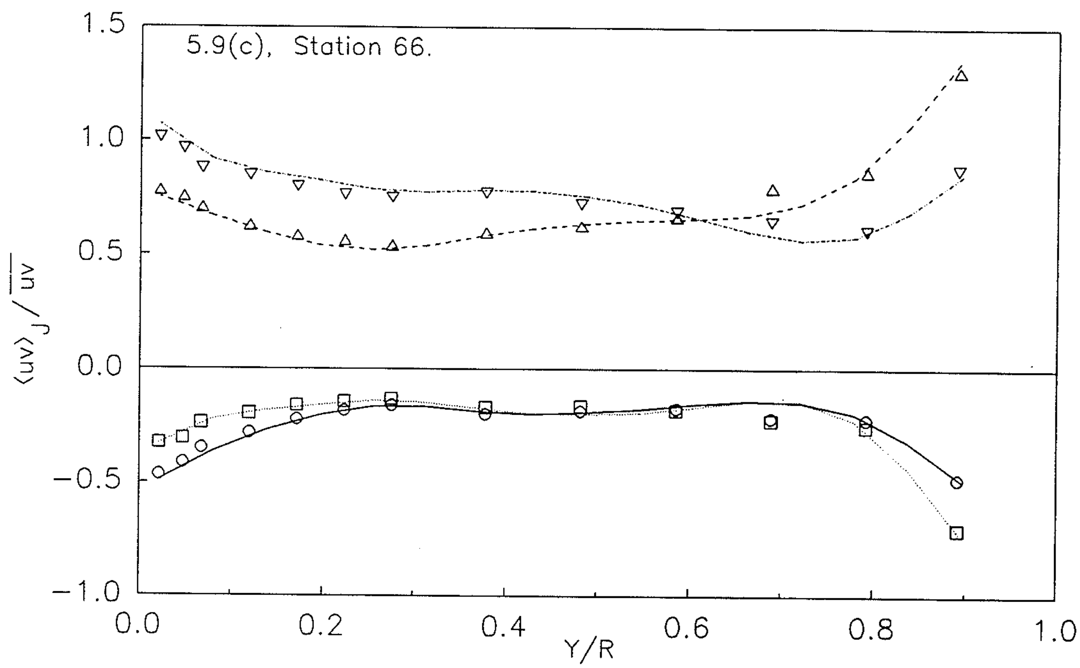

FIGURE 5.9: Fractional contributions of the different events to th averaged Reynolds stress with H=0. Experiments: ○ , J=1; △ , J=2; □ , J=3; ▽ , J=4; Equation 5.30: ——, J=1; — —, J=2; · · · · ·, J=3; — · · , J=4. Comte–Bellot et al. (1978) and Saleh (1978): ▼ , J=1; ■ , J=2; ▲ , J=3; ● , J=4.

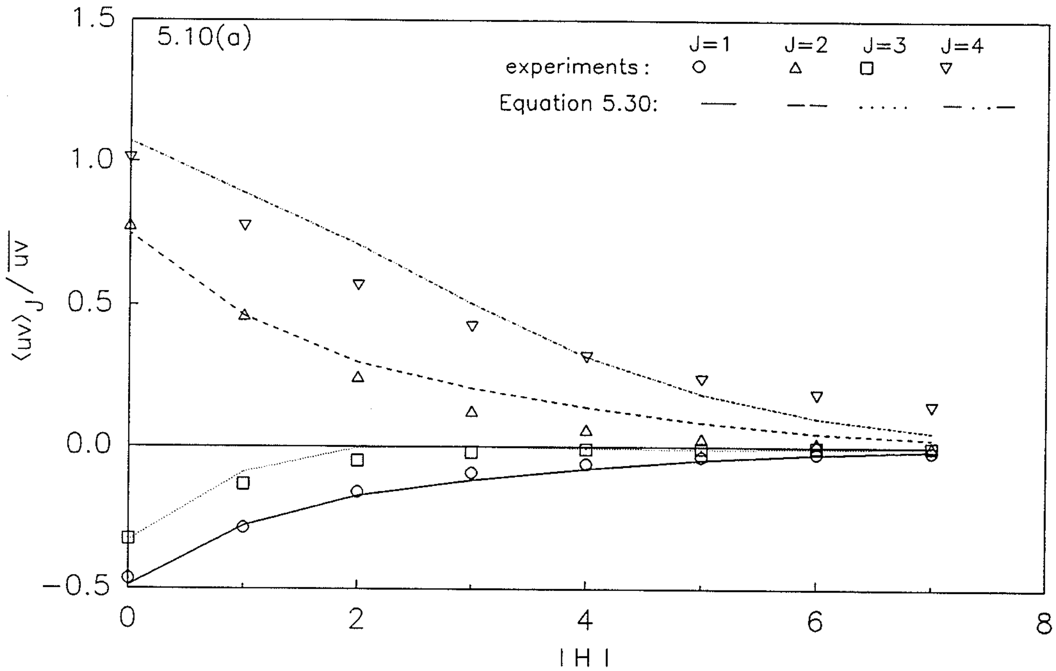
5.10(a)
J=1 J=2 J=3 J=4
experiments:
Equation 5.30:
1.5
1.0
0.5
0.0
−0.5
⟨uv⟩J / uv
0
2
4
6
8
|H|

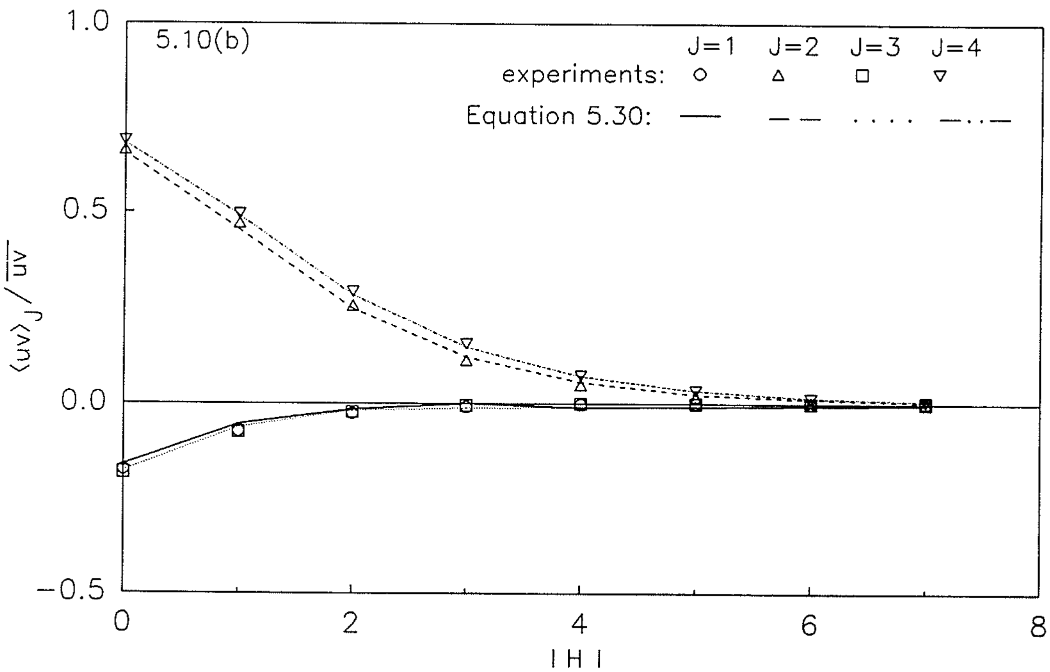
5.10(b)
J=1 J=2 J=3 J=4
experiments:
Equation 5.30:
1.0
0.5
0.0
−0.5
⟨uv⟩J / uv
0
2
4
6
8
|H|

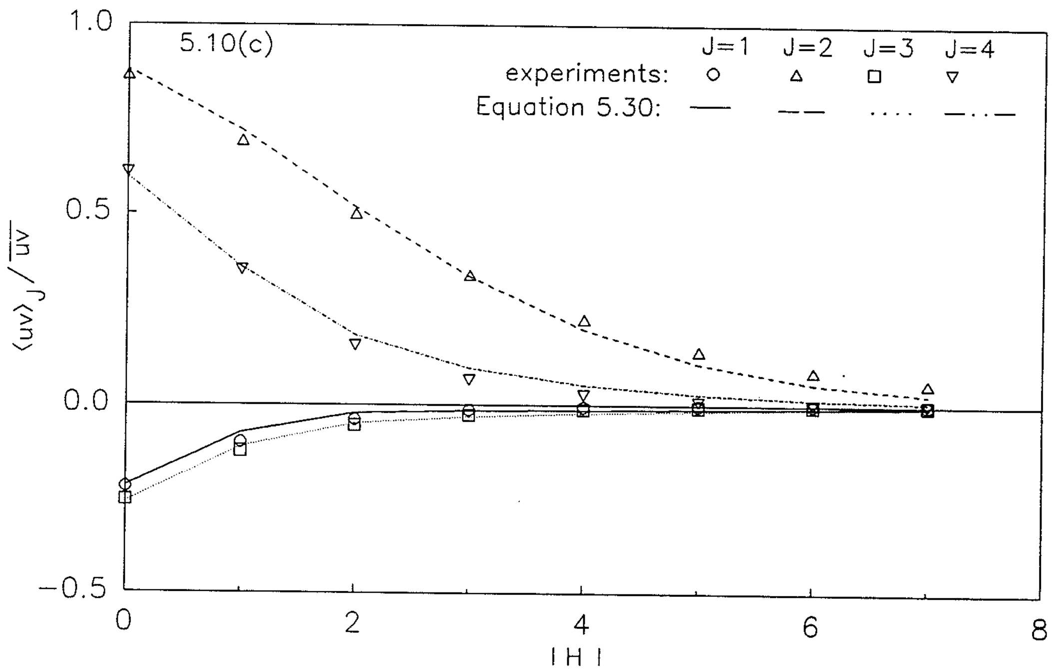

FIGURE 5.10: The contribution to $-\overline{uv}$ from different events at station 66. (a) Wall region (Y/R=0.021) (b) Peak region (Y/R=0.586) (c) Core region (Y/R=0.792).

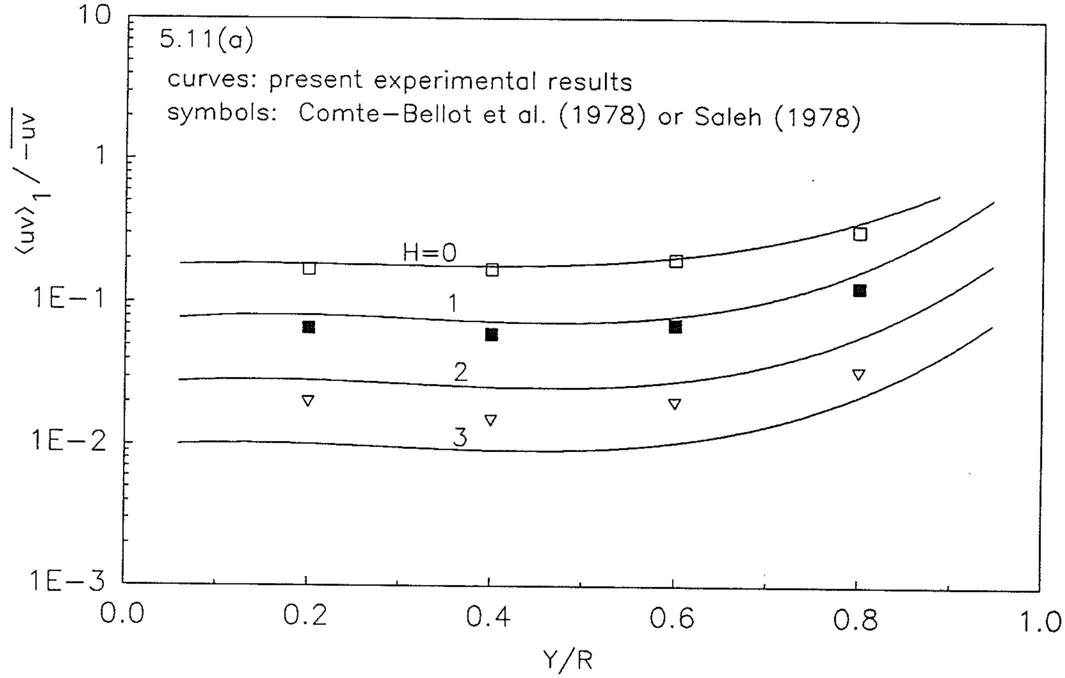
5.11(a)
curves: present experimental results
symbols: Comte–Bellot et al. (1978) or Saleh (1978)
⟨uv⟩1 / −uv
H=0
1
2
3
10
1
1E−1
1E−2
1E−3
0.0
0.2
0.4
0.6
0.8
1.0
Y/R

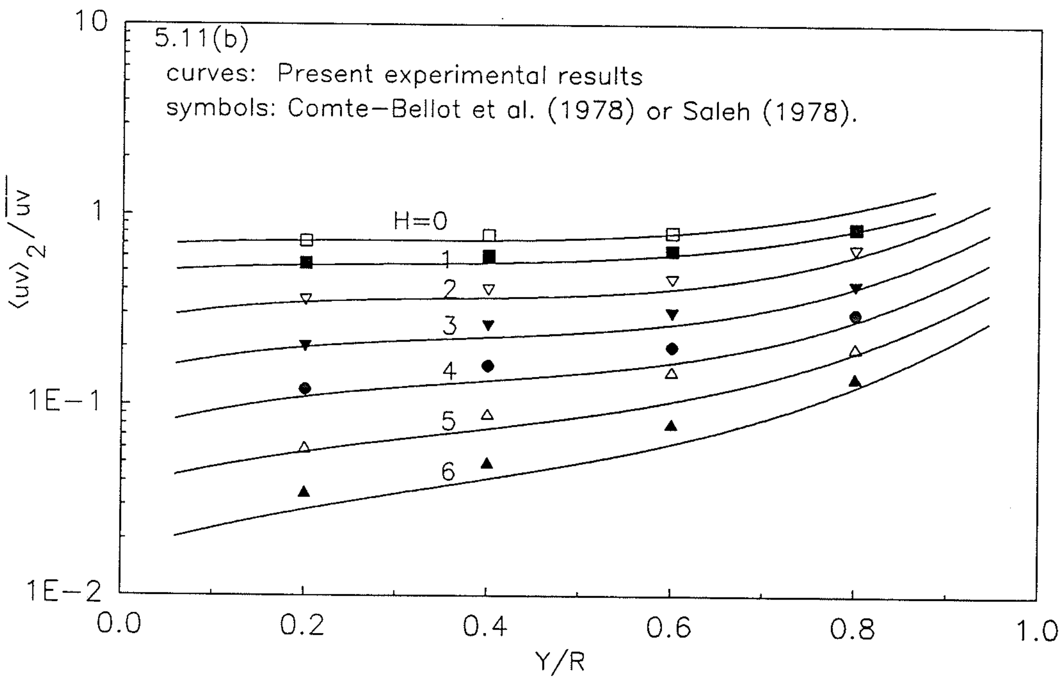
5.11(b)
curves: Present experimental results
symbols: Comte–Bellot et al. (1978) or Saleh (1978).
⟨uv⟩2 / uv
H=0
1
2
3
4
5
6
10
1
1E−1
1E−2
0.0
0.2
0.4
0.6
0.8
1.0
Y/R

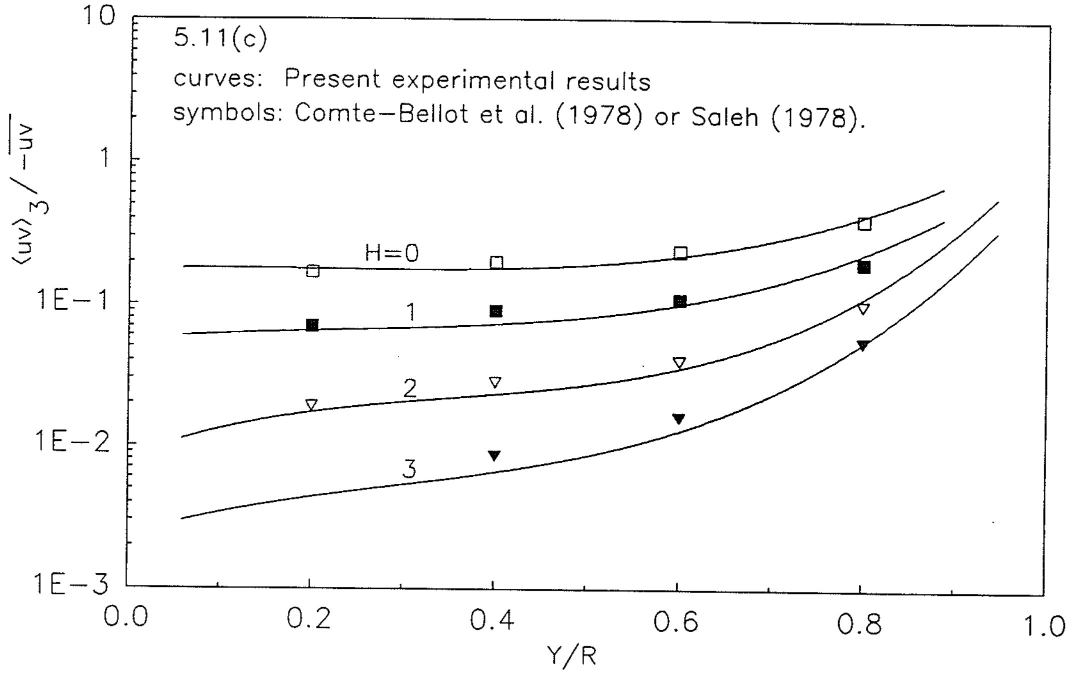

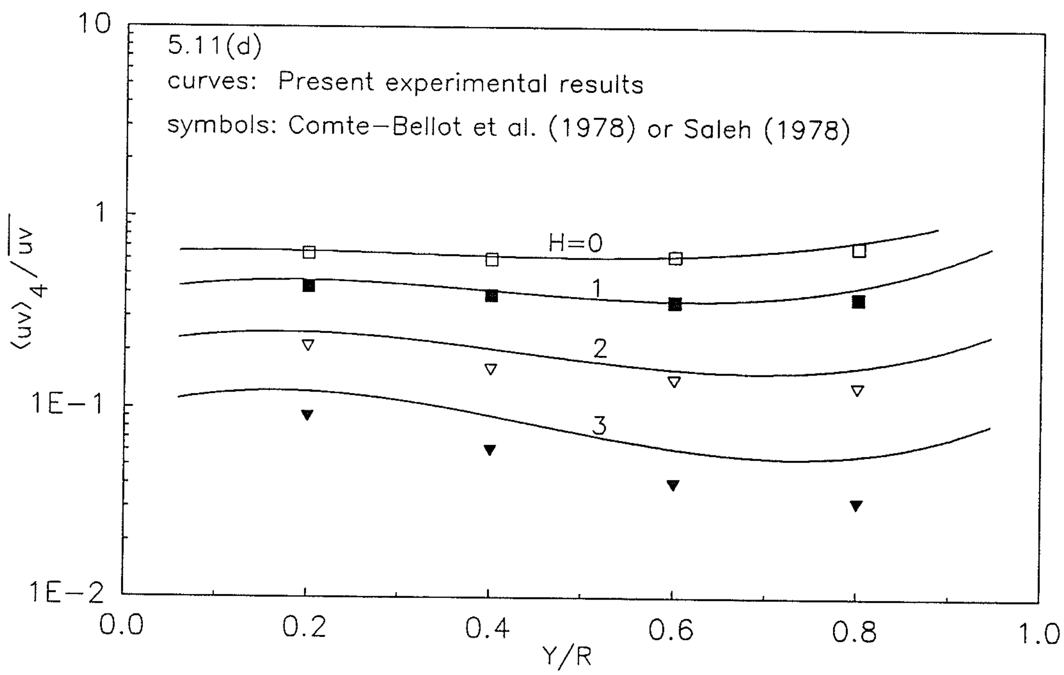

FIGURE 5.11: Variation of the contributions of different events to $-\overline{uv}$ in pipe flow with hole size. (a) Outward interactions (b) Ejections (c) Inward interactions (d) Sweeps.

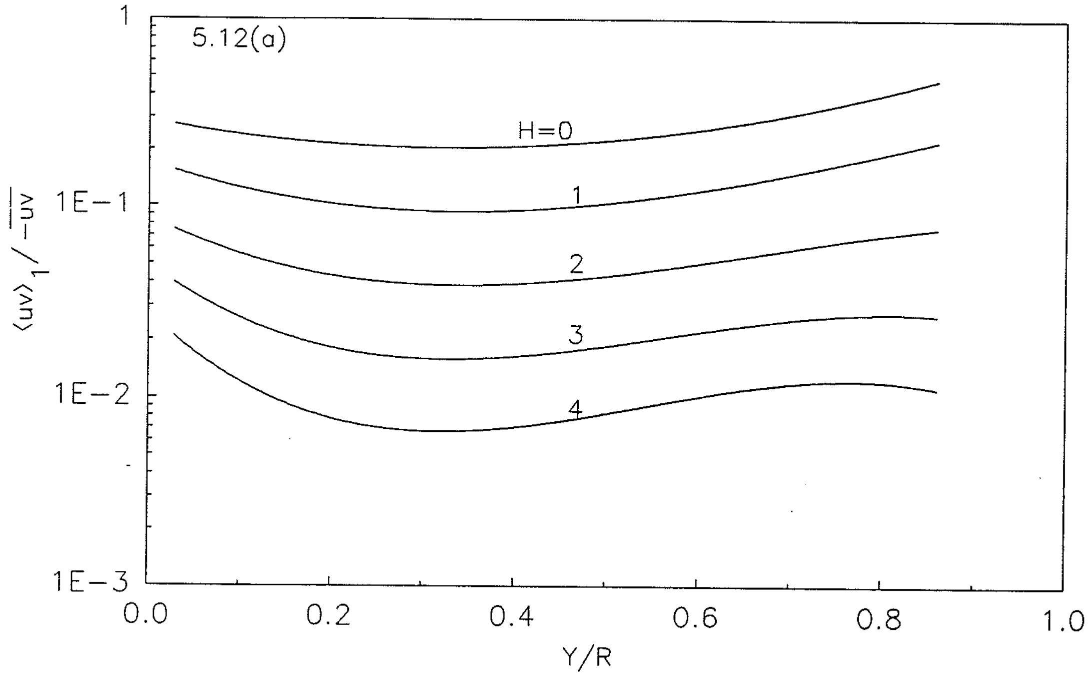
5.12(a)
H=0
1
2
3
4
1
1E−1
1E−2
1E−3
0.0
0.2
0.4
0.6
0.8
1.0
Y/R
$\langle uv \rangle_1 / \overline{-uv}$

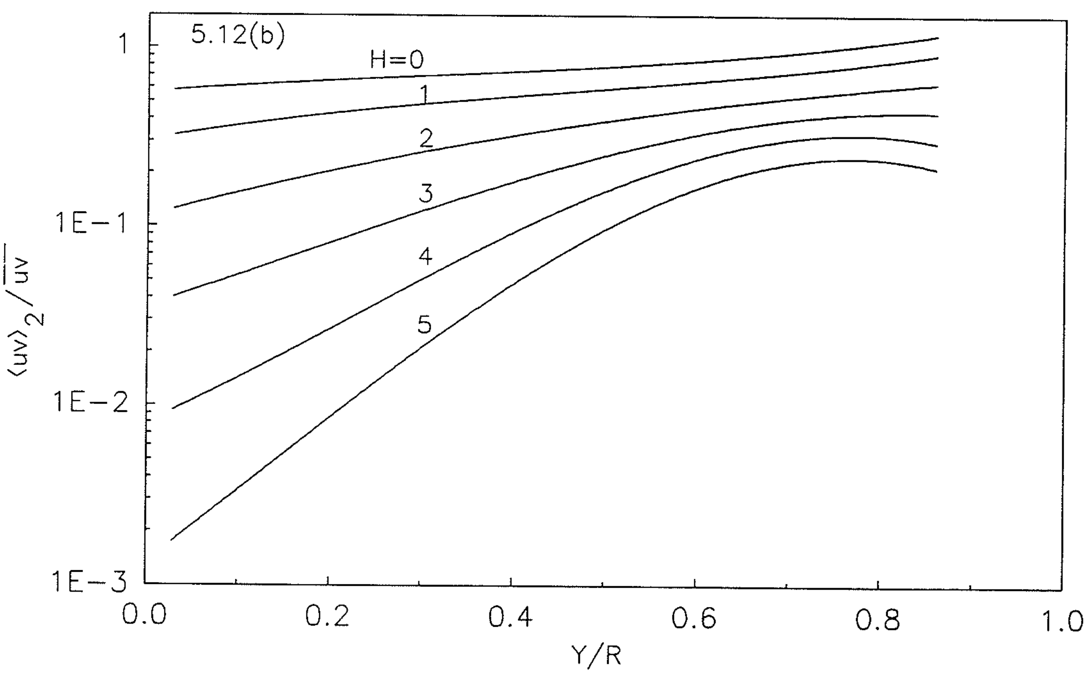
5.12(b)
H=0
1
2
3
4
5
1
1E−1
1E−2
1E−3
0.0
0.2
0.4
0.6
0.8
1.0
Y/R
$\langle uv \rangle_2 / \overline{uv}$

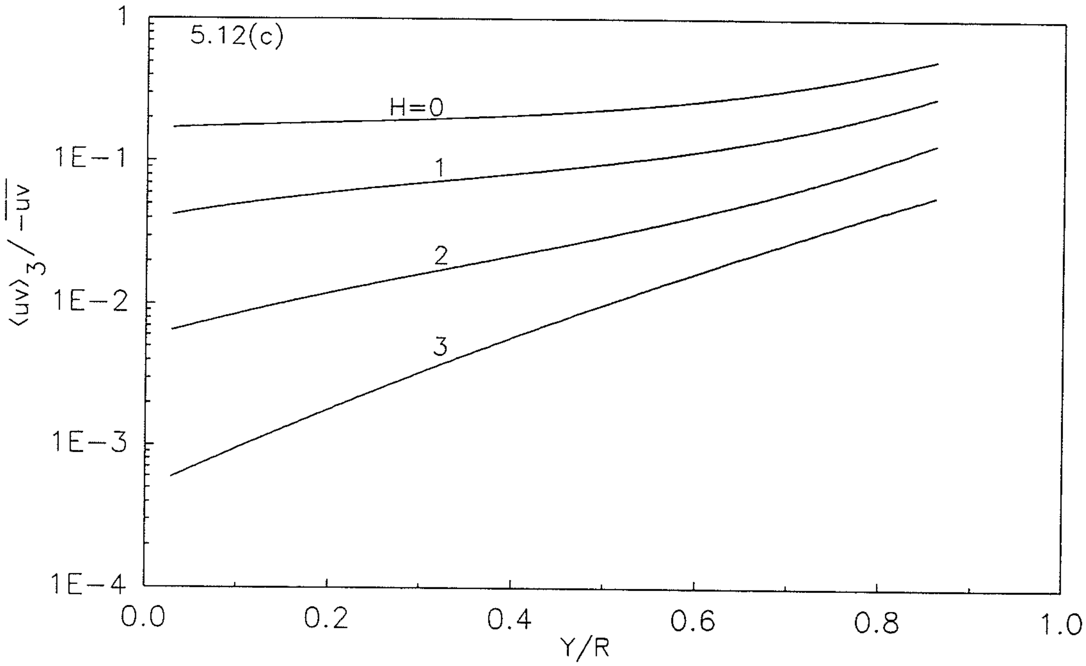

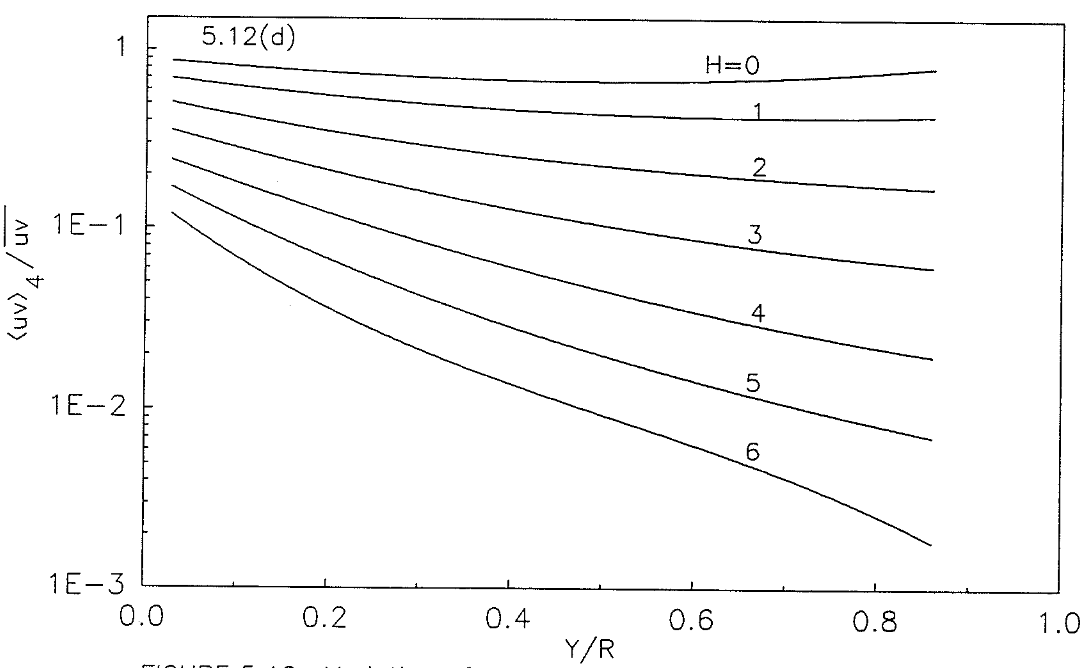

FIGURE 5.12: Variation of the contributions of different events to $-\overline{uv}$ at station 30 with hole size. (a) Outward interactions (b) Ejections (C) Inward interactions (d) Sweeps.

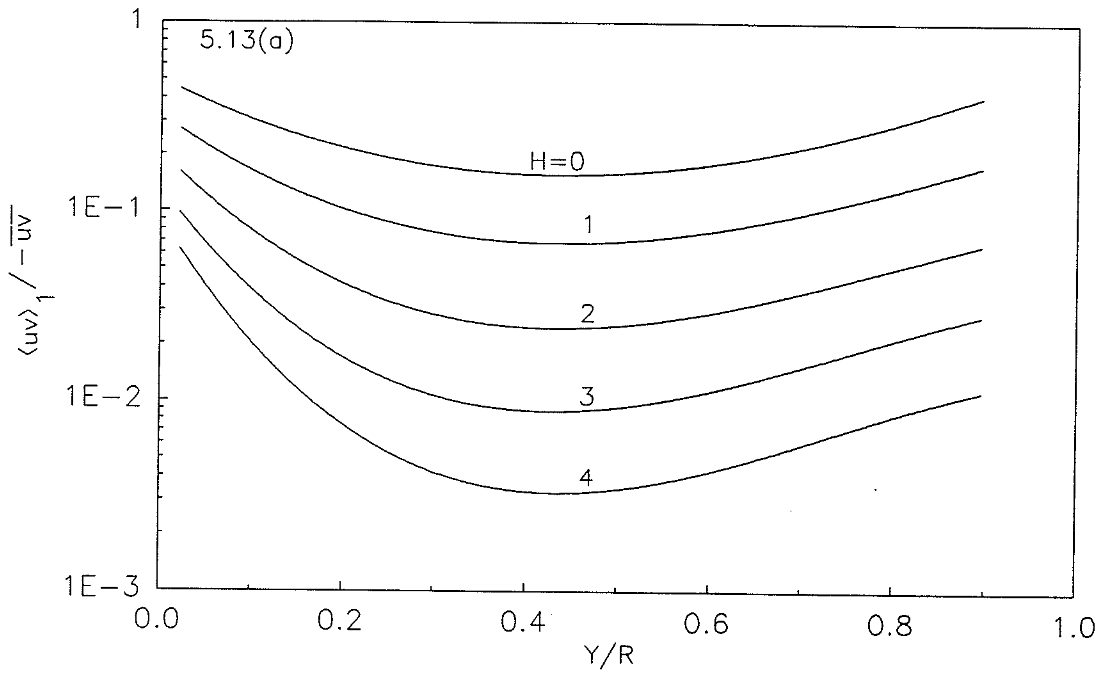
5.13(a)
H=0
1
2
3
4
1
1E−1
1E−2
1E−3
0.0
0.2
0.4
0.6
0.8
1.0
Y/R
⟨uv⟩1 / −uv

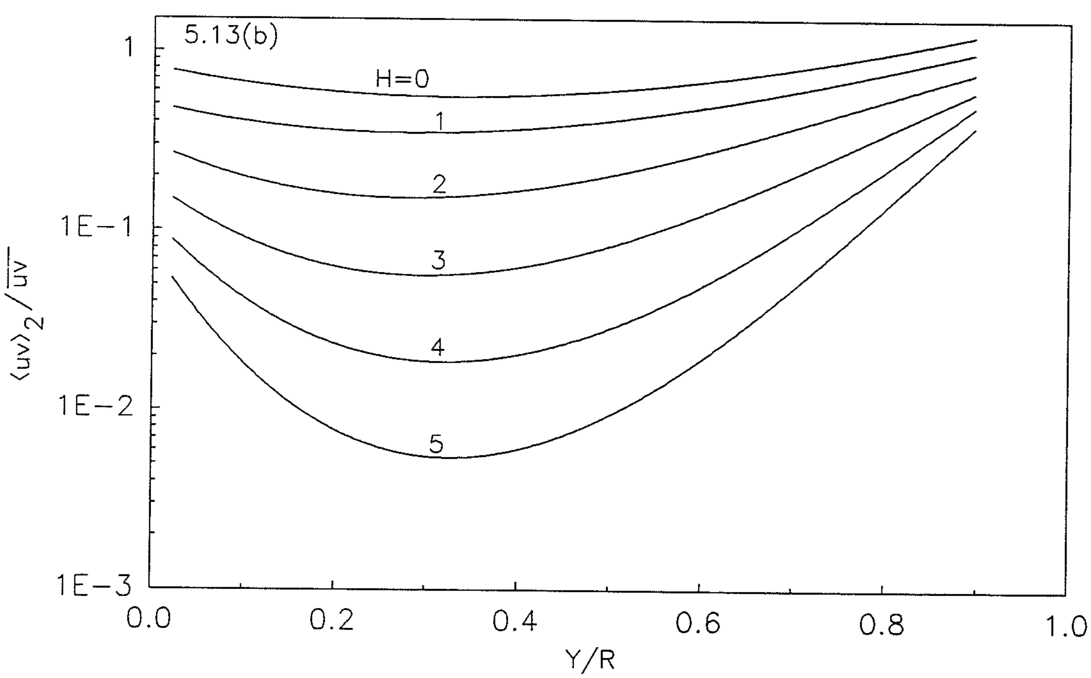
5.13(b)
H=0
1
2
3
4
5
1
1E−1
1E−2
1E−3
0.0
0.2
0.4
0.6
0.8
1.0
Y/R
⟨uv⟩2 / uv

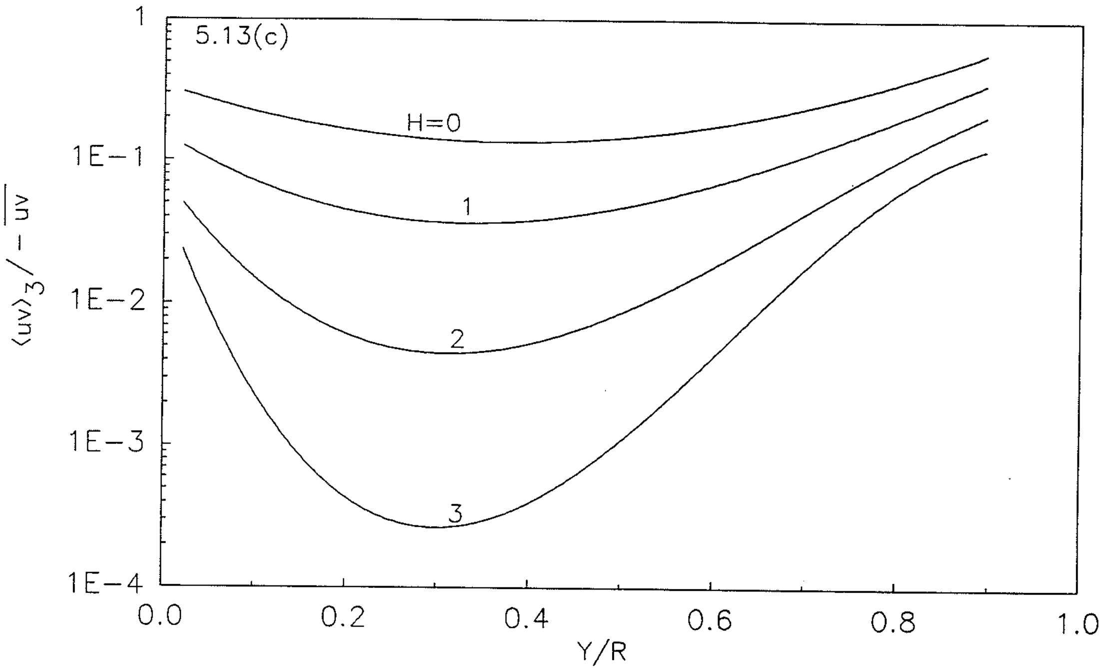

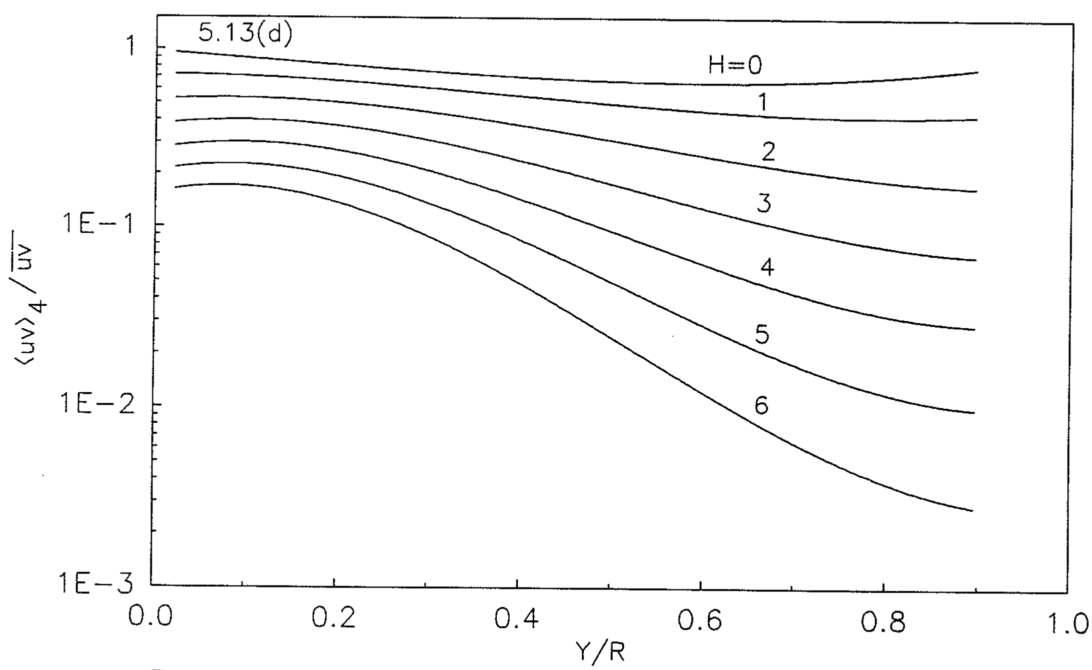

FIGURE 5.13: Variation of the contributions of different events to $-\overline{uv}$ at station 66 with hole size. (a) Outward interactions (b) Ejections (c) Inward interactions (c) Sweeps.

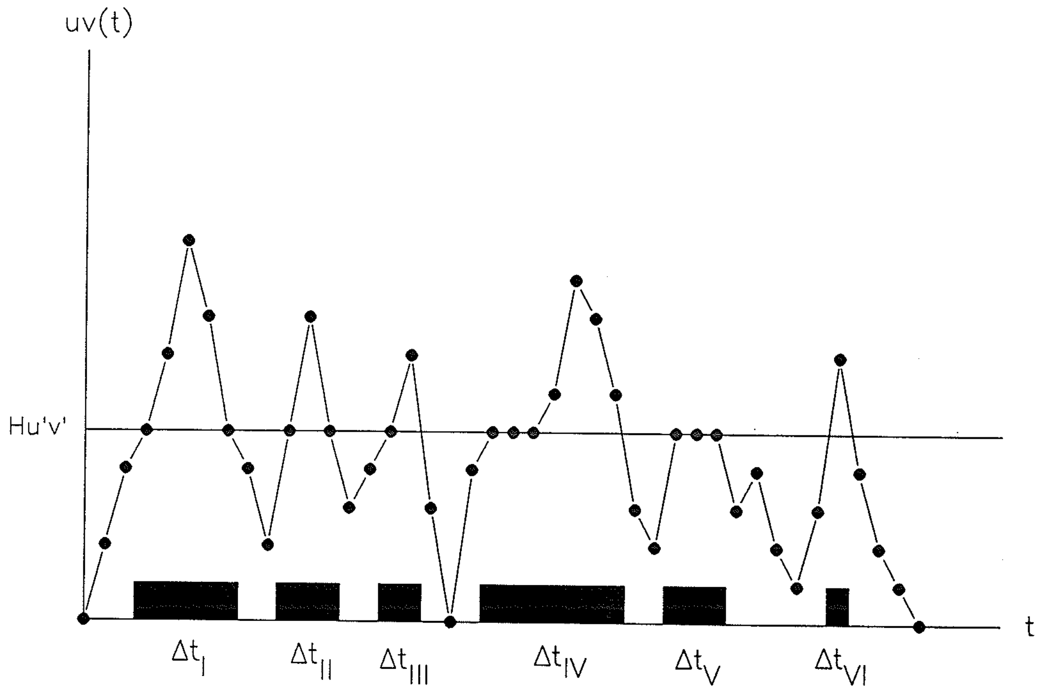

FIGURE 5.14: An illustration of some basic signal patterns above the threshold, Hu'v', in a random uv–signal.

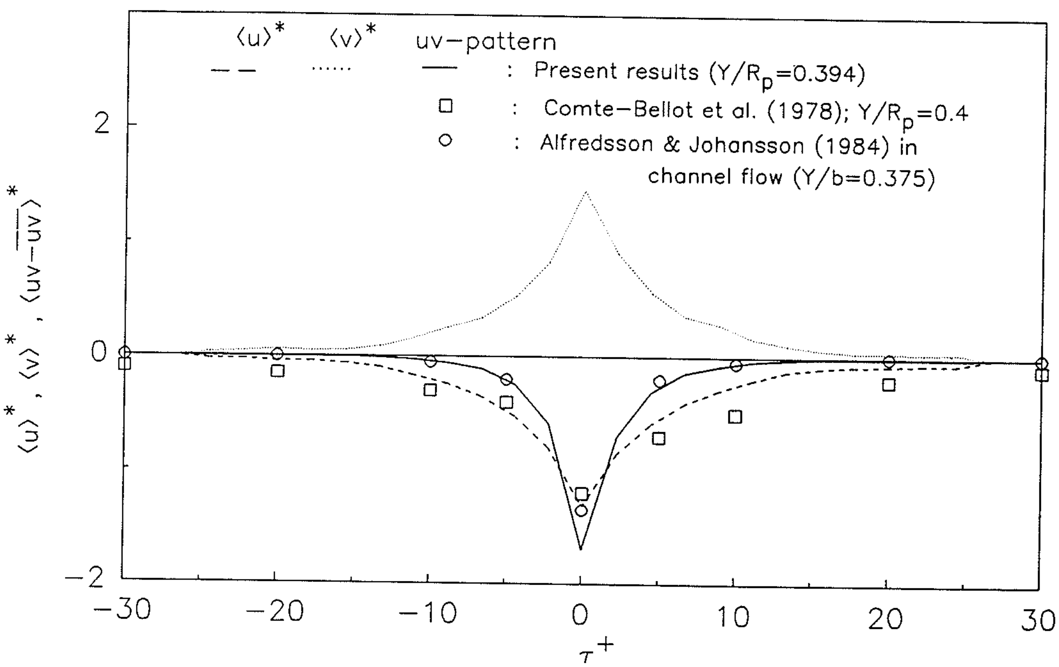

FIGURE 5.15: Comparison of ensemble averages of the uv−signal during ejections with existing results and with H=4 (pipe flow).

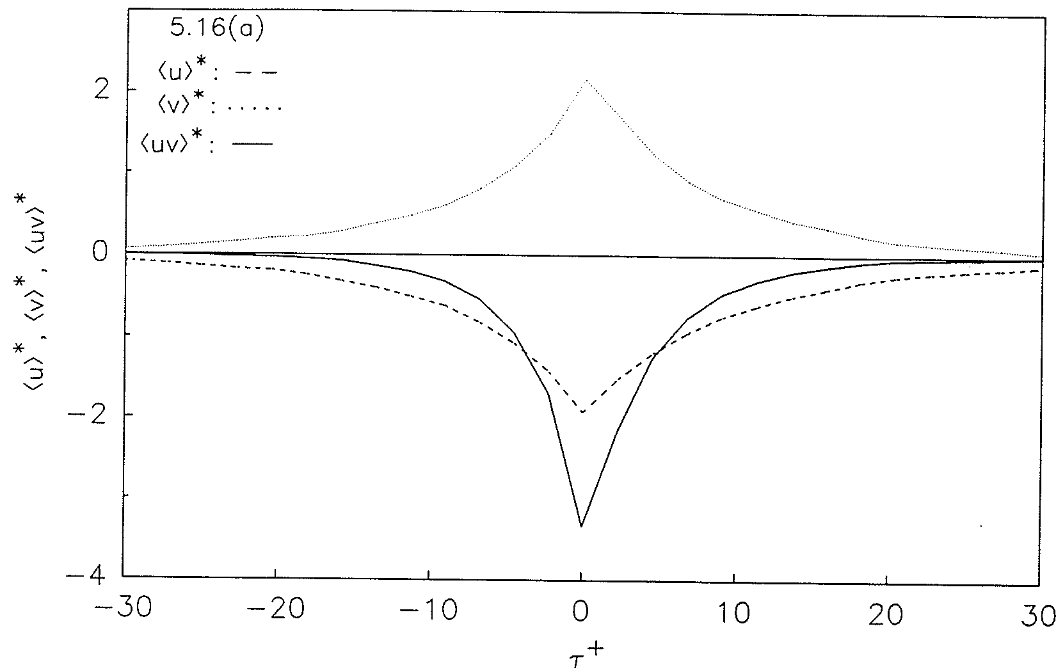

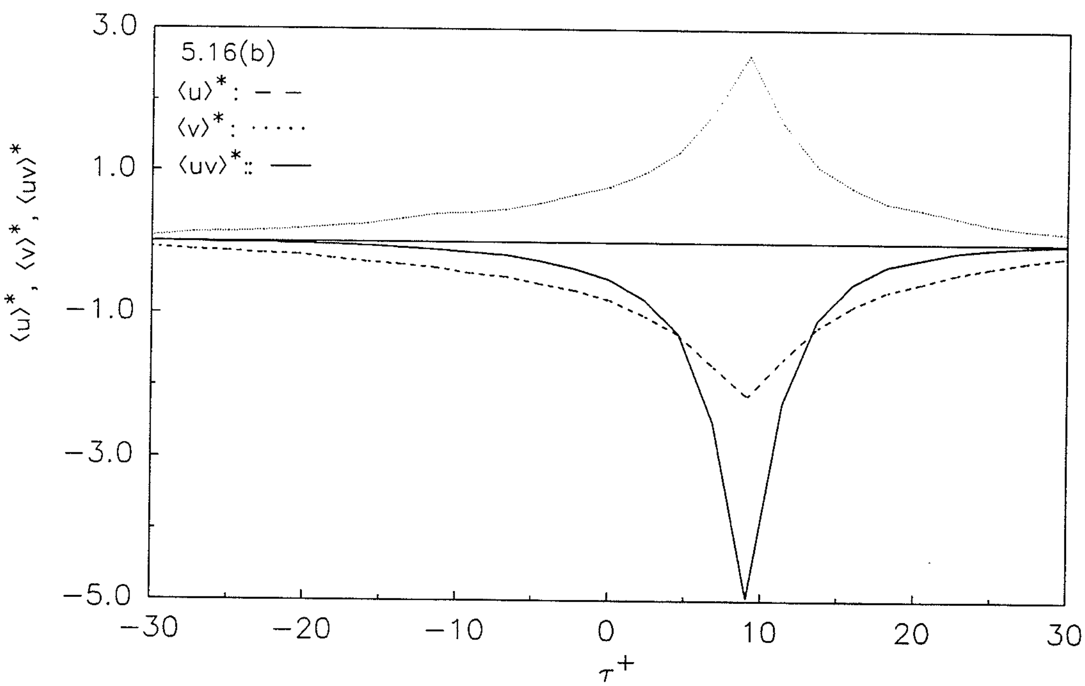

FIGURE 5.16: Ensemble averages in pipe flow (Y/R_p = 0.394) during ejections with H=1.
(a) Phase aligned with mid-point of event (b) Phase aligned with maximum uv

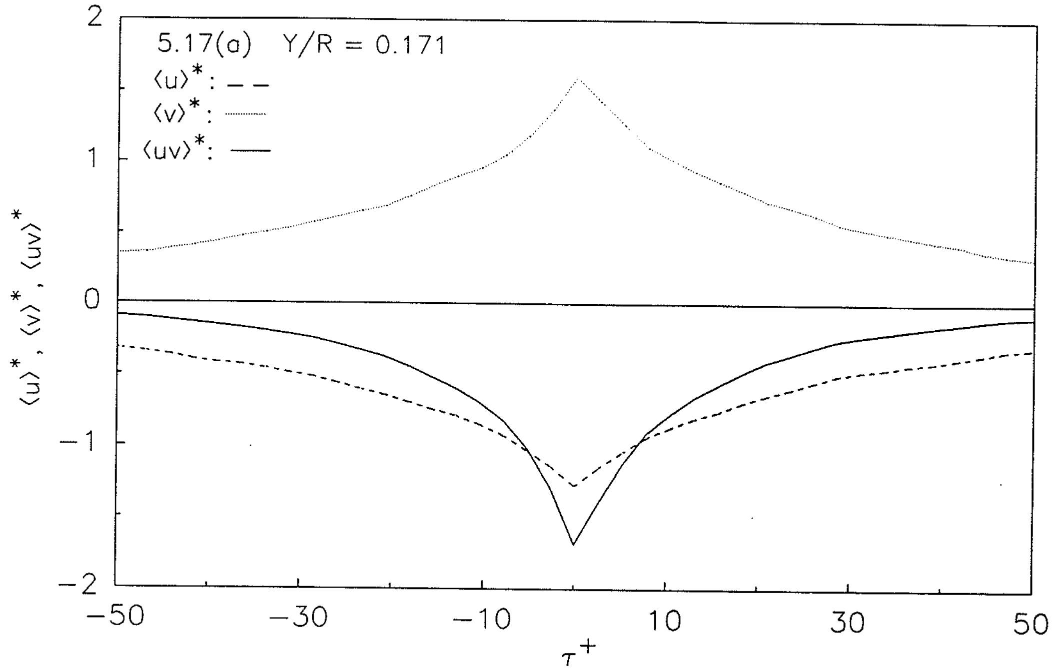
5.17(a) Y/R = 0.171
⟨u⟩*: — —
⟨v⟩*: ······
⟨uv⟩*: ——
⟨u⟩*, ⟨v⟩*, ⟨uv⟩*
τ+
2
1
0
−1
−2
−50
−30
−10
10
30
50

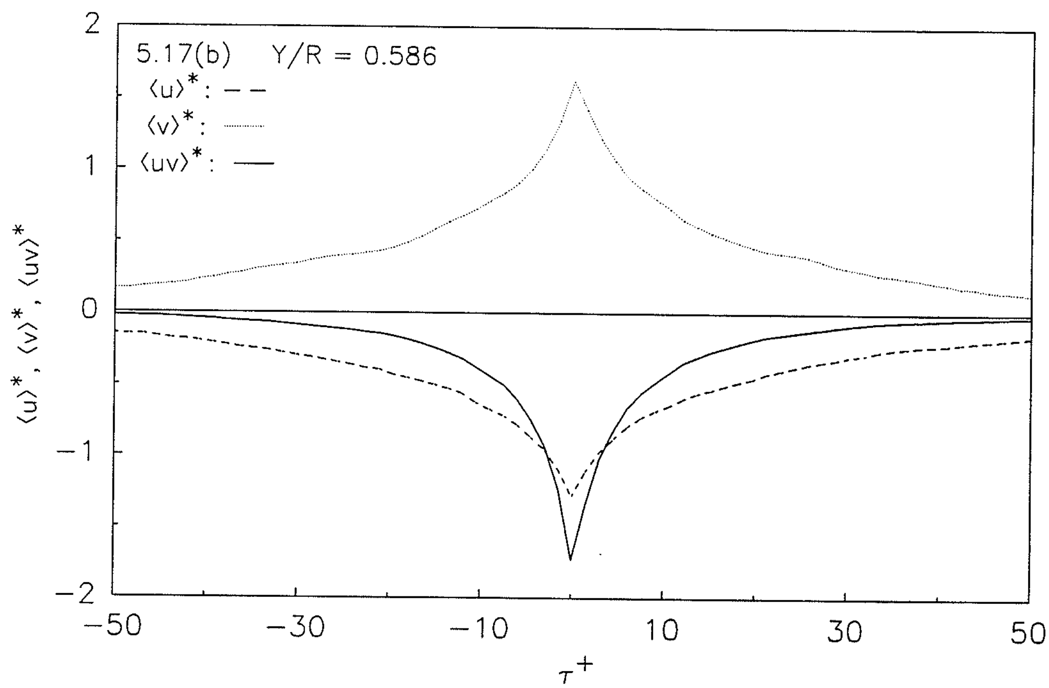
5.17(b) Y/R = 0.586
⟨u⟩*: — —
⟨v⟩*: ······
⟨uv⟩*: ——
⟨u⟩*, ⟨v⟩*, ⟨uv⟩*
τ+
2
1
0
−1
−2
−50
−30
−10
10
30
50

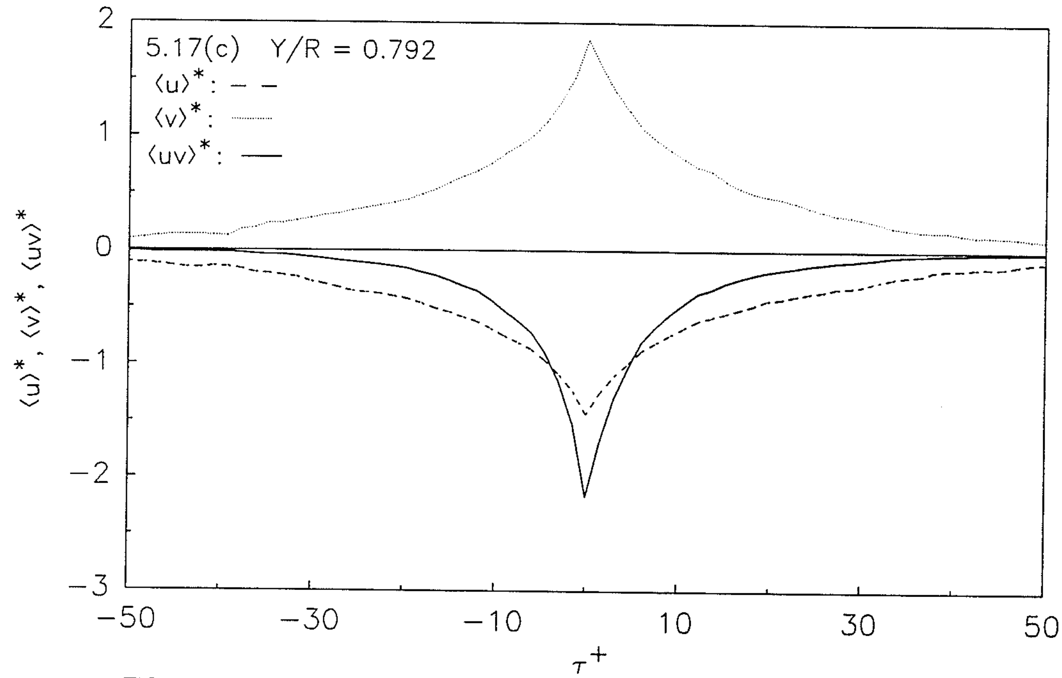

FIGURE 5.17: Ensemble averages during ejections in the diffuser flow at station 66 with H=1 (Phase aligned with the mid−point). (a) Wall region (b) Peak region (c) Core region

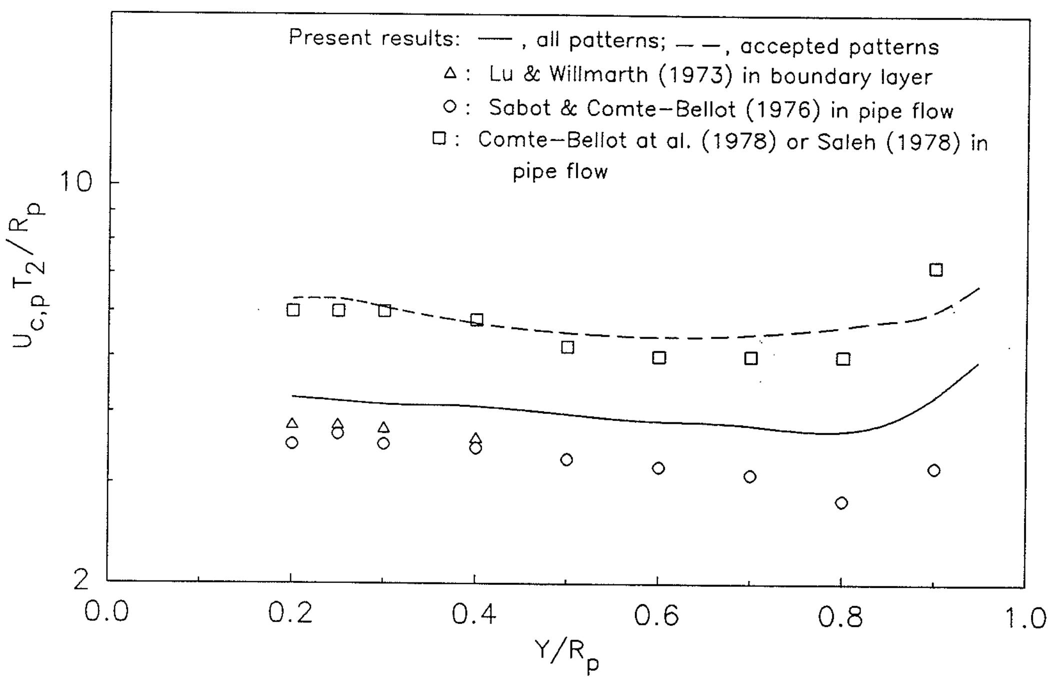

FIGURE 5.18: The effect of selecting patterns on the mean periods between ejections in pipe flow with H=4.

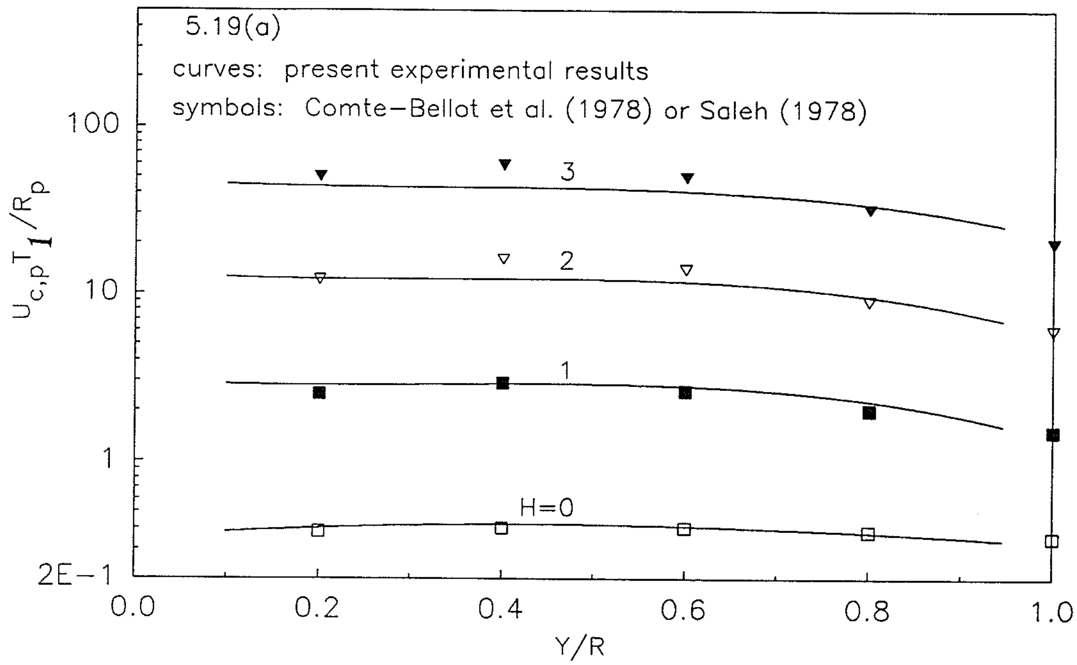

5.19(a)
curves: present experimental results
symbols: Comte–Bellot et al. (1978) or Saleh (1978)
100
10
1
2E−1
3
2
1
H=0
$U_{c,p}T_1/R_p$
0.0
0.2
0.4
0.6
0.8
1.0
Y/R

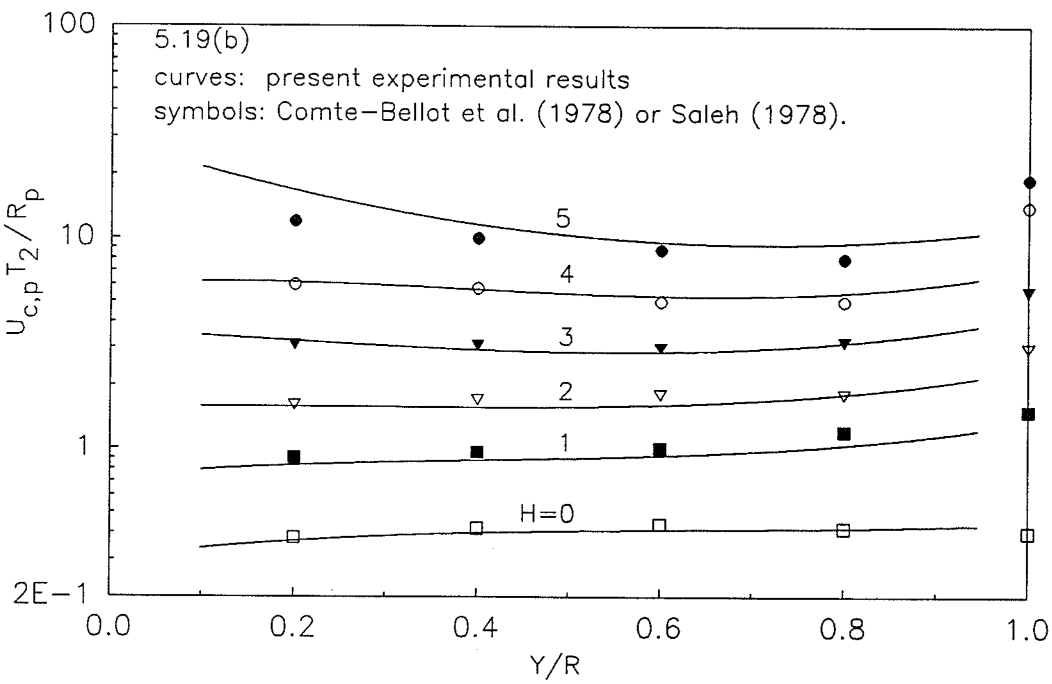

5.19(b)
curves: present experimental results
symbols: Comte–Bellot et al. (1978) or Saleh (1978).
100
10
1
2E−1
5
4
3
2
1
H=0
$U_{c,p}T_2/R_p$
0.0
0.2
0.4
0.6
0.8
1.0
Y/R

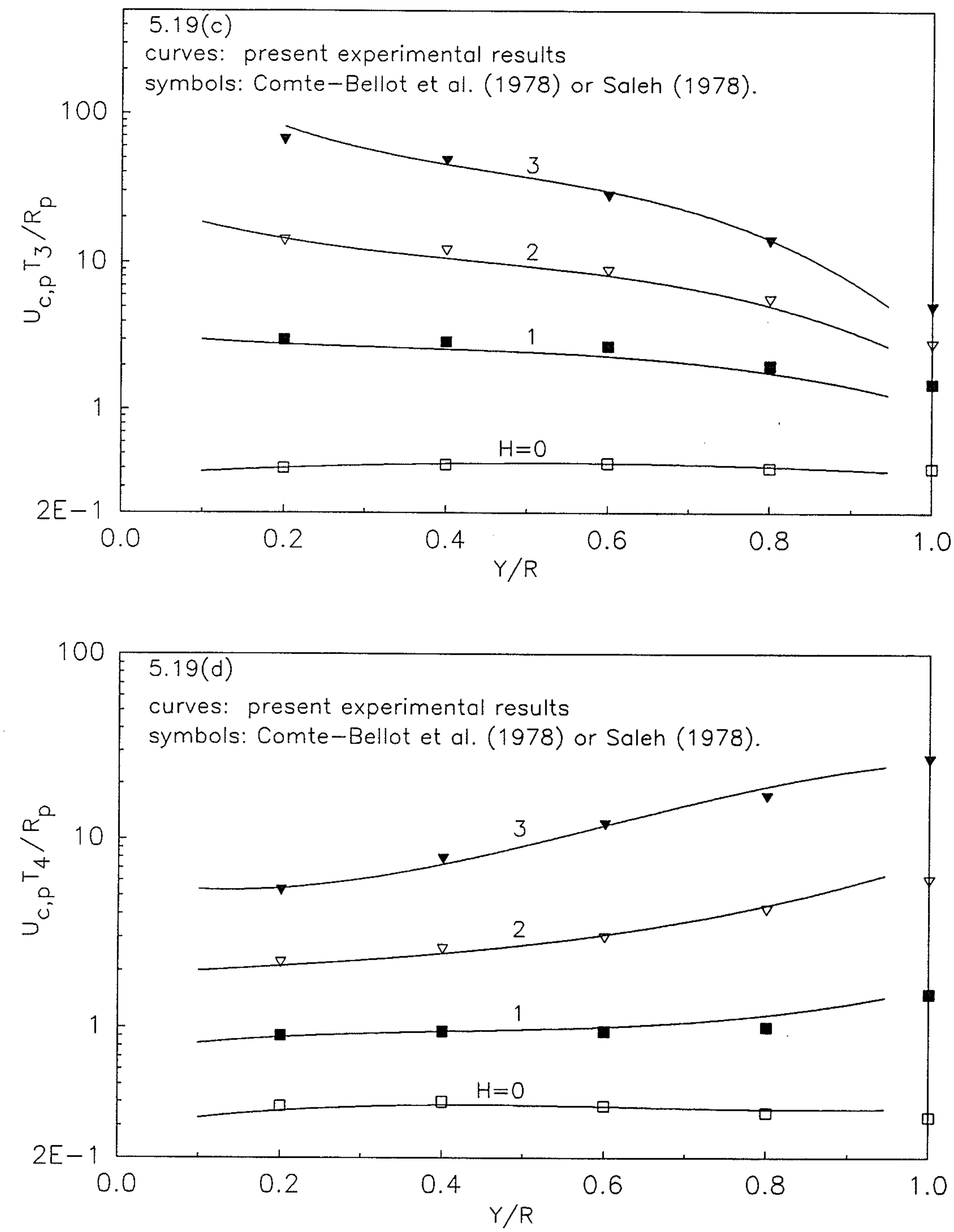

FIGURE 5.19: The distributions of the mean periods between events in pipe flow as a function of hole size. (a) Outward interactions. (b) Ejections (c) Inward interactions (d) Sweeps.

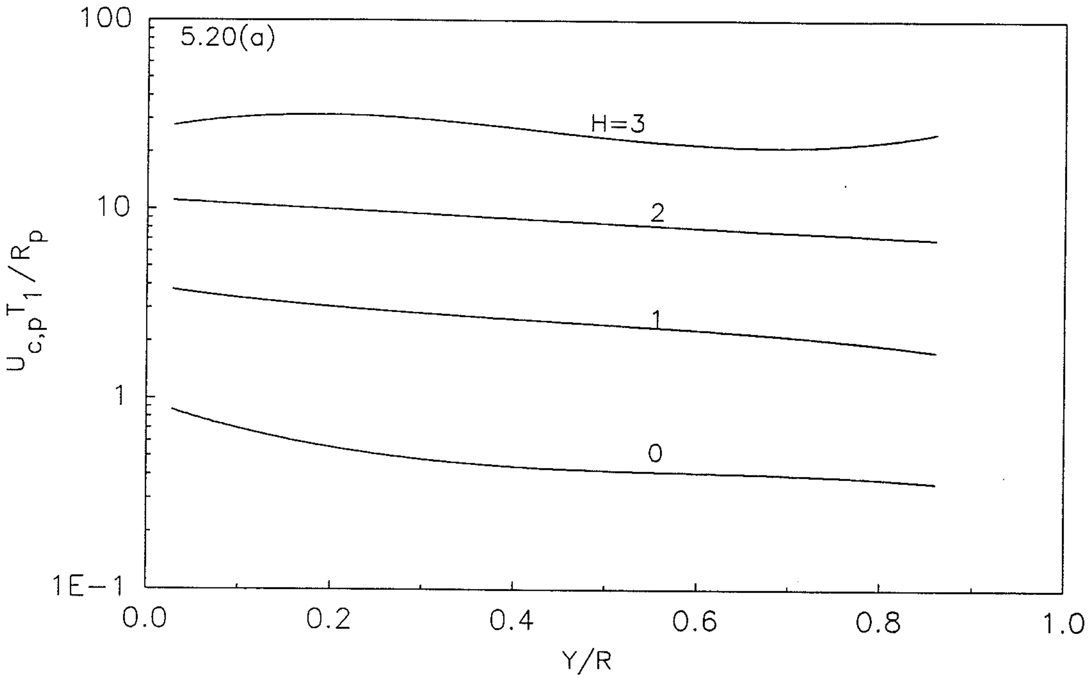
5.20(a)
H=3
2
1
0
100
10
1
1E−1
$U_{c,p}T_1/R_p$
0.0
0.2
0.4
0.6
0.8
1.0
Y/R

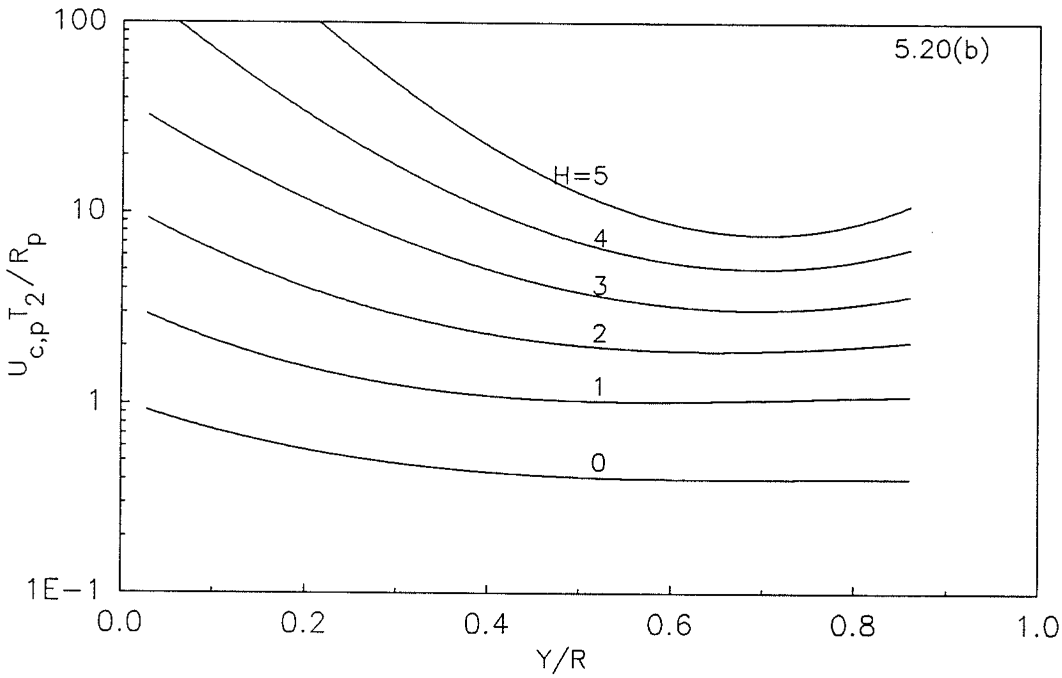
5.20(b)
H=5
4
3
2
1
0
100
10
1
1E−1
$U_{c,p}T_2/R_p$
0.0
0.2
0.4
0.6
0.8
1.0
Y/R

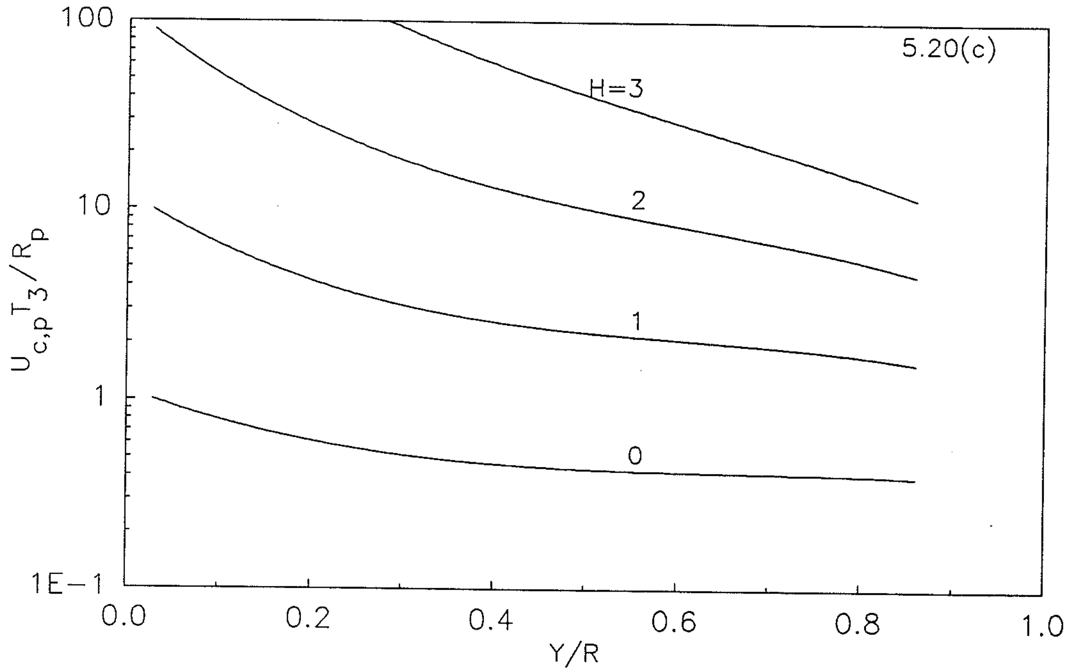

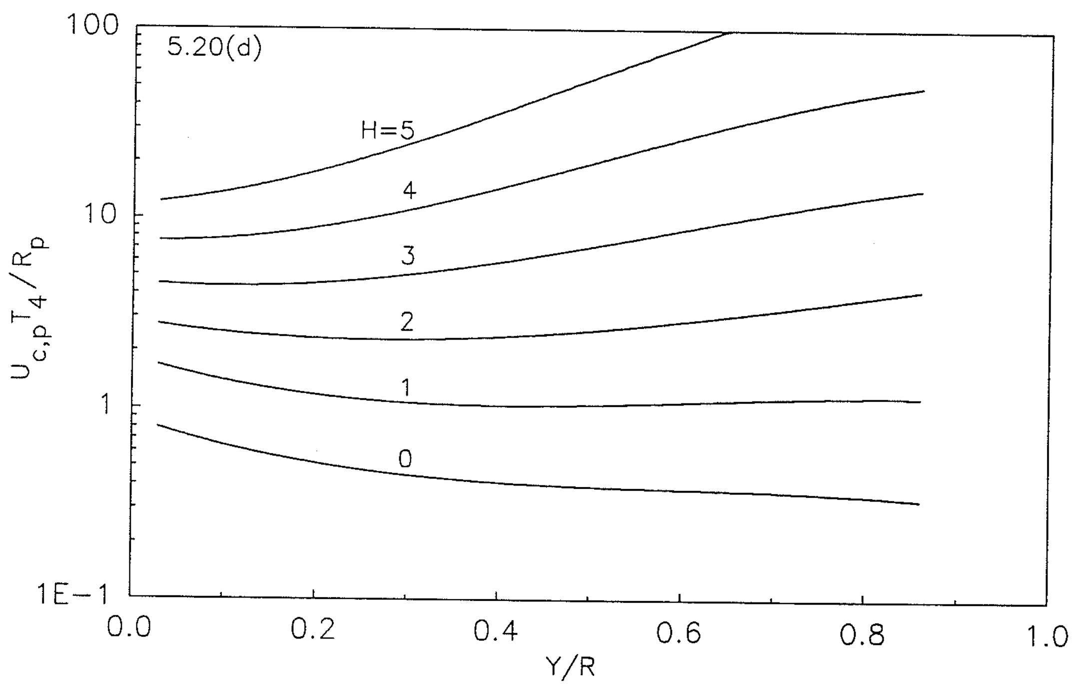

FIGURE 5.20: The distribution of mean periods between events at station 30 as a function of hole size. (curve fit of exp. points) (a) Outward int. (b) Ejections (c) Inward int. (d) Sweeps

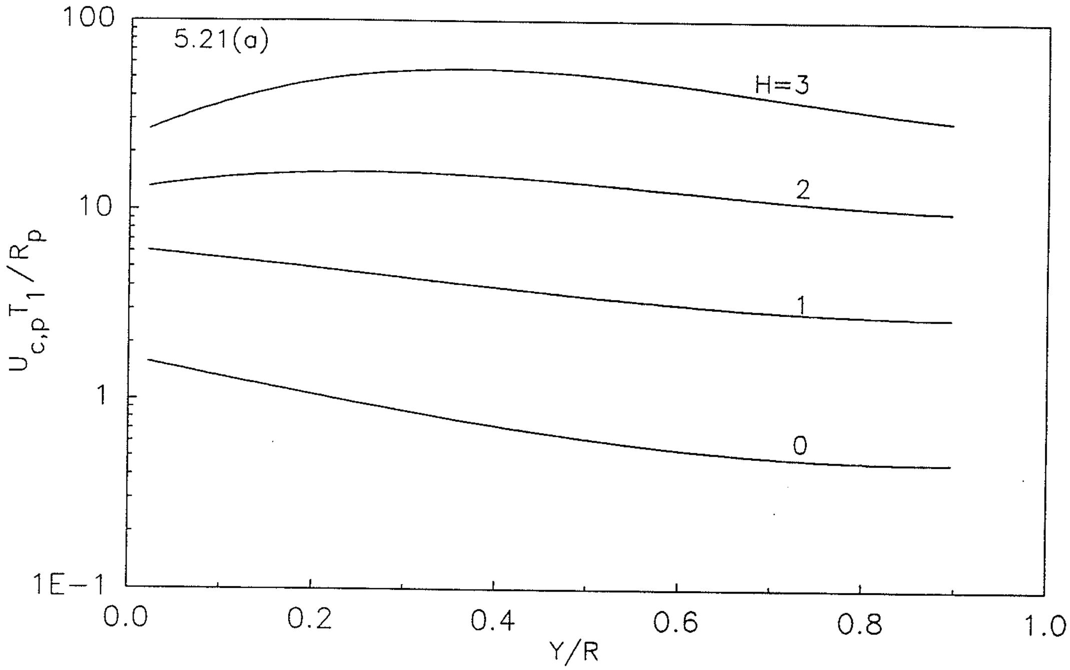
5.21(a)
H=3
2
1
0
100
10
1
1E−1
0.0
0.2
0.4
0.6
0.8
1.0
Y/R
$U_{c,p}T_1/R_p$

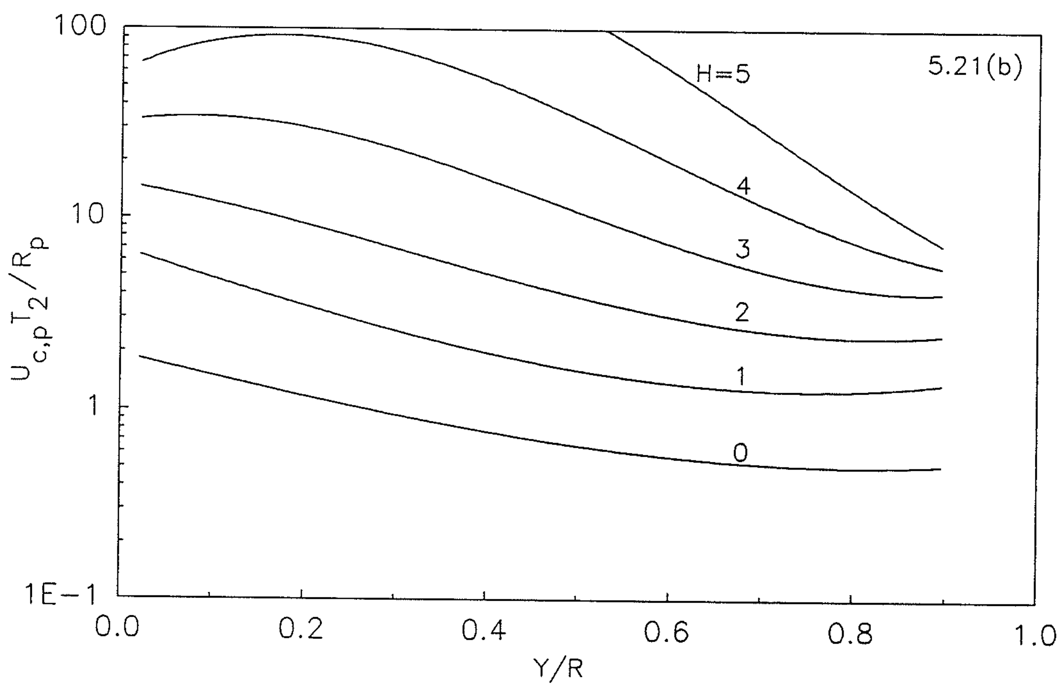
5.21(b)
H=5
4
3
2
1
0
100
10
1
1E−1
0.0
0.2
0.4
0.6
0.8
1.0
Y/R
$U_{c,p}T_2/R_p$

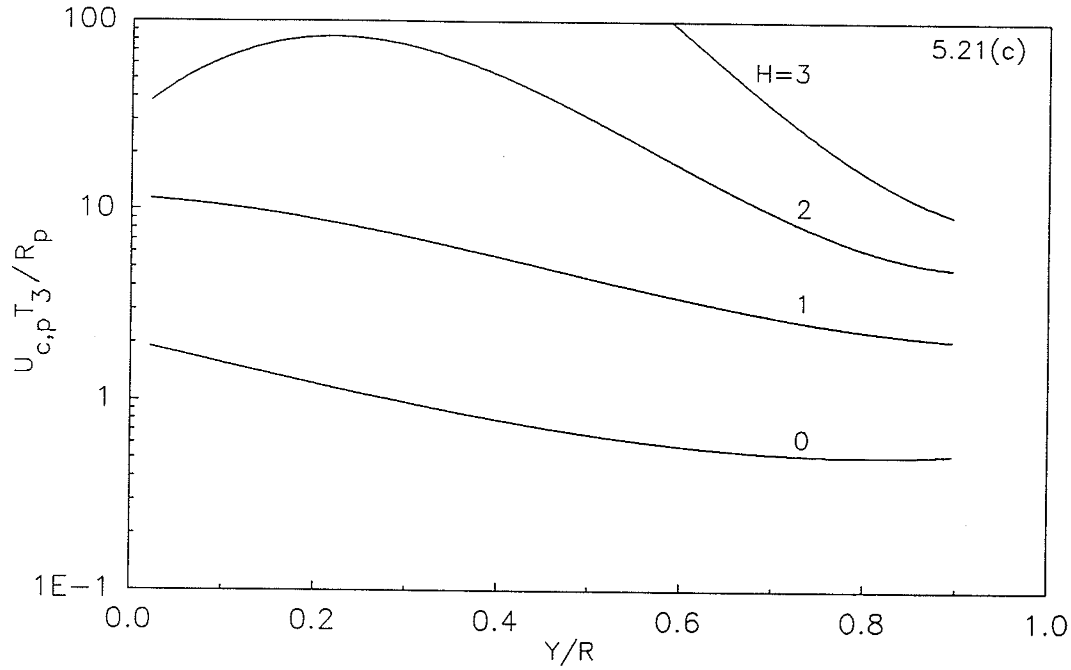

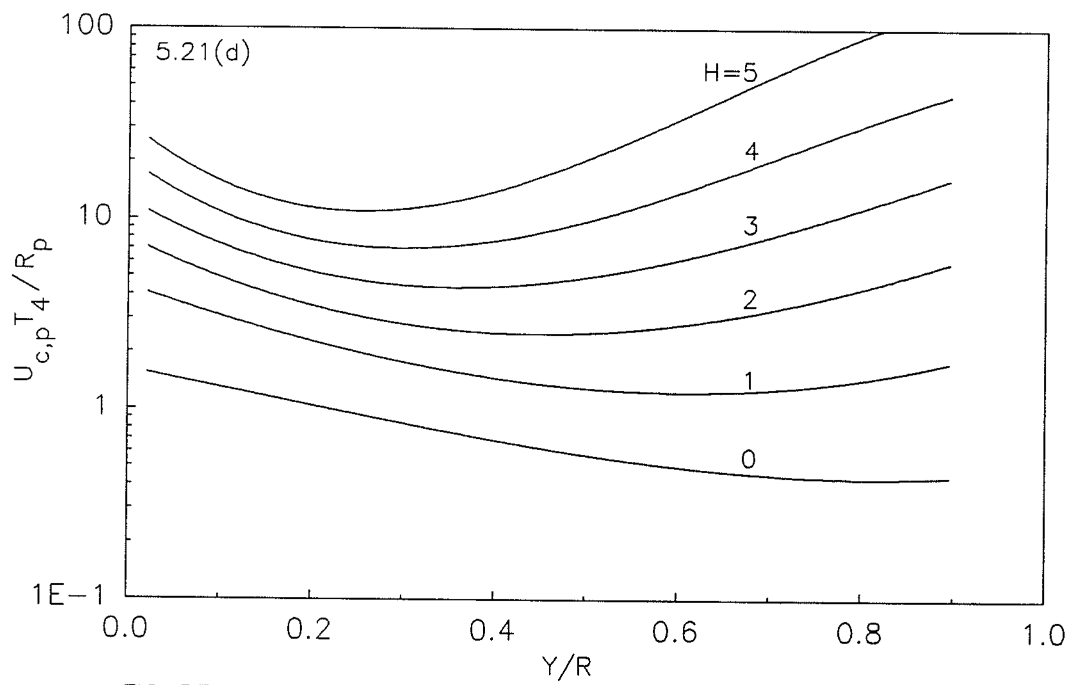

FIGURE 5.21: The distribution of mean periods between events at station 66 as a function of hole size (Curve-fit of exp. points) (a) Outward int. (b) Ejections (c) Inward int. (d) Sweeps.

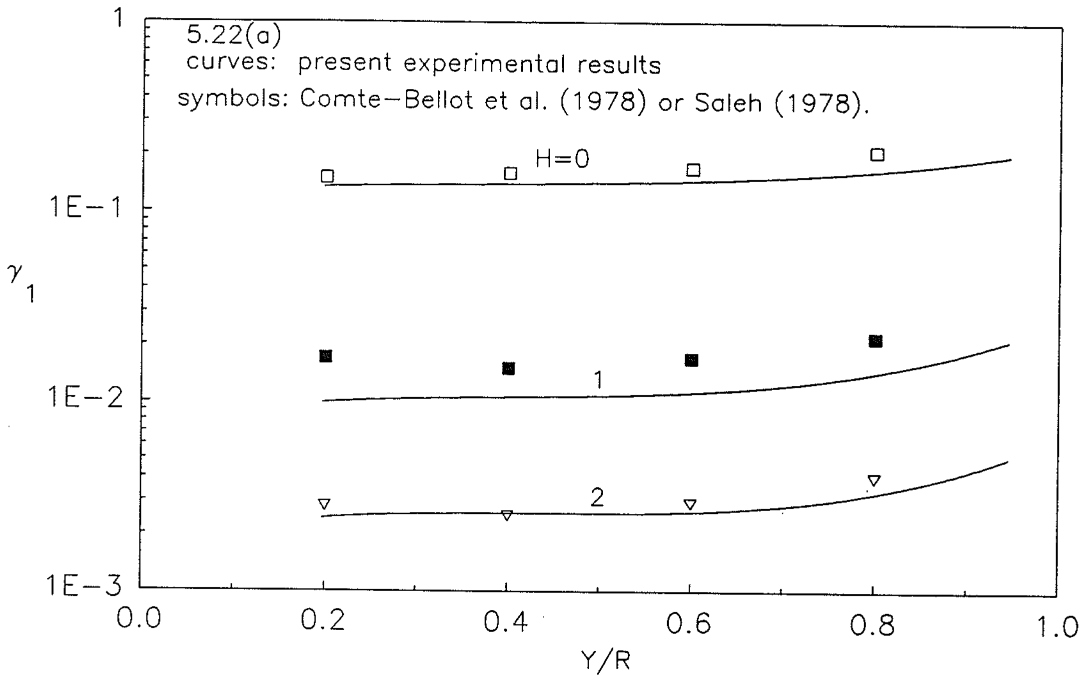
5.22(a)
curves: present experimental results
symbols: Comte–Bellot et al. (1978) or Saleh (1978).
H=0
1
2
1
1E−1
1E−2
1E−3
γ_1
0.0
0.2
0.4
0.6
0.8
1.0
Y/R

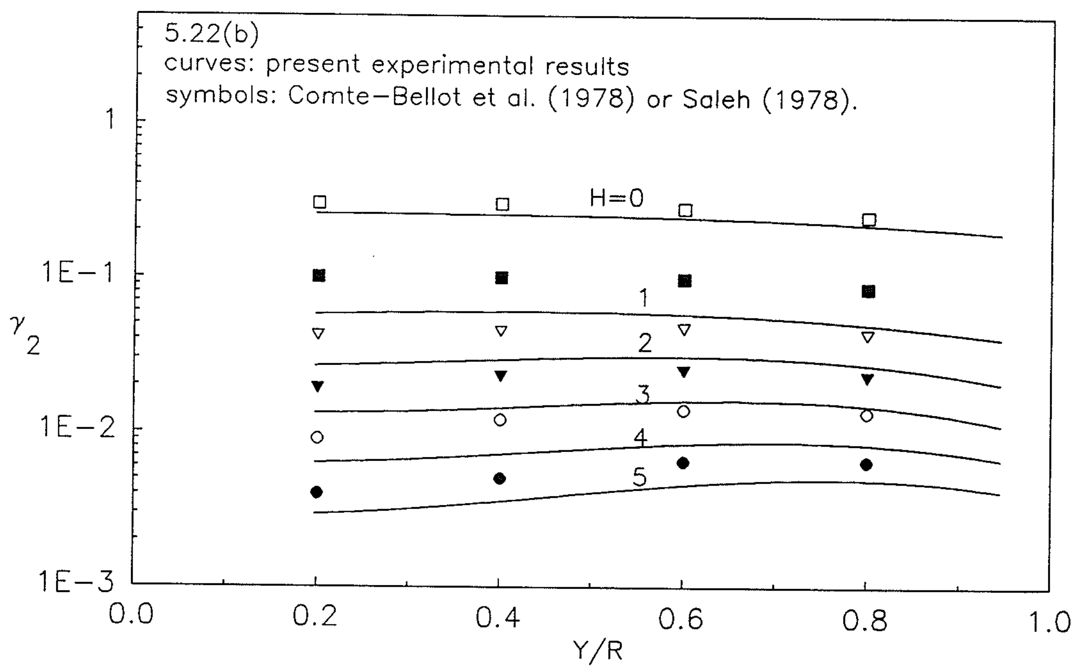
5.22(b)
curves: present experimental results
symbols: Comte–Bellot et al. (1978) or Saleh (1978).
H=0
1
2
3
4
5
1
1E−1
1E−2
1E−3
γ_2
0.0
0.2
0.4
0.6
0.8
1.0
Y/R

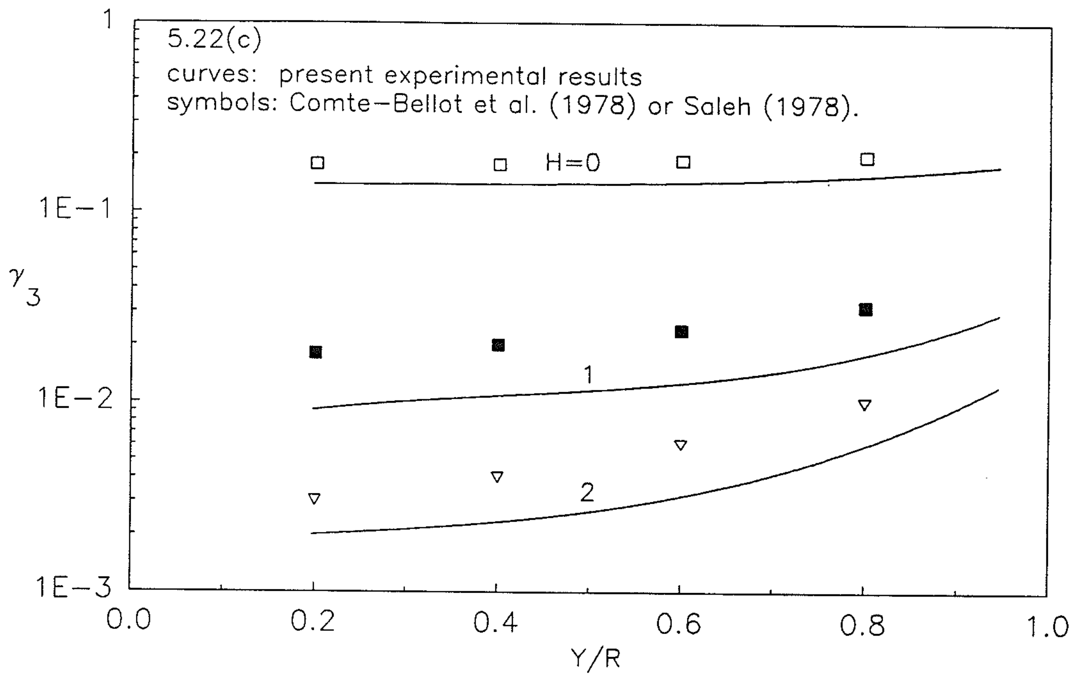

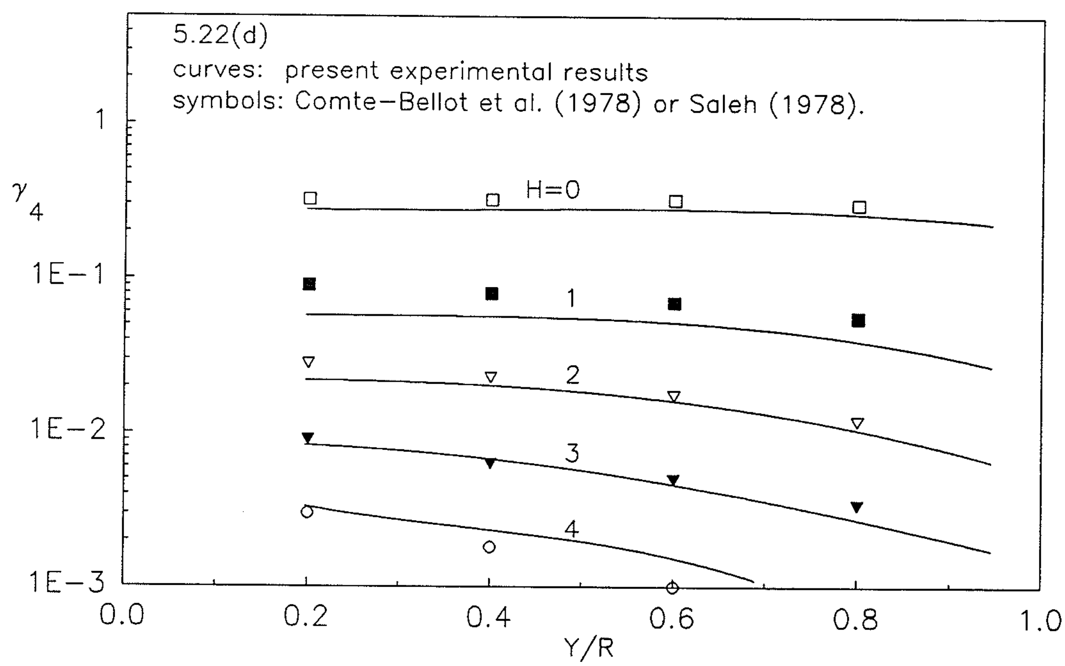

FIGURE 5.22: The distribution of the intermittency factor of $-\overline{uv}$ in pipe flow as a function of hole size. (a) Outward int. (b) Ejections (c) Inward int. (d) Sweeps.

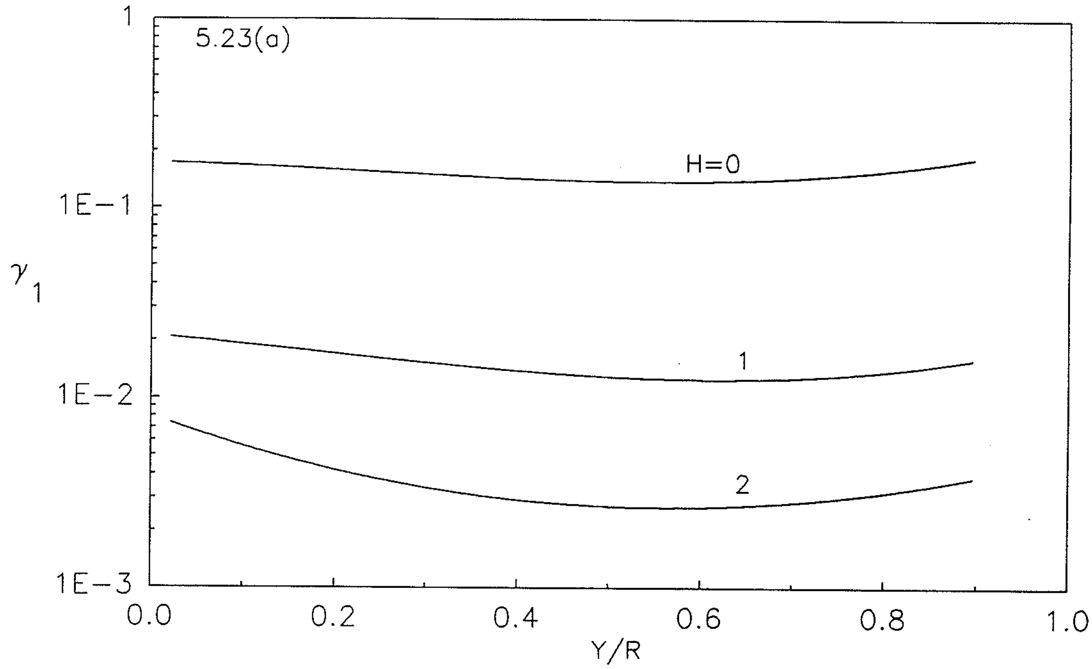

5.23(a)
1
1E−1
1E−2
1E−3
γ_1
H=0
1
2
0.0
0.2
0.4
0.6
0.8
1.0
Y/R

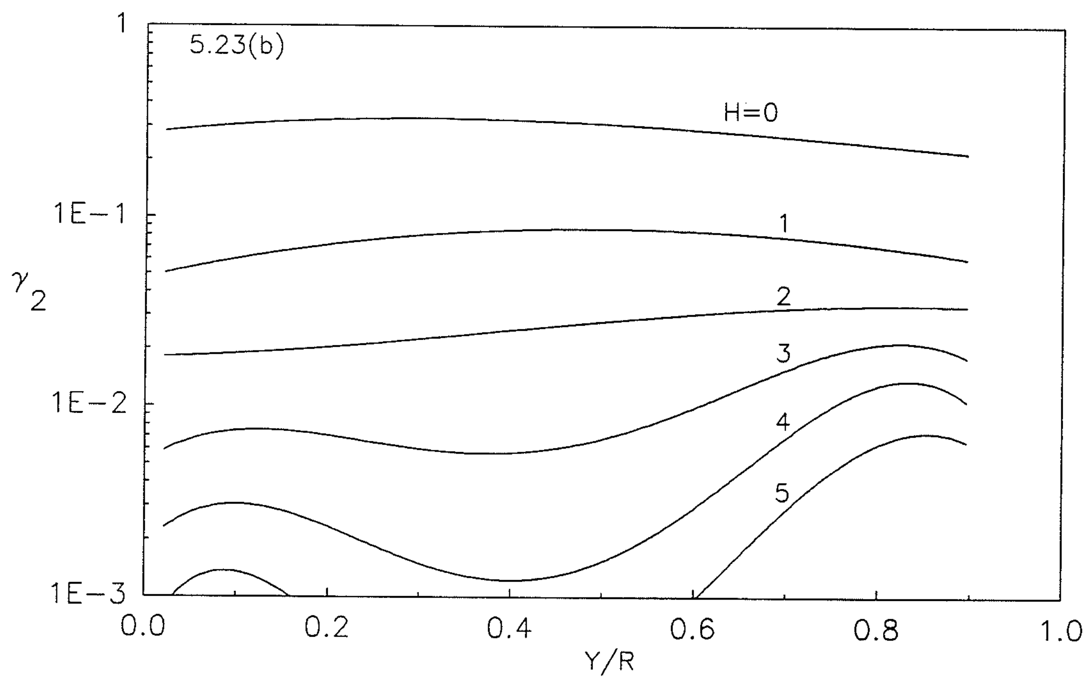

5.23(b)
1
1E−1
1E−2
1E−3
γ_2
H=0
1
2
3
4
5
0.0
0.2
0.4
0.6
0.8
1.0
Y/R

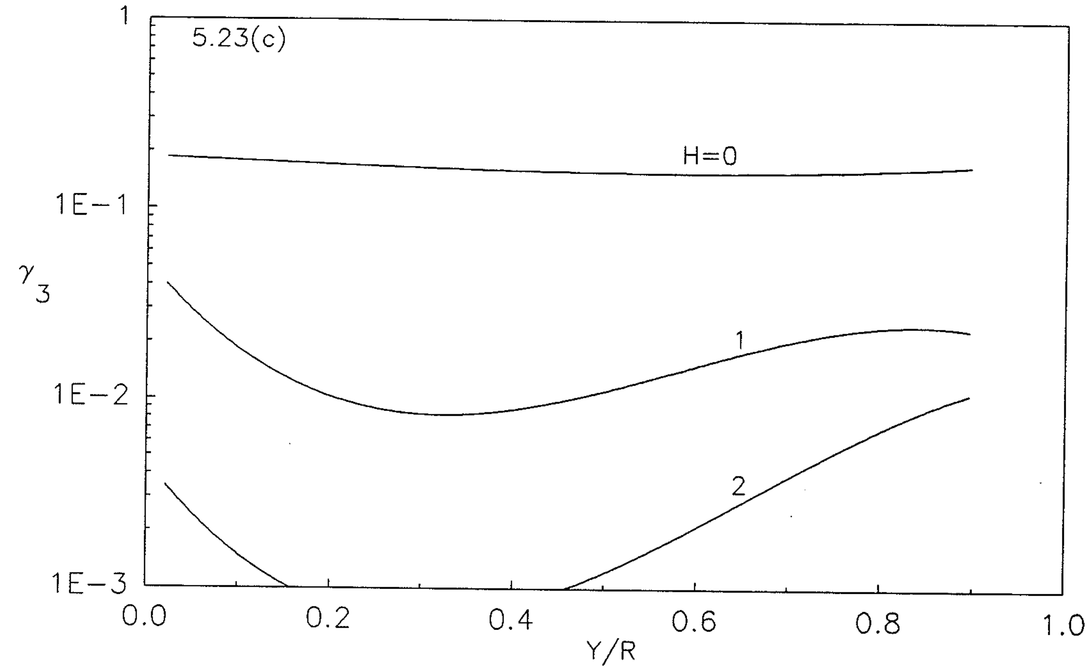

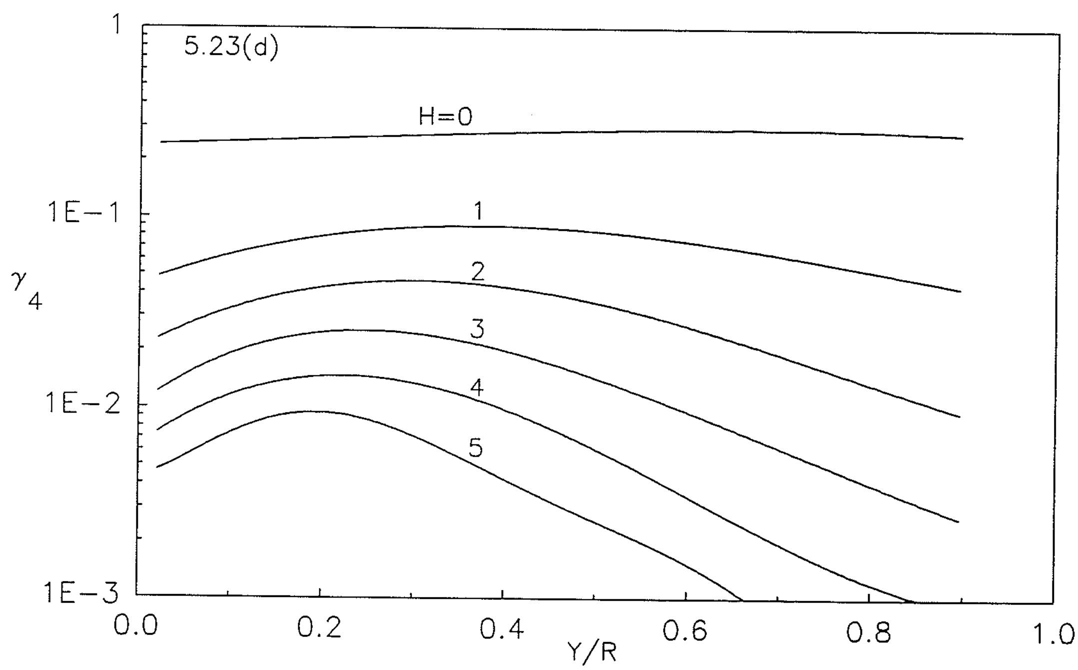

FIGURE 5.23: The distribution of the intermittency factor of $-\overline{uv}$ at station 66 as a function of the hole size (curve−fit of exp. points). (a) Outward int. (b) Ejections (c) Inward int. (d) Sweeps.

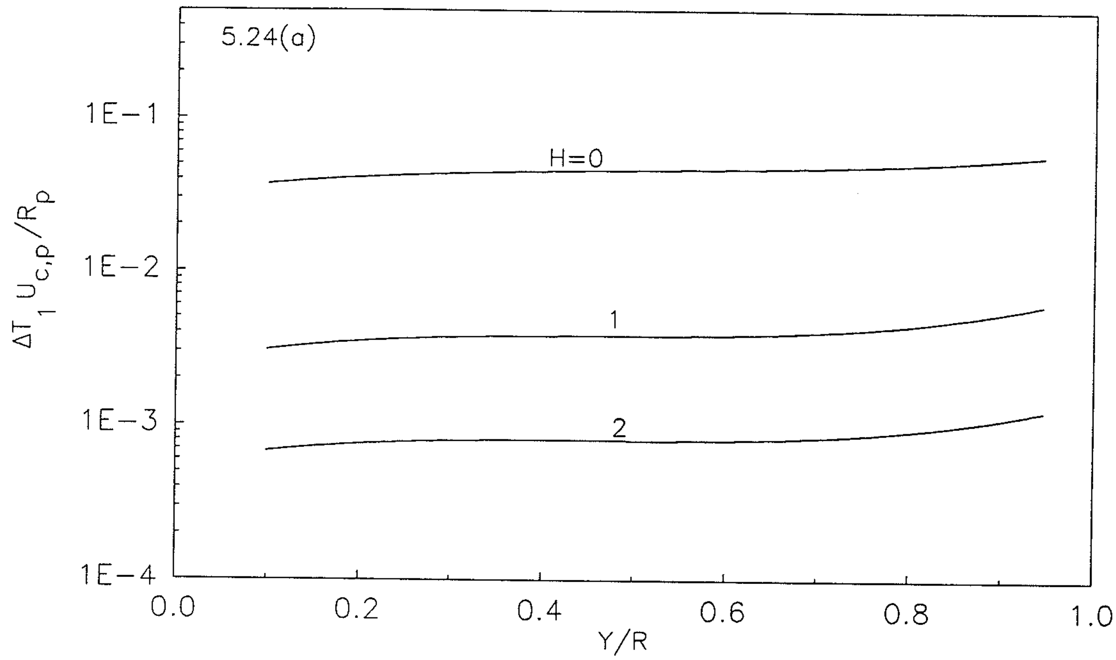
5.24(a)
H=0
1
2
1E−1
1E−2
1E−3
1E−4
$\Delta T_1 U_{c,p}/R_p$
0.0
0.2
0.4
0.6
0.8
1.0
Y/R

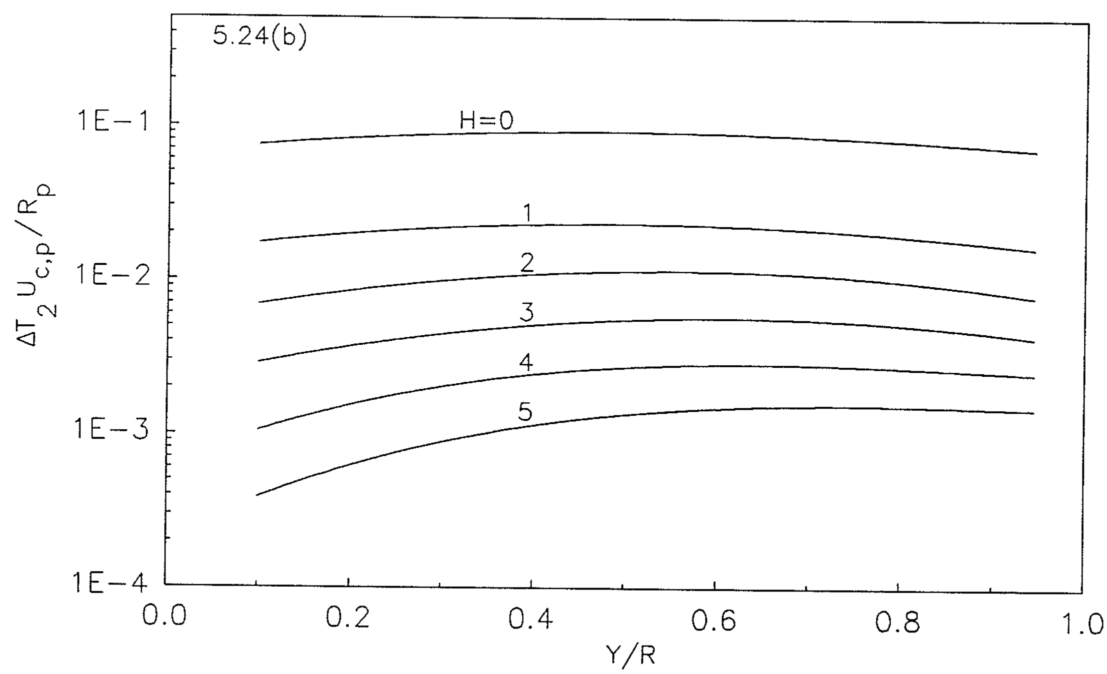
5.24(b)
H=0
1
2
3
4
5
1E−1
1E−2
1E−3
1E−4
$\Delta T_2 U_{c,p}/R_p$
0.0
0.2
0.4
0.6
0.8
1.0
Y/R

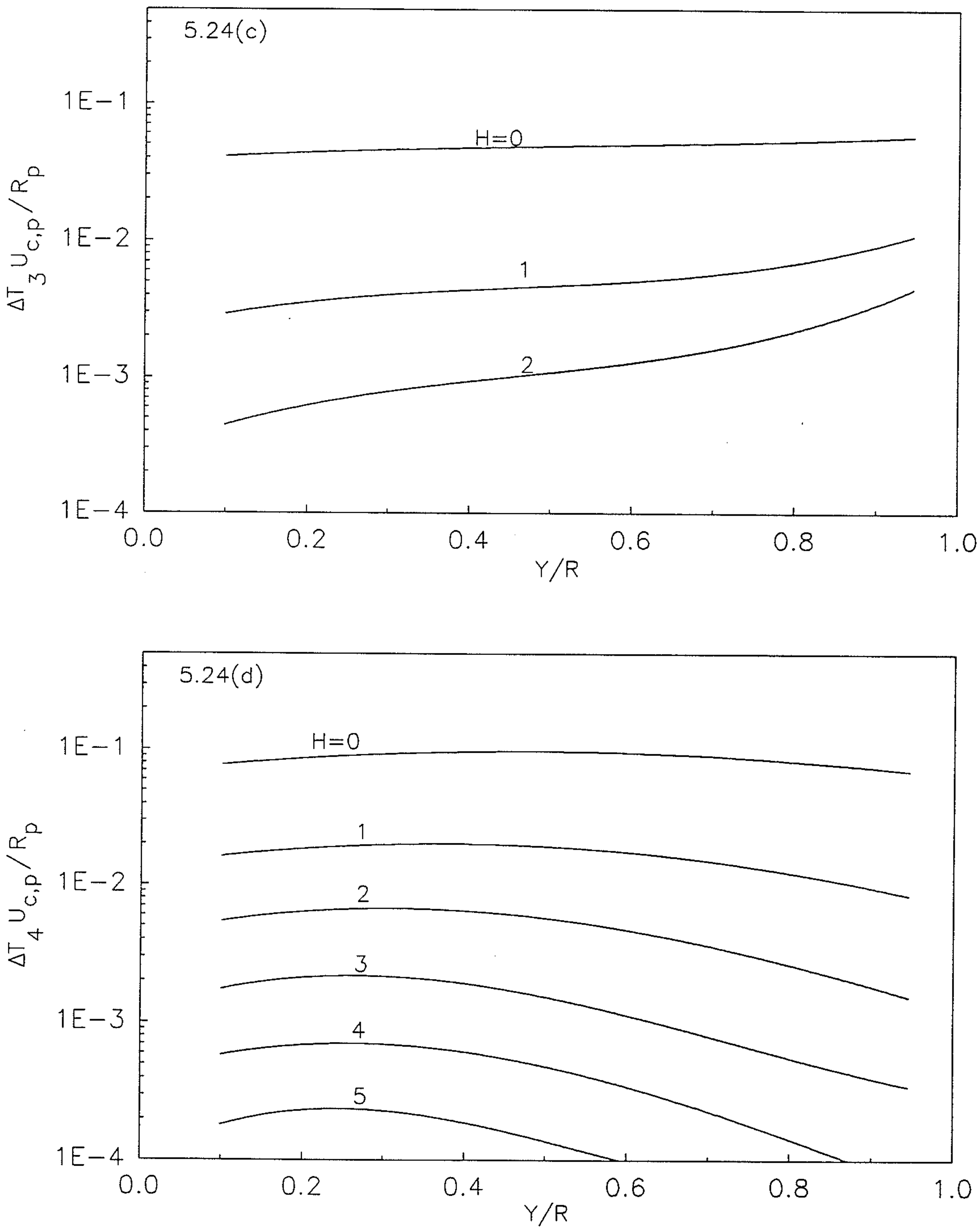

FIGURE 5.24: The distribution of the mean duration of events in pipe flow as a function of hole size (curve−fit of exp. points). (a) Outward int. (b) Ejections (c) Inward int. (d) Sweeps.

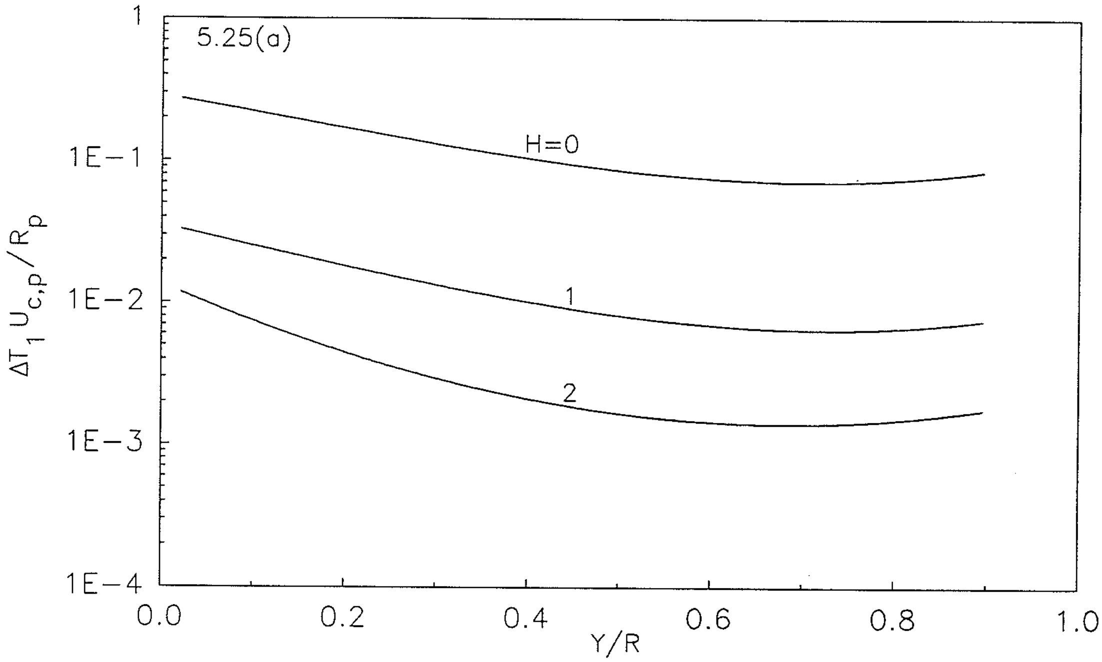
5.25(a)
H=0
1
2
1
1E−1
1E−2
1E−3
1E−4
0.0
0.2
0.4
0.6
0.8
1.0
Y/R
$\Delta T_1 U_{c,p}/R_p$

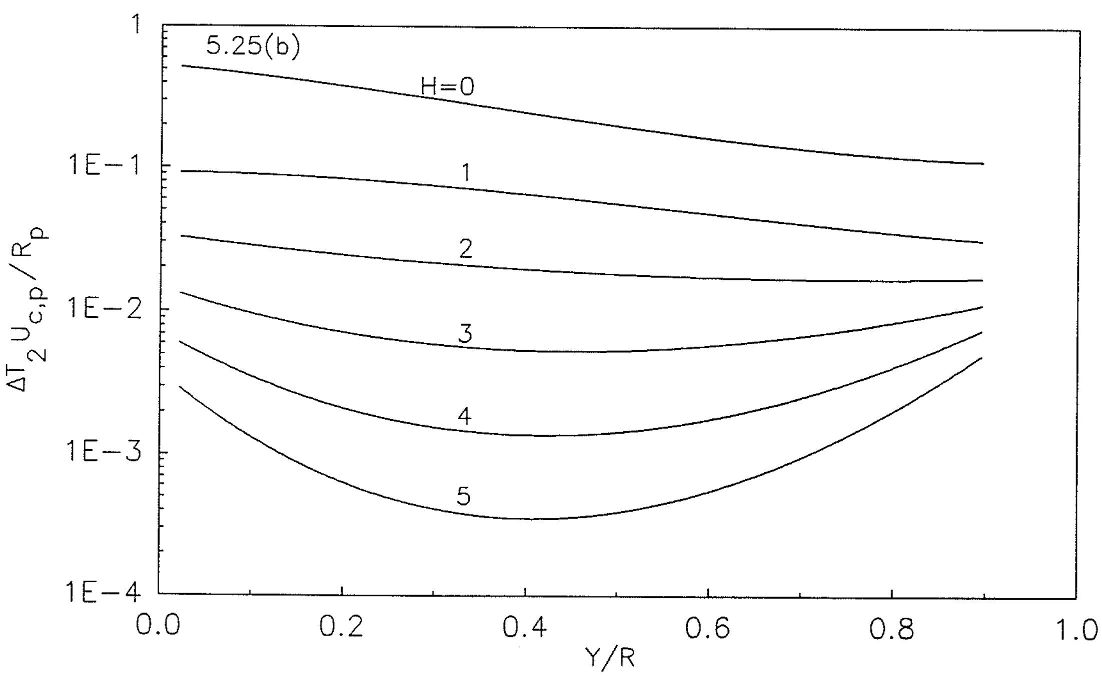
5.25(b)
H=0
1
2
3
4
5
1
1E−1
1E−2
1E−3
1E−4
0.0
0.2
0.4
0.6
0.8
1.0
Y/R
$\Delta T_2 U_{c,p}/R_p$

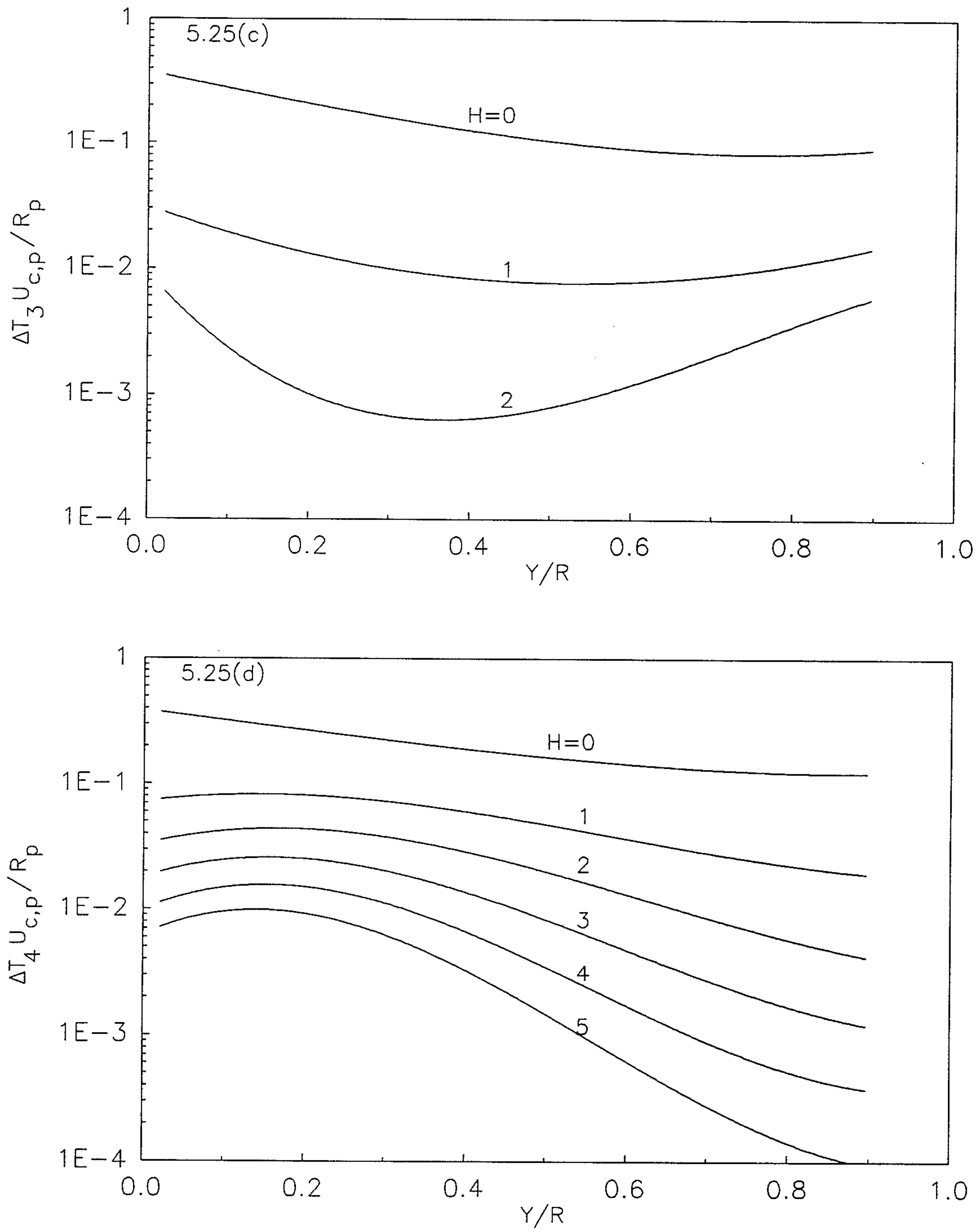

FIGURE 5.25: The distribution of the mean duration of events at station 66 as a function of hole size (curve−fit of exp. points). (a) Outward int. (b) Ejections (c) Inward int. (d) Sweeps.

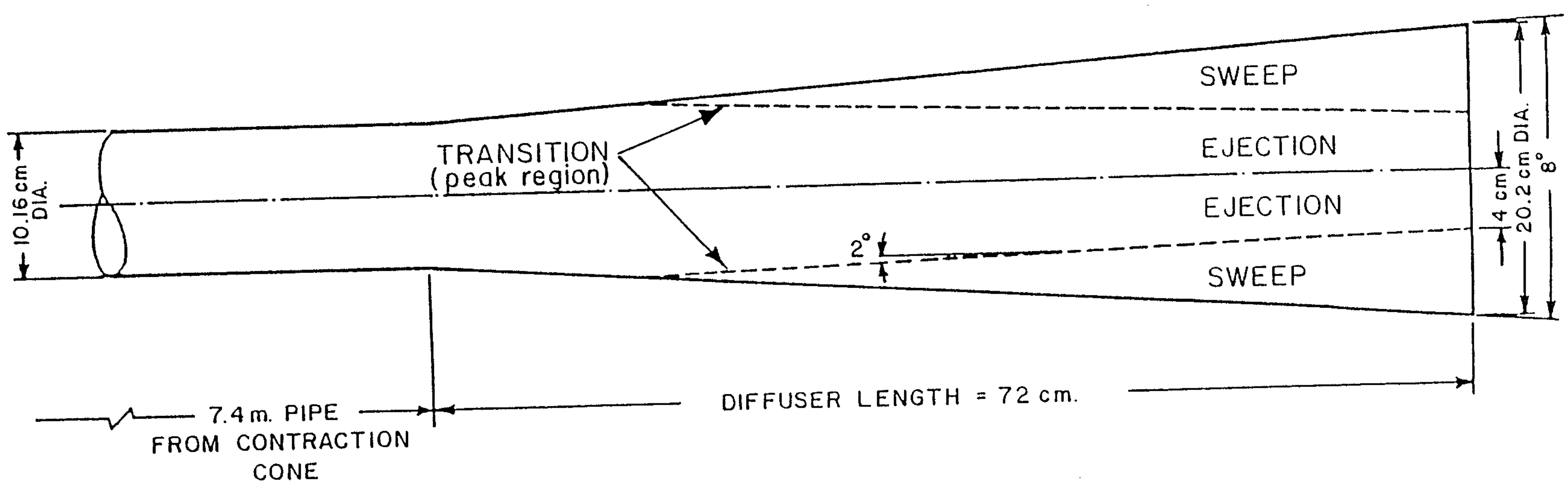

FIGURE 6.1: Sketch of the dominating coherent motions in the diffuser flow.

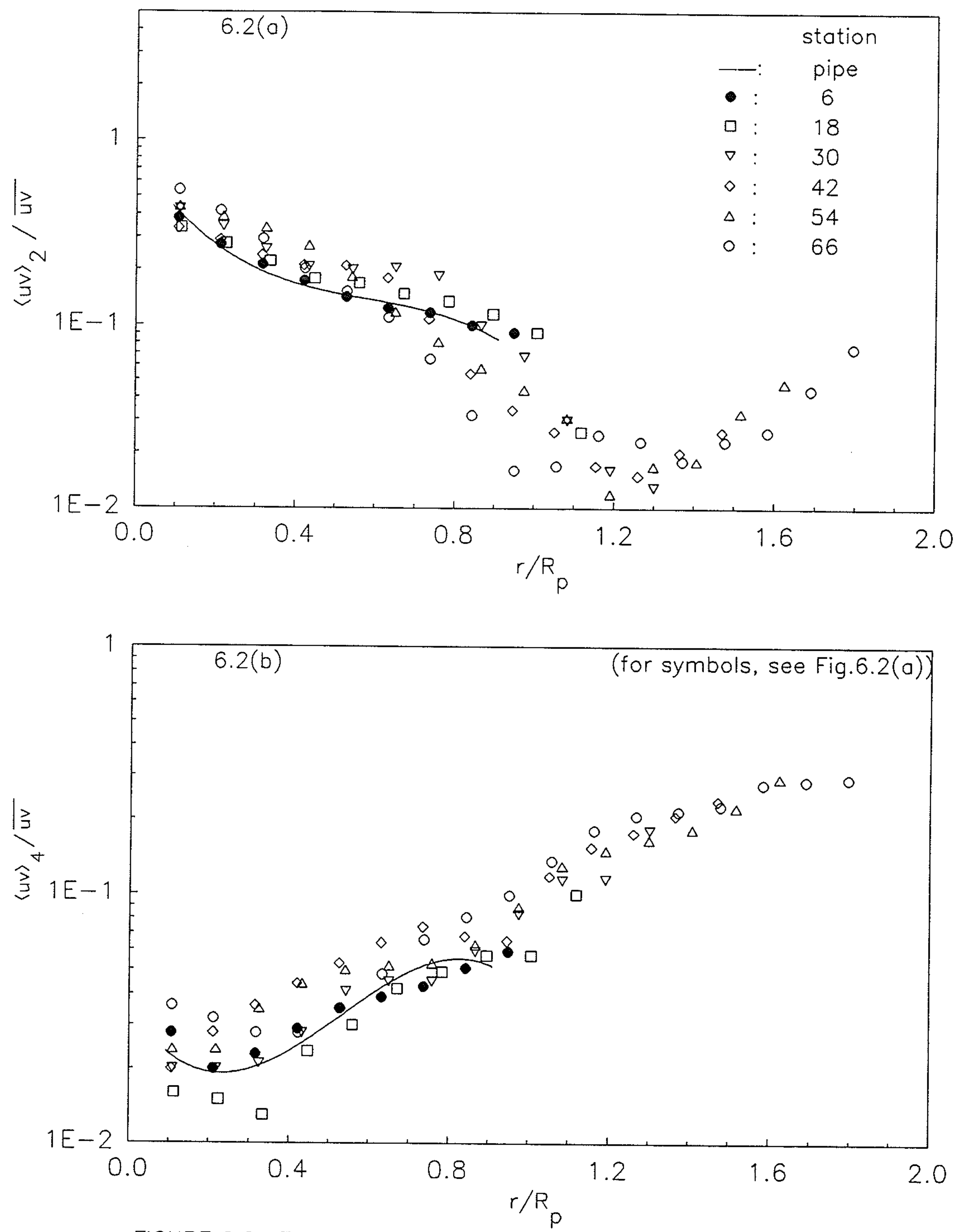

FIGURE 6.2: The distribution of conditional averages of strong events (H=4) pipe and diffuser flows.
(a) Ejections (b) Sweeps

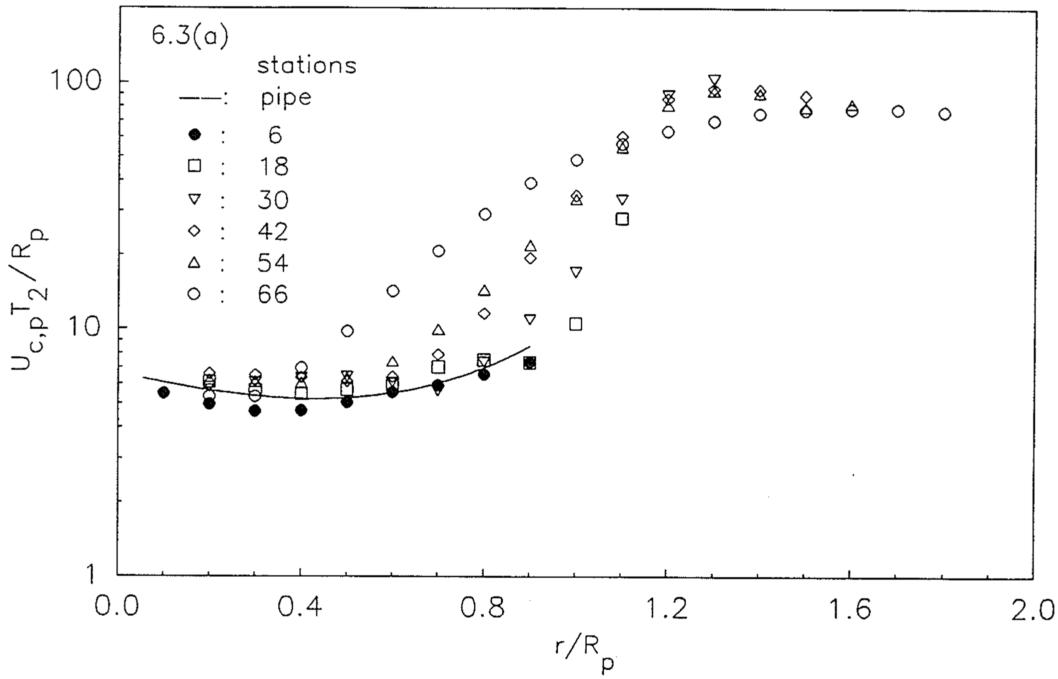

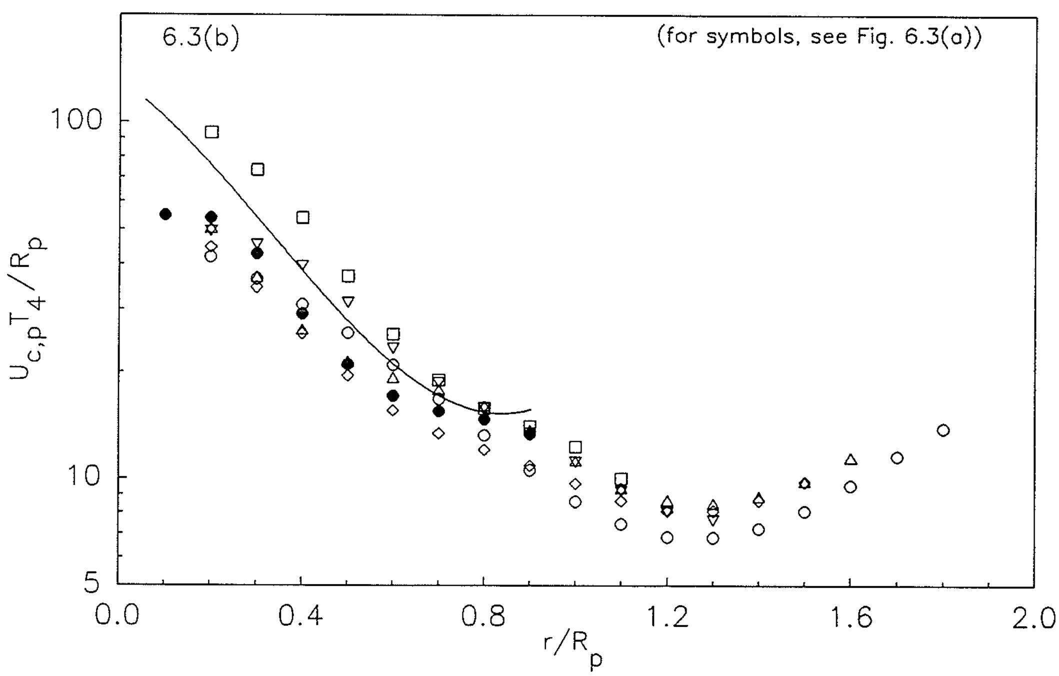

FIGURE 6.3: The distribution of the mean periods between 'strong events' (H=4) in the pipe and diffuser flows.
(a) Ejections (b) Sweeps.

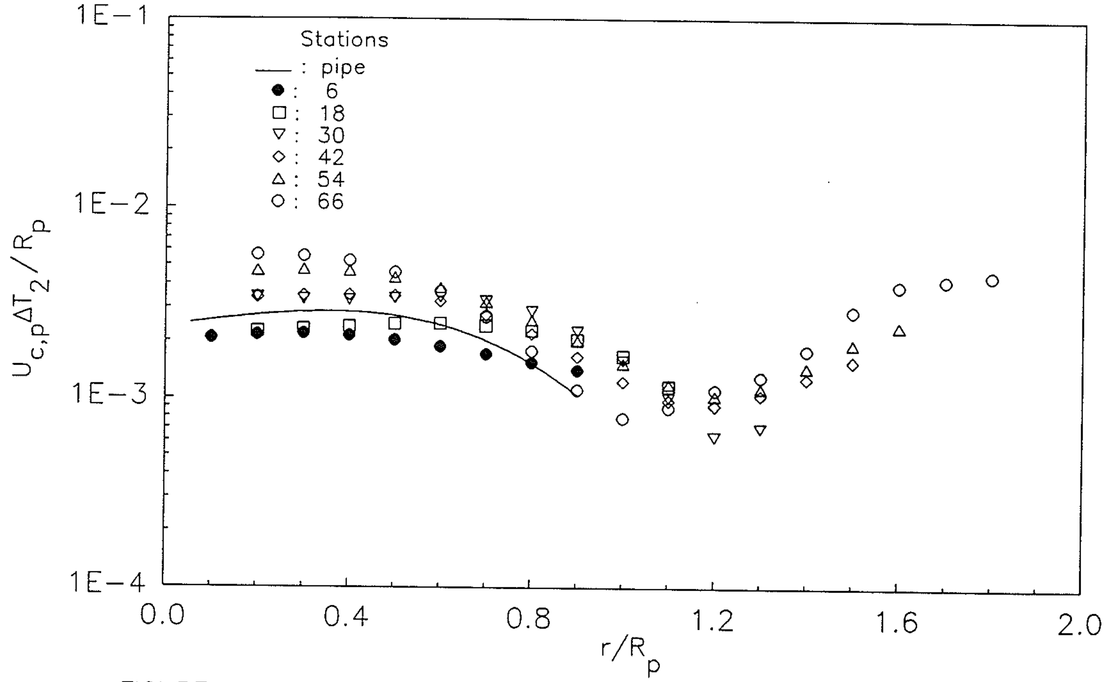

FIGURE 6.4: The distribution of the mean durations of 'strong ejections' (H=4) in the pipe and diffuser flows.

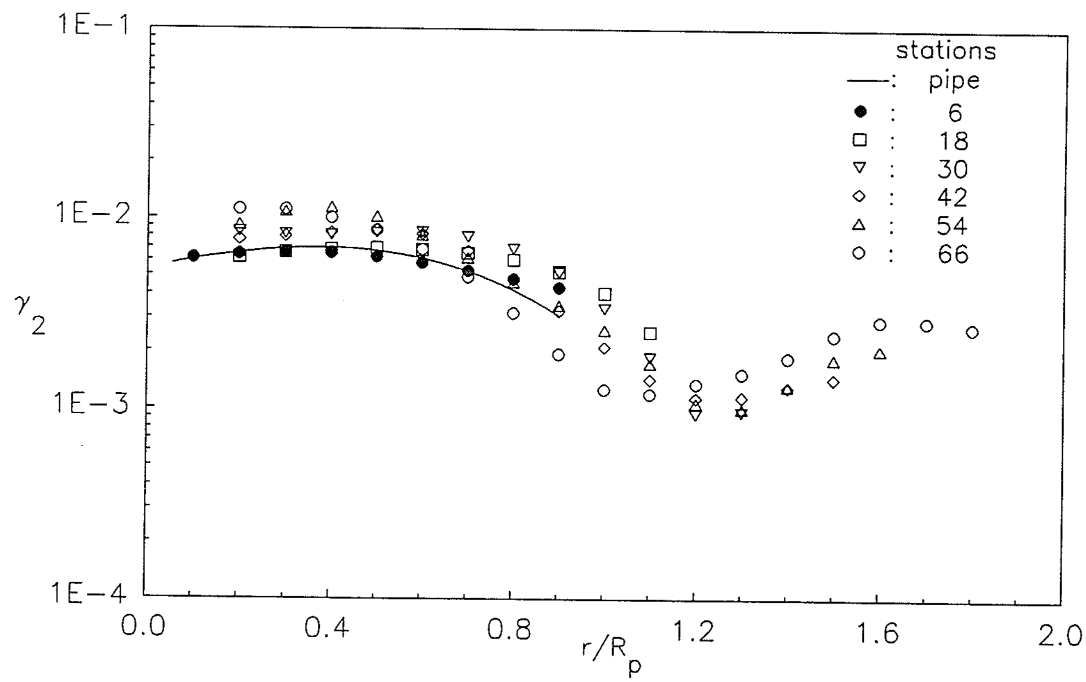

FIGURE 6.5: The distribution of the intermittency factor of uv during 'strong ejections' (H=4) in the pipe and diffuser flows.

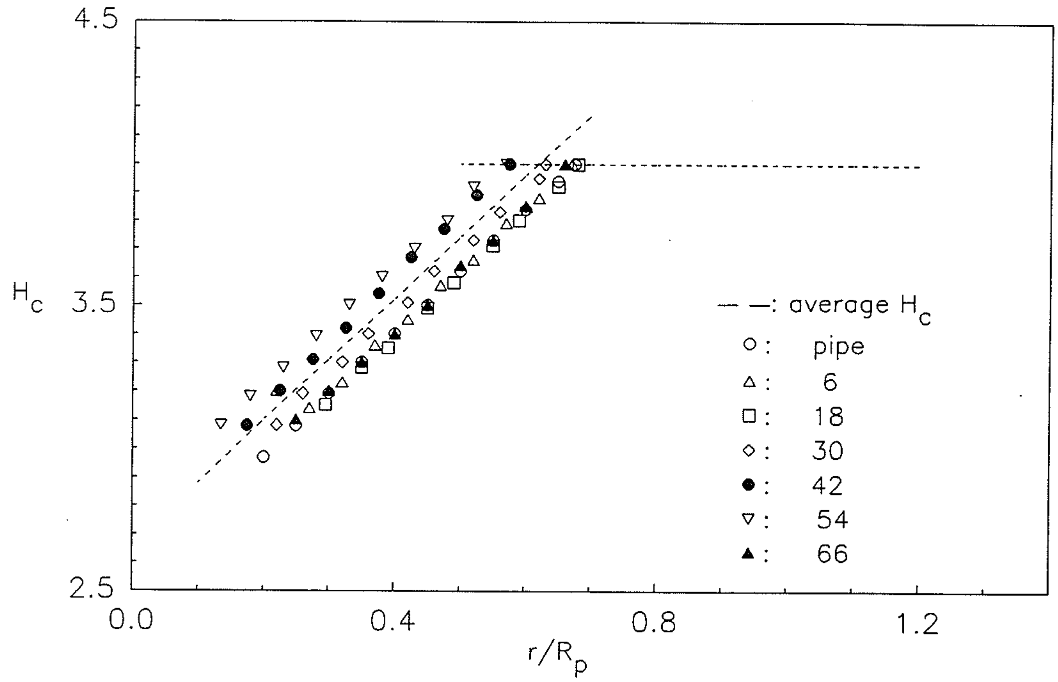

FIGURE 6.6: Variation of the characteristic hole size across the pipe and diffuser stations.

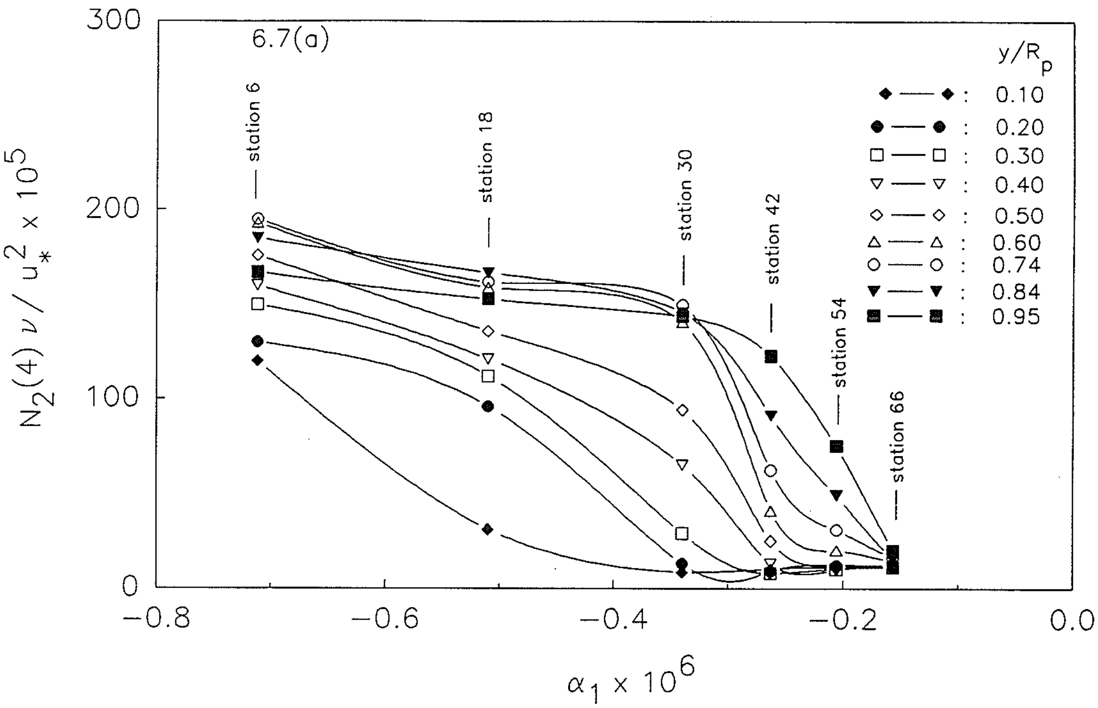

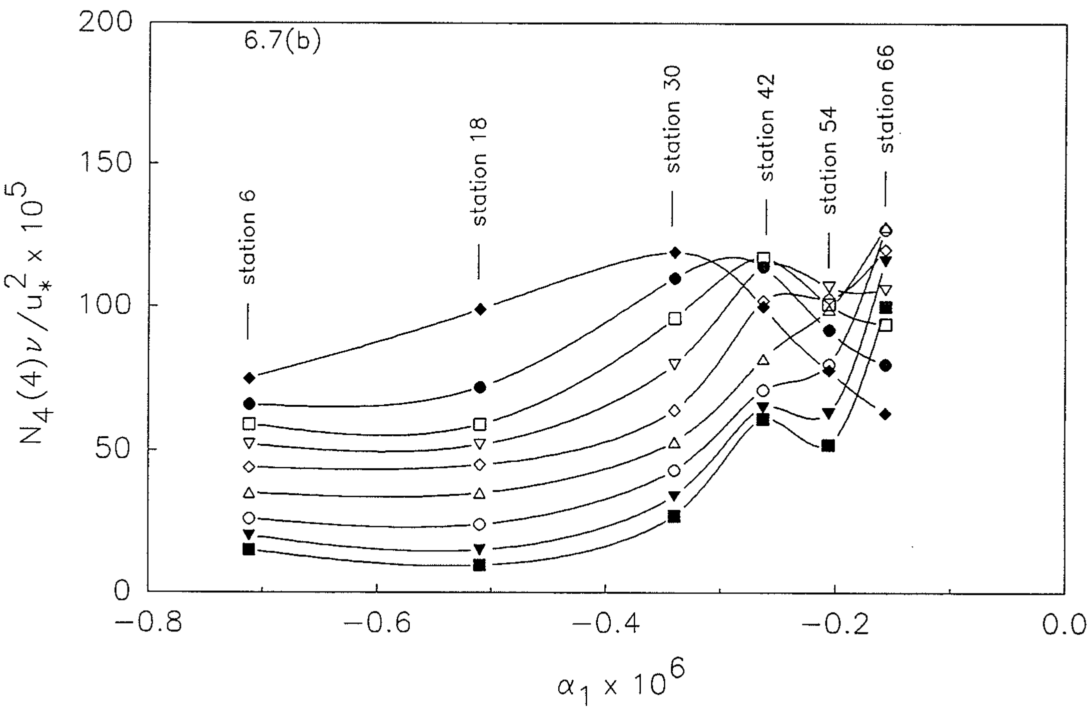

FIGURE 6.7: The average frequency of strong events in the diffuser flow as a function of the non dimensional pressure gradient parameter. (a) Ejections (b) Sweeps.

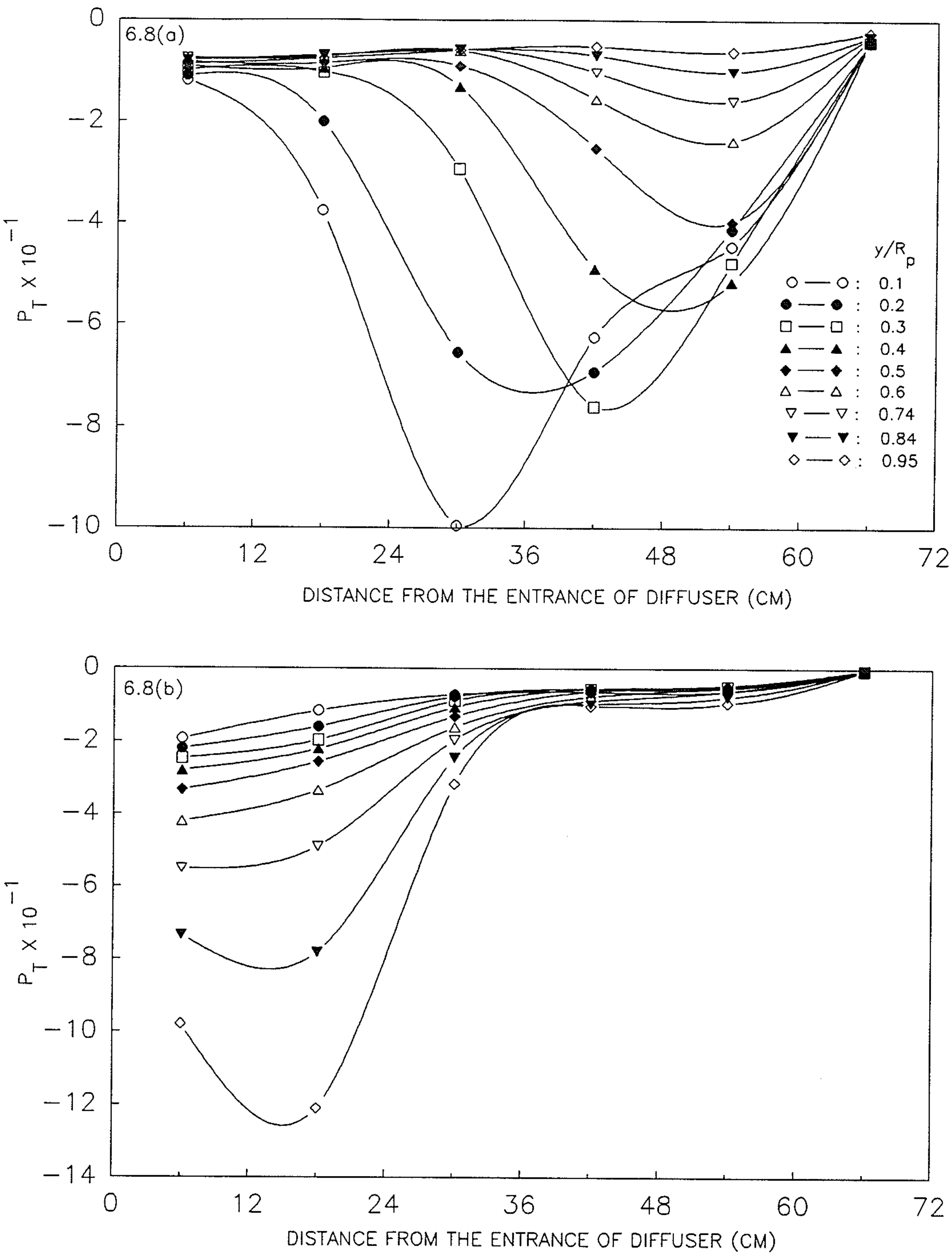

FIGURE 6.8: The variation of the non-dimensional parameter P_T in the diffuser flow.– (a) Ejections (b) Sweeps.

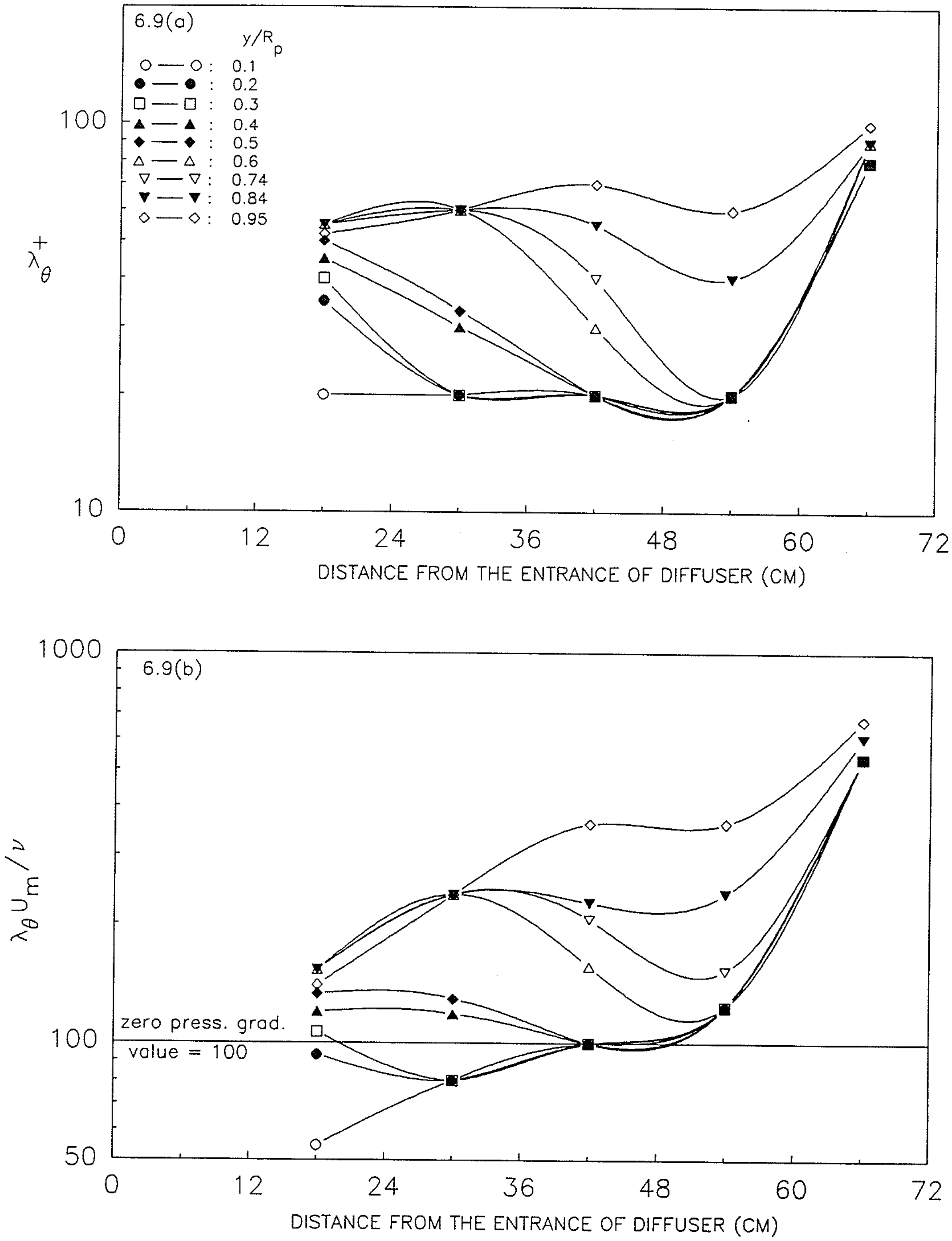

FIGURE 6.9: Variation of the non-dimensional spanwise spacings between strong ejections. (a) normalized with wall variables (b) normalized with U_m

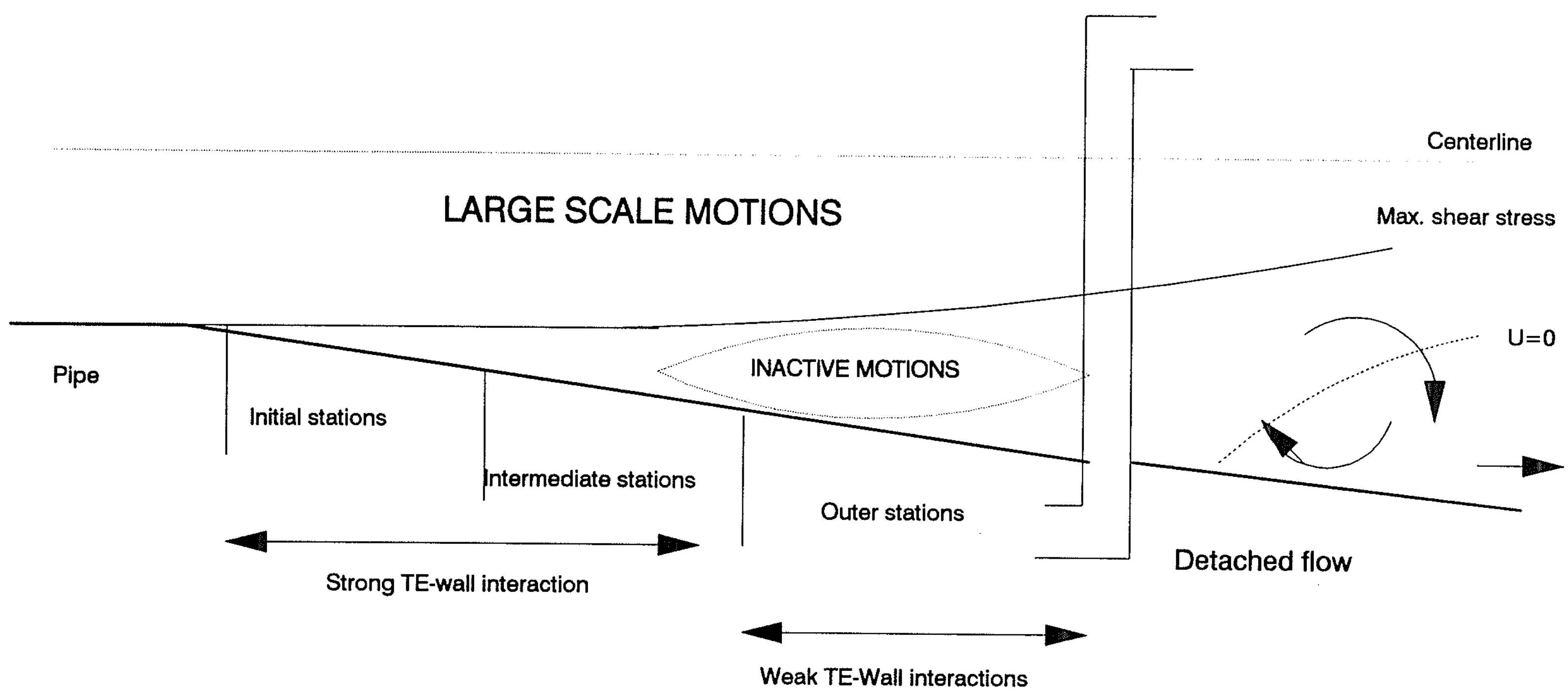

FIGURE 6.10: A flow model for the wall region of the diffuser.

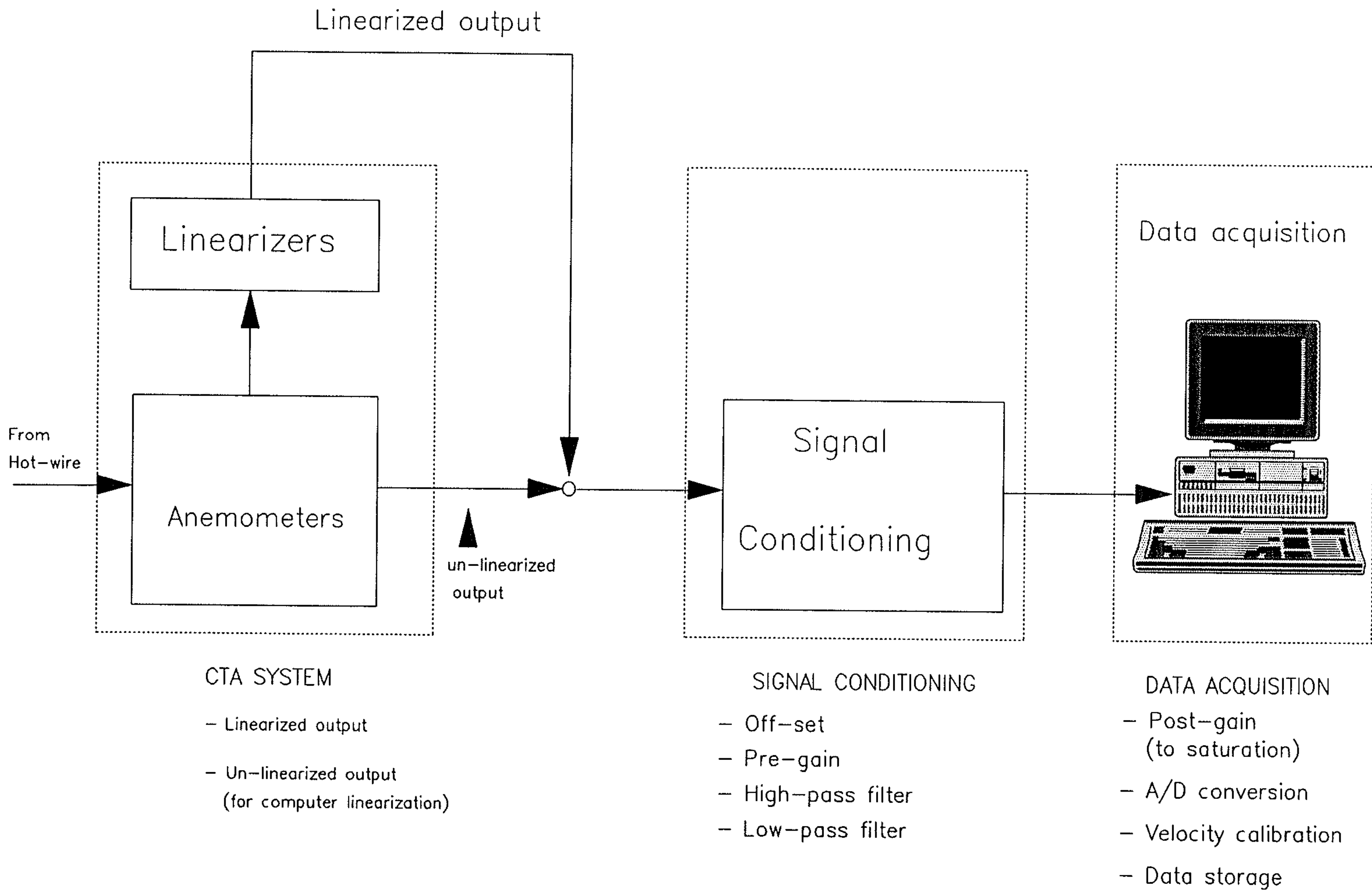

FIGURE A.1: Block diagram for signal processing sequence.

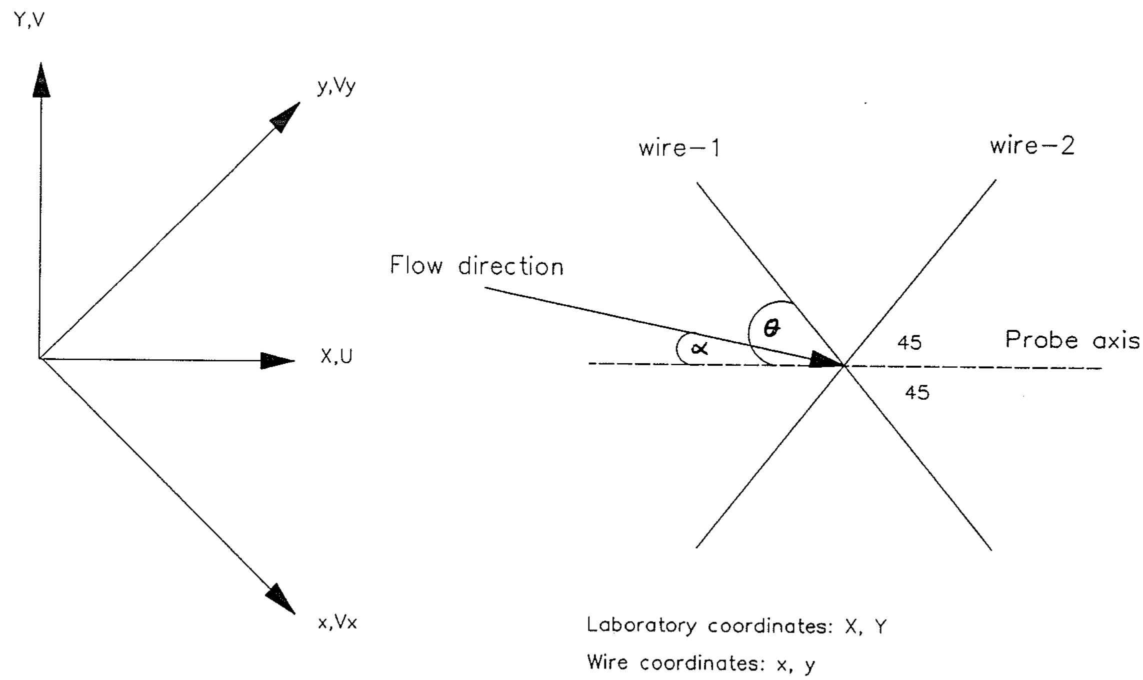

FIGURE A.2: Wire and laboratory coordinates in relation to x−wire.

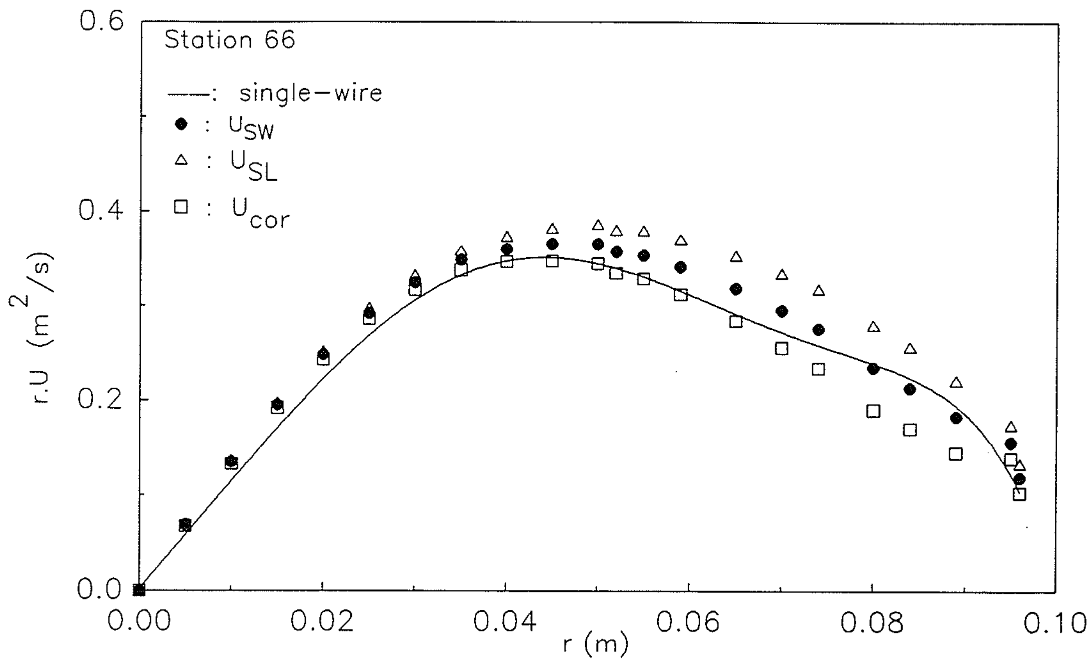

FIGURE B.1: Graphical procedure for correcting mean velocity obtained from pressure probes. See Equation B6.

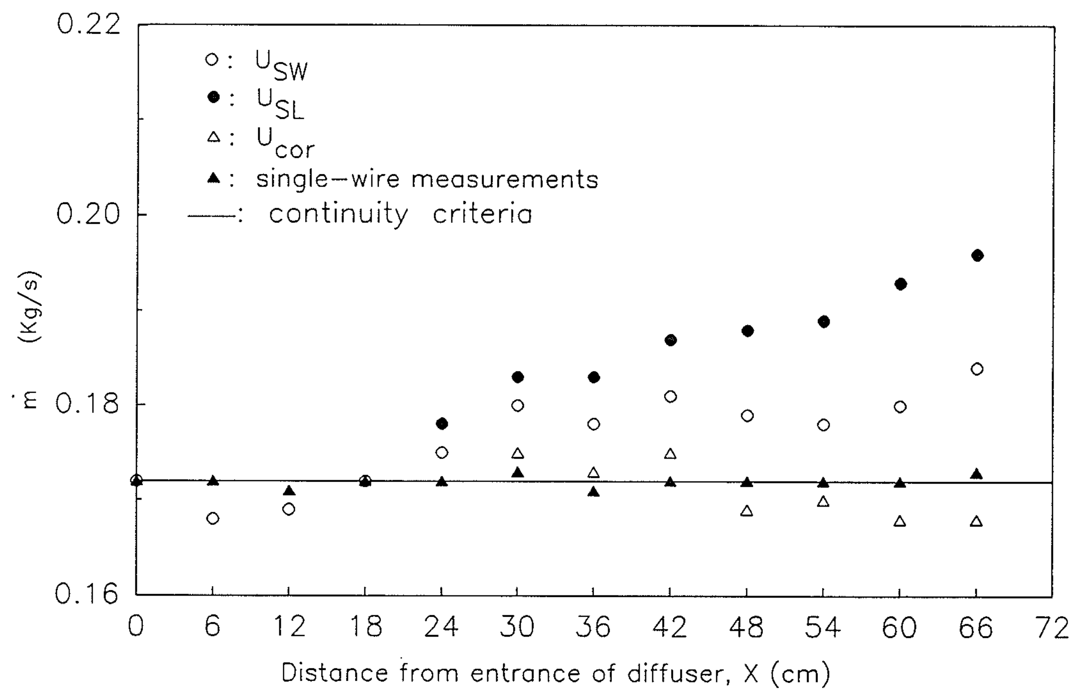

FIGURE B.2: Mass flow rate across the pipe and diffuser flows.

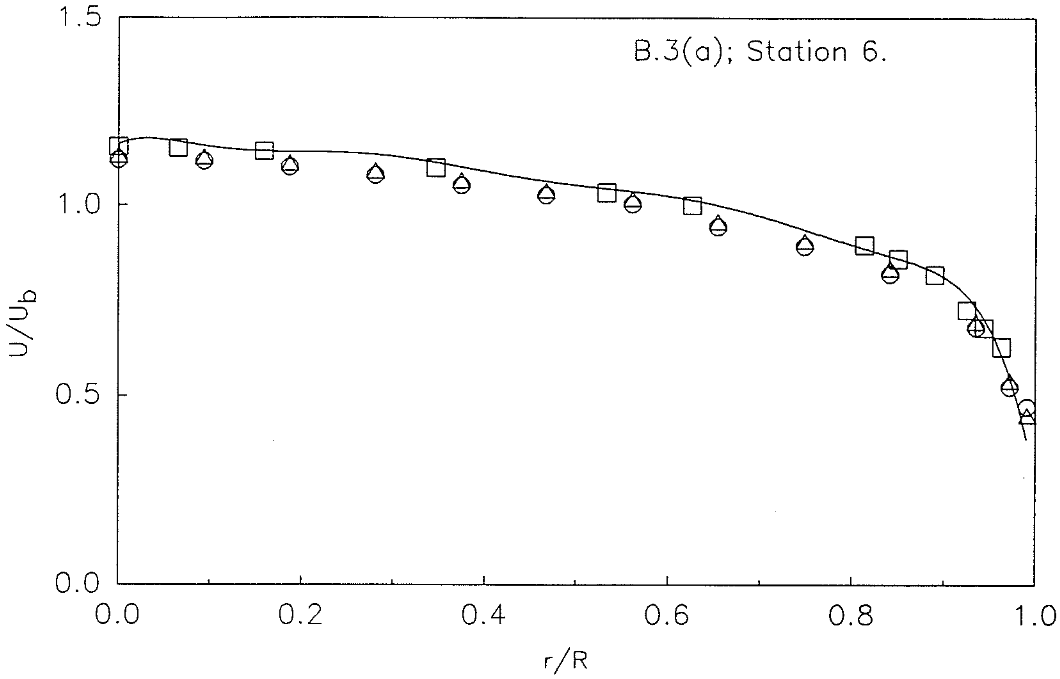

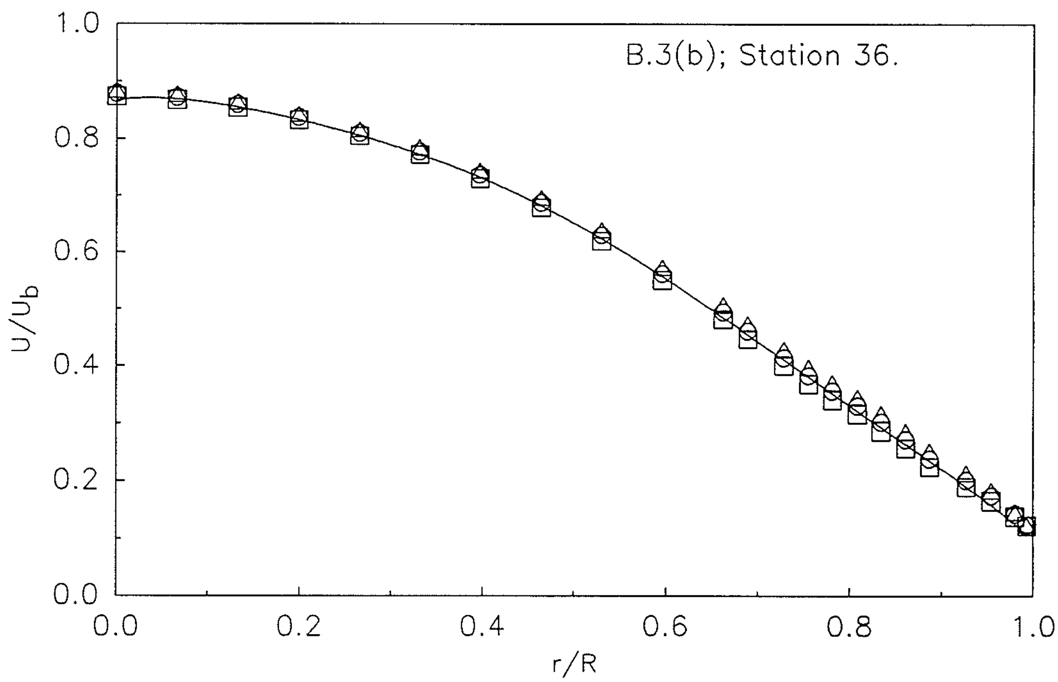

(For legend, see Fig. B.3(c))

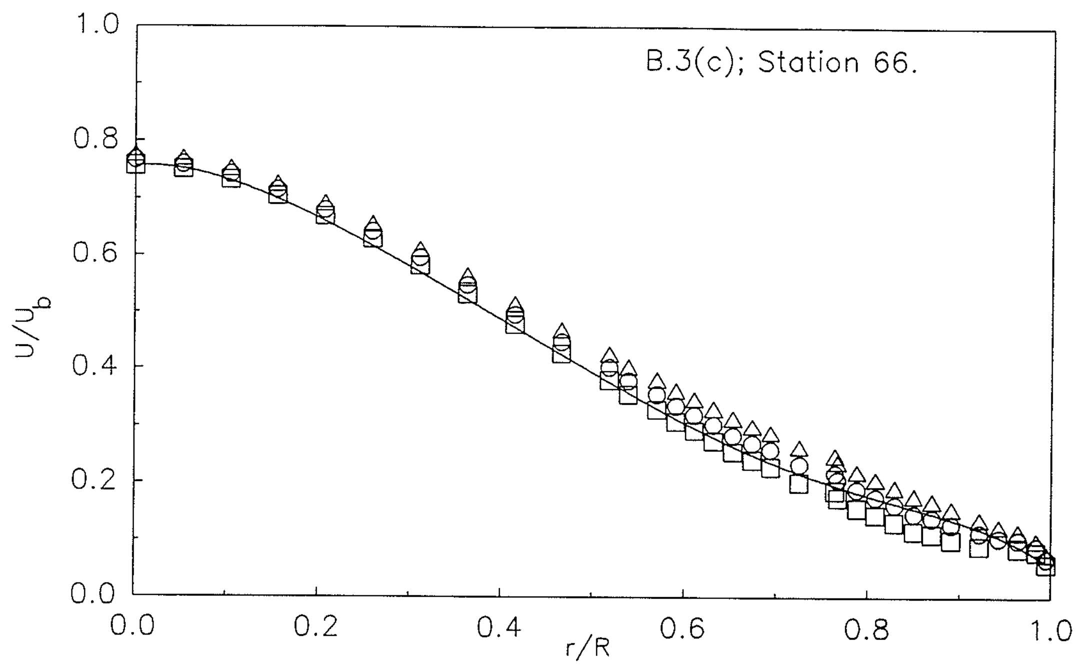

FIGURE B.3: Measured and corrected mean velocity profiles. — , hot-wire; ○ , U_{SW}; △ , U_{SL}; □ , U_{cor} (from Eq. B6 or Eq. B13). U_b=18.2 m/s (average mean velocity across the pipe).

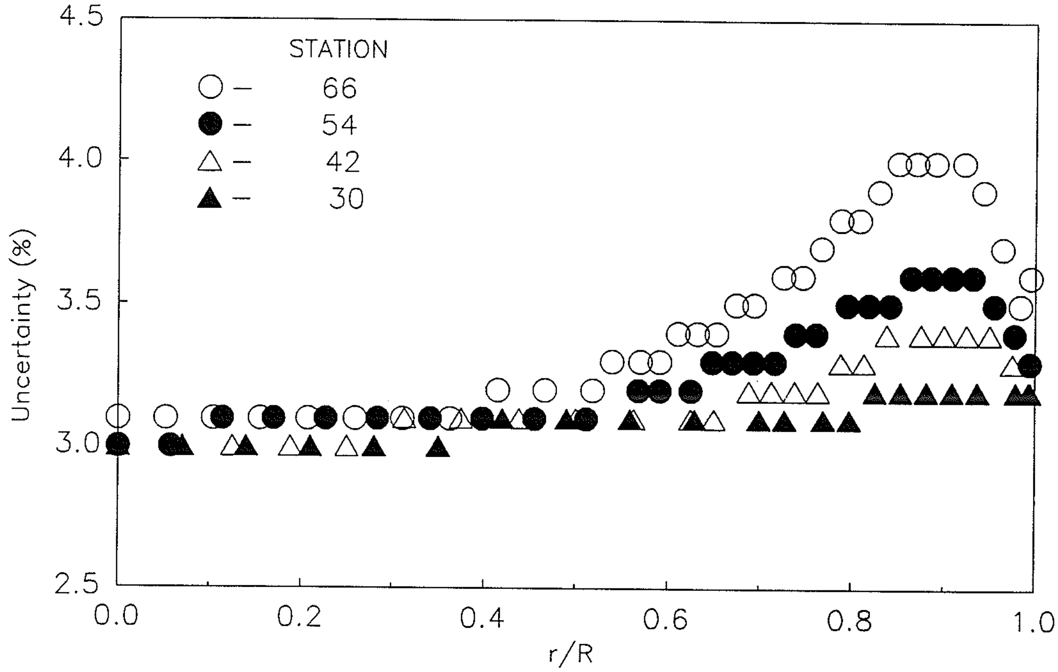

FIGURE B.4: Uncertainty analysis of the empirical correction for mean velocity.

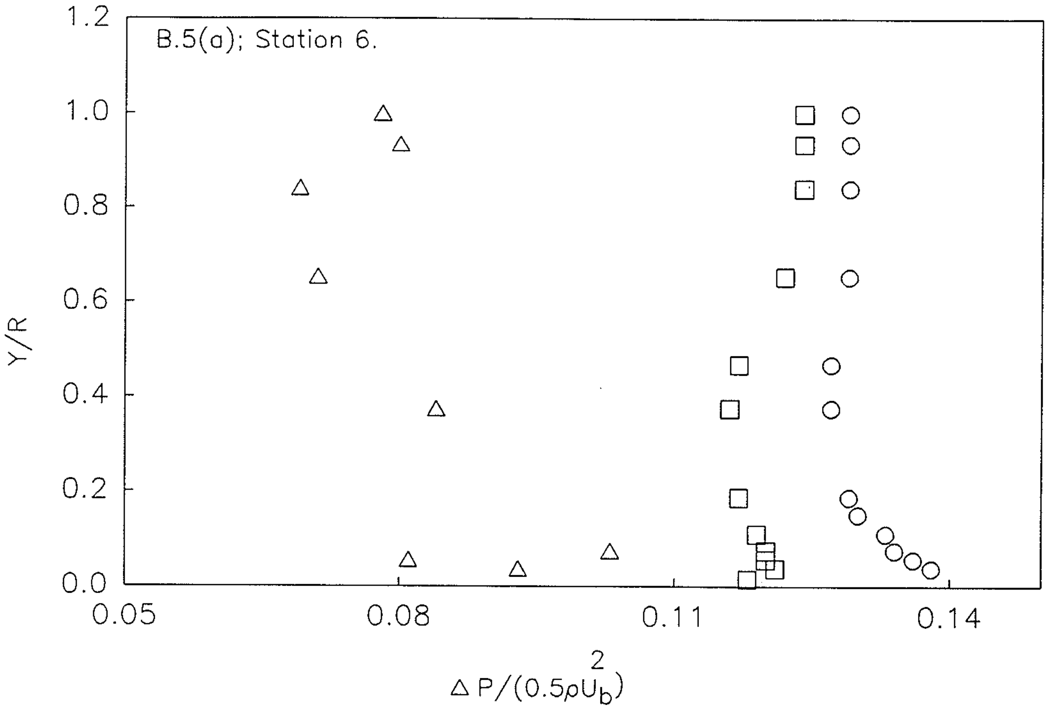

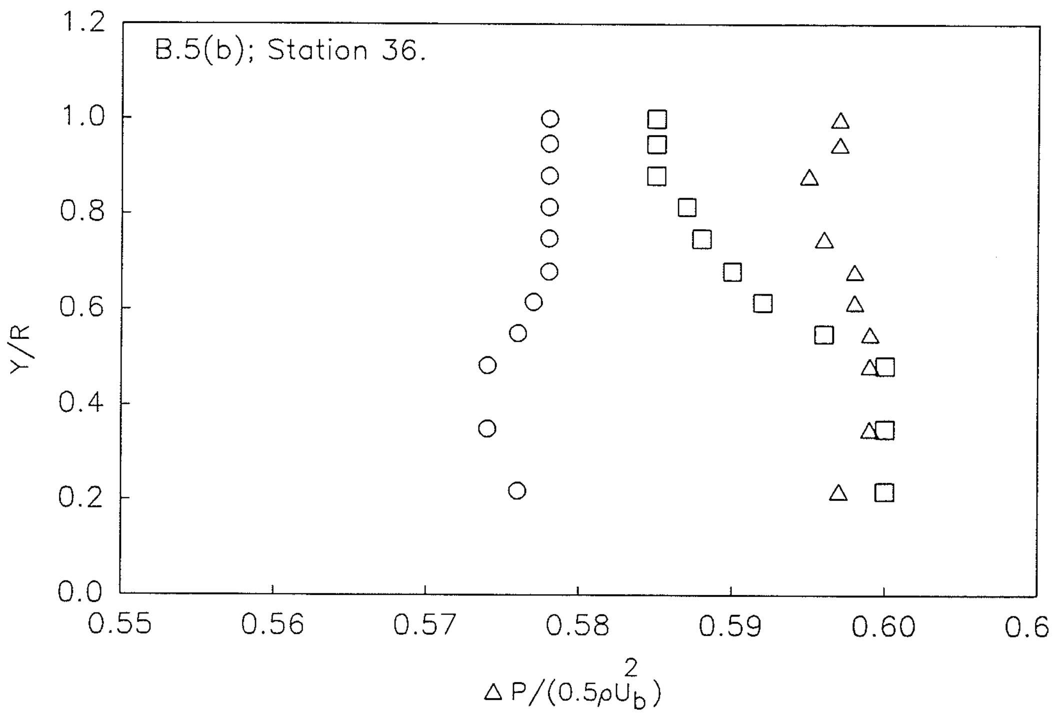

(For legend, see Fig. B.5(c))

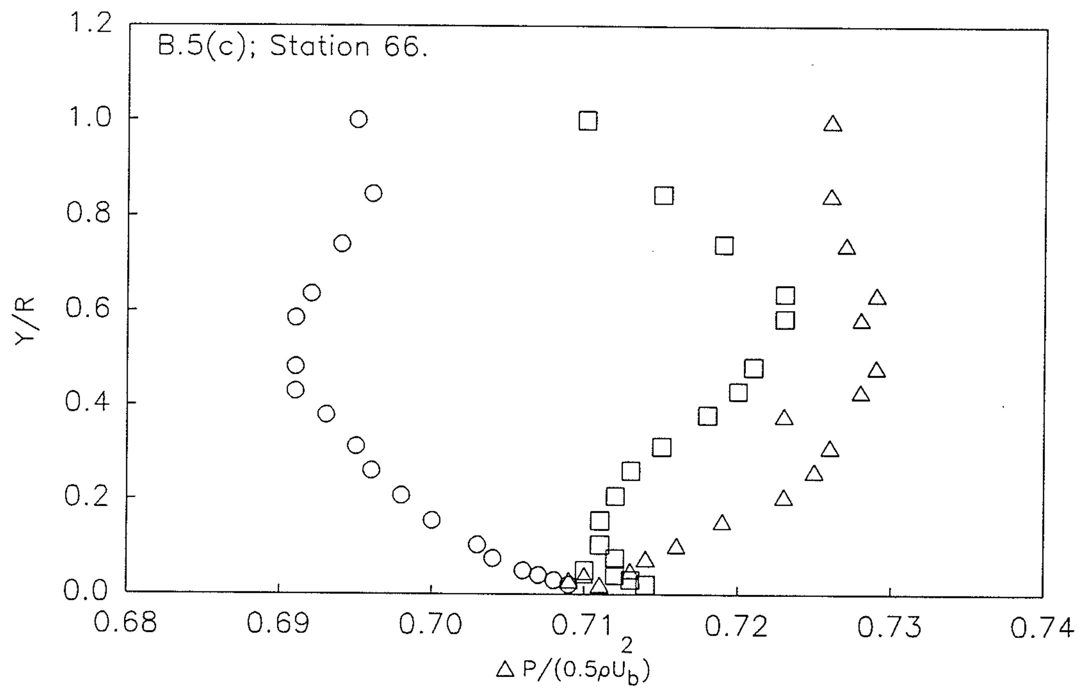

FIGURE B.5: Static pressure corrections. ○ – measured, △ – Corrected (Eq. B13), □ – Corrected (Eq. B12 with A'=1)

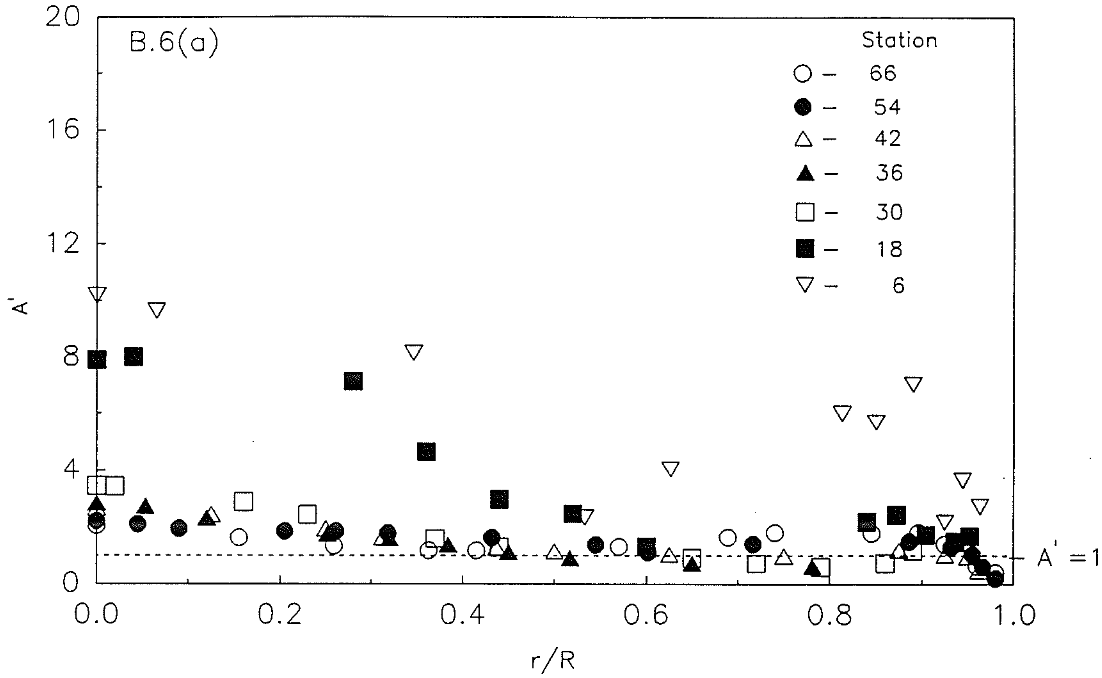

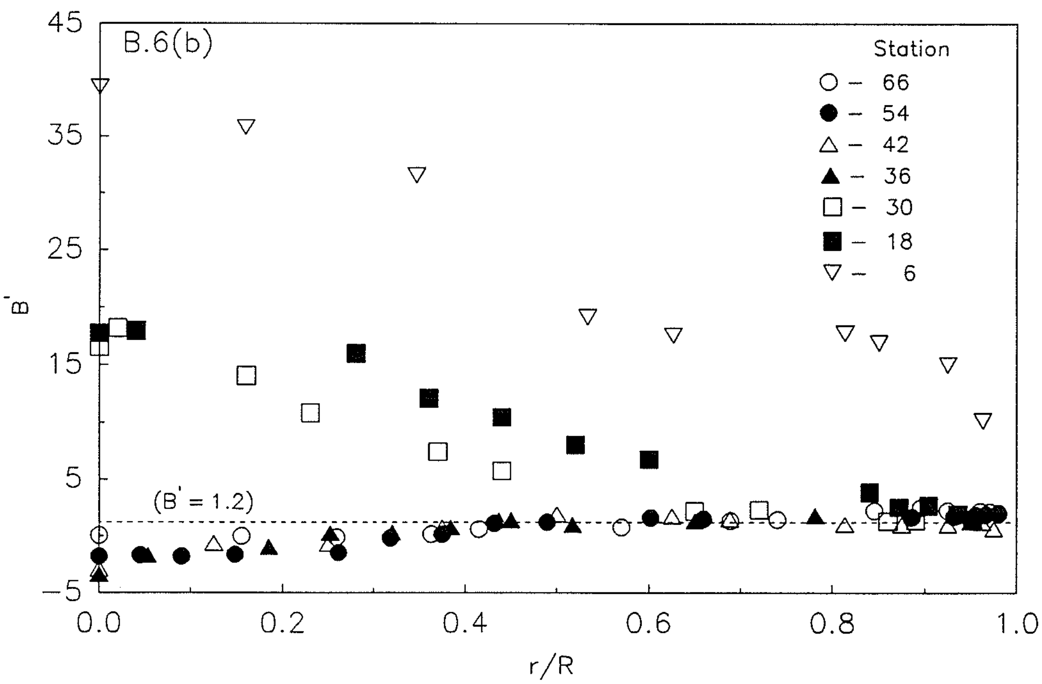

FIGURE B.6: Calibration constants of pressure probes.
(a) Static tube constant (b) Pitot tube constant.